Chemotype Exploration of Potential Tau Aggregation Therapeutics

A thesis submitted in fulfilment of the
requirements for the degree of

Doctor of Philosophy

by

Alexander Gee

2023

The University of Sydney
Faculty of Science
School of Chemistry

Table of Contents

Declaration

This thesis is a summary of research performed by the author in the School of Chemistry, University of Sydney, under the supervision of Professor Michael Kassiou between July 2019 and June 2023. This thesis contains no material which has been accepted for the award of any degree at any university. No other individual's work has been used without recognition and every effort has been made to acknowledge previously published material. This thesis contains less than 80,000 words.

Alexander Gee

As the supervisor for the candidate upon which this thesis is based, I can confirm that the authorship attribution statements above are correct.

Professor Michael Kassiou

Acknowledgements

The journey of the PhD has been a long and tumultuous one but will be an experience I will cherish for the rest of my life. Words cannot describe the invaluable lessons I have learnt in both independence and perseverance.

First and foremost, I would like to thank my supervisor Professor Michael Kassiou for allowing me the opportunity to undertake this research while providing an environment where I could govern the direction of my project. Design and synthesis of small molecules has always been a dream of mine and you have given me the freedom to do just that. Additionally you have been in great support of me over the years and words cannot describe how appreciative of that I am. I will certainly miss your humour on those days when you wandered into the lab or the office sharing a new joke.

To my colleagues Dr. Andrew Montgomery and Dr. Timothy Callis, you have been a pleasure to work beside and your guidance, mentorship and of course friendship over the years is greatly appreciated. In addition I would also like to thank Dr. Jakob Lane for his support and friendship. You have all taken time out of your days to help me and for that I am forever grateful.

Members of the Kassiou group both past and present have helped considerably in shaping this experience into something incredible. There was never a dull moment within the lab or a lull in office banter and their support through the tough times is highly treasured. Thank you for providing a fantastic work environment and I hope to share many more moments with those who I have become great friends with outside of the lab.

Thank you to the technical staff Dr. Ian Luck at NMR, Dr. Nicholas Proschogo from the MS facility as well as the technical officers Yuen Cheng and Carlos Piscicelli for all your assistance through the years.

To my parents, I am forever grateful for your support throughout these years. Without your assistance I would not have made it this far. You have always been there for me regardless of the circumstances and I could never thank you enough. Thank you to all my friends for tolerating me and being there when I needed it.

Finally, to my wonderful partner Catherine. You have supported me unconditionally and have been beside me (literally) the whole time. Here's to the next chapter of our lives.

Abstract

Current amyloid- and cholinergic-centric treatments of Alzheimer's disease (AD) have had little success to date in respect to disease-modifying therapies. Taucentric therapeutics are now a strongly pursued area for treatment of AD. The defining pathologies of AD are distinctive neurofibrillary lesions including neurofibrillary tangles (NFT), neuropil threads and dystrophic neurites that are a result of intracellular depositions of aggregated cortical tau protein deposits. Although tau-based therapeutics have mainly aimed to disrupt aggregation either directly or *via* kinase inhibition, tau-mediated neurodegeneration may potentially be a result of either soluble misfolded, hyperphosphorylated and/or mislocalised forms of tau.

Natively, tau is an unfolded protein that can take on aberrant conformational changes *via* induced misfolding of soluble tau, thus leading to the accumulation of insoluble tau aggregates and stress to the cell. Molecular chaperones, such as heat shock proteins, are a family of polypeptides with upregulated expression during times of stress that ensure cells maintain an ability to regulate various processes of protein homeostasis. This includes the refolding of misfolded and/or aggregated protein *via* adenosine triphosphate (ATP) catalysed processes as well as targeting irreparable proteins for degradation by the ubiquitin-dependent proteasomal degradation pathway. However, in the case of pathological events the processes by which protein undergoes quality control can lead to accumulation of misfolded protein, due to either a mutation or overwhelming quantities of client proteins.

Heat shock protein 90 kDa (Hsp90) is one such example of a molecular chaperone that plays a fundamental role in homeostatic regulation, including mediation of tau. Unfortunately, the targeting of Hsp90 specifically has led to pharmacological issues due to the chemical structure of inhibitors, as opposed to their chemical target. The use of co-chaperones accompanying these heat shock proteins could allow for more specific targeting while modulating substantially lower processes and thus minimising off-target effects. It has been demonstrated that ATPase homolog 1 (Aha1), a co-chaperone of Hsp90, drives the production of pathological tau aggregates. Thus, Aha1 is a viable novel target to approach the treatment of tau aggregation.

To overcome this pharmacological barrier whilst minimising off target effects, the assessment of small molecular scaffolds and their structure-activity relationships (SAR) is important to achieve a greater understanding of potential treatments of tau aggregation through novel molecular chaperone targets. A promising scaffold has been identified as an inhibitor of the Hsp90-Aha1 complex. Using this lead molecular scaffold, a library of compounds has been designed and synthesised to investigate the SAR surrounding this novel target so as to determine the potential of these scaffolds as tau aggregation therapeutics. In particular, expansion of chemical space has been carried out through chemotype exploration of the lead structural motif.

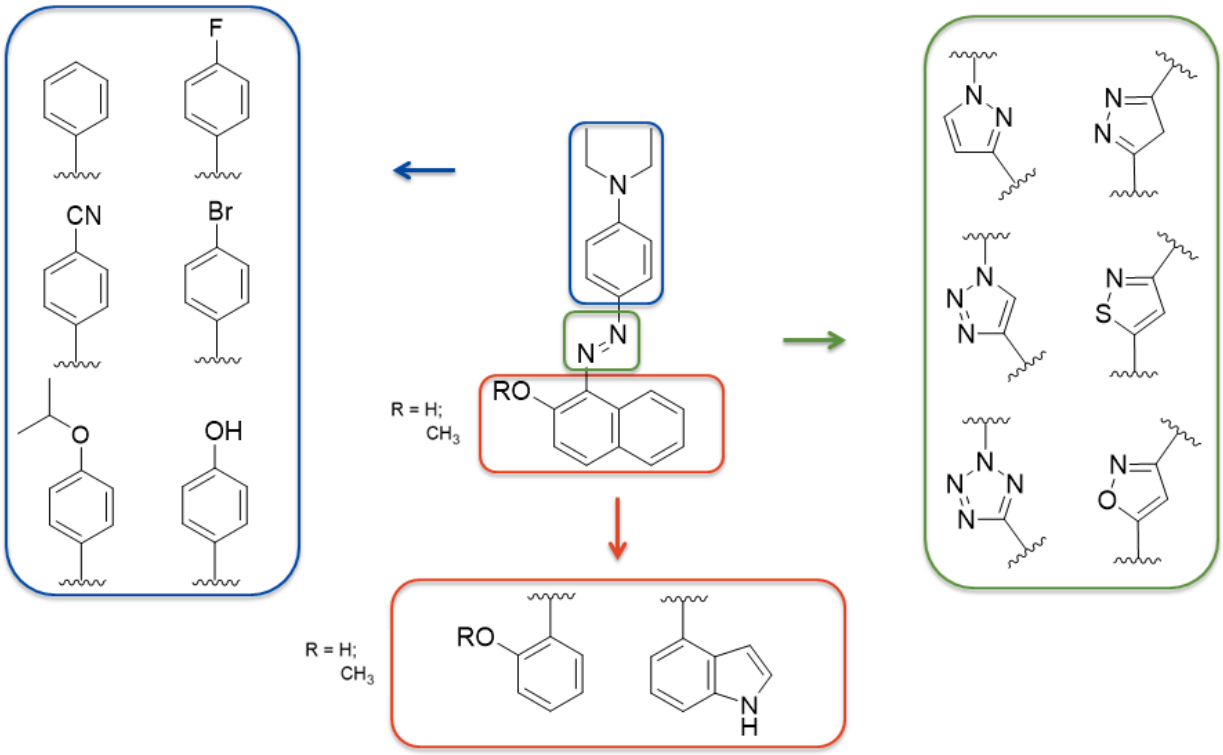

List of Abbreviations

- 3R – Three-repeat tau
- 4R – Four-repeat Tau
- 15-DSG – 15-Deoxyspergualin
- 17-AAG – 17-Allylamino-17-demethoxy-geldanamycin
- 17-DMAG – 17-Dimethylaminoethylamino-17-demethoxygeldanamycin
- Aβ – Amyloid-β plaques
- AChE – Acetylcholinesterase
- AD – Alzheimer's disease
- ADP – Adenosine 5`-diphosphate
- AFM – Atomic force microscopy
- Alpha – Amplified luminescence proximity homogenous assay
- AlphaLISA – Alpha-linked immunosorbent assay
- Aha1 – Activator of Hsp90 ATPase homolog 1
- APCI – Atomic pressure chemical ionisation
- Asp – Aspartate
- ATP – Adenosine 5`-triphosphate
- ATPase – Adenosine 5`-triphosphatase
- BBB – Blood-brain barrier
- BSA – Buried surface area
- CBD – Carboxy C-terminus domain
- $CDCl_3$ – Deuterochloroform
- $CHCl_3$ – Chloroform
- CDK-5 – Cyclin-dependent kinase 5
- CHIP – C-terminus interacting protein
- CL – Curcumin-like
- CNS – Central nervous system
- $(COCl)_2$ – Oxalyl chloride
- D_2O – Deuterium oxide
- DCE – 1,2-Dichloroethane
- DCM – Dichloromethane
- DLS – Dynamic light scattering
- DMAC – *N,N*-Dimethylacetamide

- DMAP – 4-(Dimethylamino)pyridine
- DMF – *N,N*-Dimethylformamide
- DMSO – Dimethyl sulfoxide
- DMSO-d_6 – Hexadeuterodimethyl sulfoxide
- DNA – Deoxyribonucleic acid
- DPPA – Diphenylphosporyl azide
- DTDB – Developmental therapeutics database
- EC_{50} – Half maximal effective concentration
- EM – Electron microscopy
- ESI – Electron spray ionisation
- Et_2O – Diethyl ether
- EtI – Iodoethane
- EtOAc – Ethyl acetate
- FKBP51 – FK506-binding protein 51
- FKBP52 – FK506-binding protein 52
- FRET – Förster resonance energy transfer
- FP – Fluorescence polarisation
- GSK-3 – Glycogen synthase kinase 3
- HAM – Hsp90-Aha1 modulator
- HBF_4 – Tetrafluoroboric acid
- HeLa – Human-derived cervical cancer cell Line
- HemiC – Hemi-curcumonoids
- HMGB1 – High mobility group box 1 protein
- HSF-1 – Heat shock factor 1
- Hsc70 – Heat shock cognate 70 kDa
- Hsp27 – Heat shock protein 27 kDa
- Hsp60 – Heat shock protein 60 kDa
- Hsp70 – Heat shock protein 70 kDa
- Hsp72 – Heat shock protein 72 kDa
- Hsp90 – Heat shock protein 90 kDa
- HSR – Heat shock response pathway
- IC_{50} – Half maximal inhibitory concentration
- IR – Infrared spectroscopy

- Lys – Lysine
- MAC – Monocarbonyl analogs of curcumin
- MB – Methylene blue
- MD – Middle domain
- MeCN – Acetonitrile
- MeI – Iodomethane
- $MgSO_4$ – Magnesium sulfate
- mRNA – Messenger ribonucleic acid
- mtHsp70 – Mitochondrial heat shock protein 70 kDa
- MS – Mass spectrometry
- mTau – Mutant tau
- Na_2CO_3 – Sodium carbonate
- NaH – Sodium hydride
- $NaHCO_3$ – Sodium hydrogen carbonate (aka sodium bicarbonate)
- NaN_3 – Sodium azide
- $NaNO_2$ – Sodium nitrite
- NBD – N-terminal nucleotide binding domain
- NBS – *N*-Bromosuccinimide
- NEt_3 – Triethylamine
- NIS – *N*-Iodosuccinimide
- NFT – Neurofibrillary tangle
- NMR – Nuclear magnetic resonance spectroscopy
- P301L – P301L human tau protein mutation
- p35 – Activating co-factor of CDK-5
- PHF – Paired helical fragment
- $POCl_3$ – Phosphoryl chloride
- PPIs – Protein-protein interactions
- pT231 – Form of phosphorylated tau protein
- pTau – Phosphorylated tau (phospho-tau)
- SAR – Structure-activity relationships
- SBD – C-terminal substrate binding domain
- SDS – Sodium dodecyl sulfate
- Ser – Serine

- SMILES – Simplied molecular-input line-entry system
- $SOCl_2$ – Thionyl chloride
- TBTA – Tris((1-benzyl-4-triazolyl)methyl)amine
- T22 – Form of oligomeric tau
- Tf_2O – Trifluoromethanesulfonic anhydride (aka triflic anhydride)
- THF – Tetrohydrofuran
- TAI – Tau aggregation inhibitor
- tauO – Tau oligomers
- TEM – Transmission electron microscopy
- THC – Tetrahydrocurcumin
- Thr – Threonine
- UV-Vis – Ultraviolet-visible spectroscopy
- WT – Wildtype

This is a Blank Page

Chapter 1:

Introduction

Chapter 1: Introduction

1.1 Dementia: Global Implications

In Australia, dementia is considered to be a major health concern with the population of those suffering from the disease being estimated at 401,300 in 2022, with a projection of at least 849,331 by 2058.[1] It was defined to be the second leading cause of death in 2022, representing 9.6% of overall deaths in Australia, as well as being an underlying or additional cause in a further 14% of deaths.[1] As a result, health and aged care service expenditure on individuals exhibiting dementia was estimated to be at least $3 billion across 2018–2019.[1] Dementia is an encompassing term that represents a syndrome associated with over 100 various diseases, which are characterised by the impairment of neural functions leading to a decline in cognitive skills, language, perception and memory.[2,3] Prevalent forms of dementia are Alzheimer's disease (AD) (50–75% of cases), vascular dementia (20–30%) and frontotemporal dementia (5–10%).[2] AD alone is considered to be the most frequent cause of cognitive decline in the elderly population at a worldwide scale with a projected patient population of 115 million by 2050.[4–6]

1.2 AD: The Pathology of Tau

One of the defining pathologies of AD is distinctive neurofibrillary lesions including neurofibrillary tangles (NFT), neuropil threads and dystrophic neurites that are a result of intracellular depositions of aggregated cortical tau protein deposits.[7–10] These were identified by Alois Alzheimer as the primary aberrant brain structures present in AD, however it was not until much later with the development of electron microscopy (EM) that NFTs were determined to be composed of protein filaments described as paired helical fragments (PHF's).[11,12] Typically, tau functions as a monomer-based microtubule-associated protein that undergoes binding at tubulin heterodimer interfaces and provides both structure and shape to microtubule (MT) cytoskeletons and subsequently, neuronal axons and dendrites (**Figure 1A**).[7,13–15] Although it is a natively unfolded protein, abnormal modifications and expressions of tau (such as induced misfolding of soluble tau) lead to the accumulation of insoluble tau aggregates and stress to the cell.[16] Subsequent formation of the previously mentioned neurofibrillary lesions then occurs, resulting in neurodegeneration. For example, the hyperphosphorylation of tau leads to polymerisation of tau proteins into PHFs that are hypothesised to be responsible for formation of insoluble NFTs, disintegration of microtubules, collapse of neuronal transport systems, and subsequently, depression of the

biological activity of tau (**Figure 1B**).[9,17,18] These processes are facilitated by the ability of PHFs to undergo transneuronal movement through release by degenerating neurons and subsequent internalisation *via* endocytic mechanisms by surrounding cells, leading to intracellular tau aggregation that further propagates neurodegeneration.[19–21] Interactions with microglia, astrocytes and HMGB1 (a pro-inflammatory cytokine) result from this pathogenic propagation and lead to neuroinflammation.[18]

Initially, hyperphoshorylated tau is redistributed to the somatodendritic compartment of the neuron from the axon and is considered an indicative sign of early stage onset of disease development when identified.[16,22,23] Although NFTs were originally defined to consist primarily of tubulin proteins; tau was later identified as the principal component within the framework of PHFs. This conclusion was reached after it was resolved that purified tau was able to self-assemble into PHF-like structures in the absence of other proteins.[24] Most interestingly, further investigation led to discernment of the microtubule binding region on tau as the core of the PHF polymer.[25] As a result of these realisations stemming from several decades of studies, tau is now a primary focus in research for its role within AD as well as several other clinicopathologies.

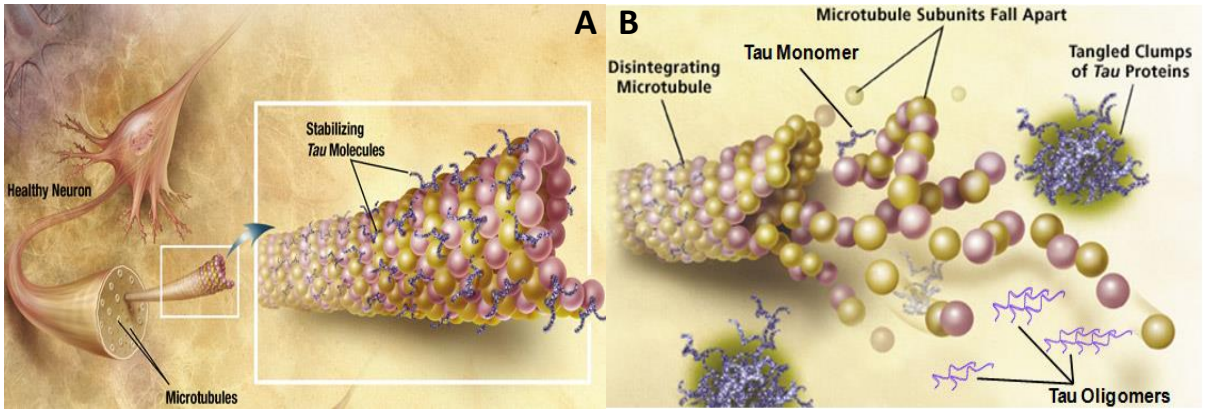

Figure 1. a) Healthy neuron with tau-stabilised microtubules and; b) Degradation of neuron *via* disintegrating microtubules and subsequent formation of tau protein aggregates.

1.2.1 Relevant Clinicopathologies of Tau

Tau serves as a biomarker not only for the diagnosis and staging of AD but is considered a central process in approximately 20 other neurodegenerative diseases (collectively known as tauopathies) including corticobasal degeneration, frontotemporal lobar degeneration, myotonic dystrophy and postencephalitic parkinsonism, amongst others.[20,26–28] Although several other protein aggregates have been associated with these disease states; tau

has been established as the fundamental therapeutic target among these pathologies. However, the underlying processes leading to the pathogenesis of these conditions is still unclear, with further research being necessary to obtain a greater insight into the relationships between these processes and the mechanisms of the defining pathologies. For example, it is yet to be answered whether the dissociation of tau from microtubules improves its substrate viability for kinases, thereby leading to additional formation of hyperphosphorylated tau or if pathogenic phosphorylation of tau lowers its overall microtubule affinity. Unfortunately there is no agreement as to which forms of tau are and are not pathogenic.[29,30] Furthermore, considerable controversy as to whether aggregate tau in the form of NFTs is pathogenic or neuro-protective in nature is still ongoing.[31,32] In fact, each clinicopathology is characterised by differing isoforms and associated ratios of tau within various regions of the brain.[20,26–28] Ultimately this drives the complexity of tau as both a pathological entity and disease-relevant target.

1.2.2 Previous Hypotheses of AD

Although tau-based therapeutics have mainly aimed to disrupt aggregation either directly or *via* kinase inhibition, tau-mediated neurodegeneration may potentially be a result of either soluble misfolded, hyperphosphorylated and/or mislocalised forms of tau.[31] It has been demonstrated through *in vivo* imaging that truncated tau leads to the formation of misfolding, soluble tau and thus results in the accumulation of NFTs, suggesting a minor supply of truncated tau may be a necessity in interceding NFT formation.[16,33] Previously, it was thought that the deposition of amyloid-β (Aβ) plaques played a central role in both the pathogenesis and pathophysiology of AD at any stage, with an estimated expenditure of $15 billion in research concerning therapeutic drug discovery targeting this hypothesis.[30] Approximately 19 individual therapeutic compounds have been proposed that share an effect in reducing amyloid pathology but have either failed or been halted during clinical trials, leading to the amyloidcentric approach to AD therapeutics being questioned.[5,6,30,34] Comparatively, it has been shown that there is a greater correlation between tau-related pathology and dementia compared to Aβ plaques, as well as evidence of substantial neurodegeneration when tau is present in the absence of Aβ pathology.[29,31] This correlation of tau presence and the onset/progression of disease has identified tau as a target for the development of potential disease-modifying treatments targeting tauopathies.

There are several conditions (such as hereditary cerebral haemorrhage with amyloidosis or sporadic cerebral amyloid angiopathy) in which levels of amyloid pathology are consistent with that of AD, yet patients exhibit no overt dementia, indicating neuronal loss and cognitive decline cannot be the sole result of amyloid pathology.[29,35,36] Axonal blockages have been observed to occur in the early stage of AD, with such blockages resembling dystrophic neurites (primarily associated with deposited Aβ). However, these axonal swellings were found to precede both amyloid and other AD disease-related pathology by a period of one year, and thus could not be formed in response to the deposition of Aβ, indicating the possibility of a causative role in AD.[10] In addition, it has been demonstrated that when induced by amyloid precursor protein, substantially elevated Aβ did not correlate to either an increase in neuronal cell death or toxic tangles of tau.[37] Thus the role of Aβ remains in question. In addition, there have been several other hypotheses proposed for the underlying pathology of AD. In a total of 2173 clinical trials, investigations have centred primarily on amyloid (22.3%), neurotransmitter (19.0%), mitochondrial cascade (17.0%) and tau-related (12.2%) pathology theories (**Figure 2**).

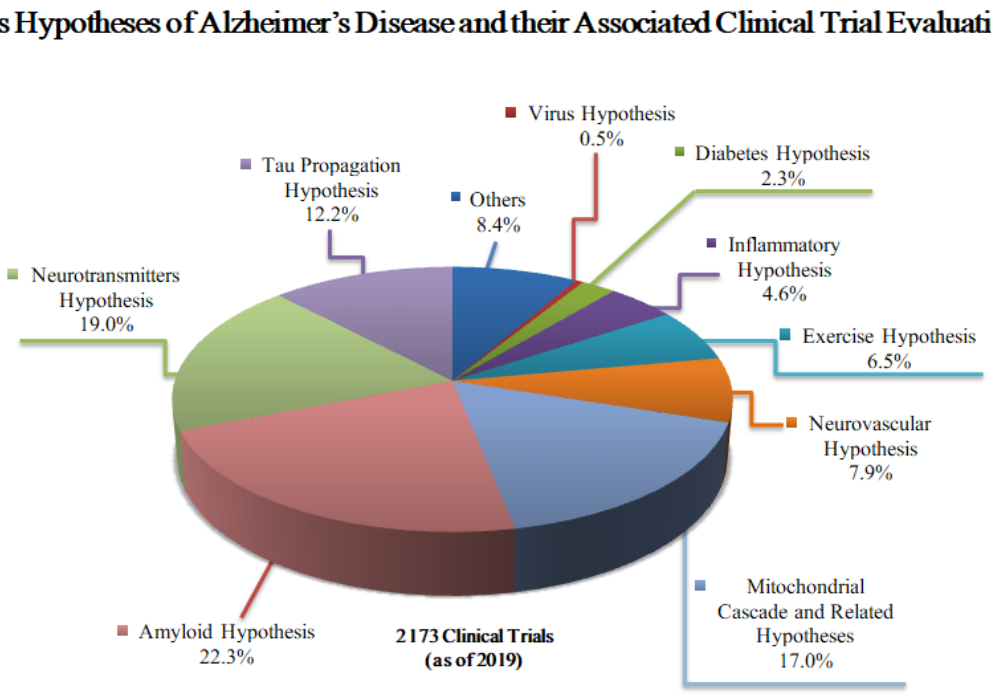

Figure 2. Various hypotheses of Alzheimer's disease and their relative percentages of clinical trials up to 2019. Adapted from Liu, P-P. *et al.*[38]

Currently, cholinergic therapies that enhance cholinergic transmission *via* the inhibition of acetylcholinesterase are the only commercially approved therapies for the limitation of AD symptoms, alongside a single antagonist of the *N*-methyl-D-aspartate

receptor.[39–41] As of 2019, there were 132 drug candidates undergoing clinical trials for evaluation in their effectiveness in the treatment of AD. Unfortunately 38 (40%) are still targeting amyloid as the principal target even though such little success has been seen within this area.[42] Although the antibody Aducanumab is the only FDA-approved disease-modifying therapy for AD, its efficacy has been found contentious alongside several controversies related to its clinical evaluation.[43,44] Nonetheless, no small molecule disease-modifying therapeutics exist on the market for the therapy of AD.[6,34,40,41] This represents a significant unmet need in the clinic, and can be highlighted by the difference in number of drug candidates being evaluated by mode of action in phase III clinical trials for either disease modifying therapies (61%), neuropsychiatric symptoms (28%) or symptomatic cognitive enhances (11%) (**Figure 3**).

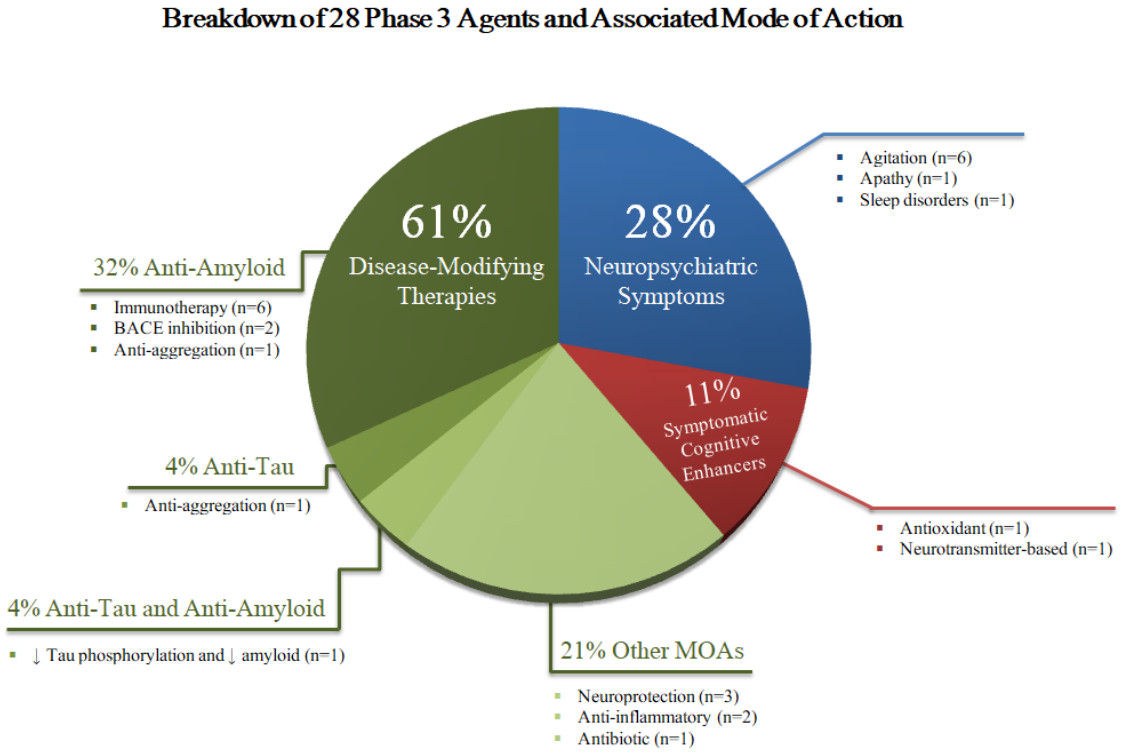

Figure 3. Percentage of targeted therapies for 28 phase III drug candidates for AD therapy in 2019. Adapted from Cummings, J. L. *et al.*[45]

1.3 Putative Therapies and Targets for Tau Aggregation

Taucentric approaches to the treatment of AD are currently being investigated (**Figure 4**), with several new approaches that exhibit strong potential having been proposed. Such examples include the direct inhibition of tau aggregation; increases in tau clearance and microtubule stabilisation; as well the inhibition of tau phosphorylation (typically *via* the activation of tau phosphatases or inhibition of tau kinases).[7–9,26,30,34,46]

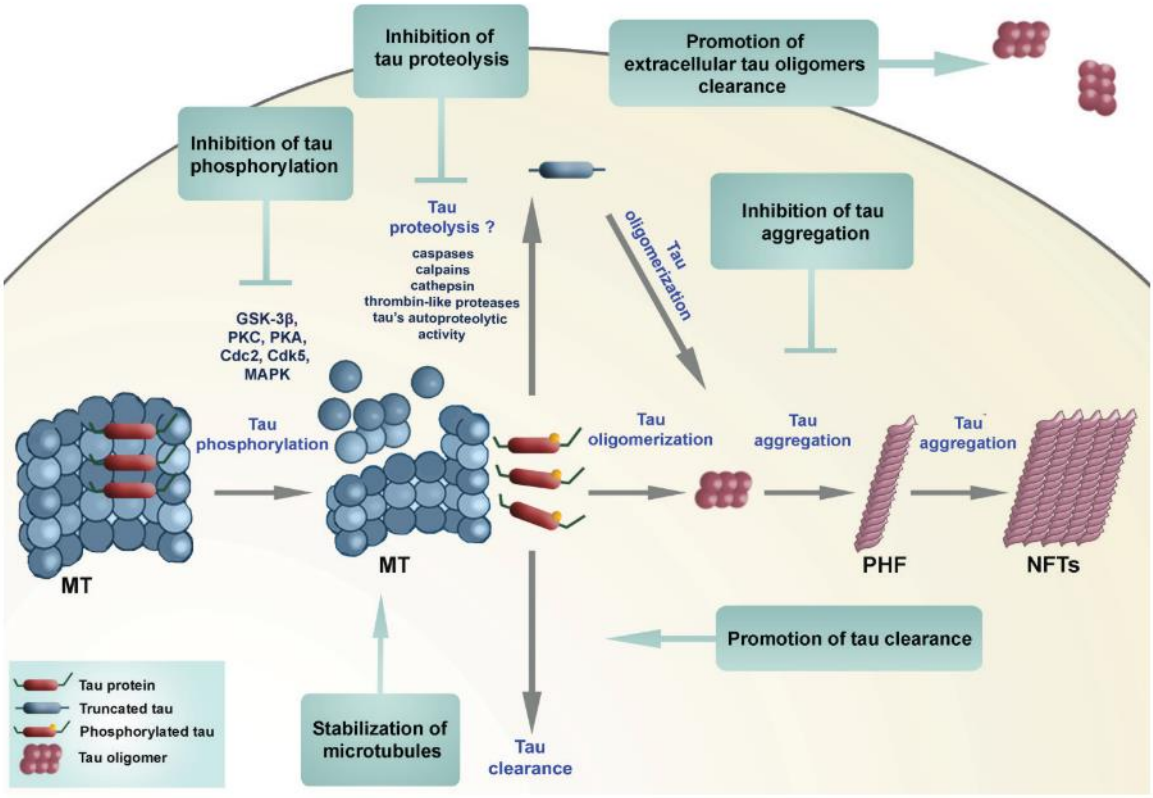

Figure 4. The process of tau aggregation and various points of potential therapeutic action. Reprinted with permission from Šimic, G. *et al.*[46]

1.4 Inhibition of Tau Aggregates

Differing by the presence of both one or two N-terminal inserts and three (three repeat tau; 3R) or four (four repeat tau; 4R) C-terminal microtubule domains, tau exists in 6 various isoforms.[29] Due to precise structural constraints present in PHF cores at the repeat domain, the tau-tau binding interaction can be determined exclusively from the tau-tubulin binding interactions seen at the normal repeat domain of healthy tau.[30] As a result, viable aggregation inhibitors could be developed with selectivity to inhibit one undesired interaction over the other. Current research on therapeutic compounds that directly target tau protein aggregation by binding and changing the conformation of tau itself can be classified into two groups: covalent and non-covalent tau aggregation inhibitors (TAI).

1.4.1 Covalent Inhibition

These inhibitors can covalently interact with tau directly, or can assist in forming covalent bonds either between, or within tau proteins that are ineffective aggregation complexes. Covalent inhibitors have the ability to interact with all species relative to an aggregation pathway but tend to be particularly effective modifiers of tau monomers.[8,9]

Typical covalent TAI molecular structures include polyphenols, phenothiazines, aminothienopyridazines, benzothiazoles/cyanines and anthraquinones.[7–9,28] Inhibition of tau fibrillisation is considered ideal as it is thought that fibrils generate the greatest total neuronal damage.[47]

For example, the natural product **1** (**Figure 5**) reduces tau filament formation through formation of Schiff bases by interaction with lysine residues that inhabit the microtubule binding repeat region, thus locking tau into its naturally unfolded state.[48,49] Similarly, **2** (**Figure 5**), a natural polyalcohol flavonoid, is oxidised *in vivo* to afford the respective quinone derivative **3** (**Figure 5**) that can undergo Schiff base formation with related tau lysine residues.[8,50] Specifically through enhancement of sodium dodecyl sulfate (SDS)-stable oligomer formations, **3** prevents fibril formation and as such aggregation of tau isoforms.[51] This is important as filamentous tau has been demonstrated to boost aggregate load within the neuron, thus impeding cellular functioning alongside burdening cellular machinery.[52]

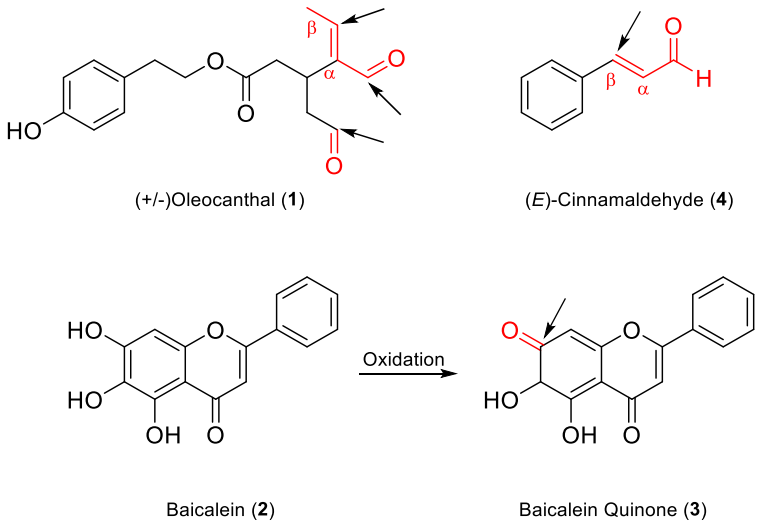

Figure 5. Examples of natural covalent tau aggregation inhibitors (TAIs).[8]

(*E*)-Cinnamaldehyde (**4**; **Figure 5**) is an example of a natural α,β-unsaturated aldehyde Michael acceptor that undergoes nucleophilic attack at the β-carbon by cysteine residues located on tau, which has been observed to be a reversible reaction.[8,53] Proteins which contain reactive cysteine residues are prone to redox modifications and as such covalent interaction with **4** may confer protective properties *via* buffering of these alterations.[53] Interestingly, George, R. C. *et al.* demonstrated that modification of tau 187 with **4** did not affect the formation of microtubules and in fact is as functionally competent as full length tau, with only the rate of assembly being marginally reduced.[53] In regards to cysteine functionalities

residing on tau, present sulfhydryls moieties can form both inter- and intramolecular disulphide bonds through oxidation in the absence of exogenous reducing agents. Accordingly, this can facilitate the inhibition of tau aggregation *via* the acceleration of disulphide bond formation by compounds such as aminothienopyridazines.[47,54] After an initial high-throughput screen of ~292,000 compounds and subsequent medicinal chemistry efforts towards SAR exploration, the novel class of aminothienopyridazine inhibitors (**Figure 6**) were initially identified by Crowe, A. *et al.*[55]

Purposeful inhibition observed across both fluorescence polarisation (FP) and Thioflavin T (ThT) interactions implied inhibitory mechanisms in the earlier steps of tau assembly were at play and therefore these compounds were of notable interest. Seven identified molecules encompassing diverse chemotypes were found to elicit at least 70% maximal inhibition within the ThT assay and favourable FP results. Of these seven, two (**5** and **6**; **Figure 6A**) contained the aminothienopyridazine core (**Figure 6B**) and were subjected to further investigation as the scaffold had not been previously reported to inhibit tau fibrillisation. Trends within the SAR were observed after derivatisation of the compounds, in particular substitutions at C_5 and *N*-acylations at the free amine (R_1) (**Figure 6B**) led to substantial loss in inhibitory activity. Replacements of the ester functionality present at C_3 with substitutions such as amide derivatives resulted in greater maximal inhibition, suggesting that inhibition of tau fibrillisation does not proceed through an acylation mechanism.

Considerable analysis to further identify the specific mechanism of inhibition was conducted by Crowe, A. *et al.*[47] It was discovered that the inhibitors revealed a large increase in tau monomer concentration and IC_{50} values near the stoichiometric equivalence of tau, suggesting prevention of fibril formation *via* monomeric tau interaction. Previously it has been described that cysteine residues within MT binding repeats of compact 4R-tau can oxidise to form intramolecular disulphide bridges. Through the use of size exclusion chromatography, it was determined formation of disulphide bridges was indeed the mechanism behind the scaffolds inhibitory activity.[56] Preceding literature reports have established *in vitro* that 4R species which present an intramolecular disulfide formation do not readily mobilise into fibrils, thus likely explaining the basis for this inhibition of fibril formation.[56–58] Conversely, it has been determined that 3R species demonstrate a greater proclivity to fibrillise due to the absence of a second MT binding repeat.[56–58] Incubation of 3R

tau with aminothienopyridazine derivatives promoted formation of intermolecular disulfide links between dimers, thus demonstrating the aminothienopyridazine scaffold is ineffective at preventing fibrillisation of 3R tau but effective for 4R tau.

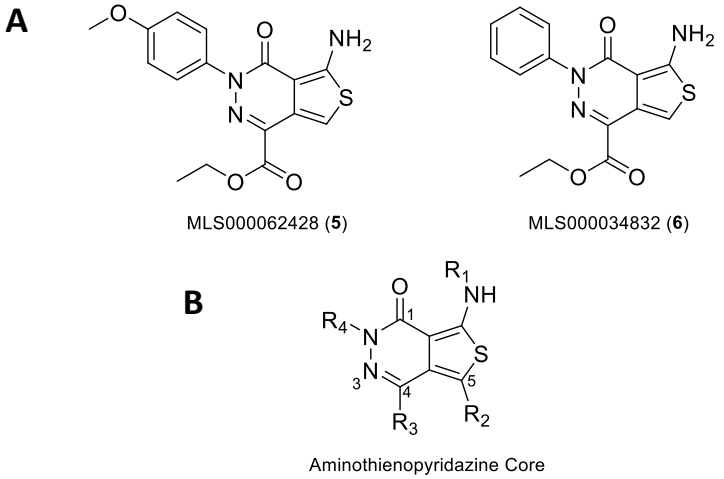

Figure 6. a) First identified aminothienopyridazine inhibitors of tau and; b) core aminothienopyridazine SAR scaffold.[55]

Although promising, a significant concern relating to covalent inhibitors is they may disturb unintended targets. In particular, this may lead to troublesome unspecific modifications or haptenisation of modified proteins that can result in an undesired immune response.[50,59] The identifying toxicities caused by biologically reactive intermediates are formed through molecular processes that are complex and not properly understood.[60] Collections of 'toxicophores' have been defined, which are chemical functionalities characterised by metabolism into reactive electrophilic species.[61] These aim to provide medicinal chemists the ability to make informed decisions that minimise potential for formation of chemically reactive metabolites at the lead optimisation phase level, but future improvements in approaching covalent inhibition is still necessary.

1.4.2 Non-Covalent Inhibition

The second group of TAIs exhibit non-covalent interactions with tau species through a variety of different mechanisms that either act alone or collectively.[8,62] An interesting feature of many non-covalent inhibitors is their similarity to dyes in regards to absorbance characteristics. Examples include the cyanine (**7**), phenothiazine (**8**) and triarylmethine (**9**) derivatives (**Figure 7**).[8] These cyanine, phenothiazine and triarylmethine compounds have been reported to be amongst the most potent of the TAIs to date[63] and share centrosymmetric structures that demonstrate considerable delocalisation of their fixed cationic charges. They

exhibit planar structure and are highly polarisable, allowing their electron density to easily shift and therefore display particularly ideal attributes for maintaining van der Waals interactions with proteins that exhibit similar highly polarisable functional moieties, such as aromatic side chains.[64–66] The interactions are nearly electrostatic in strength and advocate selective association of ligands with aromatic amino acid side chains of both tau and other aggregating proteins.[67,68] Due to the direct interactions of small molecules with tau monomers, transient interactions have been suggested to dampen entry into aggregation pathways through alteration of the rate at which unfolded polypeptides natively adopt aggregation effective conformations.[69]

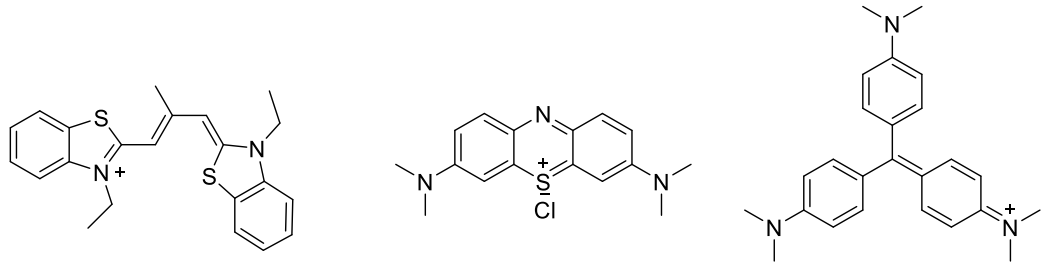

Figure 7. Examples of non-covalent tau aggregation inhibitors that share similar absorbance characteristics to dyes. The structures include cyanine, phenothiazine and triarylmethine derivatives.[8]

Amongst the myriad of known non-covalent inhibitors, methylene blue (**8**) was the first to be developed in 1876 as a dye but was repurposed in 1891 for medicinal application as an antimalarial.[70] It is a tricyclic phenothiazine-based small molecule which persists in equilibrium between its reduced (phenothiazine) form and oxidised (phenothiazin-5-ium) form.[71,72] Regardless of the route taken for administration, it has been determined to exhibit reasonable blood-brain barrier (BBB) permeability whilst being demonstrated to interfere with tau-tau interactions and thus preventing PHF formation *via* binding of the tau repeat domain.[73–75] Interestingly, it has been reported that **8** has the ability to inhibit fibril formation *via* oxidation of cysteine residues.[47] However, inconsistent *in vitro* IC_{50} values have been reported within the range of 1.9 μM – 3.5 μM.[63,76,77]

Several alternate mechanisms of action for **8** have been suggested, such as inhibition of microtubule assembly. Unfortunately to achieve this would require an unreasonable dose of 50 g of **8**/day, thus exceeding the LD_{50} in several species.[30,55] Interestingly, its role in vitiating tauopathy *via* autophagy induction as well as inhibition of Hsp70 ATPase activity has been well established.[26,78] Although Hosokawa, M. *et al.* observed significant reduction in

abnormal insoluble tau aggregates in P301L mutant mice, Zakaria, A. *et al.* identified conflicting results determining only soluble levels of tau were affected, and not insoluble levels.[79,80] These contradictory reports illustrate the difficulty in ascertaining the exact role **8** may or may not play in its interactions with tau. Although it was the first small molecule to undergo clinical trials for tau aggregation, it failed phase III trials as it was deemed to be ineffective at meeting co-primary endpoints such as the slowing of cognitive and functional declines in AD patients.[81] An investigation carried out by Soeda, Y. *et al.* determined a reduction of tau fibrils were observed with application of **8** but came alongside an associated increase in granular tau oligomers.[41] Previous research within the Takashima group had determined that the formation of granular tau oligomers were essential for neuronal death, rather than tau fibrils.[82,83] Therefore, it has been reasoned that the action of **8** being limited to inhibition of tau fibrils is the mechanistic explanation for the unsatisfactory performance observed in the clinic.

Extensive investigation has been carried out around the structural scaffold of the naturally occurring polyphenol curcumin (**10**; **Figure 8**) and its effects on tau aggregates directly. Work conducted by Rane, J. S. *et al.* reported the compound was able to inhibit tau aggregation in a concentration-dependent manner within a ThT assay.[84] Molecular docking work suggested the binding site of the compound to be at the microtubule-binding region residing on the tau surface. Most interestingly, **10** was observed to substantially diminish aggregation levels with a 75 ± 10% disaggregation. Further analysis *via* transmission electron microscopy (TEM), dynamic light scattering, and atomic force microscopy (AFM) determined the absence of tau filament formation, with tau filaments being disassembled in the presence of the compound. Despite these results, the molecule displays limited oral bioavailability as a consequence of low water solubility, cerebral permeability, absorption, fast metabolism and excretion *in vivo*.[85] Several studies indicate significantly low serum levels post-oral application in humans, with minimal 1% bioavailability observed within rat plasma levels.[86–88] Furthermore, it has inadequate physiological stability and easily undergoes photodegradation as a result of high photoreactivity.[89,90]

Due to the limitations exhibited by **10**, several different classes of structural derivatives have been designed which assess tolerated modifications on particular parts of the scaffold whilst improving physicochemical properties. Such categories include tetrahydrocurcumins (e.g THC (**11**)), curcumin-like molecules (e.g CL3 (**12**)), monocarbonyl

analogs of curcumin (focusing on central core alteration (e.g MAC3 (**13**)) and heterocyclic replacements to the core 1,3-dicarbonyl moiety (e.g CH8 (**14**)) (**Figure 8**).[85,91] The vast majority of these molecules have only been assessed for their role on Aβ-plaques rather than assessment of interaction on tau aggregates. However, promising data has been shown for compounds that have been evaluated.

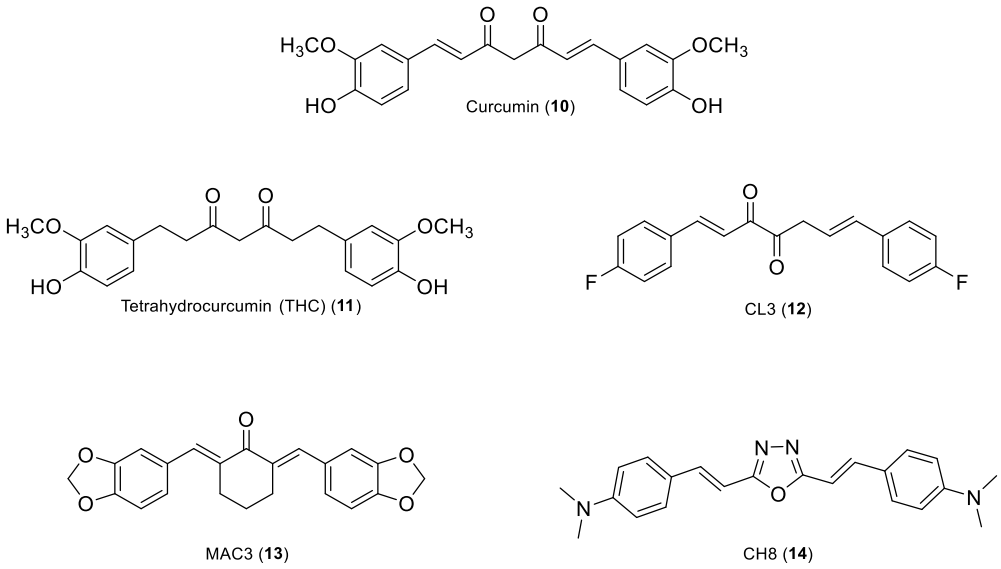

Figure 8. Molecular structure of curcumin alongside several examples of scaffold-derivatives representative of the various structural design categories.[85,91]

Cascio, F. *et al.* developed several compounds with diverse central scaffold changes, spanning across these four different classes of curcumin derivatives, to evaluate their effect on tau.[91] Removal of the β-diketo functionality was a pivotal focus, which is suspected to play a significant role in the rapid metabolism of curcumin as well as its poor solubility and low cerebral bioavailability.[91,92] In particular the curcumin-like **12** and heterocyclic replacement **14** derivatives yielded promising results, demonstrating decreases in toxic tau oligomers (tauO). However, a positive correlation with increased formation of heavier tau aggregates was discovered. Comparison of structural morphology *via* AFM determined that the molecules modulated the morphology of oligomers through formation of larger aggregates as a result of binding. These larger aggregates were not found to demonstrate cytotoxicity and are not believed to undergo cellular internalisation like tauO, accounting for an observed reduction in cytotoxicity. This mechanism of action could be a viable pathway to reduce toxic tauO levels *in vivo,* as the crucial step of transneuronal cell-to-cell spreading is cellular internalisation *via* endocytic mechanisms.[19–21]

1.5 Promotion of Tau Clearance

1.5.1 Heat Shock Proteins

Limiting tau aggregation with direct tau aggregation inhibitors is not the only potential method for therapeutic action toward tau aggregation. Alteration of tau-effector proteins can fall into various categories including chaperone modulators and microtubule stabilisers, alongside the direct inhibition of tau aggregation.[26,28] Because tau is inherently an unfolded protein that can take on aberrant conformational changes *via* induced misfolding of soluble tau, pathways involving folding of tau can be viable therapeutic targets.[16]

Molecular chaperones, such as heat shock proteins, are a family of polypeptides with upregulated expression during times of stress that ensure cells maintain an ability to regulate various processes of protein homeostasis. This includes refolding of misfolded and/or aggregated protein *via* adenosine 5`-triphosphate (ATP) catalysed processes as well as targeting irreparable proteins for degradation by the ubiquitin-dependent proteasomal degradation pathway.[26,93–96] In the case of pathological events the processes by which protein undergoes quality control can lead to accumulation of misfolded protein, due to either a mutation or overwhelming quantities of client proteins.[97] Heat shock proteins can be classified into four primary families based on their molecular weights: the large heat shock proteins, which are ATP-dependent chaperones (90 kDa (Hsp90), 70 kDa (Hsp70), 60 kDa (Hsp60)) as well as small heat shock proteins (15 – 30 kDa), in particular Hsp27, which are ATP-independent.[97] Hsp90 and Hsp70 are the most researched and therefore best characterised proteins in the heat shock family. Due to their roles in regulating cellular homeostasis *via* key cellular processes they have been implicated in a myriad of human disease states, particularly in the fields of oncology and neurodegenerative research. This has identified them as attractive therapeutic targets.[28,40,96,98–102]

Heat shock proteins play a pivotal role in the heat shock response (HSR) pathway, which is regulated by the heat shock factor 1 (HSF-1) protein, acting as the major transcription factor for various heat shock proteins. The pathway is induced not only by temperature stress, but also a variety of other stressors such as hypoxic conditions (failure of oxygenation in the cell) and exposure to contaminants.[102–105] After trimerisation and subsequent translocation into the nucleus of a cell, HSF-1 binds to DNA, thereby initiating the transcription of mRNAs that encode newly synthesised Hsp90, Hsp70 and Hsp27 proteins for folding stressed proteins.[96] The relationship between heat shock proteins, particularly

Hsp70 / Hsp90, and their mutual facilitation of tau degradation as well as ability to impede formation of tau aggregates has been reported.[96,102,106–109] This highlights the strong potential of both Hsp70 and Hsp90 as viable targets due to the role they play within the pathology of tau. Additionally, targeting the protein-protein interactions (PPIs; **Figure 9**) these chaperones participate in greatly increases the number of potential avenues for treatment.

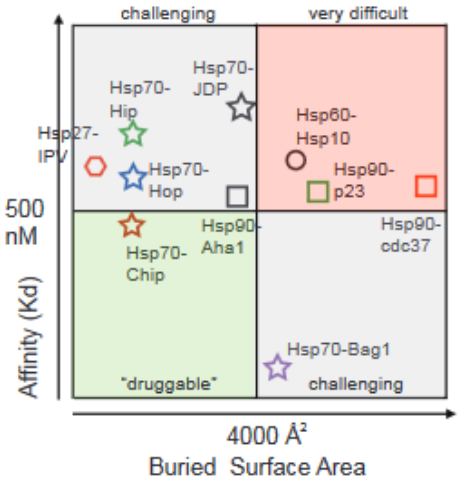

Figure 9. Classification of heat shock proteins and their co-chaperones in difficulty as druggable targets with small molecules, in correlation to their PPI affinity (K_d; nM) and buried surface area (Å^2). Reprinted with permission from Gestwicki, J. E. and Shao, H.[110]

However, difficulty remains in targeting these larger proteins and their PPIs with small drug-like compounds, as they host greater buried surface area (BSA) than enzyme-active sites.[110,111] A small drug candidate is typically less than 500 Da in size (in accordance with Lipinski's rules), but focus on meeting this criteria has substantially hindered progress in this field, alongside minimal benefits from standard library screening approaches when compared to that of screening for molecules that regulate ATP binding sites.[111] The relationship between the affinity and BSA of various heat shock proteins and their respective co-chaperones has been reported, with additional difficulty in their ability to be drug targets (**Figure 9**). Notably, it has been demonstrated that PPI inhibitors with the greatest potency interacted with PPIs that hosted reasonably small BSA values (< 2000 – 4000 Å^2) after examination in trends between approximately 200 successful PPI inhibitors.[110,112–114]

Heat Shock Protein 70 kDa (Hsp70)

Hsp70 stabilises various protein substrates against either denaturation or aggregation and is also responsible for a variety of cellular regulating processes including the unionisation and dissociation of proteins as well as the subcellular transport of vesicles and proteins, amongst the previously mentioned roles.[104] It is a highly conserved and ubiquitously

expressed protein complex with two distinct domains for substrate binding, being the 40 kDa N-terminal nucleotide binding domain (NBD) and a 25 kDa C-terminal substrate-binding domain (SBD).[96,104,105,115] A multitude of openings arise, in regards to therapeutic strategies, due to the majority of operations facilitated by Hsp70 being dependent on intercommunication between ATPase activity (binding / hydrolysis) in the NBD and substrate binding (i.e. misfolded client proteins) in the SBD *via* means of allostery, aided by a conserved, hydrophobic linker that also acts as a co-chaperone docking interface (**Figure 10**).[104,105,110,116]

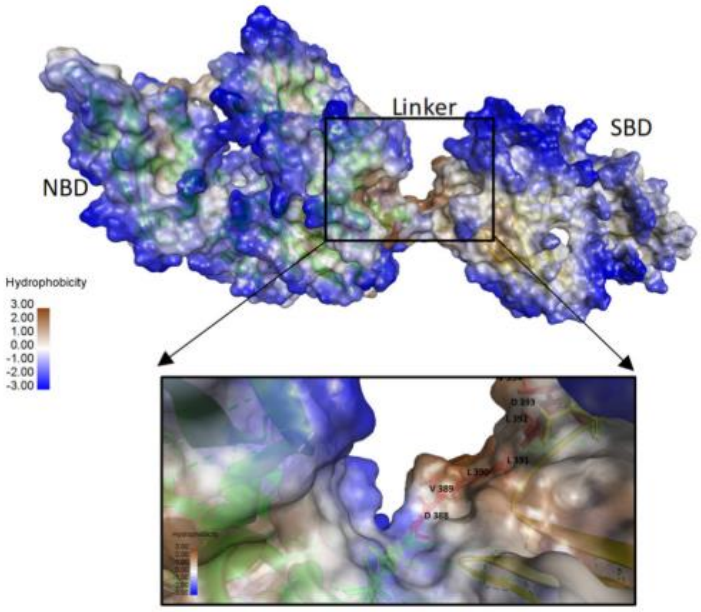

Figure 10. Three-dimensional model representation of canonical Hsp70, exhibiting the linked NB and SB domains as well as relative polarity of hosted residues. Reprinted with permission from Chakafana, G. *et al.*[116]

Upon release from microtubules, Hsp70 as well as its constitutively-expressed (always "on") isoform, heat shock cognate 70 (Hsc70), both directly bind to tau near the microtubule-binding domain.[108] As a result, the rebinding of tau to microtubules is facilitated, with evidence demonstrating a role in promoting both degradation and tau aggregation.[26,96,102,107,108] The effect of both activators and inhibitors of Hsp70 on tau protein levels has been reported (**Figure 11A**), with roughly 80% decrease in Hsp70 function being associated primarily with two classes of inhibitor: benzothiazines and flavones (**Figure 12A**).[26] This correlates with further research demonstrating the control of several synaptic protein expressions through up-regulation of both Hsp70 and Hsp40, by means of Hsp90 inhibition, while aiding the channelling of misfolded protein to the proteasome for degradation (**Figure 11B**).[102,105]

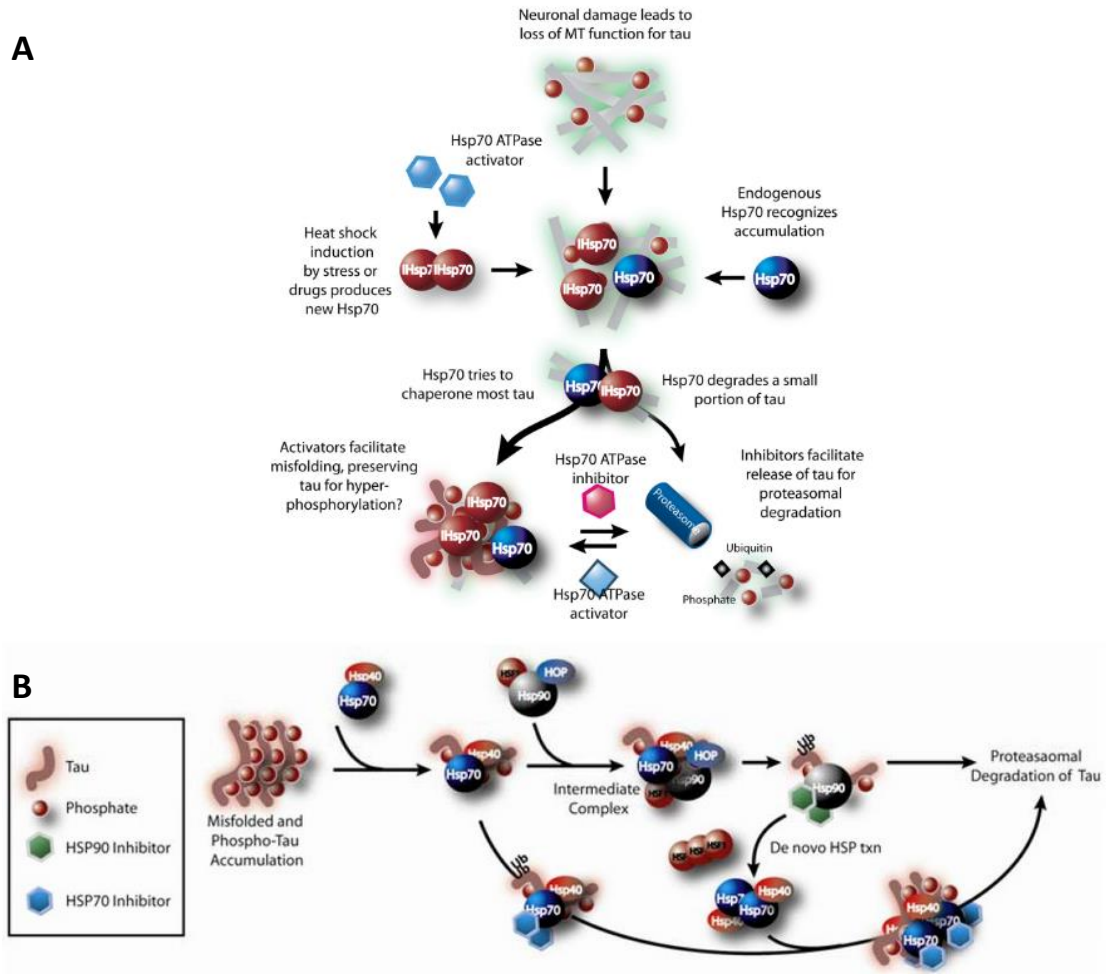

Figure 11. Proposed relationships: a) between Hsp70 and tau, when Hsp70 is either activated or inhibited by drug candidates; b) for the formation of complexes between Hsp40, Hsp70 and Hsp90 when managing both misfolded and phospho-tau accumulation, resulting in transport to the proteasome for degradation. Reprinted with permission from Holmes, B. B. *et al.*[21] and Jinwal, U. K. *et al.*[95]

N-Terminal Inhibition

The N-terminus of Hsp70 has a predominant role in ATPase activity, that being both the binding as well as hydrolysis of ATP substrate. Inhibition of Hsp70 by compounds such as **8** and **15** (**Figure 12A**) were reported to exhibit great success in the rapid degradation of tau through ATPase regulation.[26,28] Although these compounds demonstrated good *in vitro* results, translation of their efficacy to *in vivo* application has been less than ideal. Most interestingly, common N-terminal inhibitors are comprised of structures that strongly relate to known TAIs. A correlation for overlap in molecular structure between just phenothiazine (**8**; **Figure 12A**), polyphenolic (**15**; **Figure 12A**) and anthraquinone-derived (**16, 17** and **18**; **Figure 12C**) compounds alone can be observed. In particular, a strong structural similarity between oxidised anthraquinones and polyphenols is evident (**Figure 12B**; highlighted in RED) whilst reduced anthraquinones share affinity to the phenothiazine scaffold (**Figure 12B**; highlighted

in BLUE). As such, there exists a strong potential for dual inhibitors to be developed that target tau through these pathways.

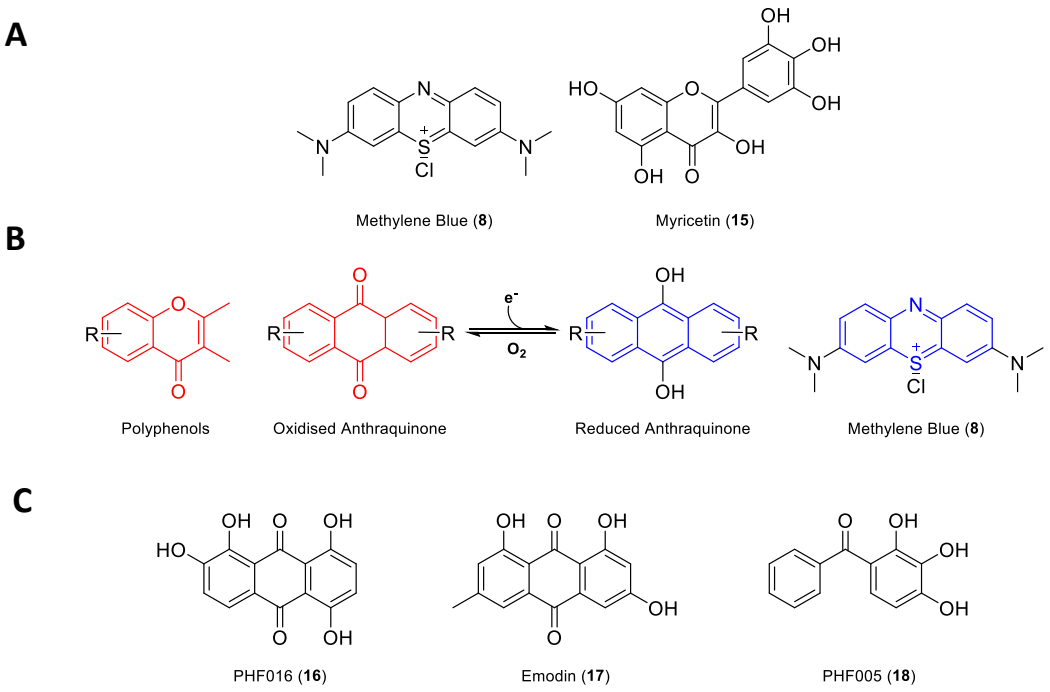

Figure 12. a) Molecular structure of the known Hsp70 inhibitors methylene blue **8** and myricetin **15**; b) oxidised (in red, left) and reduced (in blue, right) anthraquinones exhibiting structural overlap with polyphenols and methylene blue (**8**) and; c) examples of the anthraquinones **16** and **17** alongside the structurally related **18** that are identified as TAIs.[26,62]

Benzothiazines and flavones are not the only chemical scaffolds that have been evaluated in the therapeutic inhibition of Hsp70. Research conducted by Umezawa, H. *et al.* led to the isolation and characterisation of the novel natural product (–)-spergualin **19** (**Figure 13**) from *Bacillus* sp. in 1981.[117] Although determined to have meagre stability both *in vitro* and *in vivo*, spergualin analogues have been found to exhibit greater stability in pH 7 aqueous environments. One such example is **20** (**Figure 13**), a result of removing a labile hydroxyl group at the C_{15} position of **19**.[118,119] Further assessment found **20** to have a significant binding affinity to both Hsp70 and Hsp90.[120] Nonetheless, it has been reported that **19** and its analogues have a narrow activity profile in oncological applications against Hsp70.[118] Moreover, **20** has displayed insufficient bioavailability in its use as a therapeutic.[119] As a result, additional modifications were made in attempts to improve the therapeutic profile of candidates derived from the spergualin scaffold but only two retained activity (**21** and **22**; **Figure 13**). Komesli, S. *et al.* synthesised tresperimus **23** (**Figure 13**) and further derivatives **24** – **26** (**Figure 13**) to assess the effect of additional structural modifications and their

consequence on the therapeutic efficacy of the scaffold. However, only a methyl substitution at the R_1 position on **24** was tolerated without substantial loss of activity, whilst opposing stereochemical substitution at R_2 on **25** completely eradicated binding activity to Hsp70.[121]

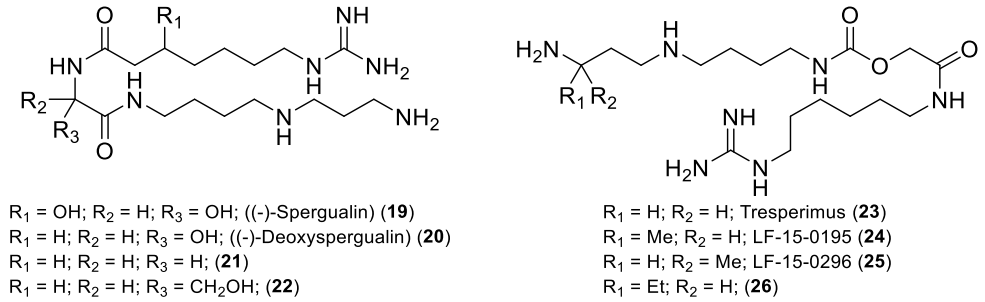

R_1 = OH; R_2 = H; R_3 = OH; ((-)-Spergualin) (**19**)
R_1 = H; R_2 = H; R_3 = OH; ((-)-Deoxyspergualin) (**20**)
R_1 = H; R_2 = H; R_3 = H; (**21**)
R_1 = H; R_2 = H; R_3 = CH_2OH; (**22**)

R_1 = H; R_2 = H; Tresperimus (**23**)
R_1 = Me; R_2 = H; LF-15-0195 (**24**)
R_1 = H; R_2 = Me; LF-15-0296 (**25**)
R_1 = Et; R_2 = H; (**26**)

Figure 13. Structures of spergualin and related polyamines.[122]

Due to the potential exhibited by the spergualin scaffold's bioactivity, Fewell, S. *et al.* used the Developmental Therapeutics Database (DTDB) at the National Cancer Institute to find related compounds that could display biological activity at Hsp70.[123] As a result, compound **27** (**Figure 14A**) was identified and found to inhibit both steady-state and J-domain stimulated ATPase activity of Hsp70 through interaction with Hsc70.[123–125] Follow-up work by Fewell S, *et al.* described a dihydropyrimidine scaffold with potential therapeutic action at Hsp70. This led to the synthesis of a series of functionalised dihydropyrimidines that inhibit Hsp70 ATPase activity with similar structural motifs to **27** (**Figure 14A** and **14B**; highlighted in BLUE, RED and GREEN). Two compounds **28** and **29** (**Figure 14B**) were found to specifically inhibit J-chaperone stimulated Hsp70 ATPase activity whilst retaining endogenous ATPase activity. Interestingly, **28** demonstrated no effect on ATP hydrolysis yet gave 4-fold reduction in the presence of a J-protein, indicating the J-protein necessary for its mode of action. Conversely, several compounds developed in the series exhibit stimulatory actions on the ATP turnover of Hsp70, in particular **30** (**Figure 14C**), which demonstrated up to a 5-fold increase.[125]

Although this research established the dihydropyrimidine scaffold as a viable biphasic modifier of the Hsp70 chaperone, in-depth SAR studies had not been undertaken. Therefore, a systematic SAR study of the previous derivatives was conducted by replacing the Ugi-derived peptide portion of the compounds with a protease-resistant β-peptide (**Figure 14C**).[126] Most importantly it was determined that aromatic, hydrophobic substitutions (**Figure 14**; highlighted in GREEN) are important for biological activity in either activating or inhibitory functions.[126] Furthermore, the positioning of the additional hydrophobic moiety appears to

have negligible effects on activity, indicating a potential binding site that is flexible or complex in nature. Although this research shows the considerable potential of the scaffold, the potency of currently reported dihydropyrimidine derivatives is lacklustre with future work needed to improve on the scaffolds therapeutic potential.

An investigation conducted by Jinwal, U. *et al.* explored whether changes in tau levels through interaction at Hsp70 were due to changes in definitive levels of the chaperone or modulation of ATPase activity.[26] This was investigated through application of the identified dihydropyrimidine activator **31** (**Figure 14B**) as well as the inhibitors **8** and **15** (**Figure 12A**). Treatment with activators found an increased operation of Hsp70 by approximately 45%. Conversely, the inhibitors **8** and **15** (**Figure 12A**) demonstrated >80% inhibition of Hsp70 function. Therefore, activators were found to be substantially driving the accumulation of tau aggregation whilst inhibitors displayed a converse effect, as displayed in **Figure 11A**. This paradoxically contradicted the initial hypothesis that activation of Hsp70 ATPase activity would result in greater clearance of tau. This can be rationally understood when it is considered that Hsp70 growth in stress events provides higher levels of the chaperone to bind unfolded stress-related substrates. Therefore, rapid increases in Hsp70 expression would lead to stoichiometric reductions in tau, with inhibition of ATPase activity promoting release of tau substrates for proteasomal degradation. This may suggest that stimulation of ATPase activity therefore favours net accumulation of tau *via* profolding complex formation and potentially additional misfolding. As such, development of inhibitors became a new focus for the treatment of aggregated tau through the Hsp70 pathway.

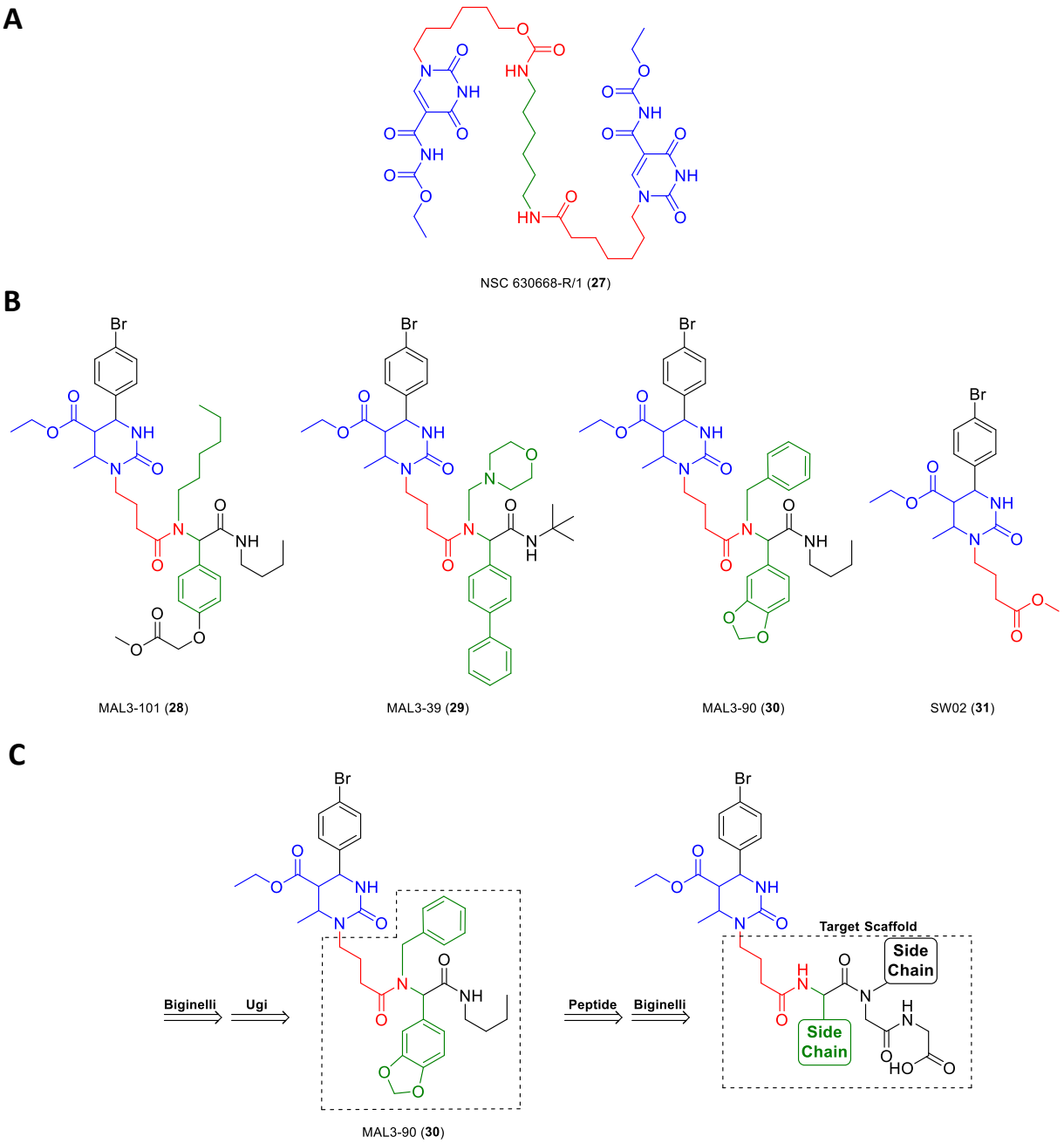

Figure 14. a) Spergualin-based scaffold of NSC 630668-R/1 **27**; b) Structures of various Hsp70 inhibitors exhibiting spergualin-type scaffolds, with indicated regions for alterations on various dihydropyrimidines and; c) An example strategy for the implementation of β-peptides into dihydropyrimidines, here demonstrating the process to imitate the functional group arrangement of **30**.[126]

MKT-077 **32** (**Figure 16**) is a delocalised cationic rhodacyanine that has been demonstrated to bind to Hsc70, mitochondrial Hsp70 and several others, which was originally evaluated for use in oncology applications.[127–129] Although **32** made it to clinical trials for various forms of advanced tumours, the trials were halted due to irreversible renal toxicity following administration.[130,131] **32** was derivatised due to these shortcomings to give **33** (**Figure 15**), which was identified and investigated as a potential therapeutic replacement that could

selectively target assorted cancer cell lines.[132] As a result, it was hypothesised that inhibition of Hsp70 through application of either **32** and **33** would result in promotion of tau clearance *via* proteasomal degradation.[133] The capacity of the molecules to inhibit ATP turnover were investigated *in vitro*, with inhibition of ATPase activity being observed when Hsp70-Hsp40 complexed but not solely on Hsp70. Previously, it has been reported that **32** acts allosterically within a negatively charged pocket residing near the NBD.[129] Therefore these results were consistent with this consideration.

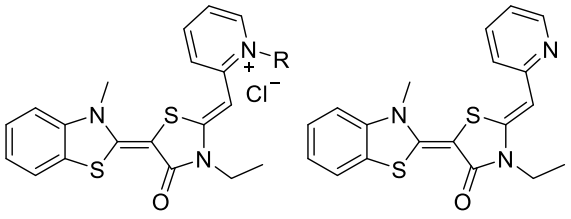

Figure 15. The chemical structure of the cationic rhodacyanine MKT-077 alongside subsequent derivatives YM-01 and YM-08.

In contrast to **32**, **33** expressed significantly improved potency with an improved 8-fold EC_{50} when reducing *in vitro* tau levels. Further assessment established reductions of tau levels by as high as ~75% in neuronal cells. Additional treatment of **33** resulted in a greater than 70% reduction of both pTau as well as total tau levels. Although these preliminary findings were promising, further iteration to the rhodacyanine scaffold was necessary to improve upon the pharmacological properties exhibited by the two compounds. In particular, neither molecule can penetrate the BBB, thereby restricting application of the scaffold as a clinical candidate or probe for exploration of Hsp70 within the central nervous system (CNS).[134,135]

To improve the pharmacokinetic profile of the rhodacyanine scaffold, Miyata, Y. *et al.* rationalised that greater BBB penetrance could be conferred *via* neutrality of the structure.[134] By substituting with a neutral pyridine motif, **34** (**Figure 15**) was predicted to express favourable properties. Testing of **34** established an IC_{50} value 10-fold greater than **32**. This firmly indicated that the cationic pyridinium moiety is not crucial for binding within Hsc70. However, complete removal of the pyridine or pyrdinium moiety eradicated binding affinity, demonstrating the functionalities to be essential for interaction. Improvements in the pharmacokinetic properties of **34** were assessed and compared to **32** and **33**. Although **33** was

prevalent within the kidney, it lacked detectable brain penetration which is consistent with reported data for **32**.[135] Conversely, generous amounts of **34** were observed within the brain alongside rapid clearance within compartments and decreased kidney retention. These results indicate **34** exhibits BBB permeability that its counterparts do not as well as potentially overcoming the renal toxicity observed previously in **32**. Therefore, additional development and subsequent iteration may see this promising rhodacyanine scaffold reach eventual clinical success for treatment of tau *via* Hsp70 interaction.

Heat Shock Protein 90 kDa (Hsp90)

Hsp90 predominately regulates the conformation, stability, translocation and degradation of client proteins, with each stage being coordinated by various co-chaperones.[96,100,136–138] It is considered to play a principal role in organism development and cell cycle control, alongside its environmental stress response.[93,139–141] Hsp90 has two isomers (Hsp90α and Hsp90β) that exist as homodimers; the two monomers both exhibit three domains in their structure: an amino N-terminus domain (NTD), a middle domain (MD) as well as a carboxy C-terminus domain (CTD).[96,97,136,142] The N-terminal acts as the main ATPase domain of Hsp90, which presents a nucleotide-binding pocket with a unique fold (known as the Bergerate fold) that can allow for its selective inhibition over various other targets that bind ATP/ADP as general substrates.[97,139,143]

Additionally it operates within open and closed conformation states (**Figure 16**).[144] Although both the binding and hydrolysis of ATP is fundamental to the function of the chaperone, Hsp90 exhibits weak ATPase activity.[139] The rate of the chaperone cycle is regulated by this ATPase activity whilst the binding state of the ATP controls the combination of co-chaperones bound at specific stages of the cycle.[145] Binding sites for client proteins as well as co-chaperones have been found to reside in the M-domain and has been found to exhibit a strong part in both ATP hydrolysis and client recognition processes.[96,142] Lastly, the C-terminus not only functions as an interface for the dimerisation of the Hsp90 protein but plays host to at least eight co-chaperones that are responsible for the regulation of ATP hydrolysis as well as management of both client protein binding and release, thereby organising the functions of Hsp90.[96,115,136,146,147]

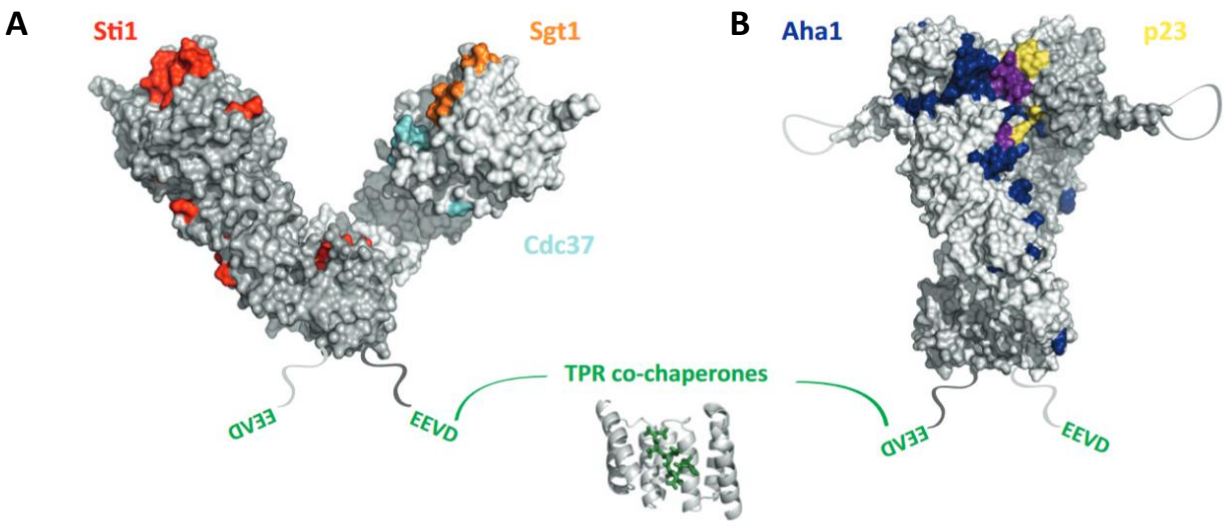

Figure 16. Three-dimensional model representation of the Hsp90 molecular chaperone in a) an open conformation with interaction sites of co-chaperones that preferentially bind (red: Sti1/Hop (stress inducible 1/Hsp70-Hsp90 organising protein; light blue: cdc37 (cell division cycle 37 homolog; orange: Sgt1 (suppressor of G2 allele of skp1) and green: TPR (tetratricopeptide co-chaperones)) and; b) a closed conformation with interaction sites of co-chaperones that preferentially bind (blue: Aha1 (activator of Hsp90 ATPase homolog1); yellow: p23; purple: overlapping regions of Aha1 and p23 and; green: TPR co-chaperones). Reprinted with permission from Röhl, A. *et al.*[144]

It can be seen that Hsp90 is a central mediator of protein homeostasis and is immersed in more than 400 PPIs, including interactions with other molecular chaperones and their corresponding client proteins.[96,110,136,139,148] Through analysis of public data, Echeverría, P.C. *et al.* have developed an interactome of the interactions observed in both human and interolog Hsp90 (**Figure 17**), allowing the magnitude of these interactions to be visualised.[148] These considerable interactions make Hsp90 a particularly attractive target due to the potential for inhibition of multiple drug targets simultaneously. Although a vast amount of research exists concerning the inhibition of Hsp90 as a therapeutic target in oncology applications, there is comparatively a limited level of research concerning its role in tauopathies. It is necessary to consider alternative approaches to that reported in literature, regarding therapeutic treatments for oncological applications, when deliberating decisions for pathways of treatment. Research has established differences in inhibitory interactions at both the N- and C-terminals, demonstrating activation of the HSR pathway *via* inhibition at the N-terminal but not the C-terminal.[28,96,98,100,115,142,143,146,149–151] Hsp90 differs biochemically in cancer cells, where it is an exclusively higher order heterocomplex comparatively to a latent, uncomplexed state in non-cancerous, healthy cells.[96] This leads to activation of the HSR *via* N-terminal inhibition and subsequent upregulation of oncologically expressed Hsp90, where protection of the cancer cell from apoptosis occurs whilst facilitating cancer growth by promotion of antiapoptotic

pathways.[136] Thus, a strong trend towards C-terminal inhibition can be see within the field of oncology. Conversely, upregulated Hsp70, Hsp90 and Hsp27 could defend against toxicity *via* increased folding or diversion of neuronal aggregate formation, which could be ideal for therapies in the treatment of tauopathies.

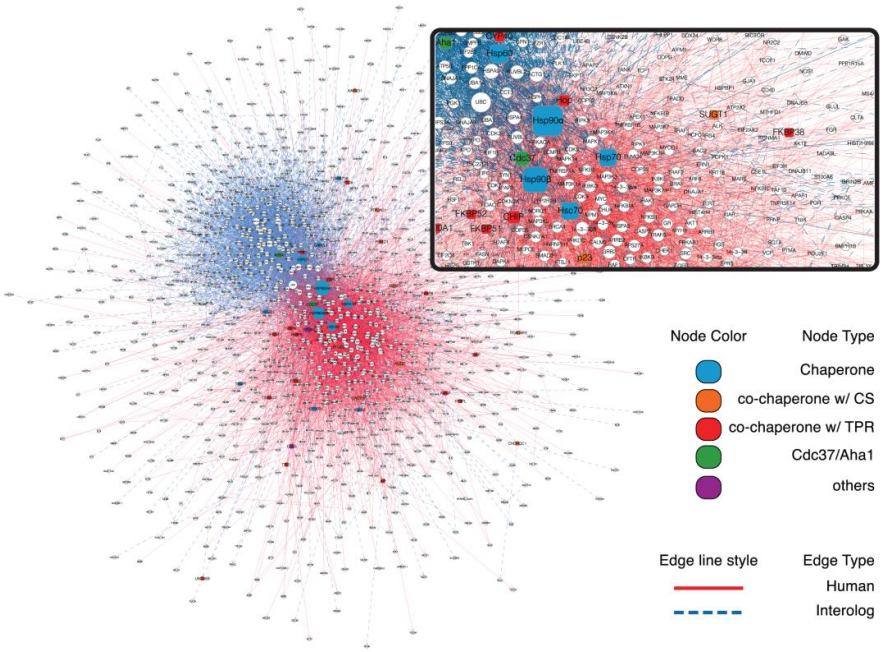

Figure 17. Predicted interaction network of Hsp90, exhibiting 1,150 nodes and 8,892 edges. Reprinted with permission from Echeverría, P. C. *et al.*[148]

It has been demonstrated by Dickey, C. *et al.* that a clear inverse correlation exists between tau levels and upregulation of these heatshock proteins *via* induction of the HSR pathway through high-throughput screening of N-terminal inhibitors.[152] As a result, substantial reduction of *in vitro* tau levels were observed. It may then be appealing to aim for incorporating such a mechanism in the overall therapeutic approach by N-terminal inhibition. Futhermore, potential for considerable selectivity could be conferred due to a highly conserved and distinctive ATP/ADP binding pocket within the N-terminal that is not present within other molecular chaperones.[153] Unlike other chaperones, the clients of Hsp90 are primarily either protein kinases or transcription factors that have roles in signal transduction.[97]

Most importantly, it has been determined by Luo, W. *et al.* that aberant mutant tau (mTau) is maintained in tauopathies by Hsp90 through a complex formation with p35 (an activator of CDK-5) and subsequently, CDK-5.[93] By investigating the effects of Hsp90 inhibition on p35 and CDK-5, it was found that degradation of aberrant tau proteins and induction of the HSR pathway had occurred, including a significant increase in Hsp70

expression. A reduction in p35 levels as a result of the Hsp90 inhibition, led to significant modulation of p35/CDK-5 and consequently mTau levels.[93] Moreover, Hsp90 has been found to facilitate the phosphorylation of tau when increased amounts of Hsp90 were added to tau protein in the presence of GSK-3 kinase as well as ATP, leading to the proposition that Hsp90 mediates a conformational change that consequently leads to increased phosphorylation.[154] Further reports implicate the role of Hsp90 in the regulation of aggregation and degradation of tau, alongside its various co-chaperones.[28,40,106,108,137,155–157]

N-Terminal Inhibition

By 2013, 47 compounds targeting Hsp90 (specifically the N-terminal) had been evaluated in their effectiveness for therapeutic application in various oncological studies. Of these compounds, 33 either did not make it to clinical trials or failed due to either high toxicity or low bioavailability, constituting a fail rate of 70%.[28] As of 2020, only 7 N-terminal inhibitors remained in either active or recruiting trials with 53% not progressing past phase I after 170 clinical trials.[158] Predominant N-terminal inhibitors, such as the first identified natural product geldanamycin (**35**; **Figure 18**) and the synthetic purine-based small molecule PU3 (**38**; **Figure 18**), have to date provided the fundamental scaffold structures that have influenced the design of further reiterations. These inhibitors have been primarily ATP-competitive at the ATPase binding pocket within the Hsp90 N-terminal. Such examples include 17-AAG **36** (a derivative of **35**; **Figure 18.**) and PU24FCl **39** (a derivative of **38**; **Figure 18**).[149,153,159,160]

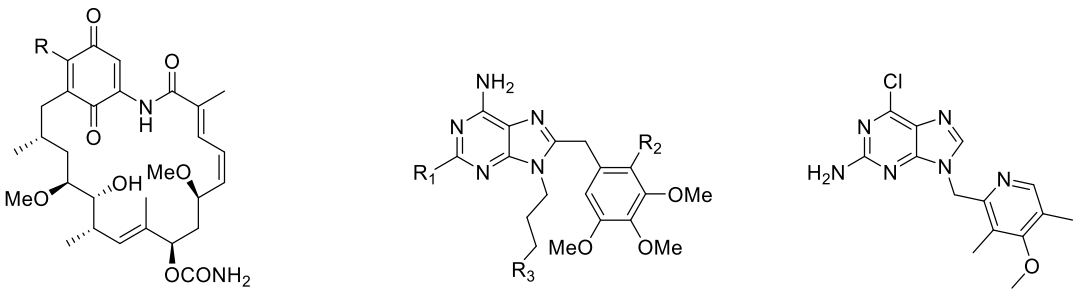

Figure 18. Natural ansamycin-based and synthetic purine-based N-terminal inhibitor scaffolds.[160]

In 1970, the ansamycin-based antibiotic **35** was isolated from *Streptomyces hygroscoicus* before being identified by Whitesell, L. *et al.* as the first known small molecule to inhibit Hsp90.[158,161,162] However, clinical development of the molecule was prevented by

both its dose limiting hepatotoxicity and low aqueous solubility.[143,163] Due to the considerable Michael acceptor capability exhibited on the scaffold (thought to be responsible for the hepatotoxicity), several derivatives were developed with reduced electrophilicity including **36** and **37** (**Figure 18**).[164] Although these derivatives improved upon aqueous solubility, complications in their cost of production, formulations and administration of safe pharmacologically relevant doses has hindered their clinical development.[160,164] In fact, dose limiting hepatotoxicity was found to persist through all derivatives and may be mediated through the production of reactive oxygen species *via* CYP450 redox cycling of the benzoquinone moiety within the scaffold.[165] As a result of the complexities exhibited by the ansamycin scaffold, development of new chemical structures were sought to obtain improved safety profiles, superior target selectivity and proportionate potency.

Research conducted by Chiosis. G. *et al.* demonstrated the rational design of the purine-based Hsp90 inhibitor **38** (**Figure 18**) through a detailed modelling study of the mode of binding (**Figure 19**).[160] Examination of the ADP/ATP binding site identified several crucial aspects that could be used to design a small molecule that could interact as an inhibitor within the pocket, thus resulting in compound **38**. In comparison to **36**, **38** was determined to bind at Hsp90 with an estimated 20-fold weaker association. However, its ease of synthesis and high solubility make the purine scaffold an attractive candidate in further medicinal chemistry endeavours. Additional purine derivatives developed greatly improved upon the affinity displayed by **38**.[166] Properties such as the length and presence of an alkyl chain and intensity of the free amine hydrogen bonding interaction was determined putative to enhancing affinity of the scaffold at Hsp90. As a result of these modifications the new purine derivative **39** (**Figure 18**) was shown to have a comparable affinity to the ansamycin scaffold, exhibiting a 30-fold higher affinity than **38** alongside ideal cellular efficacy.

Additional transposition between key binding elements determined through molecular interactions within the ATPase pocket (**Figure 19B**) led to identification of the compound BIIB021 **40** (**Figure 18**).[167] In comparison to **39**, a remarkable 12-fold increase in the EC_{50} was observed when assessed. Consequently, **40** was both the first purine-based and orally active Hsp90 inhibitor to reach clinic.[143,164,168,169] Physicochemical properties exhibited by the ansamycins and previous purine-based derivatives were substantially improved upon by **40**. However, it did not successfully pass phase II clinical trials for several oncological applications as it did not possess desirable potency or a prolonged response therefore

requiring greater doses to reach biological effects in clinic.[164,170] Frequent dose-limiting toxicities included fatigue, dizziness, nausea, hyponatremia, hypoglycaemia and rash, amongst others.[170]

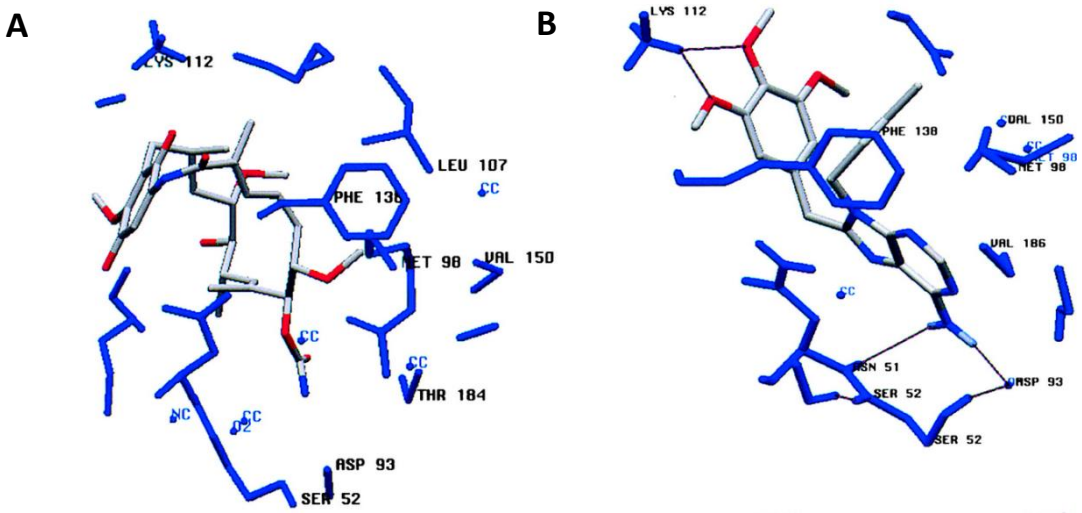

Figure 19. a) Crystal structure of geldanamycin bound to Hsp90 ATPase pocket; b) PU3 bound to Hsp90 ATPase pocket. Reprinted with permission from Chiosis, G. *et al.*[160]

As of 2022, there have been a total of 20 Hsp90 N-terminal inhibitors which have made it to clinic for oncological applications but none have been approved for treatment.[171] Apart from the safety issues previously described, there are two fundamental underlying reasons. Firstly, induction of the HSR within the patient is detrimental due to the overexpression of Hsp90 within cancerous cells. Resultantly, activation of unstable kinase functions follows which promotes carcinogenesis.[172,173] Secondly, selectivity between the four existing isoforms of Hsp90 has proven difficult as a >95% sequence identity in the NTD exists thereby leading to pan-inhibition (where all isoforms are non-selectively inhibited). This has been considered a major limitation to clinical development in oncological application, however, its role in regard to tauopathies is unknown.[158,174] As previously stated, it has been demonstrated to be beneficial to induce HSR in the treatment of tauopathies. More recently, there has been progress in development of isoform-selective (Hsp90α and Hsp90β) inhibitors but both their clinical and tau-relevant applications have yet to be investigated.[174]

C-Terminal Inhibition

Similarly to the N-terminal, inhibition of the C-terminal prevents nucleotide binding at the N-terminal *via* prohibition of NTD dimerisation.[100] Söti, C. *et al.* identified the presence of the CTD alongside its capacity to act as a secondary ATP-binding site present within

Hsp90.[175] However, it does not exhibit ATPase activity. Further studies indicated opening of the binding site to only occur when ATP conferred occupancy of the ATPase site within the NTD, contingent on a nucleotide-dependent molecular switch.[176] Coumarin-based antibiotics such as novobiocin **41**, clorobiocin **42** and coumermycin A1 **43** (**Figure 22**) exhibited great inhibition of enzyme-catalysed hydrolysis of ATP. Perhaps as a result of this inhibition as well as their structural similarities to the ansamycin scaffold, Marcu, M. G. *et al.* subsequently tested for potential activity against Hsp90.[177] It was determined that **41** was able to bind a CTD fragment but unable to bind an NTD fragment. Although **41** was the first compound to be identified as an inhibitor of the C-terminal, the development of structural analogues **42** and **43** led to 1000-fold greater efficacy within the scaffold. Furthermore, it was determined that C-terminal inhibition induced degradation of Hsp90 client proteins.[150,178] Interestingly, binding of the C-terminal with **41** displaced inhibitors bound to the N-terminal which is not a reciprocal phenomenon.[177,179] This may be a result of separation of the homodimeric CTDs *via* an induced conformational change.[180]

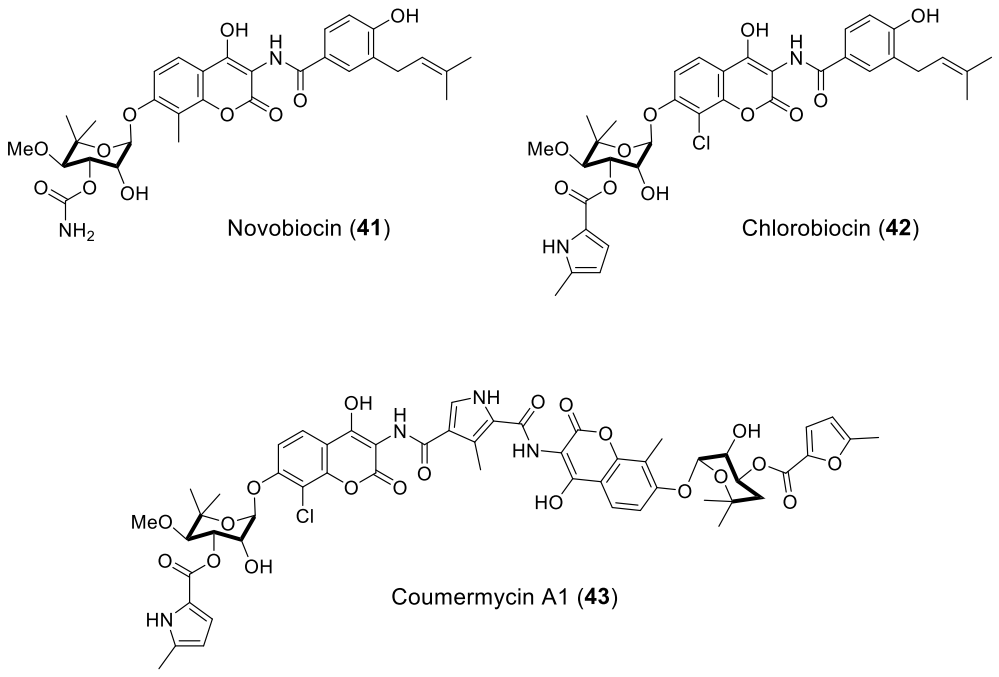

Figure 20. Molecular structures of classic coumarin-based C-terminal inhibitors.[150]

Bimoclomol **44** (**Figure 21**) was the first reported hydroxylamine scaffold-based co-inducer of the HSR pathway.[181] In fact, it was notably observed to induce a 4-fold upregulation of Hsp70 as a result of heat shock activation. A novel library of 1,4-dihydropyridine analogues derived from the scaffold were developed and reported to have selective Hsp modulating activity both *in vitro* as well as *in vivo*.[182] This was confirmed by

the co-inducing effect of two derivatives in particular, **45** (water-soluble; **Figure 21**) and **46** (water-insoluble; **Figure 21**), which significantly increased levels of Hsp27, Hsp40 and Hsp70 proteins without affecting levels of Hsp60 and Hsp90 proteins.[183] Interestingly, in the absence of heat shock stress these compounds did not alter the levels of the Hsps nor do they modify the ATPase activity of Hsp90. Additional studies on the mechanisms of action by which 1,4-dihydropyridines act found they in fact primarily target the C-terminal domain of Hsp90 but with the necessity of middle-domain interaction.[184] As a result, allosteric modulation of Hsp90 ATPase activity occurs thus leading to induction of the HSR *via* a compromised ability to chaperone. It has been demonstrated that acute overexpression of Hsps results in unwanted side effects as a consequence of unregulated Hsp induction.[185] However, upregulated expression *via* induction under stress-only conditions, proceeding through the novel mechanism exhibited by these 1,4-dihydropyrimidine compounds, may lead to a potentially favourable strategy in the treatment of tauopathies.

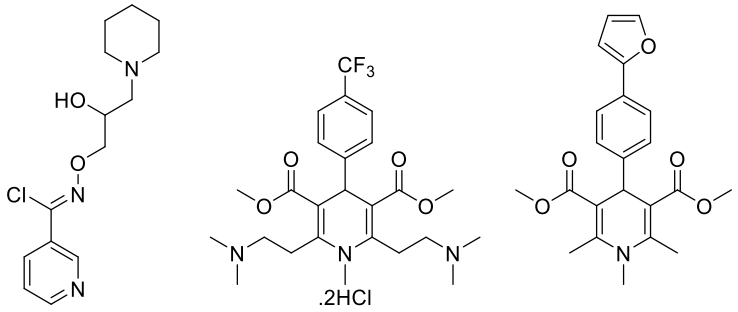

Bimoclomol (**44**) LA1011 (**45**) LA1044 (**46**)

Figure 21. Molecular structures of bimoclomol (**44**) as well as 1,4-dihydropyridine derived C-terminal inhibitors LA1011 (**45**, water-soluble) and LA1044 (**46**, water-insoluble).

1.6 Inhibition of Co-Chaperones

Although tau in structure is intrinsically disordered, it does not exhibit a stable secondary structure under physiological conditions and is able to fold after protein-protein interactions with host proteins.[186] These protein-protein interactions are dependent on the disordered structure of tau as specific binding partners influence both the conformation and properties of the complex.[187] This is important as post-translational modifications, such as site-specific phosphorylation, subsequently alter conformations of tau and changing affinity towards various molecular co-chaperones.[141] However, disturbances in the balance of molecular co-chaperones and tau-associated modifications can drive conditions that induce tau pathogenesis.[106,141,157,188] As previously discussed, targeting of heat shock proteins specifically has involved both pharmacological and isoform selectivity issues. Therefore use

of co-chaperones accompanying these heat shock proteins could allow for more specific targeting while modulating substantially fewer processes and thus minimising off-target effects.[100]

1.6.1 Activator of Hsp90 ATPase Homolog 1 (Aha1)

Activation cycles of chaperone proteins are coordinated by sequential interaction with regulatory proteins known as molecular co-chaperones. They aid maturation cycles of clients through the regulation of transition between various conformational states, typically resulting in ATP hydrolysis.[137] In regards to Hsp90, one co-chaperone has been demonstrated to significantly upregulate its activity within the cycle (**Figure 22**).[157,189]

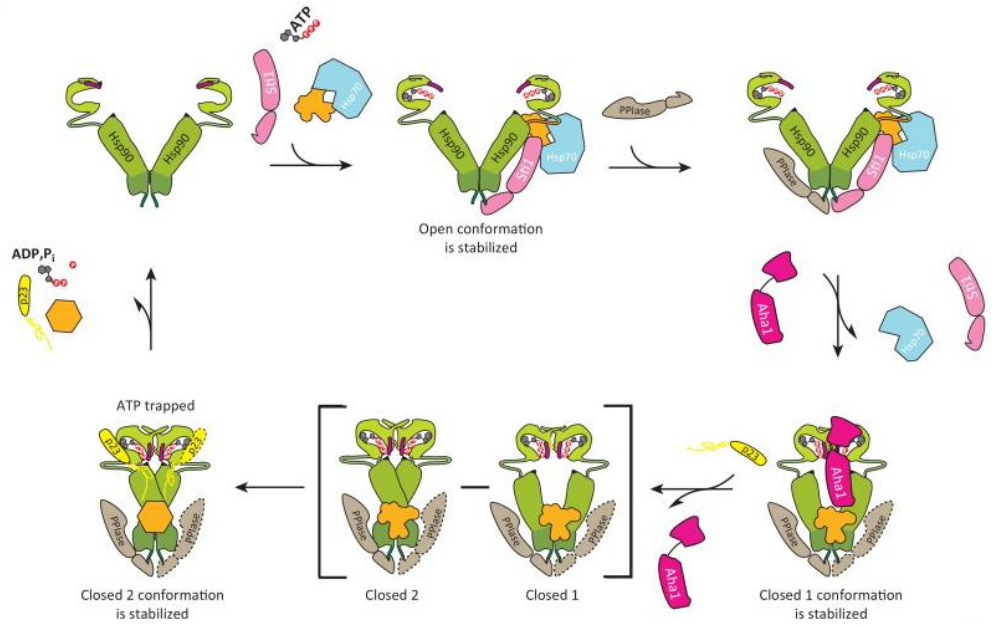

Figure 22. The maturation cycle of Hsp90, including its interaction with Hsp70 and activation by Aha1. Reprinted with permission from Röhl, A. *et al.*[144]

Activator of Hsp90 ATPase Homolog1 (Aha1), a small 38-kDa molecular co-chaperone, assists to greatly stimulate the low ATPase activity of Hsp90 *via* a three-step mechanism. Structurally, it is a two domain protein consisting of a 156 residue N-terminal domain alongside a comparably sized *C*-terminal domain that are both connected *via* an unstructured linker.[137] Through binding a catalytic loop residing in the middle domain of Hsp90 by the N-terminal domain of Aha1, conformational rearrangement of the Hsp90 *N*-domains to a close stated is observed.[137,138,151,157] The induction of this partially closed conformation accelerates the advancement of the ATPase cycle substantially.[138,157] It has been demonstrated that this occurs *via* directly reaching an I2 state in the ATPase cycle, effectively

bypassing the I1 state when in the presence of Aha1.[138,189] Similarly, interaction of the dimerised N-terminal domains of Hsp90 with the terminal *C*-domain of Aha1 also leads to stimulation of the ATPase cycle. However, neither the relative contribution or underlying mechanisms of these two interactions is known.[137] To date, there are no known commercial Aha1 selective inhibitors. As earlier described, there has been large difficulty in the direct targeting of Hsp90 due to either high toxicity / low bioavailability of compounds.[28,157,190]

To potentially overcome these complications, it has been proposed that the targeting of Aha1 may prove beneficial as an alternative treatment. Viability of Aha1 as a therapeutic target through the use of various novobiocin analogues **47** – **49** (**Figure 23A**) has been investigated.[157] In particular, biological studies identified the novel analogue **49** as a small molecule with high affinity to the Hsp90-Aha1 complex.[190] It was determined that the noviose sugar (**Figure 23A**; highlighted in RED) was critical to selective Hsp90 binding whilst the aryl amide side chain (**Figure 23A**; highlighted in GREEN) was crucial for selective binding to Aha1. Additional modelling evaluations have established that the 3'-OMe functionality residing on the side chain forms a pivotal hydrogen-bonding interaction within Aha1 that may explain this dual affinity.[151] Evaluation of **48** and **49** (**Figure 23A**) resulted in selective inhibition of Aha1 alongside significant reduction of tau fibril formation when compared with a control sample (**Figure 23B**).[157] Moreover, treatment of insoluble tau with **48** led to an increase in soluble, phosphorylated tau levels.

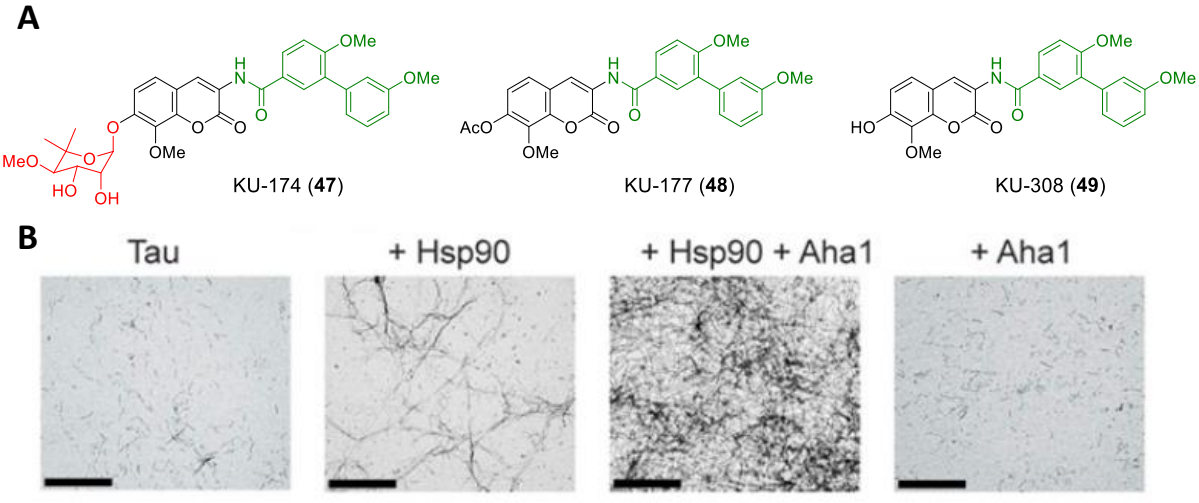

Figure 23. a) Chemical structure of novobiocin analogs KU-174 **47**, KU1-77 **48** and KU-308 **49** and; b) representative 20,000x TEM images of recombinant P301L tau fibrils formed in the presence of indicated chaperone proteins with ATP (scale bars: 2 μm). Reprinted with permission from Shelton, L. B. *et al.*[157]

Recently the over-expression of Hsp90 co-chaperones FKBP52 and Aha1 in wild-type mice has been evaluated.[188] It was determined that highly attenuated levels of total-tau and phosphor-tau species within the hippocampus were correlated to overexpression of Aha1. However, a rise in oligomeric tau was not identified in these mice, a discrepancy compared to the results found by Shelton. Regardless, phosphor-tau has been shown to be prominent in the early stages of abnormal tau processing and in driving neurodegeneration.[191–193] Additional assessment demonstrated that knockdown of Aha1 prevented tau tangle formations, rescued hippocampal neurons and reduced phosphorylated species of tau.[194]

Due to absence of small molecules in literature that can reportedly inhibit the Hsp90-Aha1 interaction, Ihrig, V. and Obermann, W. M. J. screened a collection of 14,400 chemical compounds through the amplified luminescence proximity homogenous assay (Alpha) to identify potential candidates.[99] Eight small molecules (**Figure 24**) were identified, which interestingly exhibited diazo functionalities within the centre of seven of the established molecules. Furthermore, four featured S-N bonds in the form of thiazoles or sulphonamides. These similarities may suggest a relationship between these moieties and inhibition of Hsp90-Aha1 complex formation between these chemotypes. The inhibitors **52** and **55** were identified to be the most potent of the eight. However, the exact mechanism of action for this inhibition is not understood.

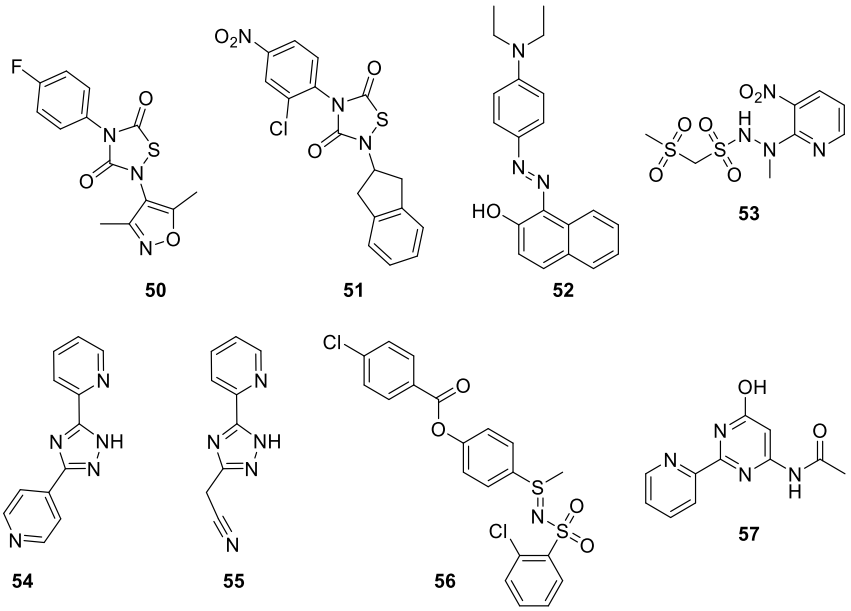

Figure 24. Eight small molecules identified in a high-throughput screening of 14,400 compounds through an Alpha assay.[99]

Stiegler, S. C. *et al.* screened approximately 15,000 chemical compounds to assess their interactions between Hsp90-Aha1 as modulators, through a Förster resonance energy transfer based assay.[195] Roughly 40 compounds were identified as Hsp90-Aha1 modulators (HAMs), with five of the most effective focused on in the study (**Figure 25**). Upon investigation, it was determined that three of these compounds were inhibitors (**Figure 25A**) of the Aha1 mediated stimulation. HAM-1 (**58**) was determined to be the most potent inhibitor, suppressing stimulation by 93%. Both **59** as well as **60** exhibited inhibitions of 27% and 19%, respectively. Two compounds were identified as stimulators (**Figure 25B**) of the ATPase activity. The activators **61** and **62** increased Hsp90/Aha1 activity by 130% and 151 %, respectively.

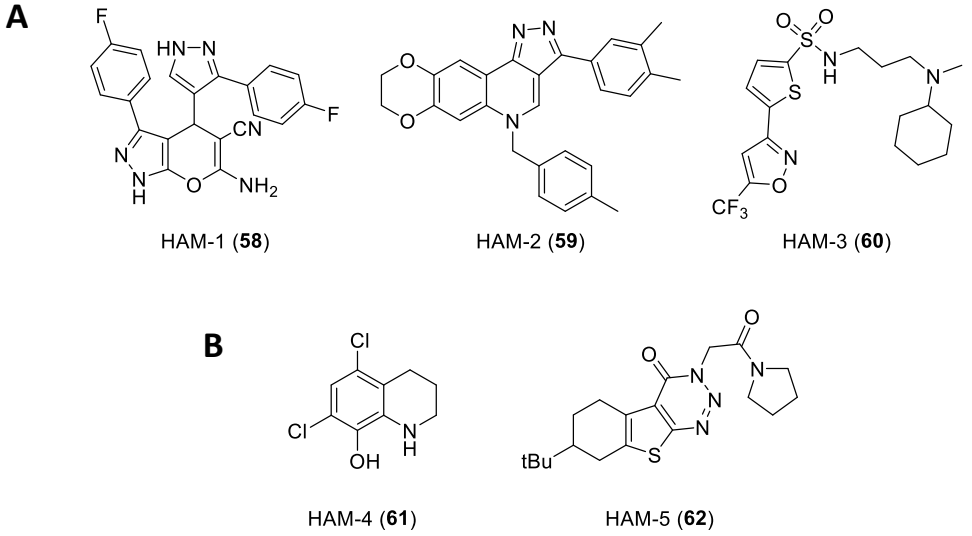

Figure 25. Five identified modulators of the Hsp90-Aha1 complex shown to either be: a). inhibitors or b). stimulators of the complex.[195]

To determine the mechanism of action of the modulators, ATPase assays were performed in the absence of Aha1 to assess whether they acted on Hsp90 alone or on the Hsp90-Aha1 complex. **58** demonstrated inhibition of the Hsp90 ATPase activity when Aha1 was not present, suggesting it may interfere with binding of Aha1 to the Hsp90-Aha1 complex. Surface plasmon resonance measurements showed affinity of Aha1 to Hsp90 was only slightly affected by the presence of **58**. Thus, it was concluded that although **58** does not prevent the formation of the Hsp90-Aha1 complex, it does prevent Aha1 from effectively stimulating Hsp90. Further analysis *via* ^{1}H-^{15}N correlated NMR spectra of ^{15}N-labeled Hsp90 conveyed that **58** binds specifically to the Hsp90 N-terminal domain, suggesting Aha1 cannot influence N-terminal activity due to the presence of **58** within the domain. On assessment of

the effect of **59** on ATPase activity, it conversely activated the ATPase 2-fold in absence of Aha1 rather than the inhibition it exhibited in its presence. This suggests a unique mechanism of action to that of **58**, although it was not further investigated. Both **61** and **62** exhibited substantial increases in ATPase activity in the absence of Aha1, with a 565% and 220% activation, respectively. These results indicate **59**, **61** and **62** may directly bind to Hsp90 but it was not further explored.

More recently, Keegan, B. *et al.* identified the 1,5-disubstituted 1,2,3,4-tetrazole **66** (**Figure 30**) which demonstrated inhibitory activity on the Hsp90-Aha1 complex.[196] Performing an SAR around the scaffold of **48** (**Figure 23A**); a library of derivatives was developed to assess tolerated functionalities on either side of the secondary amide linker. Preliminary results determined high toleration of replacement at the coumarin core with phenyl derivatives, thereby eliminating the bicyclic structure. Derivatives with *p*-CF_3 or *p*-NO_2 substitutions (**63** and **64**; **Figure 26**) retained similar inhibitory activity to **48** with substantially reduced molecular weight. Optimisation of the biaryl moiety was then undertaken with replacement of the coumarin core with the *p*-CF_3 lead derivative. Previous studies on **47** and its derivatives advised presence of the *p*-OCH_3 functionality was pivotal for inhibition at Hsp90-Aha1 complex through a hydrogen bond accepting interaction. Consequently, optimisation of the secondary biaryl ring was focused on. Substitutions at the *ortho* position of the ring were not tolerated, with no inhibitory activity observed for any derivatives. Conversely, *meta* substitutions exhibiting hydrogen accepting moieties demonstrated some level of inhibitory activity, in particular the *m*-OCH_3 and *m*-$N(Me)_2$ derivatives (**63** and **65**; **Figure 26**).

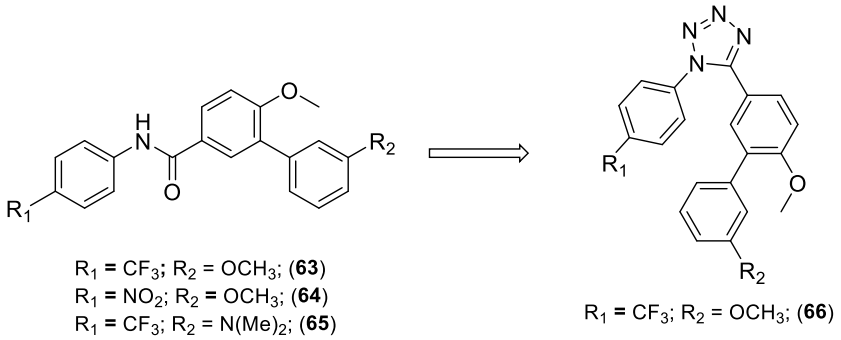

R_1 = CF_3; R_2 = OCH_3; (**63**)
R_1 = NO_2; R_2 = OCH_3; (**64**)
R_1 = CF_3; R_2 = $N(Me)_2$; (**65**)

R_1 = CF_3; R_2 = OCH_3; (**66**)

Figure 26. Compounds identified with activity at Hsp90-Aha1 and the 1,5-disubstituted 1,2,3,4-tetrazole inhibitor **66**.[196]

Finally, the central amide bond was investigated as a significant electronic trend between biaryl electron donor activity, contributing to the carbonyl functionality, as well as electron withdrawal from the nitrogen *via* the phenyl ring appeared important to Hsp90-Aha1 inhibition. As a result, the 1,5-disubstituted 1,2,3,4-tetrazole moiety of **66** was used to establish a *cis*-amide isostere. The molecule retained AlphaLISA activity whilst preventing Aha1-stimulated aggregation of P301L tau *in vitro*. Furthermore, it was discovered that it does not directly inhibit the refolding activity of Hsp90. Interestingly, expression of Hsp70 was not observed therefore implying the absence of HSR induction.

So far to date, the compounds discussed are the only known interactors of Hsp90-Aha1 in literature. The new understanding of the behaviour of this co-chaperone and limited literature on the topic specific to tau protein indicates additional studies should be conducted to further explore the potential in this area of research. In particular, a strong proof of concept has been shown that inhibition of Aha1 is a viable alternative for the therapeutic treatment of tauopathies, including AD. Therefore, discovery of compounds with substantial therapeutic benefit and/or probing capabilities is necessary through development of novel chemical scaffolds that target Hsp90-Aha1. This will provide a greater overall insight of the underlying mechanisms and pharmacodynamics of this promising target with additional therapeutic potential.

1.7 Project Aims

Hsp90-Aha1 has been demonstrated to be a viable therapeutic pathway for the reduction of tau in neurodegenerative disease states. Because the majority of currently assessed therapeutics have seen little success at the clinical level, it was considered pertinent to design new chemical scaffolds with an aim to improve on pharmacological properties whilst reducing tau through novel target interaction. As such, this project has focused on the identification, synthesis and diversification of novel chemotypes to broaden the scope of molecules that interact with this target as well as the understanding of its fundamental pharmacology.

Synthesis and Assessment of Phenyldiazenyl Naphthaleneol Derivatives (Chapter 2)

To explore the pharmacophore of the target, a lead candidate with reported inhibitory activity at the Hsp90-Aha1 complex had to be identified. Therefore **Chapter 2** focuses on the identification, synthesis and validation of this candidate. Additional SAR around the head-group of the molecule was conducted for assessment of tolerated functionalities that could be

furnished to future chemotype iterations for comparison. These candidates were evaluated for their interaction with tau aggregates in an *in vitro* model, providing promising novel action of the diazenyl scaffold on tau directly.

Chemotype Exploration of Diazenyl Substitutes (Chapter 3)

Work presented in **Chapter 3** expands on the chemical space of the previously identified scaffold through the synthesis and characterisation of chemical structures that replace the primary diazenyl motif. These alterations emphasise enhancing both biological and physical properties of the overall scaffold. Although *in vitro* assessment was not able to be conducted, it is expected that the future study of SAR between these novel chemotypes and the targets will provide a greater overall understanding of the pharmacodynamics related to the therapeutic treatments of these tauopathies.

Investigation of Naphthalene Tail-Group (Chapter 4)

Assessing the importance of the naphthalene moiety was considered pertinent to discerning the pharmacophore of the lead scaffold. Accordingly, **Chapter 4** outlines the synthesis and characterisation of several structural replacements to the naphthalene functionality. This examines a small SAR of the tail-group to determine whether a bicylic moiety is necessary and the tolerance of furnishing a privileged indole structure.

Chapter 2:

Synthesis and Assessment of 1-(Phenyldiazenyl)naphthalene-2-ol Derivatives

Chapter 2: Synthesis and Assessment of 1-(Phenyldiazenyl)naphthalene-2-ol Derivatives

2.1 Introductory Remarks

Recent advances within the area of Alzheimer's disease have focused primarily on taucentric pathways for therapeutic treatment.[9,46,72,197] This relatively novel approach targets the inhibition of tau protein aggregation through a variety of systems, as communicated in **Chapter 1**. In particular, it is important to discern a unique yet valuable drug target through which small molecule interaction can either impede formation of aggregates or facilitate their degradation. In this case, the complex formed between the Hsp90 chaperone and its co-chaperone Aha1 has been chosen as the primary point of exploration. As displayed in **Figure 9** within **Chapter 1.5.1**, this complex can be described as challenging to evaluate, but previously discussed literature establishes small molecular scaffolds with the capacity to inhibit the Hsp90-Aha1 complex and effectively reduce aggregated tau levels.[99,195,196] An essential component of developing a potential therapeutic or chemical probe which interacts with this process is identifying an appropriate molecular scaffold that can undergo diversification with ease. This can allow for greater optimisation of the SAR, refining both the binding affinity and desired interaction of the molecules at the target whilst providing the ability to overcome pharmacological barriers. These barriers may be a result of single target interaction (i.e. uncomplexed Hsp90) or chemical motifs present within the scaffold. Identification, diversification and validation of a lead molecular scaffold are the fundamental basis of the work presented within this chapter.

Chapter Aims

Due to the limited research present within literature, it was observed that a gap existed in further detailing a diverse selection of chemical scaffolds that can be used to encourage investigation of the Aha1-Hsp90 complex. More specifically, the role it plays in either preventing or inhibiting tau aggregate formations when the complex has impeded activity. Therefore, a lead candidate (**52**; **Figure 27**) with reported activity was firstly identified and synthesised alongside various derivatives (**67 – 72**; **Figure 27**) thereafter to commence primary investigation. Following the synthesis of this initial library, the role of these derivatives on tau aggregation was evaluated and assessed through an *in vitro* assay whereby the results are thoroughly discussed.

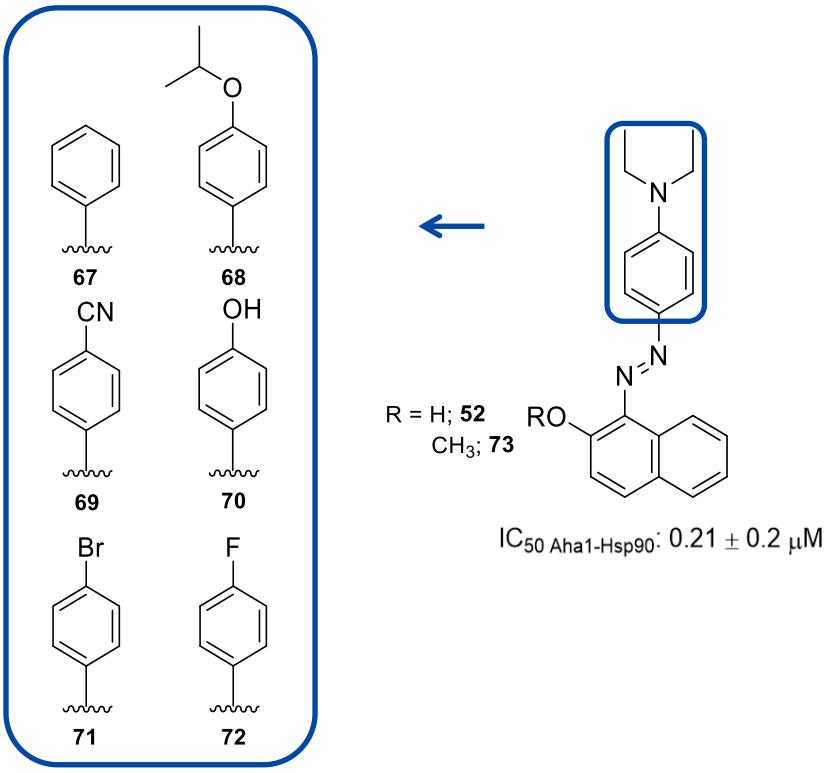

Figure 27. Lead candidate **52** alongside the reported IC_{50} at the Aha1-Hsp90 complex of 0.21 ± 0.2 μM and several substitutions made at the *para*-position of the phenylic head group.[99]

2.2 Identification and Synthesis of Lead Candidate

Initiation of this research proceeded through literature identification of promising molecular scaffolds demonstrating inhibitory activity at the Aha1-Hsp90 complex. Although several were observed, the primary lead candidate was selected from a high-throughput screening of the Maybridge Hitfinder collection of 14,400 compounds, conducted by Ihrig and Obermann.[99] This collection emphasises compounds that are deemed non-reactive while fitting the Lipinski guidelines for "drug-likeness". In particular, an identified azonaphthol scaffold was determined to be a potent inhibitor of the Aha1-Hsp90 complex shown in **Figure 27**, specifically compound **52**. Its nanomolar potency and synthetic accessibility make it an attractive candidate as a chemical probe to facilitate exploration of SAR. Moreover, the scaffold has promising capacity to undergo diversification as it hosts three regions that can be separately modified. To begin with, substitutions were made in the 4- position of the phenylic head group so as to assess their role on activity at the target with modifications between atom length, hydrogen bonding capacities and overall substituent effects. These derivatives (**67 – 72**) can be observed in **Figure 27**. To evaluate the effect of tautomerisation at the target, the lead candidate underwent alkylation at the phenol functionality (**73**; **Figure 27**) so as to restrain the ketone-imine resonance for direct comparison (**Chapter 2.2.3**, **Scheme 3**).

Although access to an assay assessing Aha1-Hsp90 complex activity was restricted, notable biological data was obtained for the role these derivatives perform on inhibiting tau aggregation directly (**Chapter 2.3**).

2.2.1 Synthesis of 1-((4-(Diethylamino)phenyl)diazenyl)naphthalen-2-ol

To begin the synthetic pathway (**Scheme 1**) toward obtaining the lead candidate **52**, the commercially available 1-fluoro-4-nitrobenzene (**74**) provided the precursor to afford the head group *N,N*-diethyl-4-nitroaniline **75** *via* nucleophilic aromatic substitution (S_NAr) with *N,N*-diethylamine in the presence of K_2CO_3. The nitroaniline **75** subsequently underwent standard hydrogenation conditions to afford the corresponding *N*',*N*'-diethylbenzene-1,4-diamine **76**. A copper-mediated transformation of 2-bromonaphthalene **77** was undertaken in order to access **78** for coupling to **76**.

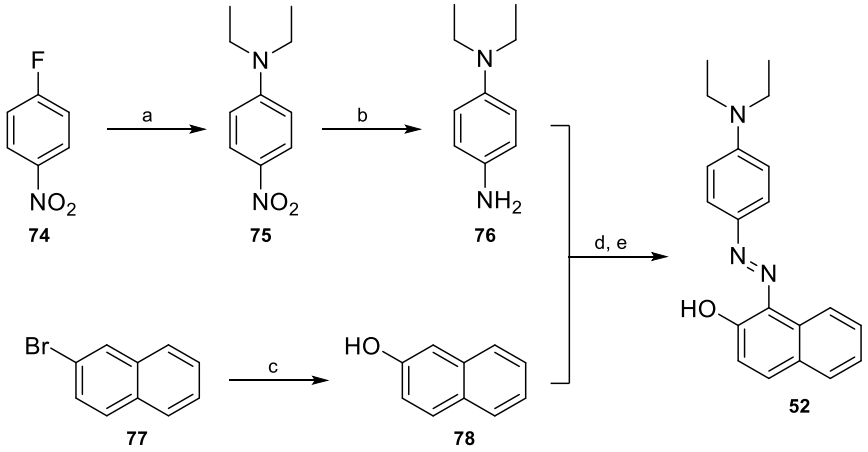

Scheme 1. Synthesis of reported lead candidate 1-((4-(diethylamino)phenyl)diazenyl)naphthalen-2-ol **52**. *Reagents and Conditions*: a) *N,N*-diethylamine, K_2CO_3, DMF, 50 °C, 1 h, quant. b) 10% Pd/C, EtOAc, RT, 2 h, quant. c) Cu_2O, 2-dimethylaminoethanol, KOH, DMSO:H_2O, 100 °C, 24 h, 98% d) **76**, 37% HCl, $NaNO_2$, 0 °C, 10 min e) **78**, 2.5 M NaOH, 2 h, 63%

Previously reported by Kim, J. *et al.*, aryl iodides were assessed in their ability to undergo copper-catalysed cross-coupling with 1,2-difunctionalised ethanes.[198] More specifically, although 1,2-difunctionalised ethanes are typically employed as ligands in such reactions, it has been observed that they can also function as reagents.[199] Aryl bromide conversion to the corresponding phenol had previously been demonstrated with similar conditions[200] and therefore it was envisioned that these new optimised reaction conditions could be applicable to the conversion of bromonaphthalene **77**. The reaction was catalysed with 10 mol % Cu_2O alongside 3 equivalents of both 2-dimethylaminoethanol and KOH. In this case, it is believed the reaction is mediated *via* chelation of the 2-dimethylaminoethanol

to the copper catalyst Cu_2O, allowing formation of the C-O bond to proceed when a cyclic bidentate ligand could be effectively formed. Ensuing KOH base-mediated intramolecular S_N2 proceeds to liberate the phenol, similarly to a Payne rearrangement pathway, to afford 2-naphthol **78**.[201] Lastly, diamine **76** was subjected to an *in situ* diazonium formation (**Figure 28**) under acidic conditions and subsequent base-promoted coupling to 2-naphthol **78** to afford the title compound **52** in moderate yield.

Two factors can account for the yield observed. Firstly, it is well known that amines and in particular anilines primarily undergo atmospheric oxidation either through interaction with molecular O_2 or •OH radicals present within surrounding environments. Secondly, this is in addition to photo-oxidation by ambient light.[202,203] As a result, these precursors typically display reasonable degradation over time. Due to the activating potential of the *N,N*-diethylamine functionality present within the molecule, this oxidation process can be observed to be heavily expedited. Within several minutes of work-up and isolation *in vacuo*, the pure residue of diamine **76** demonstrated significant degradation observed *via* thin layer chromatography (TLC). This exhibited a complex mixture of side products forming after initially presenting the sole precursor when checked under hydrogen atmosphere. Flushing the atmosphere of the isolated residue with either argon or nitrogen and subsequent storage at -21 °C appeared to slow the degradation process but after several hours still presented considerable amounts of by-product formation. Accordingly, the immediate solution was to proceed to the coupling step as soon as isolation of diamine **76** was completed. Although this did lead to formation of the title candidate **52**, the reaction mixture presented far greater by-product observation. As discussed by Konaka, R. and co-workers, oxidation of amines, specifically primary arylamines, occurring *via* molecular oxygen can proceed through a base-catalysed process.[204] As the coupling involves an alkaline environment promoted by the presence of hydroxide on addition of **78**, this may facilitate increased oxidative by-products and hence the rise in detected by-product formation. A tediously slow yet fruitful purification by flash chromatography afforded the title compound **52** in excellent purity for *in vitro* assessment. For a long-term solution, future reactions (notably discussed within **Chapter 3**) were conducted with isolated diazonium salts.

Mechanistically, the formation of the diazonium is a fascinating process, as shown in **Figure 28**. Initially, addition of the $NaNO_2$ to the aqueous solution allows dissociation of the nitrite ion **79** and subsequent formation of nitrous acid **80** *via* HCl-mediated protonation.

Additional protonation produces the oxonium ion **81**, which liberates as a result of being a stable leaving group within an acidic environment, thereby affording the nitrosonium ion **82**. As the nitrosonium ion displays positive polarity, it exhibits excellent electrophilic properties and as such can undergo attack from the lone pairs of the nucleophilic primary amine of **76**. As a result, a nitrosammonium ion is formed that subsequently results in the formation of the stable *N*-nitrosamine **83** intermediate *via* deprotonation by a molecule of water. Further, the nitroso functionality of **83** lends to the formation of the hydroxydiazene after the occurrence of proton shuffling. After acquiring a final proton *via* interaction with a hydronium ion, the oxonium leaving group is liberated through an elimination to afford the final diazonium **84**. For this mechanism to work, it must be noted that a primary amine is required due to the loss of both hydrogen atoms attached, thereby leading to the final diazonium evolution. In the case of a secondary amine, the *N*-nitrosamine **83** intermediate is the furthest the mechanism can proceed as there is no hydrogen to further drive the final elimination of the oxonium functionality. Finally, tertiary amines cannot form *N*-nitrosamines or diazoniums as they do not present any hydrogen atoms for removal.

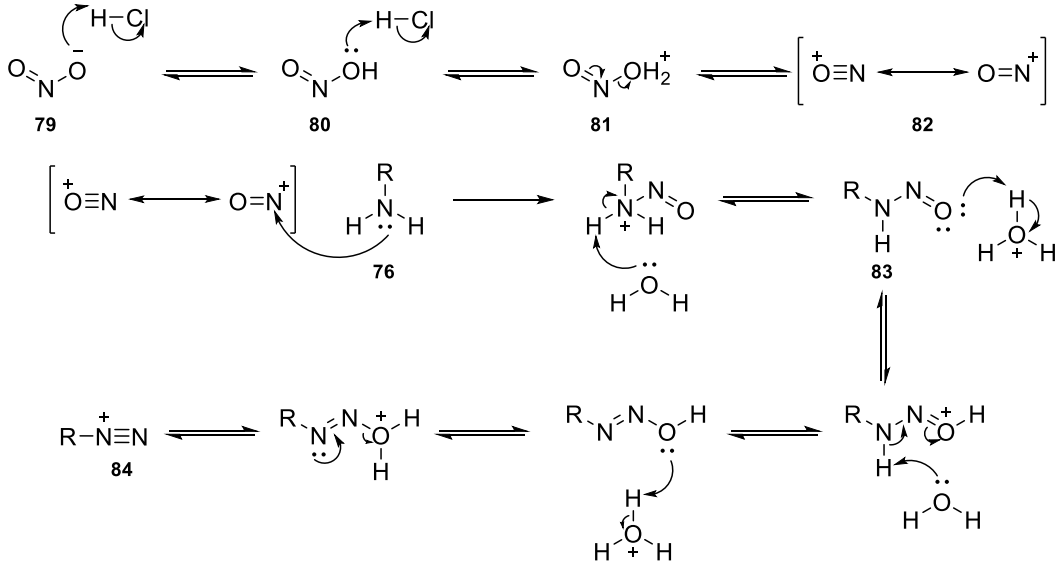

Figure 28. Proposed mechanism for diazonium formation.

2.2.2 Synthesis of 4-Substituted 1-(Phenyldiazenyl)naphthalen-2-ol Derivatives

Following the pathway displayed in **Scheme 2**, the several derivatives identified as **67 – 72** and **92** were accessed using the commercially available aniline derivatives **85 – 91** and the standard *in situ* diazonium formation as described above. Substituent choices were made to broadly assess the potential effect of varying atom length, hydrogen bonding capacities and

overall substituent effects across the several derivatives. This range of substituent selections would allow for initial *in vitro* evaluation that would later inform the appropriate approach for future SAR optimisation. Practically the syntheses of these were straightforward, proving not to be particularly troublesome other than compound **70**. Although formation of the diazonium itself did not appear hindered, the alkaline coupling of **78** to the respective diazonium proceeded poorly. Due to the pK_a of the phenol moiety being approximately 9.51, it most likely formed the phenolate due to deprotonation by hydroxide (pK_a = 16).[205] As a result, several by-products were observed but not isolated from the reaction.

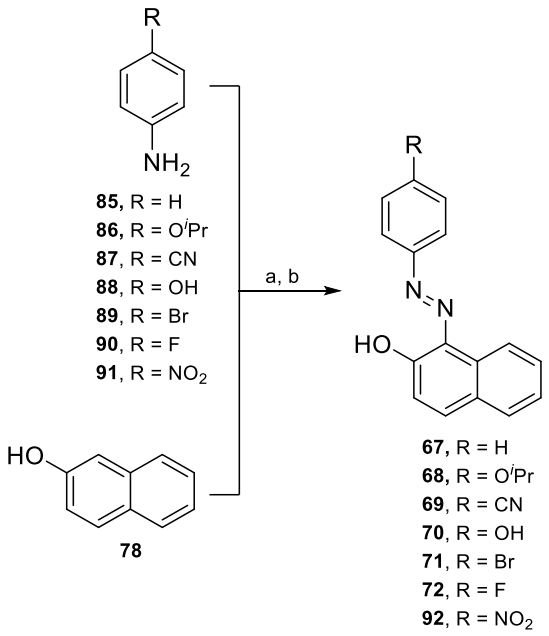

Scheme 2. Synthesis of 4-substituted 1-(phenyldiazenyl)naphthalen-2-ol derivatives **67 – 72** and **92**. *Reagents and Conditions*: a) 37% HCl, $NaNO_2$, 0 °C, 10 min b) **78**, 2.5 M NaOH, 2 h, 55 – 94%

Although there is potential for the diazonium to undergo addition by a phenolate, this appears unlikely due to the zwitterionic property exhibited by the precursor when the anion is formed through hydroxide interaction. Alternatively, the hydroxide anion may add to the diazonium thereby evolving formation of the hydroxydiazene motif. If future attempts at synthesis were necessary, ideally use of a non-nucleophilic base such as K_2CO_3 would be substituted as the base. Alternatively an initial protection of the phenol from a precursor such as 4-nitrophenol can be done; however this would add a number of steps to the synthetic pathway. Regardless, compound **70** was obtained in acceptable yields for *in vitro* assessment. It is worth noting that the excellent yields acquired for both **69** and **92** could be attributable to the withdrawing effects exhibited by these highly electronegative functionalities. As a result, this allows greater electron density to be removed from the diazonium thus drastically

increasing its ability to function as an effective electrophile. Unfortunately, **92** could not be subjected to *in vitro* assessment due to poor solubility and undesirable solvent interaction. In fact, addition of DMSO to the compound led to instant formation of a black solid – most likely a resulting degradative product, although this was not further investigated.

2.2.3 Synthesis of *N,N*-Diethyl-4-((2-methoxynaphthalen-1-yl)diazenyl)aniline

Due to the nature of the 1-diazenylnaphthalen-2-ol motif, tautomerisation can occur between the hydroxyl functionality and diazenyl bridge as displayed in **Scheme 3**. Experimental investigation conducted by Ferreira, G. *et al.* determined a strong intramolecular hydrogen bond can occur between the phenol form (O—H•••N) or hydrazone form (O•••H—N) due to the planarity of the azonaphthol scaffold.[206] These can be explained by a high degree of electronic delocalisation within the scaffold when either tautomeric form is exhibited As a result, a tautomer consisting of a hydrazone moiety (**93**, **Scheme 3**) presents itself, with the ability to undergo hydrogen bond donor capacity at the secondary amine attached to the phenylic head group. It can then be observed that ability to act as a hydrogen bond donor is transferred between the two tautomers and the placement of this may play a pivotal role in biological activity. To assess both the effect of tautomerisation and to discern whether importance of a specific tautomer over the other was prevalent in conferring activity at the target, it was envisioned that the tautomerisation could be prevented through alkylation of the phenolic motif. Although alkylation of the derivatives was an option, it was decided that only alkylation of the lead candidate would be necessary for an initial evaluation thus serving to inform future decisions based on the results obtained from *in vitro* evaluation. Following from this, alkylation with a simple methyl group was found preferable so as to limit the additional atom length initially being conferred.

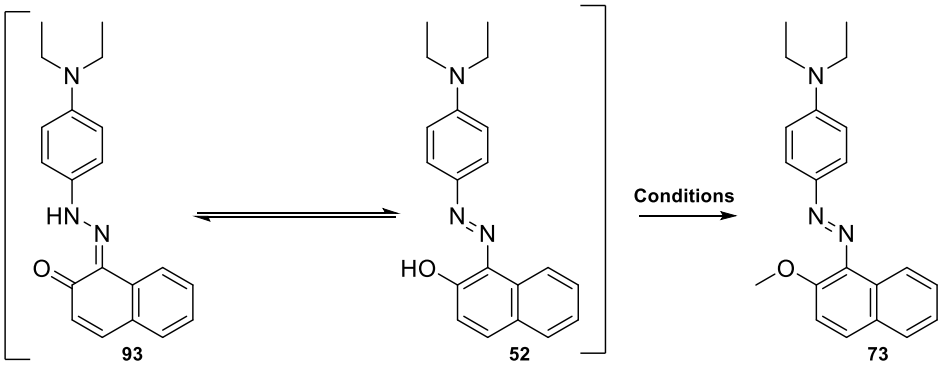

Scheme 3. The equilibrium for tautomerism can be observed alongside the general synthetic scheme to access derivative **73**. Specifically, tautomerisation leads to the formation of a hydrazone moiety that may play a pivotal role in activity at the target. Conditions for synthesis are in **Table 1**.

Several conditions (**Table 1**) were trialled before compound **73** (**Scheme 3**) was obtained successfully. Originally reported by Spagnolo, P. *et al.* on a library consisting of various 2-naphthol-derived diazenyl compounds, it was perceived that a standard alkylation under mild conditions would be sufficient to induce 2-methoxy formation.[207] Again, the phenolic moiety present on the 2-naphthol tail group has been experimentally shown to exhibit a pK_a of 9.51 at 25 °C in water.[205] Although the presence of the diazenyl functionality may cause fluctuation in this pK_a, it was not unreasonable to consider that K_2CO_3 (pK_a = 10.25) would be able to appreciably base-mediate the methylation process as it had been previously demonstrated with similar molecules. Therefore the initial trial of alkylation conditions consisted of the methylating agent MeI and K_2CO_3 in acetone at RT (**Table 1**, **Entry 1**), based on the reported conditions by Spagnolo, P. *et al.* However, monitoring of the reaction over a 24 h period in fact resulted in no reaction being observed and simply led to recovery of the starting material. This could be explained in that the pK_a of the phenolic moiety of **52** may be higher than 2-napthol **78** due to inductive resonance as a result of the *N,N*-diethylamino functionality residing on the phenylic head group. A greater electron density being delocalised around the scaffold would inherently raise the pKa of the phenolic moiety.

Table 1. Reaction conditions trialled and subsequent results for formation of **73**.

Entry	Reaction Conditions	Result
1	MeI, K_2CO_3, Acetone, RT, 24 h	No reaction, SM recovered
2	MeI, Ag_2O, DMF, RT, 24 h	Complex reaction mixture
3	MeI, NaH, THF, RT, 2 h	Clean conversion 67% yield

Resultantly, an Irvine-Purdie methylation was attempted that had also been reported by Spagnolo, P. *et al.* on a separate set of comparable derivatives.[207] Although this reaction is typically used for the methylation of glycosides, it was considered ideal as it is conducted under mild conditions in a neutral solvent.[208] Subsequently the reaction was carried out with MeI and Ag_2O in DMF at RT (**Table 1**, **Entry 2**), as previously reported. Although complete consumption of the starting material was observed, several side products were formed while

being monitored over a 24 h period. The product **73** was not observed either in electrospray ionisation mass spectrometry (ESI-MS) or through nuclear magnetic resonance (NMR) analysis of the isolated compounds after purification by flash chromatography. This route was abandoned as it was considered that reaction conditions yielding a cleaner conversion could be established rather than futilely troubleshooting a reaction producing several undesired side products. Lastly, the decision to attempt methylation *via* harsher conditions was justified after previously pursuing mild conditions. In this case, NaH was chosen with the rationale that it would deprotonate the phenol due to its highly basic properties (pK_a = 35) and drive methylation *via* irreversible deprotonation through H_2 gas evolution. Therefore the reaction was carried out in the non-reactive polar aprotic solvent THF at RT (**Table 1**, **Entry 3**). Monitoring of the reaction over a 2 h period displayed clean conversion but did not go to completion. After work-up, the crude product was subsequently purified *via* flash chromatography to afford recovered starting material **52** as well as compound **73** in moderate yield and excellent purity for testing.

Curiously, the presence of the hydrazone tautomer is not observed in the ^{1}H-NMR spectra for compound **52** (**Figure 29**) nor the FTIR spectra (**Appendix A**). This is particularly odd as it is well reported in literature to typically be present within both solid-state and solution phases of common azonaphthol derivatives such as Sudan I (**67**) and Para Red (**92**) in both NMR and FTIR.[206] In fact, a singlet can be observed at 15.49 ppm (highlighted in RED; **Figure 29**) which is consistent with the presence of the OH moiety rather than the hydrazone NH that is characteristically observed at greater than 16 ppm chemical shift. Moreover, the directly attached carbon to the phenol demonstrates a chemical shift of 155.2 pm (**Appendix A**) that is agreeable to the reported carbon shifts for the phenolic tautomer in similar derivatives. Comparatively, the hydrazone isomer is reported to exhibit a carbon shift much closer to 180 ppm.[206] Accordingly the FTIR spectra obtained for compound **52** (**Appendix A**) confirms the presence of the phenol isomer within the solid-state phase. Specifically an intense band can be observed at 1561 cm^{-1} that can be attributed to in-plane (δ) deformation of NH bending as a result of intramolecular hydrogen bonding between the phenolic and azo moieties (Ar-N=N•••H-O-Ar).[209] This is further enforced by the presence of a weak ν_sOH frequency at 3048 cm^{-1} that is indicative of an intramolecular bonded OH functionality.

In regards to characterisation of compound **52**, a typical chemical shift for the methoxy functionality can be observed as a singlet at 3.94 ppm (highlighted in BLUE) in the ^{1}H-NMR spectra displayed in **Figure 29**. Accordingly a corresponding ^{13}C-NMR carbon for the newly alkylated moiety is observed at 57.6 ppm (**Appendix A**). Although an unlikely possibility, due to the tautomeric-dependent potential of alkylation to occur at either the phenolic moiety, thereby conferring the formation of the methoxy moiety (compound **73**), or methylation of the NH present within the hydrazone tautomer (compound **93**, **Figure 30**), 2D NMR was carried out to observe through space ^{1}H-^{1}H interactions (**Figure 30**) *via* nuclear Overhauser effect spectroscopy (NOESY) (**Figure 30**) to confirm the chemoselectivity of alkylation.

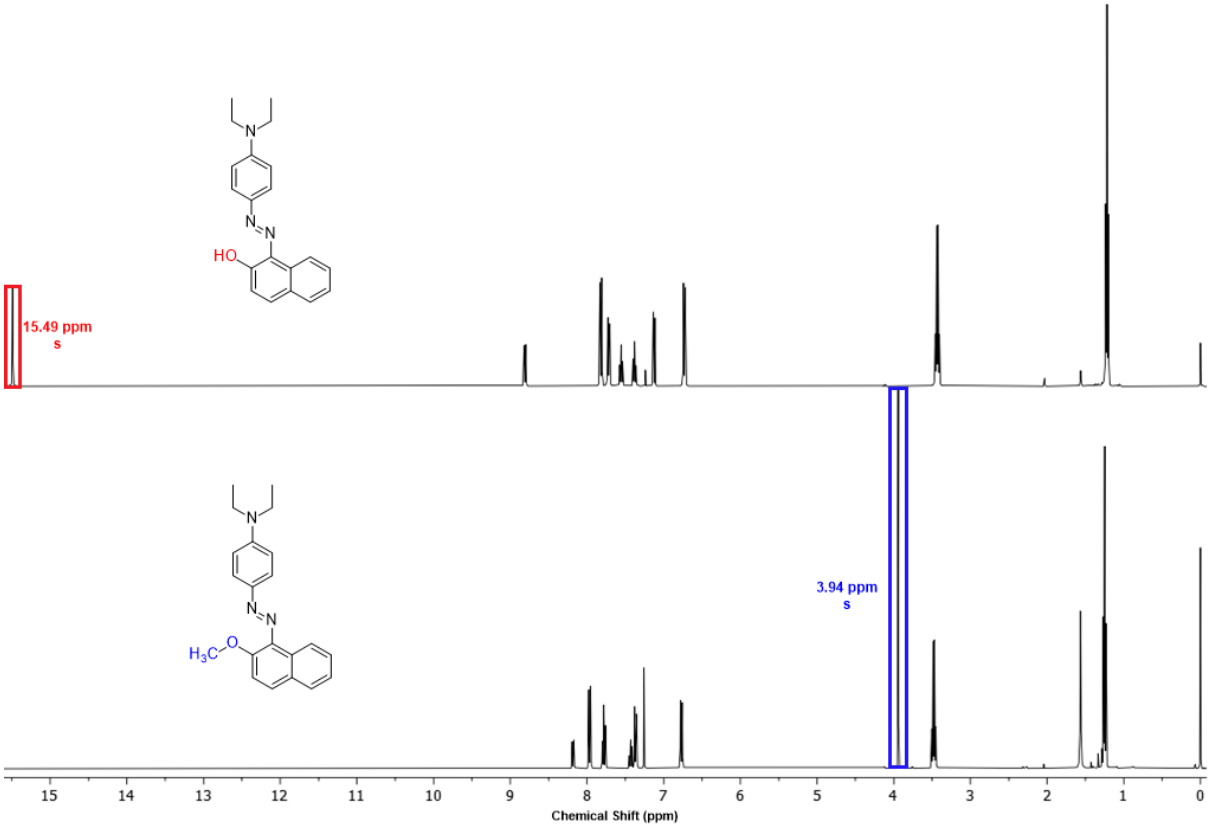

Figure 29. ^{1}H-NMR (400 MHz, $CDCl_3$) spectrum for compounds **52** and **73**. Phenol moiety and characteristic phenolic tautomer chemical shift for compound **52** is highlighted in RED. Newly conferred methoxy functionality and correlated chemical shift is highlighted in BLUE for compound **73**. Multiplicity and integration of each respective chemical shift can be seen in **Chapter 6**.

It can be observed that a correlation between the methoxy peak at 3.94 ppm and multiplet at 7.51-7.31 ppm can be observed (highlighted by the BLUE box in **Figure 30**; multiplet proton chemical shift is highlighted by a BLUE asterisk). This multiplet consists of

the naphthalenic doublet that can be attributed to the adjacent proton highlighted in BLUE within **Figure 30** as well as an apparent triplet designated to the equivalent proton residing on the opposite side of the naphthalenic ring (highlighted by a BLUE asterisk on **73**; **Figure 30**). As such, this confirms that the methoxy moiety has in fact been conferred to the phenolic position. Conversely, if the amino group had been alkylated then a through space correlation would be seen between the methylated amine protons and phenylic protons residing on the lower part of the ring (highlighted in RED on **94**; **Figure 30;** ^{1}H NMR chemical shifts highlighted by a RED asterisk; **Figure 30**). It should be noted that correlation spectroscopy (COSY) correlations could not be used to determine the placement of the methylation because in either case no relatable protons exist within a single bond distance.

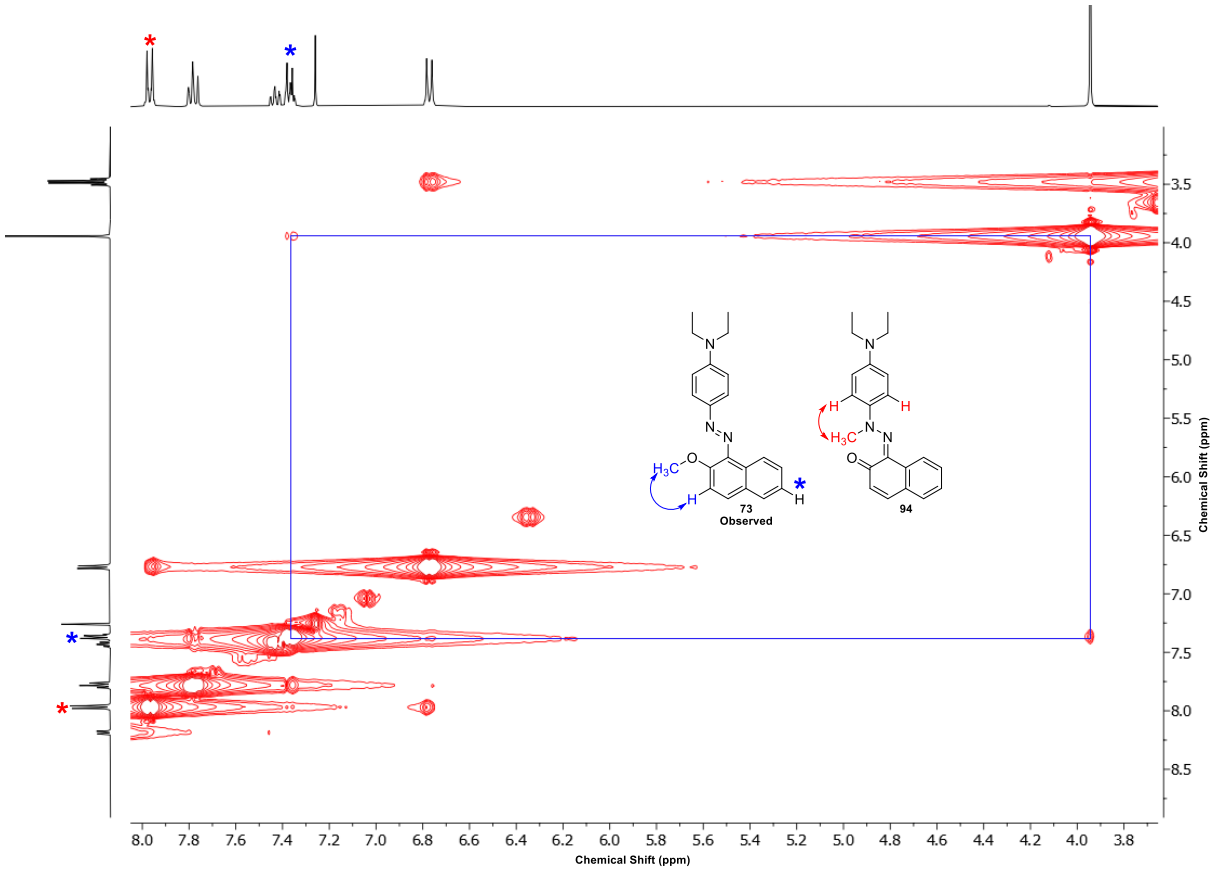

Figure 30. NOESY NMR (400 MHz, $CDCl_3$) spectrum for compound **73**. Observed through space correlations are highlighted by a BLUE box. The correlated multiplet (consisting of the adjacent related proton and equivalent respective proton on the opposite side of the ring) is highlighted by a BLUE asterisk along with the additional proton. Phenylic protons on the lower portion of the ring are highlighted by a RED asterisk.

2.3 Biological Results and Discussion

Although current access to an assay assessing the specific interaction of these compounds with the Aha1-Hsp90 complex is restricted, it was considered relevant to

investigate the potential role these derivatives may play with tau aggregates directly. Previously discussed within **Chapter 1.4**, there are two modes of inhibition that can affect the aggregation of tau directly. However, the most relevant is inhibition through non-covalent properties that typically proceed *via* polarisable interactions. Azonaphthol chemical scaffolds are well established for their use as commercial dyes, pigments and indicators as a result of the absorbance characteristics stemming from their highly conjugated systems. As such, vivid colours are produced due to absorbance of visible light by the delocalised electrons within the system.[210] Furthermore, the scaffold exhibits planar structure and demonstrates resemblance to known non-covalent TAIs (**Chapter 1.4.2**, **Figure 7**). These attributes are ideal in maintaining interactions with proteins that demonstrate similarly polarisable functionalities. Therefore, assessment of the scaffold with interaction at tau directly was deemed a rational decision. The following *in vitro* evaluations that are presented herein were performed and analysed by Dr. Liming Hou in the laboratory of Professor Lars Ittner at the Department of Biomedical Sciences at Macquarie University. In particular, the evaluation of compounds was carried out using a Thioflavin T (THT; **95**, **Figure 31**) fluorescence assay and comparison made to the known direct TAI altenusin (**96**, **Figure 31**).[211] The assay employs the use of the 4R tau isoform that only consists of microtubule binding domains that demonstrate significant affinity for aggregation.[211]

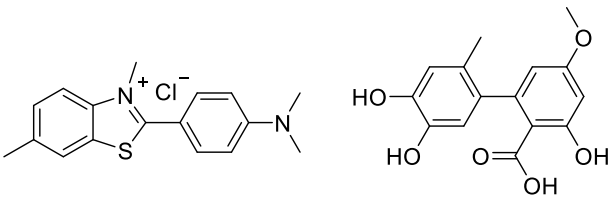

Thioflavin T (**95**) Altenusin (**96**)

Figure 31. Structures of the compounds Thioflavin T (**95**, used as a source of fluorescence in the ThT assay) and the direct TAI altenusin (**96**).

2.3.1 Azonaphthol Scaffold Biological Results

A majority of the derivative library presented in this chapter were subjected to screening in the aforementioned ThT assay. Fluorescence is the primary measure of tau aggregation within this assay, which occurs as a result of the fluorescent dye Thioflavin T binding to paired helical fragments formed from heparin induced aggregation.[211] Accordingly, a reduction in fluorescence then implies a decrease in levels of tau aggregates. Conversely an increase in fluorescence suggests an increase in aggregation. Further details for this assay are available in **Chapter 6**.

Initially the results of this screening were surprising (**Figure 32**), with several derivatives demonstrating significant reductions in normalised relative intensity that were comparable to that of the altenusin (shown in RED). Greatest reduction in relative intensity was observed with compound **68** (**Figure 32B**), showing a greater decrease in intensity than that of altenusin. Comparable declines in intensity were observed between compounds **52** and **73** (**Figure 32A** and **32G,** respectively) relative to one another and altenusin. These results are most likely due to the highly activating nature of the *N,N*-diethylamine (**52** and **73**) and isopropoxy (**68**) functionalities present on the molecules, allowing for a greater degree of polarisation that induces non-covalent interactions. In the case of **52** and **73**, the results are particularly interesting as it demonstrates that the effect of tautomerisation appears to be negligible on apparent inhibition of tau aggregation directly. However it is difficult to say whether this is because both tautomers behave similarly or one is predominant in equilibrium. Absence of a substitution at the *para*-position of the ring lead to alleviation of intensity reductions for compound **67** (**Figure 32C**), with similar results observed with the 4-fluoro derivative **72** (**Figure 32E**).

After consideration, overall these results were unsurprising for two reasons. Firstly, due to the unsubstituted nature of the *para*-position, strong substituent effects are not observed that contribute to significant delocalisation of electrons within the scaffold, whether it be donating or deactivating in disposition. Presence of functionalities that contribute greatly to this delocalisation can be observed within the remaining compounds and therefore can greatly improve the ability to undergo polarisable non-covalent interactions with protein fragments. Secondly, although fluorine exhibits a significantly high electronegativity and is considered to be weakly deactivating, it is non-polarisable and is the most likely reason for the lack of activity observed.[212] Conversely, the 4-bromo derivative **71** (**Figure 32D**) demonstrated a good reduction in relative intensity, which may be attributed to the polarisable property of the bromine atom and thus contributing to the scaffolds ability to undergo non-covalent interactions. Lastly, compound **69** (**Figure 32F**) displayed a modest decrease in relative intensity and is an example of a substituent functionality with greater withdrawing capacity. Therefore, substituents conferring significant electron delocalisation, despite their disposition, may produce polarisation allowing non-covalent inhibition of tau aggregation directly.

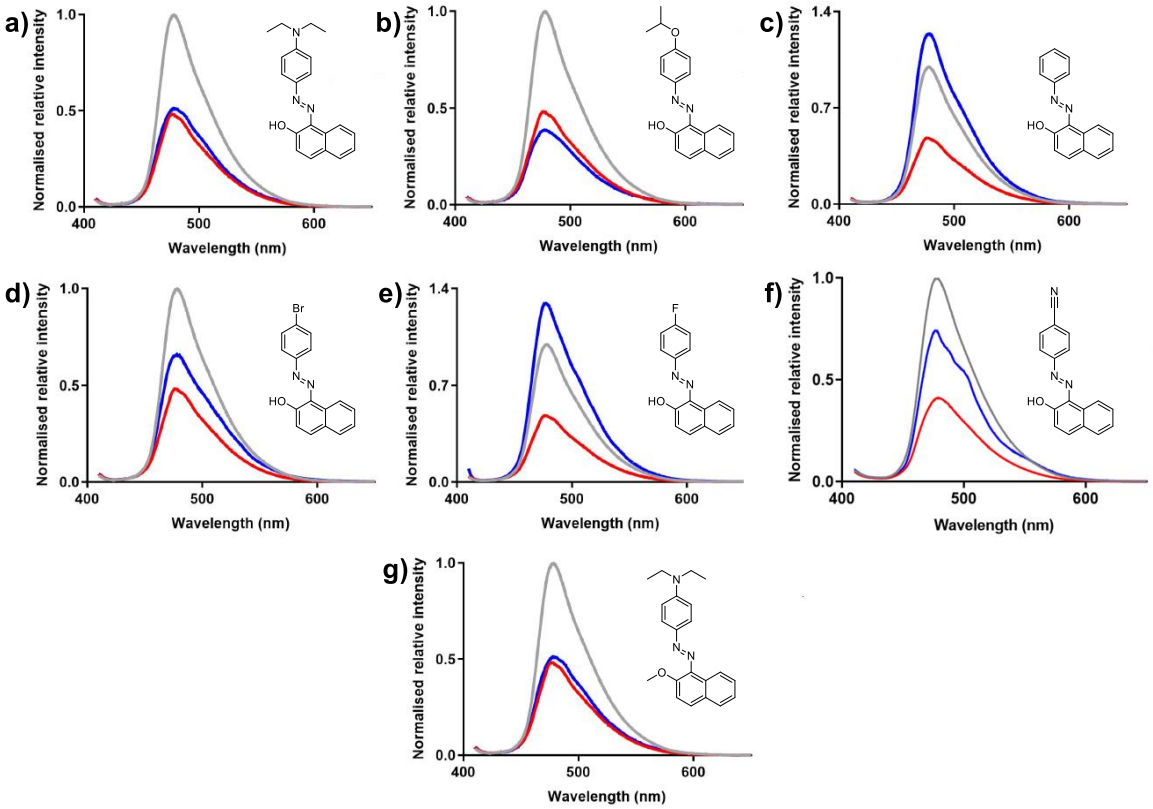

Figure 32. Biological results from azonaphthol derivatives a) **52**, b) **68**, c) **67**, d) **71**, e) **72**, f) **69** and g) **73** in ThT assay. GREY = PBS, BLUE = Compound Treatment, RED = Altenusin. Wells containing 20 μM 4R tau and 5 μM heparin in 100 mM, sodium acetate at pH 7 were incubated with or without compounds or Altenusin for 48 h at 37 °C. A 12.5 μM solution of ThT was then added for a further 1 h. ThT fluorescence was measured with an excitation wavelength of 440 nm and emission spectra recorded from 450 – 640 nm.

2.3.2 Validation of Biological Results

Due to the nature of the scaffold exhibiting strong dye characteristics, it was considered necessary to ensure that the molecules were not quenching the fluorescence within the assay and thus providing false-positive results. As such, several derivatives were selected for analysis of their fluorescent and absorption character as well as potential ability to quench fluorescence. In particular, it appeared appropriate to select two well performing compounds (**52** and **68**), two poorly performing compounds (**67** and **72**) and one modestly performing compound (**69**) to accurately assess the potential of fluorescent quenching across the library. Firstly, it was imperative to discern the absorbance properties of the molecules to understand if their UV-Vis absorption overlapped with the fluorescence of ThT and therefore potentially playing a role in fluorescent quenching. Because ThT can only fluoresce in the presence of tau aggregates, a fluorescent dye known as fluorescein was used as a comparison due to the similarities in their emission wavelengths (ThT = 482 nm, fluorescein = 517 nm).[211,213,214] Analysis of the absorption characteristics for the compounds as well as the fluorescein can be observed in **Figure 33A**. As it can be seen, the compounds exhibit absorptions around the

wavelength of ~380 nm – ~530 nm. However, notably **52** has a shifted absorption from ~400 nm – ~560 nm. These measurements initially suggest that fluorescent quenching may be involved due to the obvious overlap of the absorption wavelengths exhibited by the compounds with that of the reported emission of ThT at 482 nm.

To confirm the fluorescent emission of fluorescein and identify any fluorescing properties of the compounds themselves, fluorescence measurements were taken that can be seen in **Figure 33B**. As expected, the emission maximum of fluorescein is at 517 nm (in BLACK) and most notably the compounds all exhibit negligible, if any, fluorescent capacity. This can then rule out the possibility that the molecules display fluorescent emission that may interfere with the results seen from the assay when excited at a wavelength 440 nm. Lastly, potential for quenching was evaluated by mixing equivalent concentrations (1.56 mM) of the fluorescein with the selected derivative and measuring the change in fluorescence from the baseline fluorescein measurement, as displayed in **Figure 33C**. Although reductions in intensity greater than 50% of the original emission were measured across all derivative interactions, compounds **67** (in RED) and **72** (in PURPLE) demonstrated the highest reductions in emission. This is particularly peculiar as these compounds performed poorly within the assay, with even slight increases in relative normalised intensities (**Figure 32C** and **32E**, respectively). Conversely, compound **52** (in ORANGE) and **68** (in GREEN) were the highest performing compounds in the assay (**Figure 32A** and **32B**, respectively) but presented the lowest intensity reductions. Although the majority of the compounds do not exhibit a strong absorbance within the wavelength range of the fluorescent emission of fluorescein, **52** demonstrates a significant maximum absorbance around 520 nm but curiously did not produce the greatest reduction in fluorescence from fluorescein. These measurements may potentially suggest that the assay results are in fact not false-positives as outcomes of fluorescent quenching but the distinction is difficult to conclude without direct assessment with ThT. Ideally application of a non-emission based assay, such as a phenotypic assay, to evaluate the activity of these compounds on tau aggregation directly would be a more accurate and compelling route to discerning the results conclusively.

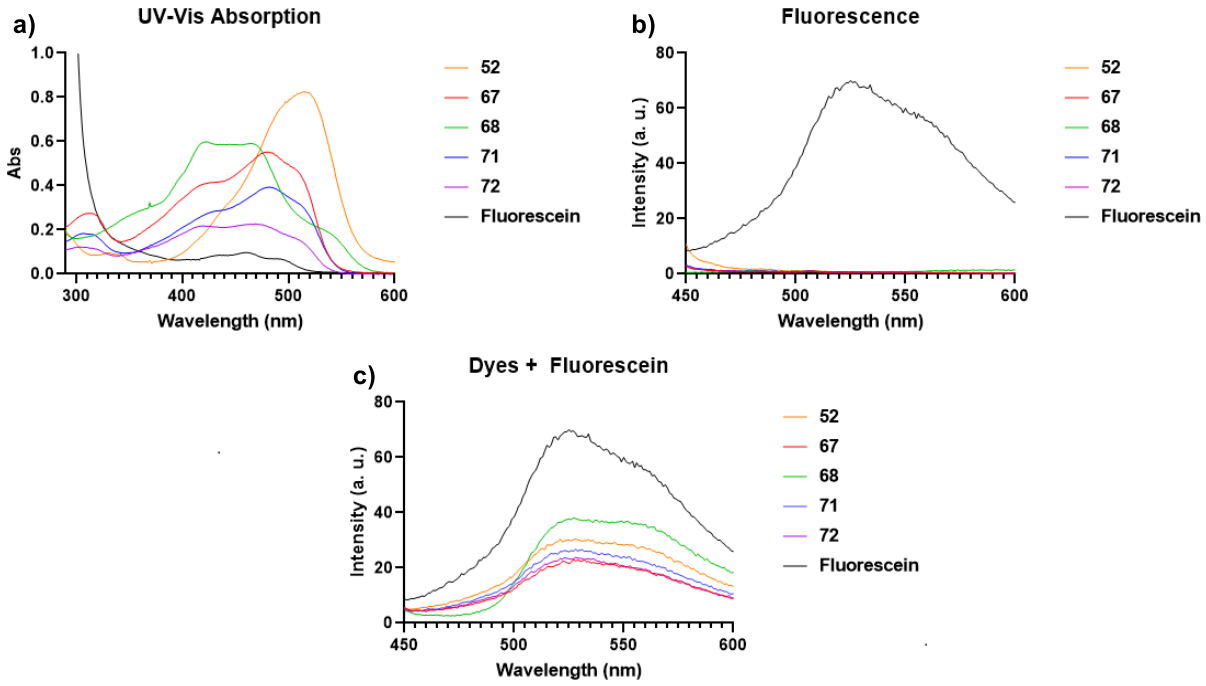

Figure 33. Analysis of selected derivatives to ascertain their potential to quench fluorescence within the ThT assay. ORANGE = **52**, RED = **67**, GREEN = **68**, BLUE = **71**, PURPLE = **72** and BLACK = Fluorescein. a) UV-Vis absorption and associated wavelengths; b) individual fluorescent intensities and associated wavelengths and; c) mixed (fluorescein + compound) fluorescent intensities and associated wavelengths. The excitation wavelength was 440 nm with a 10 mm pathlength Quartz cuvette for all measurements. Compounds were dissolved in DMSO at a consistent concentration of 1.56 mM.

2.3.3 ThT Assay Complications

As previously stated in **Chapter 2.3.1**, the aggregation of 4R tau filaments within the assay is induced *via* application of heparin and is the primary method of *in vitro* assembly.[211] However, a report by Zhang, W. *et al.* determined that heparin-induced tau filaments differed to those isolated from patients presenting AD.[215] More specifically, cryo- and immuno-EM were used to characterise 4R recombinant full-length tau that was assembled in the presence of heparin and then compared to that of those assembled as a result of AD. It was discerned that heparin-induced aggregates adopted 'kinked hairpin' folds whereby the second and third microtubule-binding repeats bundle upon one another. Conversely, aggregates from AD patients were found to adopt dissimilar conformations that exhibited larger core structures alongside a variety of differing repeat compositions. Due to the environment-dependent versatility of structure within aggregates, it then lends to ask whether the *in vitro* assembly of 4R tau *via* heparin is disease relevant in nature. However, a more recent study conducted by Lövestam, S. *et al.* (2022) investigated and identified relevant *in vitro* assembly conditions for AD-relevant recombinant tau filaments. Through biosynthetic application of *E. Coli* bacteria, tau proteins were able to be expressed that were then subjected to an optimised

filament assembly process. Assessment of the filaments *via* cryo-EM ascertained that they presented an identical helical symmetry and left-handed twist character that is distinguishing of that of AD. Interestingly, a total of 76 differing cryo-EM structures that were a result of *in vitro* assembly were reported. In fact, conformations and isoforms of pathogenic tau across the tauopathies of chronic traumatic encephalopathy (CTE), Pick's disease and AD exhibit distinct differences thus highlighting the complexity of tau and its role within various tauopathies.[215,216] These findings were paradigm shifting for *in vitro* studies as aggregation of 4R tau filaments *via* heparin induction has been a fundamental practice within this field of research.

2.4 Concluding Remarks

This chapter has discussed the basis of lead candidate identification, synthesis, characterisation and *in vitro* assessment of an azonaphthol library for their activity against tau directly. In particular, methylation of the lead candidate phenolic position on the naphthol tail group was achieved and confirmed to discern correct placement of the alkylation (**Figure 30**). Due to inability to access a Hsp90-Aha1 complex relevant assay, the library was screened through a ThT assay to investigate their effects on tau directly. This decision was reasonable due to the similarities they exhibit when compared to known non-covalent inhibitors, as discussed in **Chapter 2.3**. Interestingly, several derivatives performed excellently in their ability to reduce the relative normalised intensity within the assay therefore suggesting the possibility of being potent inhibitors of direct tau aggregation (**Figure 32**). To ensure that false-positives were not occurring due to fluorescent quenching within the assay as a result of overlapping absorption characteristics of the compounds, select compounds were subjected to further analysis. Their absorption, fluorescent emission and fluorescent quenching properties were measured against the dye fluorescein which fluoresces at a similar wavelength to that of ThT (**Figure 33**).

Although not conclusive for reasons discussed, the results are extremely promising and may lead to the novel discovery of the azonaphthol scaffold as a viable direct TAI with further optimisation. However, the relevance of heparin-induced *in vitro* assembly is questionable and additional evaluation with disease-relevant tau conformations is necessary to discern their activity more accurately. Because future iterations to the scaffold cannot be informed by *in vitro* testing for the Hsp90-Aha1 complex, the synthetic progression shown in the forthcoming chapters is driven by rational optimisation further discussed herein.

Chapter 3:

Chemotype Exploration of the Diazenyl Motif

Chapter 3: Chemotype Exploration of the Diazenyl Motif

3.1 Introductory Remarks

Although tau-pathology is a promising approach for the therapeutic treatment of AD, a greater understanding of the biochemical mechanisms underlying this pathology is necessary. Such endeavours require extensive investigation of relevant targets and subsequent pathways that play a role within this complex pathology. Novel avenues, such as targeting the Aha1-Hsp90 complex, demonstrate encouraging capacity as targets. However research concerning the medicinal chemistry space and underlying biochemistry of this complex is limited. As such there is a clear need for the discovery of molecular scaffolds that can function as both potential therapeutic agents and chemical probes. Furthermore, these scaffolds should exhibit the ability to undergo extensive SAR diversification for ease of future optimisation efforts. Previously discussed in **Chapter 2** was the synthesis of the lead candidate **52**, several derivatives assessing *para*-substitutions on the phenylic head group (**67 – 72** and **92**) and alkylation of the naphtholic phenol moiety (**73**). This chapter will outline the exploration and synthesis of chemotypes replacing the primary diazenyl linker motif between connecting aryl functionalities.

Harmful properties of certain azo dyes including their carcinogenic, mutagenic and genotoxic effects are well reported. This has subsequently led to strict regulation surrounding their use within the textile and food industries due to safety concerns.[217–220] These effects are primarily the result of metabolism of the parent azo-containing compound to aromatic amines *via* reductive-cleavage pathways within the intestine and liver.[217,219,220] Therefore it was considered imperative to identify chemotype alternatives that initially maintain the principle azo functionality residing within the lead candidate **52** whilst eliminating the metabolic liability presented. Additional benefits arise from modification of the diazenyl linker with heterocyclic structures, such as removing the variability of *cis*- and *trans*-isomerism exhibited by the linker and improved hydrophilicity *via* heteroatom hydrogen bonding interactions. Due to the nature of heterocyclic rings, several anchor points are installed to the scaffold thus allowing diversification of substitutions. This can lend to greater SAR scope in future iterations of any given chemotype and considerably more control over optimisation efforts.

Chapter Aims

This chapter addresses several proposed chemotype modifications to the primary diazenyl linker of the lead candidate scaffold **52**. In particular, this chapter focuses on the synthetic approach to modification of the lead candidate **52** diazenyl motif with comparable azo-containing heterocyclic scaffolds such as pyrazole (**97** – **98**) and triazole (**99** – **100**) varieties, a tetrazole (**101**) replacement and an oxazole (**102**) motif (**Figure 34**). Although the primary goal is to explore chemotype variations for the lead candidate, synthetically accessible derivatives of various chemotypes have been synthesised. These can undergo comparison to the initial library so as assess the effect of *para*-substitutions at the target. Unfortunately, biological assessment was not carried out for the novel derivatives outlined within this chapter due to the complications noted in **Chapter 2.3.3** for the ThT assay nor their activity on the Aha1-Hsp90 complex due to accessibility issues.

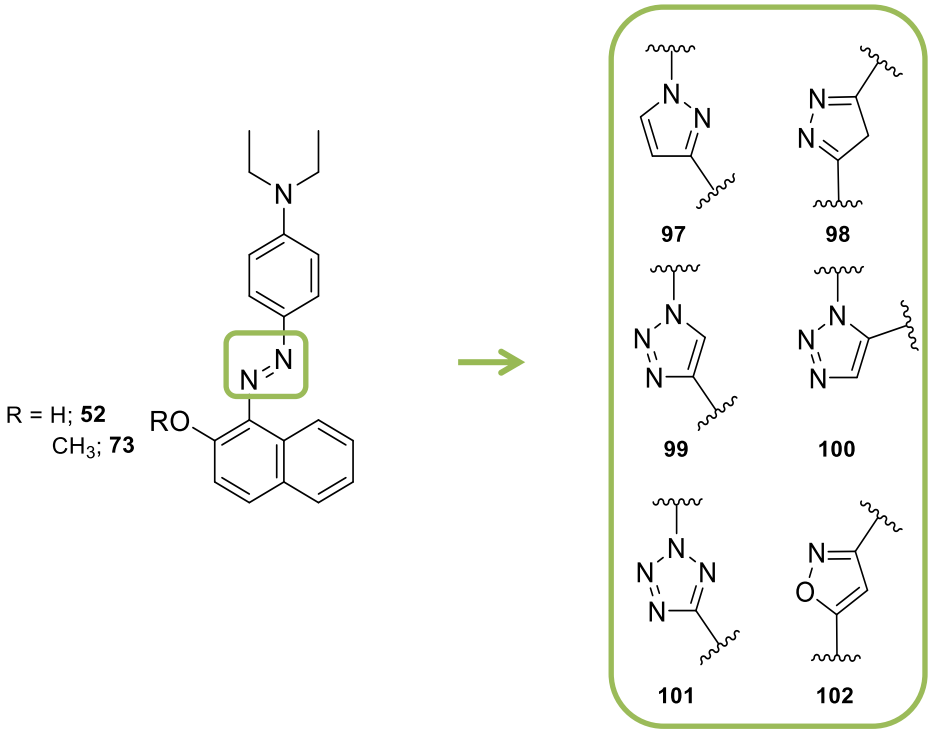

Figure 34. Lead candidate **52** and several heterocyclic modifications proposed to replace the primary diazenyl linker motif.

3.2 Synthesis of Pyrazole Derivatives

3.2.1 Synthesis of 1,3- and 1,5-Disubstituted Pyrazoles

Hydrazone route

It was envisioned (**Scheme 4**) that the lead 1,3-pyrazole derivative **107** could be obtained through a convergent synthesis. Beginning with the aniline **76,** conversion to the respective hydrazine **103** could be achieved *via* diazonium salt formation followed by a reduction. Subsequent imine condensation with **105**, obtained through alkylation of **104**, would afford the associated hydrazone **106**. Lastly, lithiation of the hydrazone and ensuing Claisen-type condensation with methyl formate would afford the final 1,3-pyrazole **107**. Primarily the benefit of approaching the ring closure *via* the hydrazone intermediate **106** alleviates the potential to afford the 1,5-regioisomer as deprotonation is restricted and therefore selectively affords the 1,3-regioisomer.

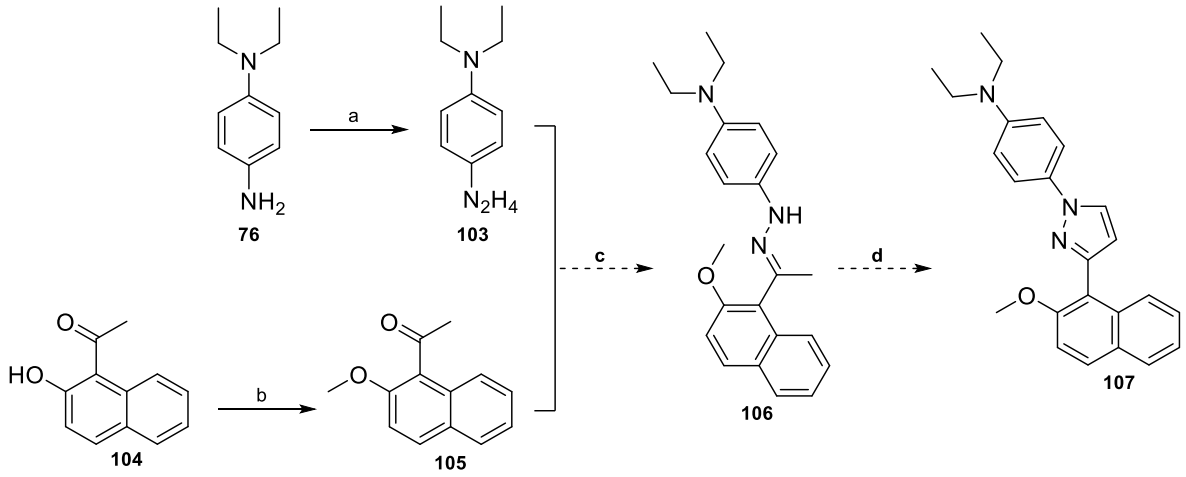

Scheme 4. Envisioned synthetic pathway to achieve lead 1,3-disubstituted pyrazole derivative **107** *via* hydrazone-based route. *Reagents and Conditions*: a) conditions outlined in **Table 2** b) MeI, K_2CO_3, Acetone, 50 °C, 82% c) AcOH, 10% NaOH, RT, not attempted d) i. *n*-BuLi, THF, -78 °C ii. Methyl formate, -75 °C – RT, not attempted

An initial conversion of aniline **76** to an isolatable diazonium tetrafluoroborate salt (**Table 2**, **Entry 1**) was undertaken rather than utilising the *in situ* diazonium formation method outlined in **Chapter 2**. This was done for two reasons. Firstly, compound **76** exhibits substantial degradation at room temperature and therefore can lead to either unwanted side-product formation within a reaction it is involved in and/or difficulties in purification of the product afforded due to a complex reaction mixture being obtained. Isolation and subsequent washing of the diazonium tetrafluoroborate salt with diethyl ether allows for easy purification of degradative products, with the added benefit of additional shelf-life due to the increased

stability of the salt. This is because the tetrafluoroborate anion is both similar in size and energy state to that of the diazonium cation, thus efficiently stabilising the complex.[210] Secondly, if reaction conditions require temperatures lower than that of 0 °C then diazonium-chloride complexes are reported to crystallise thus affecting the reaction from proceeding effectively.[210] After the synthesis of the diazonium tetrafluoroborate salt, the initial reaction conditions for the subsequent reduction were carried out with $SnCl_2$ and 6 N HCl at room temperature (**Table 2**, **Entry 1**), as reported by Jacob and co-workers.[221] This reaction proceeded to afford the parent aniline compound in quantitative yield, leading to the hypothesis that the diazonium had been over reduced to the aniline after initial reduction to the hydrazine.

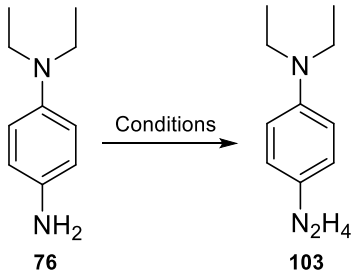

76 **103**

Table 2. Reaction conditions trialled and subsequent results for conversion of **76** to **103**.

Entry	Reaction Conditions	Result
1	1. HBF_4, Isopentyl Nitrite, AcOH, RT, then Et_2O, -40 °C 2. $SnCl_2$, 6N HCl, RT	Quantitatively afforded parent aniline **76**
2	1. HBF_4, Isopentyl Nitrite, AcOH, RT, then Et_2O, -40 °C 2. $SnCl_2$, 6N HCl, -25 °C	Desired hydrazine observed *via* ESI-MS Could not be isolated

Frahn, J. L & Illman, R. J. reported that when this reaction was conducted at 0 °C for several derivatives, secondary reductive cleavage of the N-N bond of the hydrazine in the presence of excess stannous chloride occurs. As a result, ammonia is liberated thus affording the parent aniline. The nature of the substituent and its position on the ring significantly affects the ability of both primary and secondary reduction to occur. Substituents conferring greater electron donating capacities were not able to be successfully reduced at temperatures lower than -25 °C to the desired hydrazines as they underwent secondary reduction rapidly.[222] Therefore the reaction was re-trialled at -25 °C and the desired hydrazine was observed on

ESI-MS in the crude mixture (**Table 2**, **Entry 2**). Unfortunately the hydrazine (**103**) was not able to be isolated as it exhibited significant degradation and led to the formation of a complex reaction mixture upon concentration *in vacuo*. Moreover, the difficulty of separating $SnCl_2$ from the reaction is well known and typically results in low yields of desired hydrazine products.[223] This makes isolating the hydrochloride salt of the hydrazine considerably challenging as majority of the degradation observed occurred after the workup. In addition to the free-base being unstable, it is reported that hydrochloride salts of hydrazines demonstrate rapid decomposition unless the substituent is strongly electron withdrawing.[222] Due to the high reductive potential of $SnCl_2$, it is not a chemoselective method for the reduction of the diazonium. Labile functionalities, such as nitro groups, residing on the precursor molecule will undergo simultaneous reduction.[224] In this case substitution of **76** with 4-nitroaniline to form the hydrazone **110** (**Scheme 5**) would not be viable. Ideally this would be followed by ring closure to **109**, a subsequent reduction and then dialkylation of **108** to afford compound **107**. For these reasons, synthetically obtaining the hydrazines was abandoned.

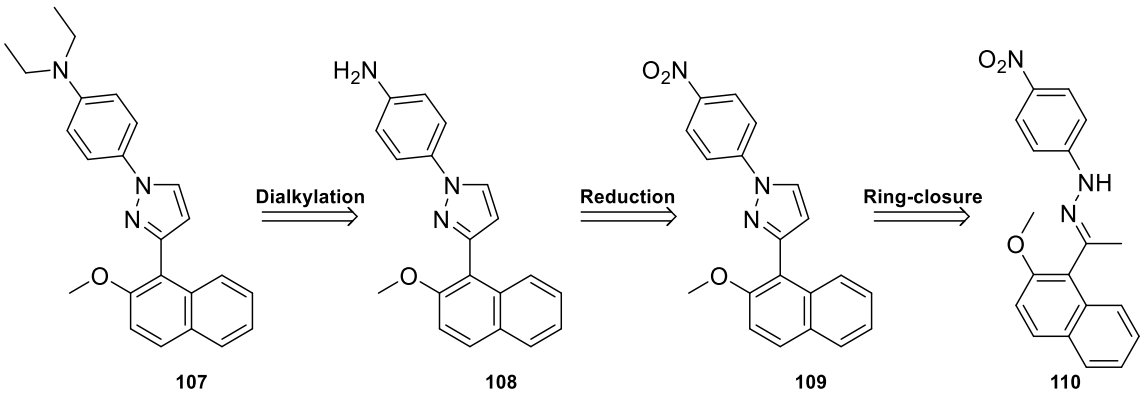

Scheme 5. Proposed retrosynthetic pathway utilising *para*-nitro functionality for accessing lead pyrazole derivative **107**.

It was decided to use commercially available 4-nitrophenylhydrazine hydrochloride **111** in place of 4-nitroaniline to access the key hydrazone intermediate (**110**), through the retrosynthesis of lead derivative **107** (**Scheme 5**). Due to the strongly electron-withdrawing nature of the nitro functionality, the hydrochloride salt of the hydrazine is sufficiently stable. As such, to obtain compound **105** so as to couple **111** *via* a condensation reaction to form the hydrazone **110**, **104** underwent standard alkylation conditions with MeI, K_2CO_3 in acetone at 50 °C. Alkylation of the phenol moiety was carried out to minimise any potential interference with the formation of the hydrazone as a result of potential interaction with the hydrazine motif present on **111** and could be removed using BBr_3 at a later date. Additionally, the activity of the alkylated derivative could be assessed comparatively to that of the lead

methylated derivative **73**. Several methods were trialled to afford the hydrazone derivative **110** (**Table 3**). Typical reaction conditions for the formation of hydrazones were originally tested by subjecting the compounds to AcOH at room temperature to initiate the condensation. However, no reaction took place after monitoring *via* TLC over several hours (**Table 3**, **Entry 1**).

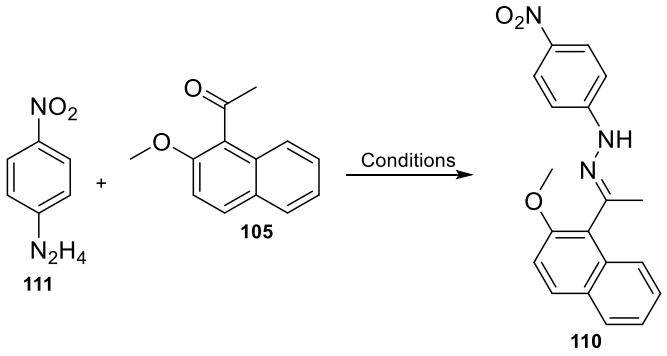

Table 3. Reaction conditions trialled and subsequent results for obtaining hydrazone **110**.

Entry	Reaction Conditions	Result
1	neat. AcOH, RT	No reaction
2	neat. AcOH, 10% NaOH, RT	No reaction
3	Toluene, cat. *p*-TsOH, RT	No reaction
4	Toluene, cat. *p*-TsOH, Reflux	Did not proceed to completion

Due to the nature of the condensation (**Figure 35**), the rate of reaction is strongly dependent on the concentration of acid. If the lone pair of the terminal nitrogen residing on **111** is protonated, then it cannot aptly perform a nucleophilic attack on the acetyl functionality of **105**. Conversely, if performed under alkaline conditions then the aminoalkanol (**112**, **Figure 35**) will be in the primarily in the deprotonated form and unable to subsequently undergo the required dehydration step. After further investigation it was determined to be ideal to conduct the reaction at a pH of ~5 so that both the initial nucleophilic attack and subsequent acid-catalysed dehydration (**113**, **Figure 35**) can occur at a useful rate.[225] Due to the pH of neat conc. glacial AcOH residing at 2.5, reported conditions by Harikrishna *et al.* were trialled that include the addition of 10% NaOH to modulate the pH as necessary (**Table 3**, **Entry 2**).[226] Unfortunately, this led to the eventual precipitation of a

white solid over an hour that was identified as NaOAc with no observable hydrazone formation *via* TLC. To eliminate the potential of salt formation as well as modulating pH with substantially lower amounts of acid and improve overall solubility of the substrates, toluene as a solvent was trialled with catalytic amounts of *p*-TsOH (**Table 3**, **Entry 3**). However, after monitoring the reaction there was no observable change in starting material consumption or new product formation. Due to the strongly electron withdrawing nature of the nitro functionality present on **111**, it was considered that the terminal hydrazine nitrogen may not possess sufficient electron density to initiate nucleophilic attack on the acetyl moiety of **105**. Therefore, the reaction was trialled again at reflux to provide additional energy for the reaction to proceed (**Table 3**, **Entry 4**). Additionally, a Dean-Stark apparatus was used to aid removal of water and shift the equilibrium towards product formation.[227] Within an hour, a new product spot was observed but the reaction did not proceed to completion despite extended reaction time. Assessment of the crude mixture through ESI-MS determined the presence of the desired product **110** but it could not be isolated from the starting materials by workup or flash chromatography purification methods as this would result in hydrolysis of the product **110** to the starting materials. Due to complications associated with synthesis of a number of intermediates in this proposed synthetic pathway, exploration of alternative methods to access the desired pyrazole linked derivatives was required.

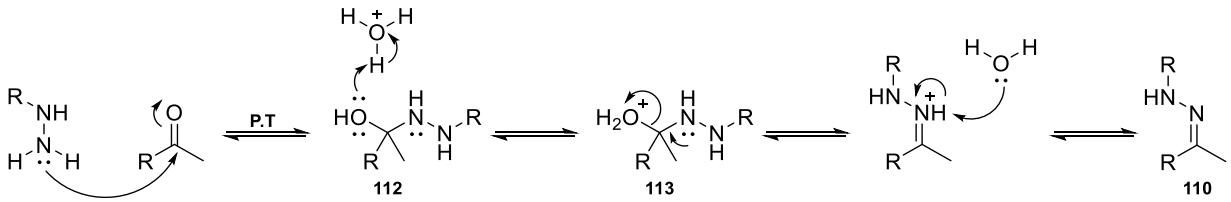

Figure 35. Mechanism for the formation of the hydrazone intermediate **110** *via* condensation. P.T = proton transfer

Oxopropanal route

It was envisioned that a one-pot method *via* formation of the oxopropanal intermediate **119** (**Figure 36**) to synthetically access the hydrazone followed by subsequent ring closure *in situ* (Knorr pyrazole condensation) would be a viable path to affording **109** (**Scheme 6**).[228] The main downfall of this approach, compared to the previously discussed hydrazone coupling approach, is the lack of regioselectivity observed (**Figure 36**). This is a result of which carbonyl of the oxopropanal **119** the Knorr pyrazole condensation proceeds. However, this was considered useful in that both regioisomers could theoretically be obtained and subsequently purified simultaneously.

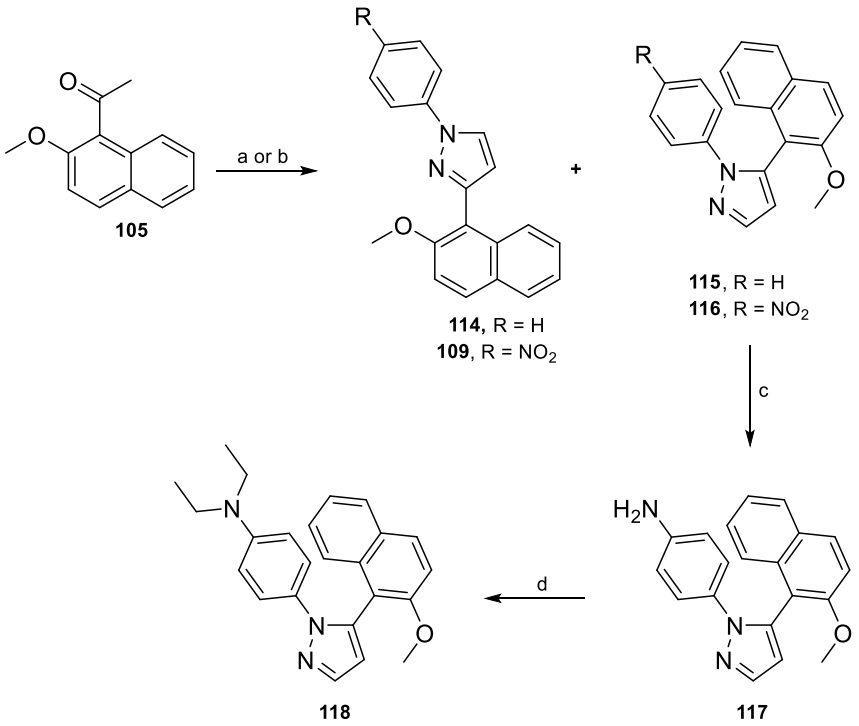

Scheme 6. Oxopropanal pathway for accessing pyrazole derivatives **114**, **115 - 118**. *Reagents and Conditions*: a) i. NaH, Methyl formate, THF, 0 °C – 50 °C, 2 h ii. PhN_2H_4, 3 M HCl, 100 °C, 24 h, 30 – 70% b) i. NaH, Methyl formate, THF, 0 °C – 50 °C, 2 h ii. **111**, 3 M HCl, 100 °C, 1 h, quant. c) **116**, H_2, Pd/C, EtOAc, RT, quant. d) EtI, K_2CO_3, Acetone, 50 °C, 4 h, 83%

With **105** already in hand, a Claisen condensation was carried out with standard conditions using NaH and excess methyl formate in THF at 50 °C to afford the oxopropanal **119** *in situ*. Although Claisen condensations are typically conducted at reflux, the reaction was conducted at a lower temperature due to methyl formate exhibiting a boiling point of 38 °C, with additional excess to compensate any loss. After conversion to the oxopropanal **119** at 2 h, 3M HCl was subsequently added to the reaction to simultaneously quench the reaction and catalyse the subsequent Knorr pyrazole formation. Addition of phenyl hydrazine or **97** followed by reflux afforded the compounds **114**, **115** and **116** in excellent yields.

Surprisingly, only one pyrazole regioisomer was observed when 4-nitrophenyl hydrazine **111** was used whilst both were observed when phenyl hydrazine was used. In particular, the nitro 1,5-regioisomer **116** was exclusively obtained which was especially unexpected as it was anticipated that the steric hindrance of the molecule would dictate the formation of the 1,5-regioisomer to be energetically unfavourable. This result may be further explained by the significant reduction in electron density at the terminal hydrazine nitrogen due to the electron withdrawing properties of the nitro functionality on the ring. Consequently the nitrogen may not demonstrate sufficient nucleophilic propensity and therefore can only

initiate nucleophilic attack at the more electrophilic terminal aldehyde of **119**. Additionally, the decreased steric hindrance of the aldehyde would also favour 1,5-regioisomer formation (**Figure 36** in RED). This can be substantiated by the result of the 1,3- and 1,5-formation observed for derivatives **114** and **115**, respectively, which were isolated when phenyl hydrazine was used. Although the phenylic moiety on the phenyl hydrazine elicits delocalisation and thus lowers electron density present on the terminal hydrazine nitrogen, it does not do so at such a magnitude as that of the nitrophenyl ring on **111**. Therefore, the phenyl hydrazine evidently exhibits acceptable nucleophilic ability to attack at either the ketone (**Figure 36** in RED) or aldehyde (**Figure 36** in BLUE) of the oxopropanal **119**. Regardless, attack through the aldehyde is preferential as the regioisomers were afforded in a ~1:2 ratio for the 1,3- and 1,5-regioisomers, respectively.

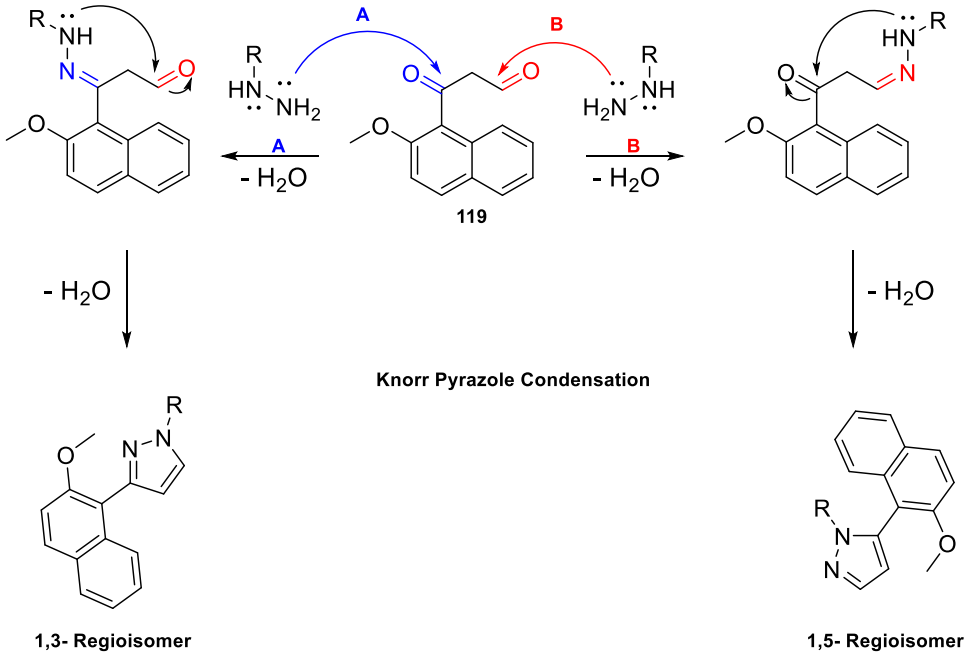

Figure 36. Mechanism for the formation of the 1,3- and 1,5- regioisomers. Pathway A (in BLUE) proceeds through initial condensation at the ketone functionality of the oxopropanal intermediate **119** to afford the 1,3-regiosomer. Pathway B (in RED) proceeds through initial condensation at the terminal aldehyde functionality of the oxopropanal intermediate **119** to afford the 1,5-regioisomer.

Regioisomerism of the pyrazole structures **114** and **115** was confirmed through NMR analysis, as characteristic proton and carbon shifts can be used for identification. Utilisation of valence bonds as a method for recognition of 1,2,3-triazole regioisomers has been reported by Creary, X. *et al.*[229] Similarly this approach can be used to rationalise the shifts seen in the pyrazole isomers. In regards to the 1,3-regioisomer, these shifts can be logically explained through the resonance structures of the pyrazole (**Figure 37**). Of the two characteristic pyrazolic protons, the proton that resides at the most downfield position is observed at 8.10 ppm (**Figure 38**; H_a is highlighted in BLUE). Due to the proximity of H_a to the adjacent N_1 position, it experiences significantly higher deshielding than H_b (**Figure 38**; H_b is highlighted in BLUE). Correlation of H_a can be found to be directly attached to the C_5 carbon which demonstrates a substantially upfield shift of 126.9 ppm (**Figure 38**; C_5 highlighted in RED). When the most stable resonance structure **114B** (**Figure 37**) is obtained, this carbon holds a formal negative charge. This results in a strong shielding effect that can explain the chemical shift of the C_5 position. Conversely, the C_3 atom exhibits a strong downfield shift compared to its C_5 counterpart due to the strong electronegativity of the adjacent N_2 position. These correlations were confirmed using ^{1}H-^{13}C heteronucelear single quantum coherence (HSQC) and ^{1}H-^{13}C heteronuclear multiple bond correlation (HMBC) NMR (**Appendix A**).

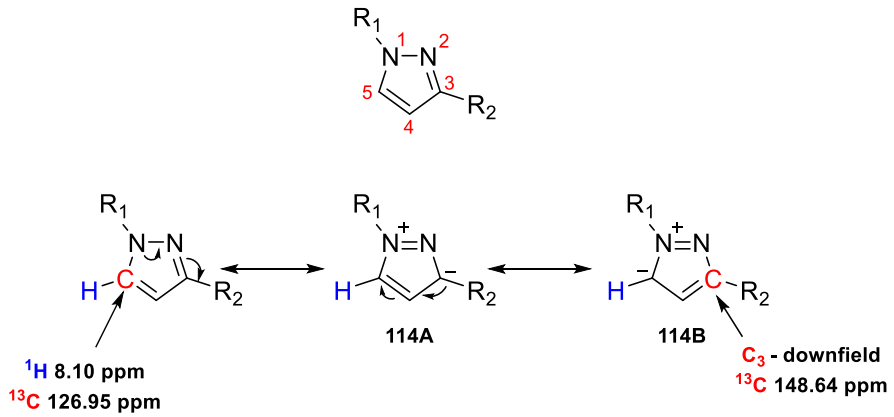

Figure 37. Resonance structures of 1,3-disubstituted pyrazoles, using the chemical shifts of phenyl derivative **114** as an example. Downfield pyrazolic proton highlighted in BLUE with respective C_3 and C_5 highlighted in RED.

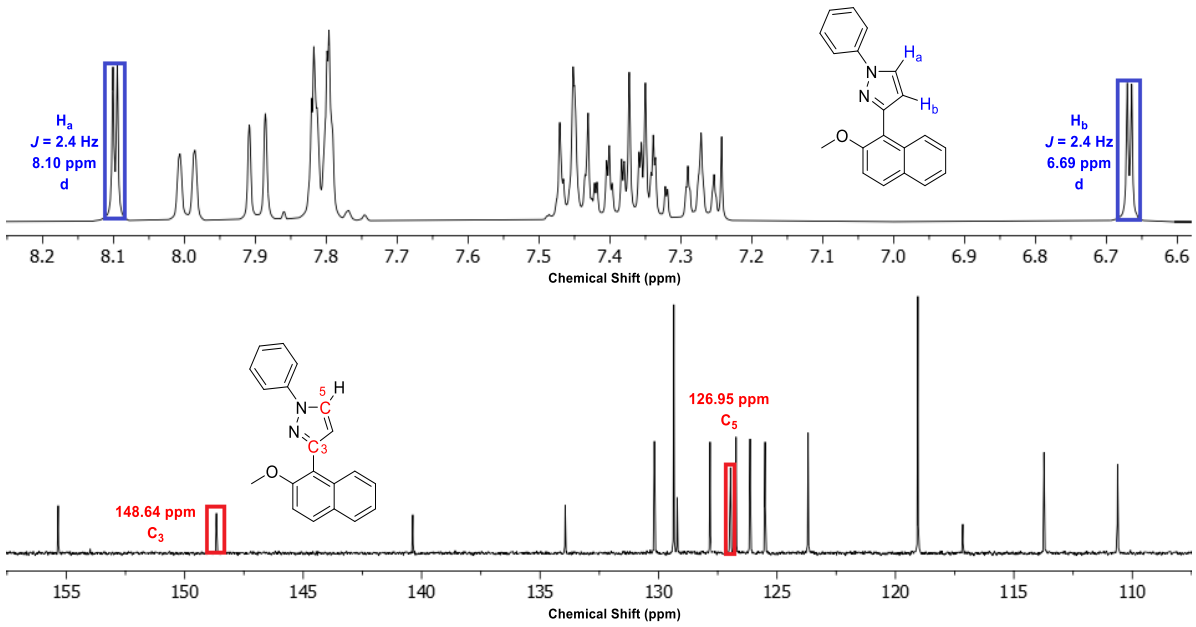

Figure 38. ^{1}H-NMR (400 MHz, $CDCl_3$) and ^{13}C-NMR (101 MHz, $CDCl_3$) spectrum for compound **114**. Characteristic pyrazolic proton chemical shifts are highlighted in BLUE. Respective C_3 and C_5 chemical shifts are highlighted in RED. Multiplicity and integration of each respective chemical shift can be seen in **Chapter 6**. Full spectral data in **Appendix A.**

For the 1,5-regioisomer **115**, the resonance structures can again be used to discern the rationale behind the chemical shifts observed (**Figure 39**). Of the two pyrazolic protons, the proton H_a (**Figure 40**; highlighted in BLUE) attached to the C_3 position is observed to be the most downfield at 7.87 ppm (**Figure 40**; H_a highlighted in BLUE) of the two pyrazolic protons. Due to the positioning of H_a next to the adjacent N_2 atom, it experiences a significant deshielding effect as a result of the electronegativity of the N_2 position. Similarly, the corresponding C_3 position (**Figure 40**; highlighted in RED) exhibits a slightly greater deshielding at 140.2 ppm than that of its C_5 counterpart because of the similar proximity to the N_2 atom. On the other hand, the C_5 position demonstrates a marginally upfield shift at 136.9 ppm (**Figure 40**; highlighted in RED). This upfield shift can be explained by the most stable resonance structure **115B** (**Figure 39**), whereby placement of the formal negative charge on C_5 results in the shielding observed. Compared to the 1,3-regioisomer **114**, the close proximity of the C_5 shift to the C_3 is likely the result of additional delocalisation experienced through the directly substituted naphthalene moiety. Subsequently a greater deshielding effect at C_5 is observed leading to the substantially lower shift range seen between the two positions. These correlations were confirmed using ^{1}H-^{13}C HSQC and ^{1}H-^{13}C HMBC NMR (**Appendix A**).

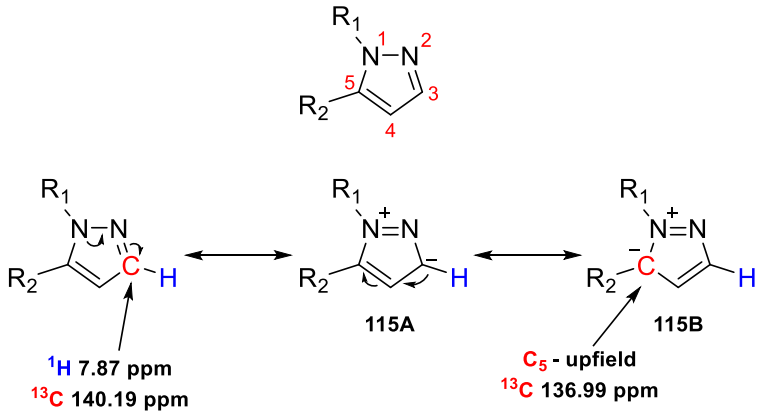

Figure 39. Resonance structures of 1,5-disubstituted pyrazoles, using the chemical shifts of phenyl derivative **115** as an example. Downfield pyrazolic proton highlighted in BLUE with respective C_3 and C_5 highlighted in RED.

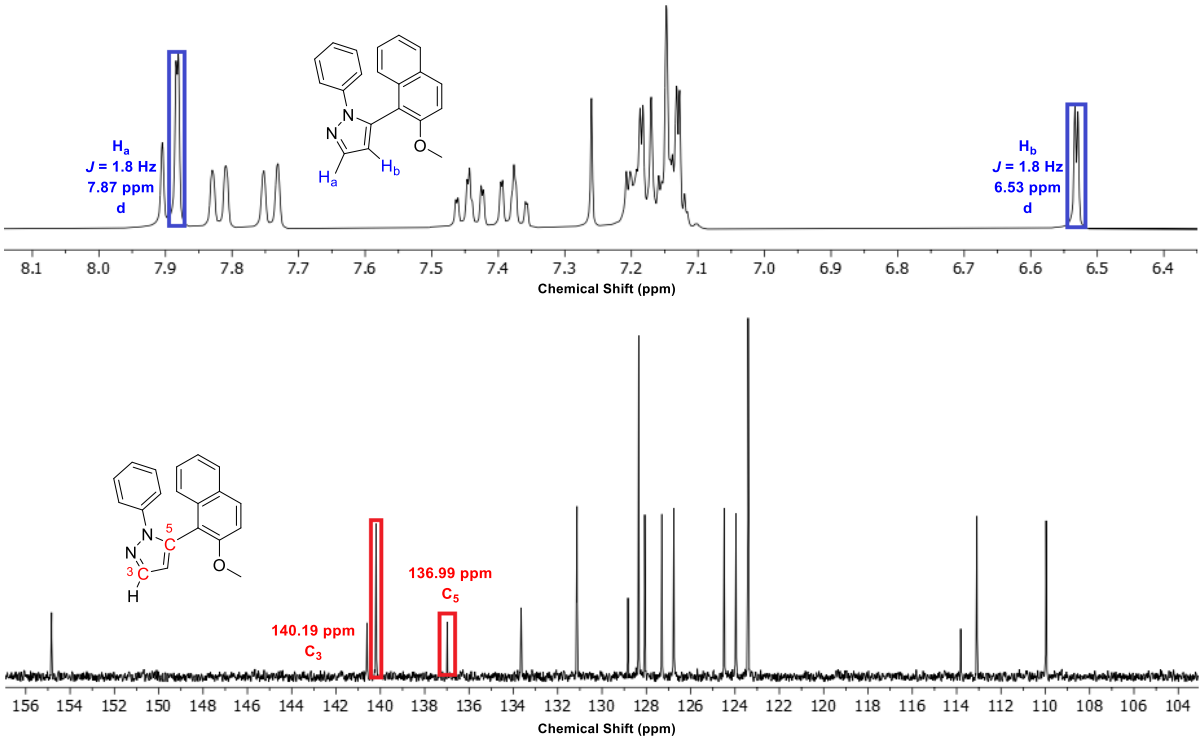

Figure 40. ^{1}H-NMR (400 MHz, $CDCl_3$) and ^{13}C-NMR (101 MHz, $CDCl_3$) spectrum for compound **115**. Characteristic pyrazolic proton chemical shifts are highlighted in BLUE. Respective C_3 and C_5 chemical shifts are highlighted in RED. Multiplicity and integration of each respective chemical shift can be seen in **Chapter 6**. Full spectral data in **Appendix A.**

It can then be easily seen that the lead derivative **118** was obtained exclusively in the 1,5-regioisomeric form. Following the chemical shift of the H_a proton (**Figure 41**; highlighted in BLUE), it can be seen at a downfield position of 7.82 ppm. The corresponding C_3 position this proton is attached to exhibits a shift at 139.3 ppm (**Figure 41**; highlighted in RED). Both the H_a proton and C_3 atom present downfield shifts as a result of the electronegativity of the adjacent N_2 atom. Conversely, the C_5 position displays a slightly more upfield position at

136.7 ppm (**Figure 41**; highlighted in RED) due to the placement of the formal negative charge as observed in the most stable resonance structure **115B** (**Figure 39**). As observed for the 1,5-regioisomer **115**, the lead derivative does not demonstrate a significant shift range between the C_5 and C_3 positions (**Figure 41**; highlighted in RED) when compared to the 1,3-regioisomer **114** (**Figure 38**; highlighted in RED). Again, this can be attributed to the delocalisation experienced by the C_5 atom through the naphthalene moiety, similarly resulting in the lower shift range seen. These correlations were confirmed using ^{1}H-^{13}C HSQC and ^{1}H-^{13}C HMBC NMR (**Appendix A**).

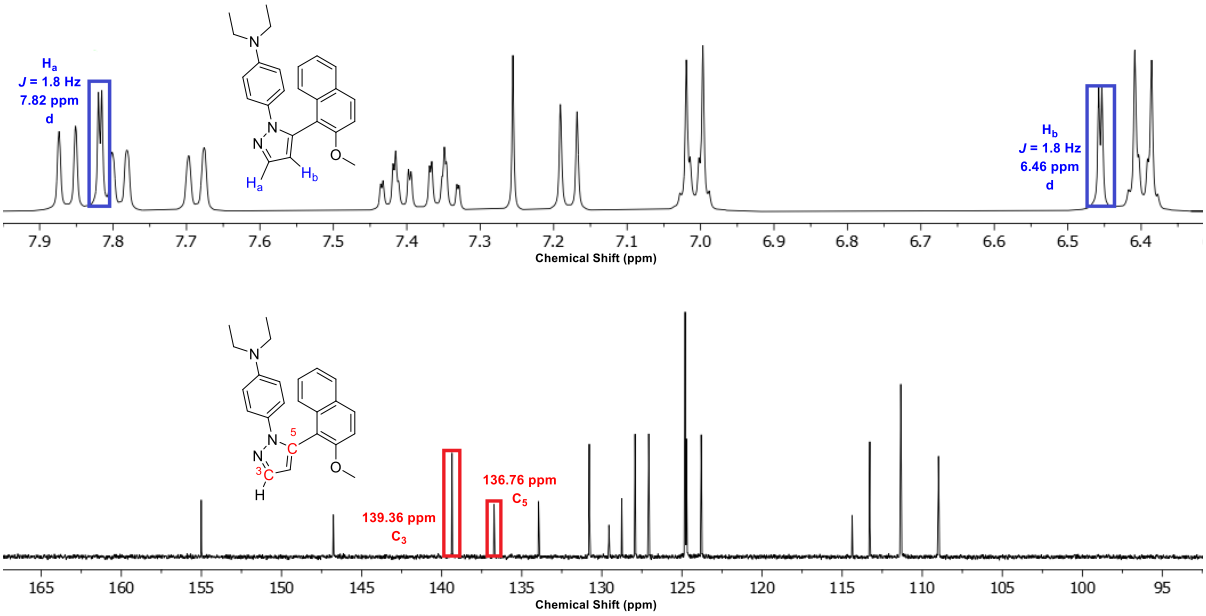

Figure 41. ^{1}H-NMR (400 MHz, $CDCl_3$) and ^{13}C-NMR (101 MHz, $CDCl_3$) spectrum for compound **118**. Characteristic pyrazolic proton chemical shifts are highlighted in BLUE. Respective C_3 and C_5 chemical shifts are highlighted in RED. Multiplicity and integration of each respective chemical shift can be seen in **Chapter 6**. Full spectral data in **Appendix A.**

To attain the 1,3-regiosiomer for the lead derivative **107**, it has previously been reported that 1,3-disubstituted pyrazoles be selectively obtained through benzoyl esterification of oxopropanal **119**.[230,231] This would afford the nitrated derivative **109**, which could be reduced and subsequently dialkylated to afford **107** (**Scheme 5**). Although the mechanism is not known, a proposed mechanism is shown in **Figure 42**. In theory, addition of either pyridine or **120** (4-(dimethylamino)pyridine; DMAP) allows for activation of the benzoyl chloride derivatives **121** and **122** (**Figure 42A**). In fact, **120** has been found to increase acylation rates by factors as large as 10,000 when compared to reactions catalysed by pyridine. It is thought that this works mechanistically *via* the formation of *N*-acylpyiridinium salts (**123A** and **123B**, **Figure 42A**) that can transfer acyl functionalities more

effectively than the acid chloride itself.[232] This is a result of resonance stabilisation (**123A** and **123B**, **Figure 42A**) that allows increased reactivity due to charge delocalisation as well as an increase in equilibrium concentration of the acylpyridinium salts.[232]

Once the acylpyridinium salt (**123A**/**123B**) is formed, it can undergo nucleophilic attack by the enol **124** (**Figure 42B**) to afford the desired ester **125**. In this case, the formation of the benzoyl ester **125** substantially reduces the electophilicity of the aldehyde carbonyl position thereby being less susceptible to nucleophilic attack. Subsequently, the ketone is then comparably more electrophilic and thus favours the formation of the 1,3-regioisomer **109** in a manner similar to pathway A (**Figure 36**; highlighted in BLUE) on addition of the hydrazine derivative **111**. This is consistent with the proposal by Auwers, K.V. & Mauss, H. that presence of the ester forces condensation to occur at the ketone when a hydrazine derivative is introduced to the reaction.[233] Formation of the pyrazolium **126** follows condensation of the hydrazine at the ketone and ensuing ring closure. A 1,3,5-substituted 4,5-dihydropyrazole (**127**) results from deprotonation of **126**, which then undergoes ester hydrolysis to provide the final 1,3-regiosiomer **109**.

Several attempts at forming the vinyl benzoyl ester **125** are outlined in **Table 4**. Initially the conditions reported by Auwers, K. V. and Mauss, H. were trialled by using pyridine to activate the acid chloride **121** but with a solvent change to THF from Et_2O made due to solubility issues with the oxopropanal **119** (**Table 4**, **Entry 1**). After monitoring the reaction for 3 h, no reaction was observed so heat was gradually applied until reflux (**Table 4**, **Entry 2**). No reaction was detected despite heating and extended reaction times. Resultantly it was decided to substitute the acid chloride **121** for the 4-nitrophenyl substituted acid chloride **122** (**Table 4**, **Entry 3**). This adjustment was made in consideration of the strong electron withdrawing effect of the *para*-nitro substituent, thus significantly increasing the electrophilic character of the acid chloride. In addition to the activation of **122** by pyridine, it was hoped that this may compensate for the insufficient nucleophilicity exhibited by the enolate of **124**. However no reaction was observed after 3 h stirring at room temperature. Due to the greater rates of acylation reported for **120**, a final attempt was trialled with the reaction conducted at reflux (**Table 4**, **Entry 4**). Again, no reaction was observed by TLC despite extended reaction times. Unfortunately it appears the nucleophilicity of the enol motif is not sufficient enough to allow coupling for formation of the desired vinyl ester intermediate **125**. This may be a result of delocalisation through the naphthalene moiety thereby diminishing nucleophilic

potential at the enol functionality. Comparatively, Auwers, K. V. and Mauss, H. reported successful conversion to the desired vinyl ester by use of 3-oxo-3-phenylpropanal which may exhibit sufficient nucleophilicity as it does not contain a bicyclic moiety that draws additional delocalisation. In any case, due to time constraints additional investigations into obtaining the lead 1,3-regioisomer **107** were unable to be explored.

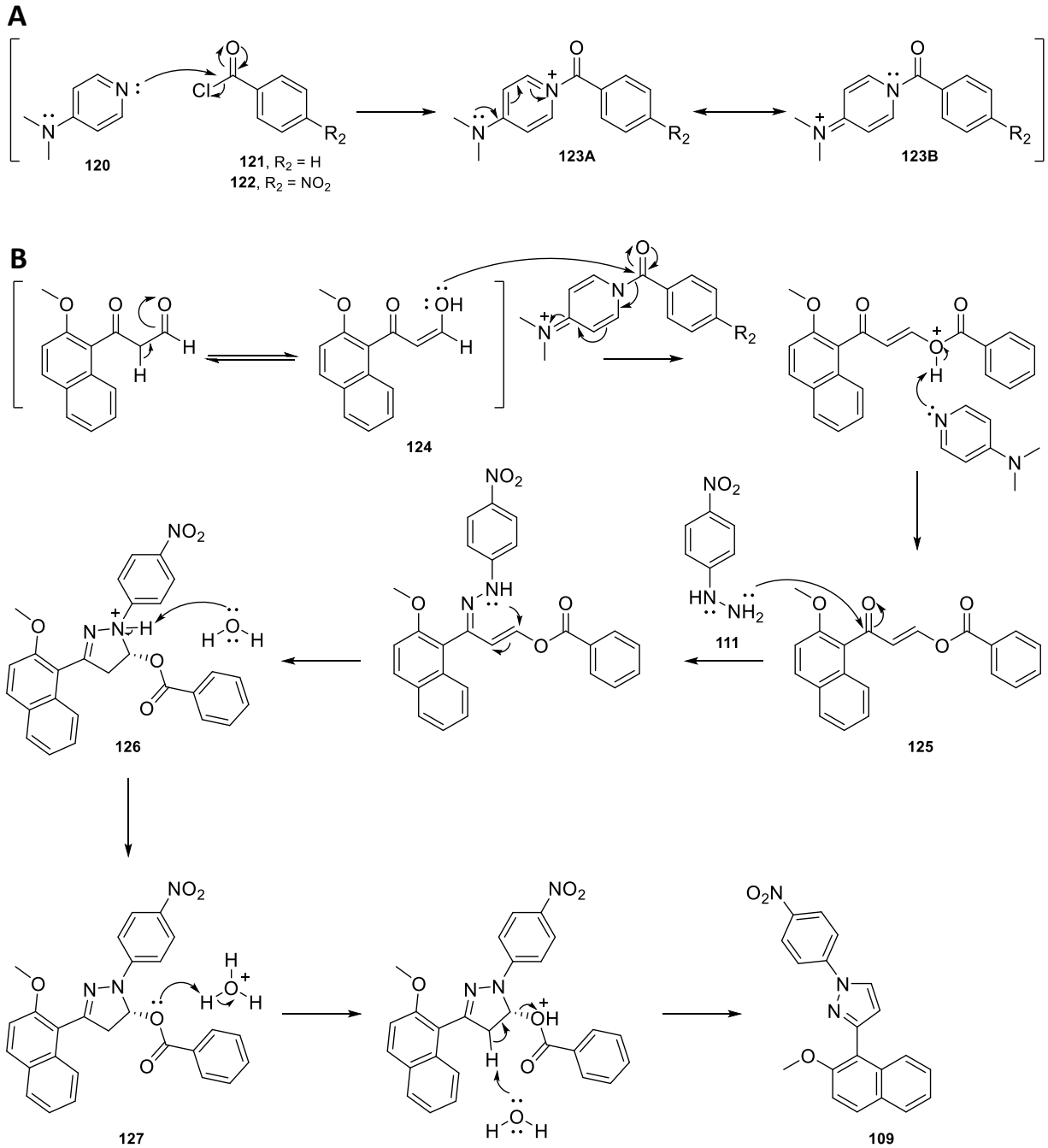

Figure 42. Proposed mechanism for the formation of the 1,3-regioisomer **109** *via* benzoyl esterification of **119**.

Table 4. Reaction conditions trialled and subsequent results for obtaining vinyl ester **125**.

Entry	Reaction Conditions	Result
1	**121**, 1.5 eq. Pyridine, THF, RT	No reaction
2	**121**, 1.5 eq. Pyridine, THF, RT – 78 °C	No reaction
3	**122**, 1.5 eq Pyridine, THF, RT	No reaction
4	**122**, 1.5 eq **120**, THF, 78 °C	No reaction

3.3 Synthesis of Triazole Derivatives

3.3.1 Synthesis of 1,4-Disubstituted 1,2,3-Triazoles

In approaching the synthesis of the lead 1,4-regioisomer triazole derivative **146** and other associated derivatives in the series (**147 – 151**), it was envisioned that they could be afforded *via* click chemistry in a convergent synthetic pathway (**Scheme 7**). Beginning with various aniline derivatives **76** and **85 – 89** could be transformed into diazonium tetrafluoroborate salts **128** – **133**. Subsequent subjection to an azide substitution would afford the azide derivatives **134** – **139**. These azide derivatives **134** – **139** would then be coupled to alkyne **145** to form the 1,4-regioisomers **146 – 151**. To obtain the desired alkyne **145**, **78** was to be halogenated to afford the brominated naphthol derivative **140** or the iodinated derivate **142**. An ensuing Sonagashira coupling (**Table 5**) would be followed by deprotection to afford the requisite alkyne **145**. This was not a viable pathway due to complications involving the phenolic moiety of both **140** and **142** (further discussed below) and so it was necessary to alkylate the phenolic functionality to form the methylated halogenated derivatives **141** and **143**. Consequently these derivatives would then be subjected to the Sonogashira coupling and then deprotected to afford the alkyne **145** (**Table 6**).

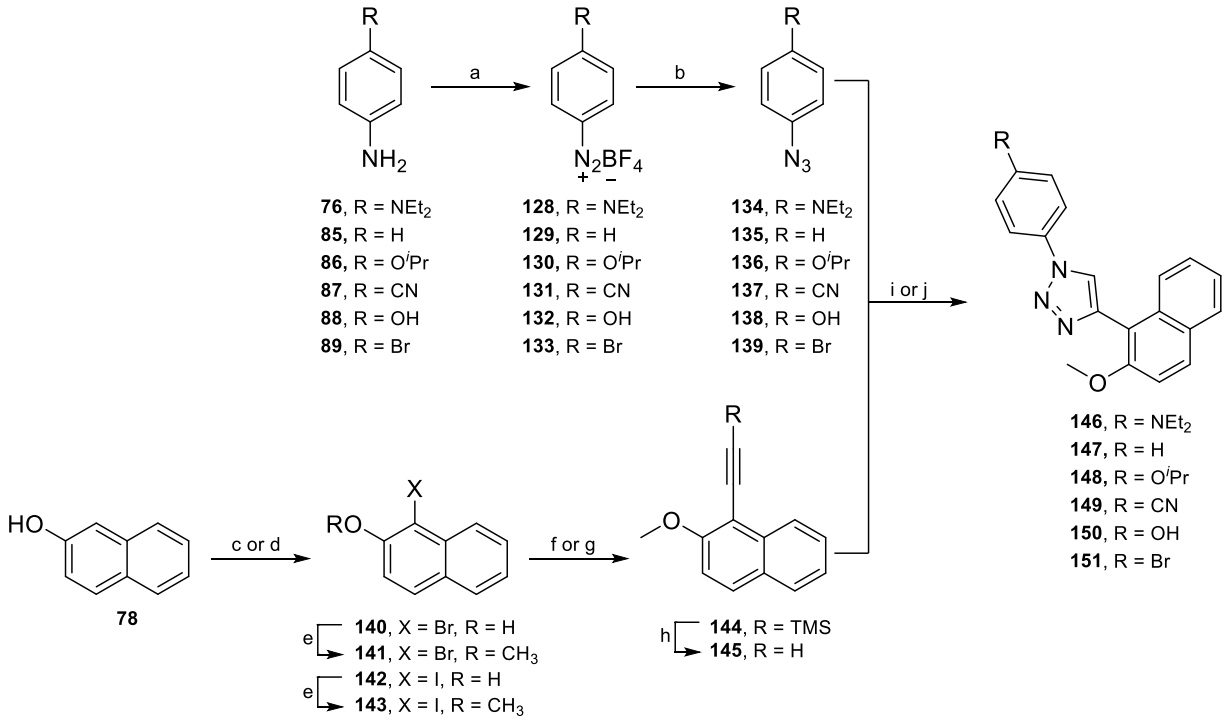

Scheme 7. Convergent synthetic pathway for accessing 1,4-triazole regioisomer library. *Reagents and Conditions*: a) HBF_4, Isopentyl Nitrite, AcOH, RT, 15 min then Et_2O, -40 °C, 50 – 98% b) NaN_3, THF, RT, 24 h, 57 – 94% c) NBS, $CHCl_3$, RT, 2 h, quant. d) TsOH, NIS, MeCN, RT, 6 h, 83% e) NaH, MeI, THF, 0 °C – RT, 86 – 94% f) **140**, $Pd_2(dba)_3$, Xphos, TMS-acetylene, CuI, Et_3N, Toluene, 110 °C, 8 h, 80% g) **142**, $PdCl_2(PPh_3)_2$, TMS-acetylene, CuI, Et_3N, 40 °C, 8 h, 95% h) TBAF, THF, RT, 4 h, quant. i) **158**, CuI, Sodium ascorbate, THF:H_2O, 70 °C, 8 h, 64% j) $CuSO_4 \bullet 5H_2O$, Sodium ascorbate, THF:H_2O, 70 °C, 8 h, 28 – 43%

The desired halogenated derivatives **140** and **142** were synthesised using either NBS or NIS, respectively from **78**. Both were obtained in high yields and then subjected to several attempted Sonogashira coupling conditions (**Table 5**). Beginning with the brominated derivate **140**, standard Sonogashira conditions were performed using $PdCl_2(PPh_3)_2$, CuI and TMS-acetylene in neat Et_3N at 70 °C (**Table 5**, **Entry 1**). Monitoring of the reaction over several hours saw complete consumption of the material. However upon workup and subsequent purification, the sole product isolated was observed to be naphthol **78**. As discussed by Surry, D. S and Buchwald, S. L. hydrodehalogenation can occur as a result of either catalyst decomposition or inefficient reductive elimination.[234] Therefore it was decided to trial both $Pd(PPh_3)_4$ and $Pd_2(dba)_3$ (**Table 5**, **Entry 2** and **3**, respectively) in identical conditions to determine if any success could be observed. Subjection to $Pd(PPh_3)_4$ led to quantitative hydrodehalogenation whilst $Pd_2(dba)_3$ did not provide any reaction at all. These results are likely due to the inadequate reductive potential of the $Pd(PPh_3)_4$ to promote reductive elimination whilst likely that $Pd_2(dba)_3$ was unable to facilitate the initial oxidative addition process. Consequently it was decided to move forward with the iodinated derivate

142 as the lability of the iodo functionality in Pd-catalysed reactions is substantially greater as the C-I bond is weaker due to the larger atomic radius of iodine.[235,236]

Table 5. Reaction conditions trialled and subsequent results for obtaining **144** from **140** and **142**.

Entry	Reaction Conditions	Result
1	**140**, 10 mol % $PdCl_2(PPh_3)_2$, 6 mol % CuI, TMS-acetylene, Et_3N, 70 °C	100% hydrodehalogenation
2	**140**, 10 mol % $Pd(PPh_3)_4$, 6 mol % CuI, TMS-acetylene, Et_3N, 70 °C	100% hydrodehalogenation
3	**140**, 10 mol % $Pd_2(dba)_3$, 6 mol % CuI, TMS-acetylene, Et_3N, 70 °C	No reaction
4	**142**, 10 mol % $PdCl_2(PPh_3)_2$, 6 mol % CuI, TMS-acetylene, Et_3N, 70 °C	100% hydrodehalogenation
5	**142**, 10 mol % $PdCl_2(PPh_3)_2$, 6 mol % CuI, TMS-acetylene, Et_3N, RT	100% hydrodehalogenation

Subjecting the iodoniated intermediate **142** to the initial standard conditions trialled again resulted in hydrodehalogenation (**Table 5**, **Entry 4**). As mentioned above, the other potential circumstance in which this occurs is catalyst decomposition in which the prescribed solution is to lower the temperature of the reaction.[234] Accordingly the reaction was then attempted at room temperature with consideration to gradually increase the temperature if no reaction was observed by TLC analysis (**Table 5**, **Entry 5**). Surprisingly the reaction afforded quantitative hydrodehalogenation with no additional heat applied. At first it was considered that the phenol may be in some cases be coordinating the Pd species and therefore resulting in the hydrodehalogenation in some respect. However, it was found that Rousseaux, S. and co-workers investigated the role of Pd-catalysed arlylative dearomatisation in phenols that can lead to rearomatisation processes and subsequently the hydrodehalogenated product.[237] A proposed mechanism with consideration of the catalytic cycle in respect to the halogenated derivatives **140** and **142** can be seen in **Figure 43.** Oxidative addition occurs with the

catalytically active Pd^0 species to provide the intermediate **152**. It is likely that the reductive elimination pathway is primarily unfavourable due to steric strain of the 4-membered transition state exhibited (**153**), thereby not leading to an observed dearomatised side product. Consequently the molecule then undergoes rearomatisation processes that results in the hydrodehalogenated naphthol **78**.

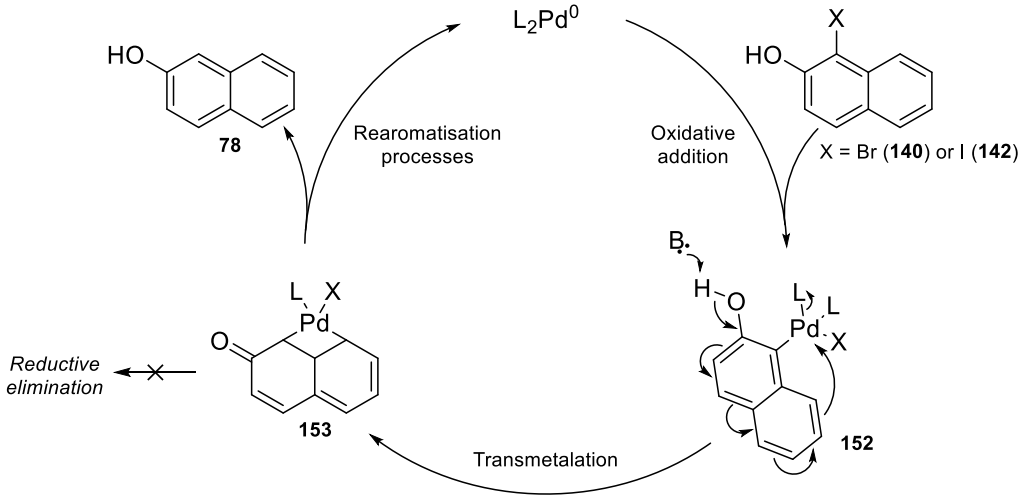

Figure 43. Proposed mechanisms for the hydrodehalogenation of derivatives **140** and **142**, thereby returning to the compound **78**.

To overcome base-promoted phenolic abstraction, it was decided to alkylate the phenol. As such the halogenated derivatives **140** and **142** were methylated with standard conditions of MeI and NaH dissolved in THF at room temperature to afford the derivatives **141** and **143** in great yields. Initially the brominated derivative **141** was subjected to original standard Sonogashira coupling conditions trialled (**Table 6**, **Entry** 1). Quantitative hydrodehalogenation was observed, which was surprising as **141** cannot proceed through the mechanism previously discussed. In this case it was then considered that reductive elimination was not occurring as the ligand present did not exhibit a sufficient reductive potential. Therefore, it was decided to trial a dialkylbiarylphosphine ligand. This decision was made for several reasons. Firstly, the overall size of the ligand used in the reaction plays the role of slowing the rate of oxidation by O_2 thereby stabilising the Pd-arene interaction and facilitating reductive elimination.[234,238] Typically the secondary aryl ring of a ligand is modified to increase the overall bulk as well as the size of the moieties present on the phosphorus atom. Additionally, substituent choices that fix that conformation of the primary aryl ring (directly bonded to the phosphorus atom) promote the rate of reductive elimination.

Following methodology reported by Łączkowski, K. and co-workers on similar substrates, **141** was subjected to modified Sonogashira conditions whereby XPhos was trialled as the dialkylbiarylphosphino ligand (**Table 6**, **Entry 2**). This is due to its high reductive potential and was found to be the most superior ligand assessed.[239] Further, it was used alongside $Pd_2(dba)_3$, (*i*-Prop)$_2$NH as well as toluene to aid solubility of the ligand. Monitoring the reaction at reflux for several hours resulted in a great yield of the TMS-protected alkyne **144**. Lastly, the iodinated derivative **143** was subjected to the initial standard conditions trialled and afforded the TMS-alkyne **144** in excellent yields (**Table 6**, **Entry 3**). Subsequent deprotection of **144** with tetra-*n*-butylammonium fluoride (TBAF) in MeOH afforded quantitative yields of the alkyne **145**.

Table 6. Reaction conditions trialled and subsequent results for obtaining **144** *via* **141** and **143**.

Entry	Reaction Conditions	Result
1	**141**, 10 mol % $PdCl_2(PPh_3)_2$, 6 mol % CuI, TMS-acetylene, Et_3N, 70 °C	100% hydrodehalogenation
2	**141**, 20 mol % $Pd_2(dba)_3$, 5 mol % XPhos, 6 mol % CuI, TMS-acetylene, (*i*-Prop)$_2$NH, Toluene, 110 °C	80% yield
3	**143**, 10 mol % $PdCl_2(PPh_3)_2$, 6 mol % CuI, TMS-acetylene, Et_3N, 70 °C	95% yield

With the alkyne **145** in hand, synthesis towards the azido derivatives **134 – 139** was undertaken beginning with various aniline derivatives **76** and **85 – 89**. Aside from **76**, which the synthesis has been previously discussed in **Chapter 2**, **Scheme 1**, all aniline derivatives were used from commercial sources. These were converted to the respective tetrafluoroborate diazonium salts **128 – 133**, using the previously outlined conditions in **Table 2**, in high yields. Following this, the diazonium salts were suspended in THF for the subsequent azide formation. Although the salts are partially soluble in the solvent, it presents a sufficient medium to carry out the azido substitution without interference due to its polar aprotic nature. Addition of NaN_3 with stirring overnight resulted in the azido derivatives **134 – 139** in good to excellent yields. It is worth noting that on completion of the reaction, the afforded products were fully dissolved in solution. This indicated that as the solvated salts undergo substitution,

equilibrium drives the salts in suspension to be slowly dissolved and thus leads to consumption of materials.

To achieve the triazole regioisomers, it was originally considered to conduct a standard Husigen azide-alkyne 1,3-dipolar cycloaddition that would afford both the desired regioisomers. However, for the purposes of purification it was decided more ideal to undergo selective synthesis of the regioisomers separately. In the case of the lead 1,4-regioisomer **146**, a standard copper-catalysed azide-alkyne cycloaddition (CuAAC) (**Table 7**, **Entry 1**; **Figure 44**) was conducted.[240,241] It has been by proposed that this proceeds *via* two copper atoms.[241] Mechanistically the catalytic cycle (**Figure 44**) begins when an alkyne coordinates to a Cu^{I} atom to form the σ-bound copper acetylide **154**. A secondary Cu^{I} atom is then recruited, leading to the loss of a proton and formation of the catalytically active π-bound copper acetylide **155**. Subsequent introduction of an azide species results in reversible coordination to the π-bound copper acetylide thereby forming the complex **156**. This undergoes stepwise annulation resulting in the triazolide-copper derivative **157,** followed by protonolysis to provide the desired 1,4-disubstituted 1,2,3-triazole derivative.

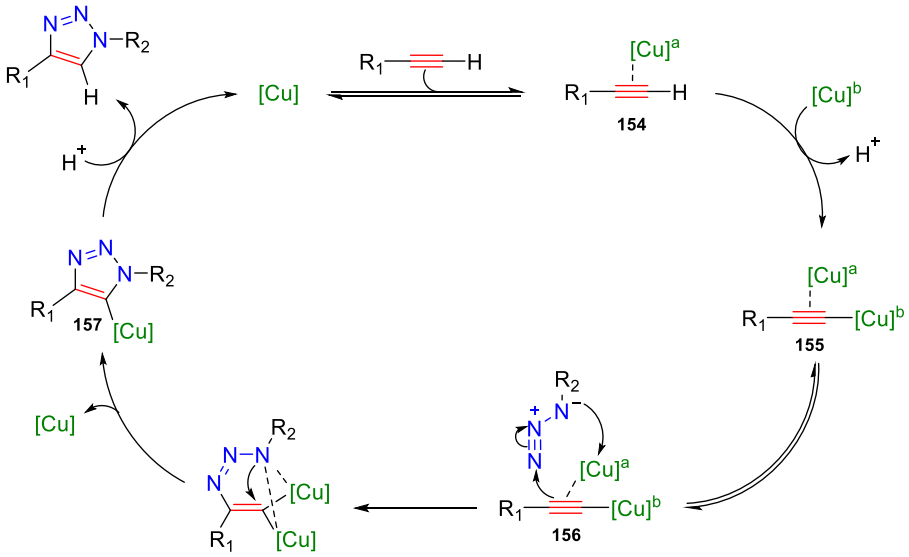

Figure 44. Proposed catalytic cycled for the formation of copper-catalysed 1,4-disubstituted 1,2,3-triazoles.[241]

After stirring for 8 h, although the starting materials were found to be completely consumed, a basic workup of the organic layer did not yield any material. The expected mass to charge ratio (m/z) was observed for the compound **146** in analysis of the aqueous layer by ESI-MS, leading to the assumption that the tertiary amine moiety may be coordinating to the copper thus forming an irremovable complex. For example, the polytriazole tris((1-benzyl-4-

triazolyl)methyl)amine (TBTA; **158, Figure 45**) has been reported to effectively contain the catalytically active Cu^{I} component through its tetradentate binding ability thus preventing potential destabilising interactions from occurring by occupying all binding sites available (**159**, **Figure 45**).[242] The coordination of TBTA (**158**) to Cu^{I} is a consequence of the tertiary amine and 1,2,3-triazole functionalities residing on the molecule. Similarities between TBTA (**158**) and the lead 1,4-regioisiomer **146** can be observed (**Figure 45**), with both purporting 1,4-disubstituted 1,2,3-triazole functionalities (highlighted in BLUE) as well as tertiary amines (highlighted in RED). As such it may be the case that several molecules of **146** are similarly caging the copper species and cannot be isolated from the complex after formation. Therefore it was considered the Cu^{I} may be preferentially caged with addition of TBTA (**158**) as a consequence of the tetradentate functionality thus preventing **146** from forming a copper coordinated complex. Furthermore, use of sodium ascorbate in the reaction is typically used to allow *in situ* reduction of the Cu^{II} species (in this case $CuSO_4 \cdot 5H_2O$) to the catalytically active Cu^{I}. However, oxidation to Cu^{II} proceeds readily as a result of the thermodynamic instability of Cu^{I} and potential disproportionation to both Cu^{0} and Cu^{II}.[242] To ensure that the required Cu^{I} species was readily available and not a problematic variable, CuI was substituted in place of $CuSO_4 \cdot 5H_2O$ alongside sodium ascorbate. With these modified conditions (**Table 7, Entry 2**) the lead derivative was found to be easily isolated from the reaction mixture when worked up under basic conditions and afforded the desired compound **146** in good yields. Additionally a solution of EDTA in an NH_3/NH_4Cl buffer (2 M, pH 9.5) was used in conjunction with the aqueous layer to assist any potential chelation of unwanted copper species.

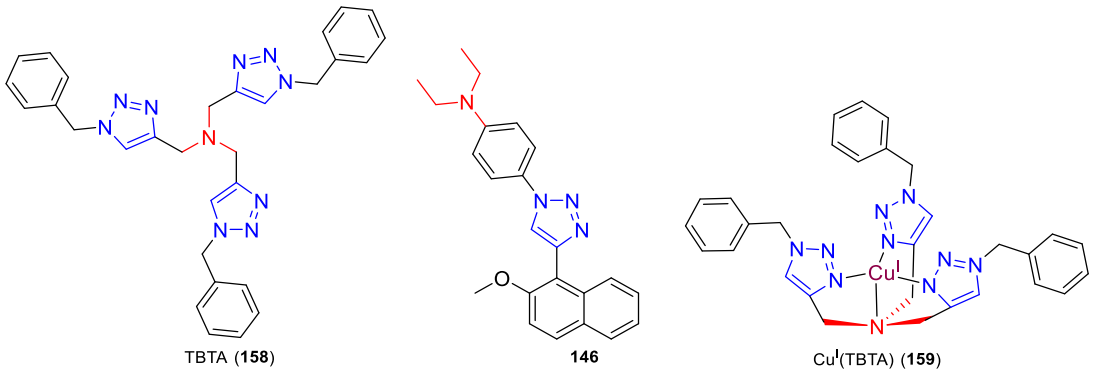

Figure 45. Structures of TBTA (**158**), lead 1,4-regioisomer **146** and complexed Cu^{I}(TBTA) **159**, respectively. 1,4-Disubstituted 1,2,3-triazole functionalities are highlighted in BLUE whilst tertiary amine moieties are highlighted in RED.[243]

Table 7. Reaction conditions trialled and subsequent results for obtaining lead triazole 1,4-regioisomer **146**.

Entry	Reaction Conditions	Result
1	**134**, **145**, $CuSO_4 \cdot 5H_2O$, Sodium Ascorbate, THF:H_2O, 70 °C	Coordinated to copper Irremovable from aqueous layer
2	**134**, **145**, **158**, CuI, Sodium Ascorbate, THF:H_2O, 70 °C	64% yield

Due to the well-reported nature of the regioselective synthesis of 1,4-disubstituted 1,2,3-triazoles *via* the CuAAC route, it is expected that the products obtain exhibit the 1,4-regioisomerism. Unfortunately no distinctive ^{1}H-^{1}H NOESY correlations can be observed between the triazole proton and the lower protons of the phenylic head group or the methoxy group of the naphthalene for the 1,4-regioisomers. However, methods for determining the 1,4-regioisomer products of the triazoles by identifying the relative shifts of the C_5 position have been reported by Creary, X. *et al.*[229] Distinctive chemical shifts in the triazole proton (**Figures 47** and **50**; highlighted in BLUE) and its relative carbon C_5 (**Figures 47** and **50**; highlighted in RED) can be observed when compared to the 1,5-regioisomers (discussed in **Section 3.3.2**). These can be rationalised by the differing resonance structures exhibited by the regioisomers (1,4-regiosiomers in **Figure 46**; 1,5-regiosiomers in **Section 3.3.2**, **Figure 49**). In particular, it can be seen that when the resonance structure **146B** of the 1,4 product is obtained the formal negative charge resides on the C_5 position which is next to the formally positively charged N_1.

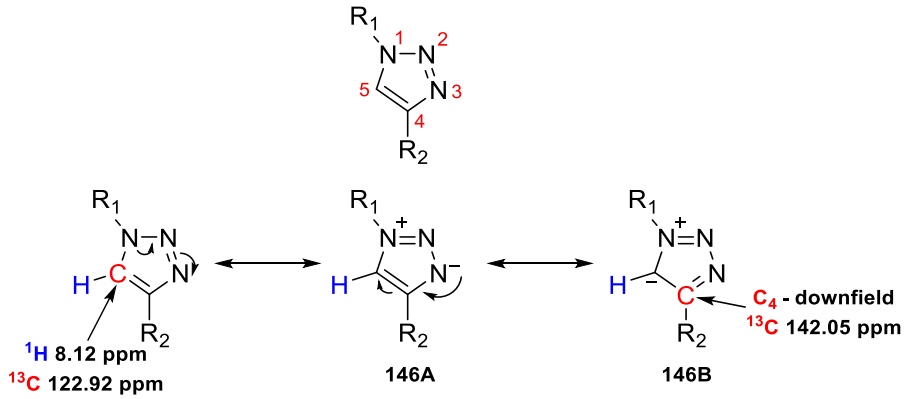

Figure 46. Resonance structures of 1,4-disubstituted 1,2,3-triazoles using the chemical shifts of lead derivative **146** as an example. Triazolic proton highlighted in BLUE with respective C_4 and C_5 highlighted in RED.

Using the lead 1,4-regioisomer derivative **146** as an example, the characteristic triazolic proton (**Figure 47**; highlighted in BLUE) attached to C_5 is observed at 8.21 ppm. Correspondingly, the C_5 position of the 1,4 product **146** presents an upfield shift at 122.9 ppm (**Figure 47**; highlighted in RED). The upfield shift of the C_5 in **146** can be explained by the resonance structure of **146B** (**Figure 46**) whereby the formal negative charge resides on the C_5 position resulting in a shielding effect being experienced. Consequently then the C_4 position can be observed at a greater downfield shift of 142.1 ppm (**Figure 47**; highlighted in RED) as a result of deshielding experienced through the electronegativity of the formally negatively charged N_3 in **146A**. In addition, delocalisation through the substituted naphthalene moiety at the position would result in an increased deshielding effect to be experienced. This correlation was confirmed using ^{1}H-^{13}C HSQC and ^{1}H-^{13}C HMBC NMR (**Appendix A**).

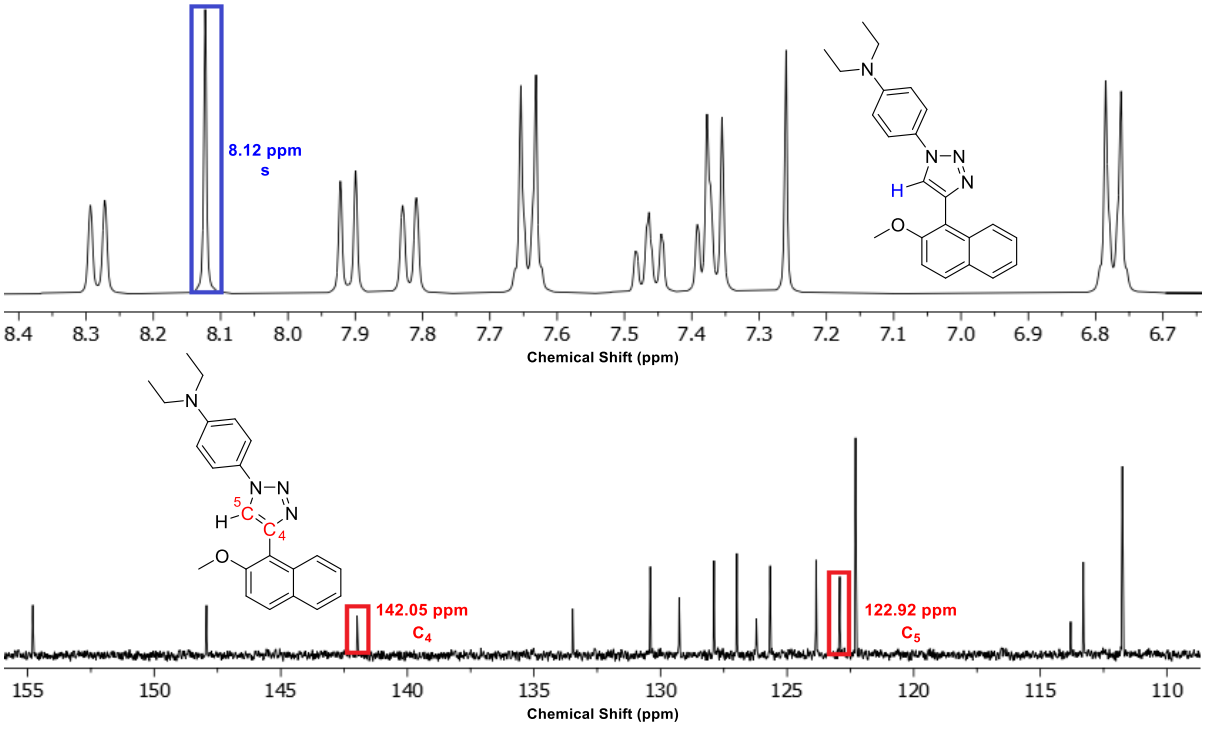

Figure 47. ^{1}H-NMR (400 MHz, $CDCl_3$) and ^{13}C-NMR (101 MHz, $CDCl_3$) spectrum for compound **146**. Characteristic triazolic proton chemical shift is highlighted in BLUE. Respective C_5 chemical shift is highlighted in RED. Multiplicity and integration of each respective chemical shift can be seen in **Chapter 6**. **Full spectral data in Appendix A.**

For the remaining 1,4-regiosiomer derivatives, standard conditions (with $CuSO_4 \bullet 5H_2O$ substituted for CuI) worked reasonably to afford **147 – 151** in varying yields. It is expected following this method that 1,4-regiosiomerism is present in all the derivatives, with similar correlations observed for the above derivative **146** in ^{1}H NMR and ^{13}C NMR chemical shifts. Subsequent purification of the derivatives *via* flash chromatography provided the compounds

in excellent purity for future *in vitro* assessment.

3.3.2 Synthesis of 1,5-Disubstituted 1,2,3-Triazoles

Using the previously described synthetic approaches to provide alkyne **145** and azido-derivatives **134 – 137** and **139**, a convergent synthesis to selectively achieve the 1,5-regiosiomers was undertaken (**Scheme 8**). It is known that ruthenium-catalysed pathways using pentamethylcyclopentadienyl ruthenium chloride [Cp*RuCl] complexes can achieve 1,5-disubstituted 1,2,3-triazoles regioselectively.[244] Therefore ruthenium-catalysed azide-alkyne cycloaddition (RuAAC) was trialled to achieve the desired lead derivative **160** as well as **162** concurrently to ensure that the tertiary amine was not a problematic variable in respect to any potential coordination interferences as previously observed (**Table 8**, **Entry 1** and **Entry 2**, respectively). In standard conditions outlined by Boren, B. *et al.*, initial attempts trialled $Cp^*RuCl(PPh_3)$ as the source of [Cp*RuCl] complex in a solution of 1,4-dioxane at reflux.[244] In either case no reaction was observed. It is unlikely that the nature of inactivity is due to catalyst degradation as the reagent was newly obtained from a commercial source or coordination of the NEt_2/O^{i}Pr moieties present on **134** and **136**, respectively. As such, it may be the case that the substrates **134** and **136** were incompatible with the [Cp*RuCl] catalyst used in the reaction. Therefore an alternative synthetic pathway to afford the 1,5-regioisomeric products was sought.

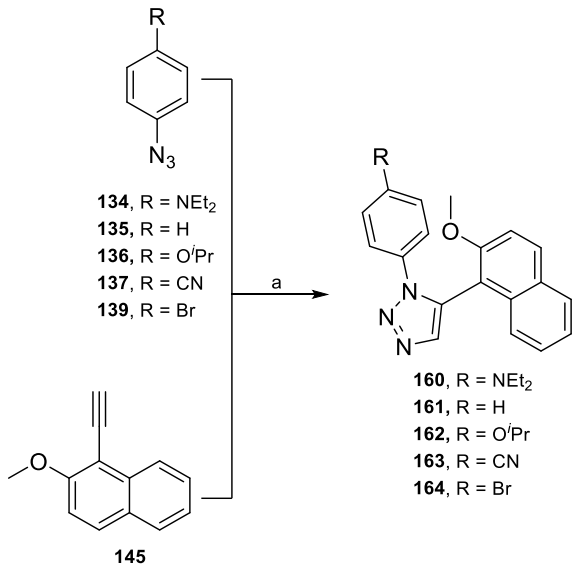

Scheme 8. Convergent synthetic pathway for accessing 1,5-triazole regioisomer library **160** – **164**. *Reagents and Conditions*: a) 10% NMe_4OH, DMSO, RT, 15 – 34%

Table 8. Reaction conditions trialled and subsequent results to obtain the 1,5-regioisomers **160** – **164**.

Entry	Reaction Conditions	Result
1	**134**, **145**, 2 mol % $Cp^*RuCl(PPh_3)$, 1,4-dioxane, 80 °C	No reaction
2	**136**, **145**, 2 mol % $Cp^*RuCl(PPh_3)$, 1,4-dioxane, 80 °C	No reaction
3	**134 – 139**, **145**, 10 mol % NMe_4OH, DMSO, RT	15 – 45% yield

An interesting base-catalysed approach reported by Kwok, S. *et al.* was trialled (**Table 8**, **Entry 3**), with a proposed catalytic cycle shown in **Figure 48**.[245] It has been established that aryl acetylenes exhibit greater acidity when solubilised in DMSO, with additional studies of quaternary ammonium hydroxide base-catalysed alkynylation reactions occurring in DMSO medium.[246,247] This provides the basis of the reaction pathway proposed in **Figure 48**. To begin with, the alkyne **145** undergoes reversible deprotonation by OH^- (from NMe_4OH) to form the acetylide **165** as the favoured product in equilibrium. Subsequent nucleophilic attack of the acetylide **165** onto the positive nitrogen terminus of an azido derivative results in the formation of triazenide intermediate **166**. A resulting 5-*endo-dig* cyclisation or 6π-electrocyclisation proceeds thereby producing the 1,5-disubstituted 1,2,3-triazolyl anion **167**. Completion of the catalytic cycle occurs when the anion **167** deprotonates a molecule of DMSO, the alkyne **145** or water present in the reaction mixture. In fact, when Kwok, S. *et al.* carried these reactions out in d_6-DMSO, it was found that incorporation of deuterium into the products was observed.[245] It is important to note that selective formation of 1,5-disubstituted 1,2,3-triazoles occurs with no production of 1,4-regioisomers as the azido derivatives cannot undergo nucleophilic attack by acetylide **165** at the negative nitrogen and therefore can only proceed *via* the positive terminus to form 1,5-regiosiomers. Following the conditions outlined by Kwok, S, *et al.*, catalytic amounts of NMe_4OH were used when the azido derivatives **134** – **137** and **139** were dissolved in a solution of DMSO at RT with alkyne **145** and stirred for 8 h. These conditions resulted in manageable yields of the 1,5-regioisomers **160** – **164** being afforded.

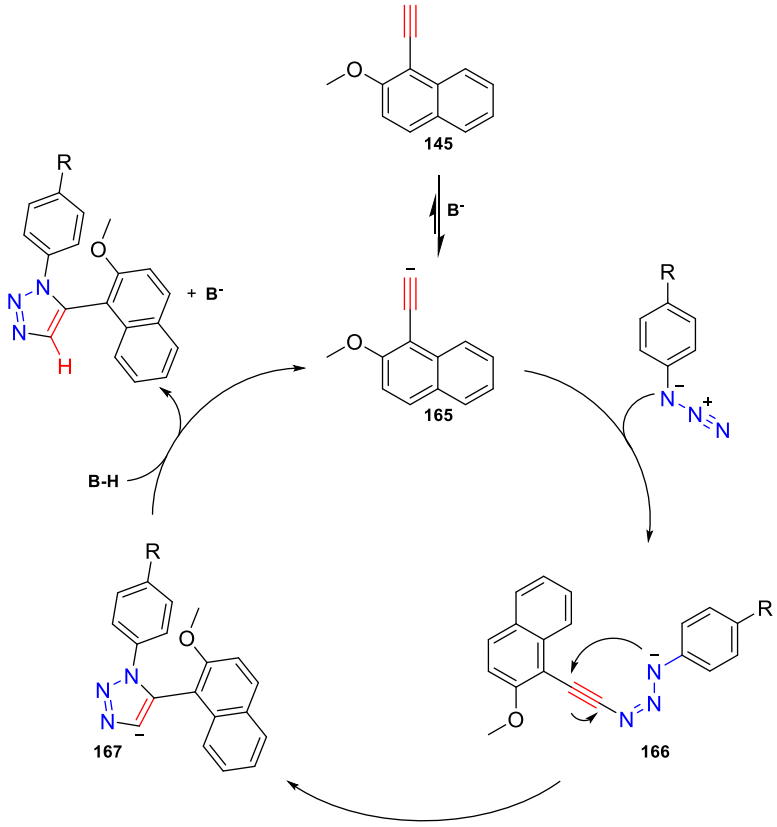

Figure 48. Proposed mechanism for the base-catalysed formation of the 1,5-disubstituted 1,2,3-triazoles.[245]

In terms of the characterisation of the regioisomers, no ^{1}H-^{1}H NOESY correlations can be used to determine the regioisomerism due to the positioning of the triazolic proton (**Figure 49**; highlighted in blue;). However, using the methods outlined by Creary, X. *et al.*, characteristic shifts in NMR were used to distinguish the 1,5-regioisomer from the previously discussed 1,4-regioisomers. Distinctive chemical shifts are observed for the triazolic proton (**Figure 50**; highlighted in BLUE) as well as C_4 (**Figure 50**; highlighted in RED;) when compared to the 1,4-regioisomers as previously discussed in (**Section 3.3.1**). Similarly, by using the resonance structures of the 1,5-regioisomer, these shifts can be readily rationalised (**Figure 49**). In particular, when resonance structure **160A** is obtained the formal negative charge is observed on the N_3 position whilst the formal negative charge resides at C_5 in structure **160B**.

Using the 1,5-regioisomer derivative **160** as an example, this consequently results in the C_4 position exhibiting a greater downfield shift of 135.2 ppm (**Figure 50**; highlighted in RED) than the C_5 of its 1,4-regioisomeric counterpart **146** due to the deshielding it experiences through the adjacent N_3 atom. The characteristic triazolic proton (**Figure 50**; highlighted in BLUE) attached to C_4 is observed at 7.81 ppm. Conversely, the C_5 position of

the 1,5 product is located upfield at 127.6 ppm (**Figure 50**; highlighted in RED). This can be explained by resonance structure **160B** whereby the formal negative charge residing on the C_5 position induces a significant shielding effect when compared to the C_4 position. These correlations were confirmed using ^{1}H-^{1}H NOESY, ^{1}H-^{1}H COSY, ^{1}H-^{13}C HSQC and ^{1}H-^{13}C HMBC NMR (**Appendix A**).

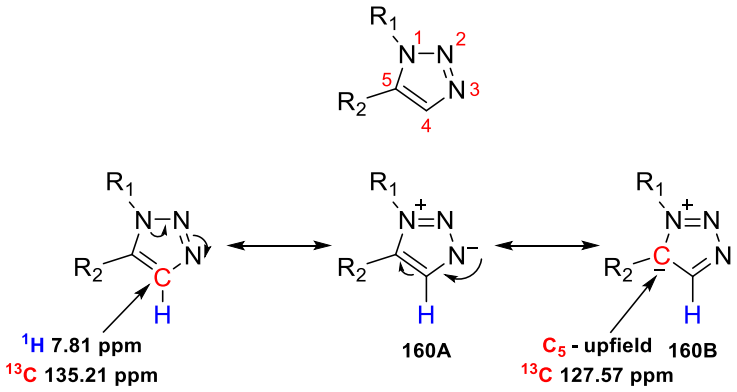

Figure 49. Resonance structures of 1,5-disubstituted 1,2,3-triazoles, using lead derivative **160** chemical shifts as an example. Triazolic proton highlighted in BLUE wih respective C_4 and C_5 highlighted in RED.

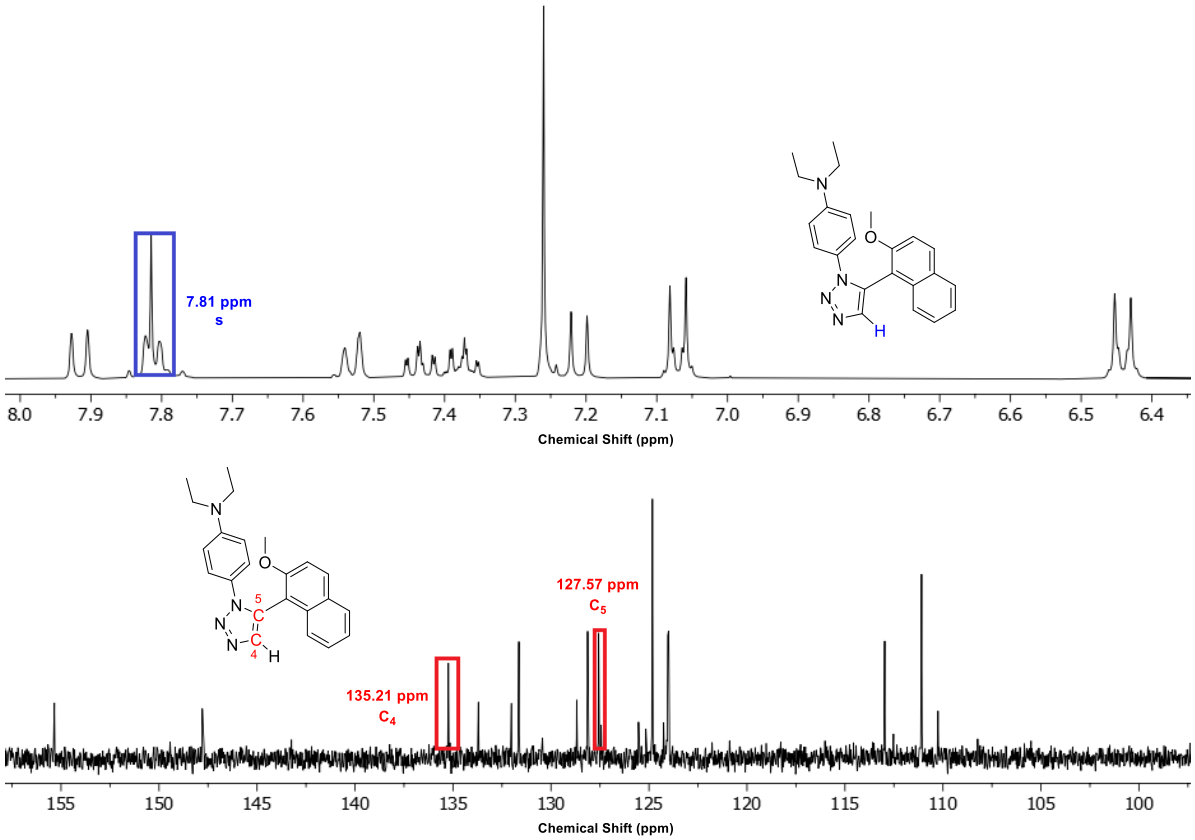

Figure 50. ^{1}H-NMR (400 MHz, $CDCl_3$) and ^{13}C-NMR (101 MHz, $CDCl_3$) spectrum for compound **160**. Characteristic triazolic proton chemical shift is highlighted in BLUE. Respective C_5 chemical shift is highlighted in RED. Multiplicity and integration of each respective chemical shift can be seen in **Chapter 6**. **Full spectral data in Appendix A.**

3.3.3 Synthesis of 4,5-Disubstituted 1,2,3-Triazole

Due to the similarity in spatial geometry, a convergent synthetic approach (**Scheme 9**) towards the lead 4,5-disubstituted 1,2,3-triazole derivative **171** was considered appropriate for comparison to the lead 1,5-regioisomer **160**. To begin with, iodination was considered for the tertiary aniline **168**, which could take place by a standard electrophilic aromatic substitution (S_EAr) to afford the iodinated derivative **169**. Subsequent convergence of **169** with the previously obtained alkyne **145** by Sonogashira coupling would afford the alkyne-linked compound **170**. Lastly, formation of the 4,5-disubstituted 1,2,3-triazole **171** was thought accessible through a radical-based homolytic addition and subsequent cyclisation. Iodination of the tertiary aniline **168** proceeded well when subjected to a mixture of H_5IO_6 / KI in a solution of DCM:H_2O affording **169** in good yield. Reaction of the KI with H_5IO_6 results in an *in situ* formation of molecular iodine (I_2) which can then undergo a S_EAr reaction at the nucleophilic *para*-position of **168**. This reaction is ideal as although I_2 is a versatile reagent, it is extremely corrosive and toxic thus making its use as a reagent undesirable. Therefore *in situ* formation of the I_2 becomes both practically useful and safe. Moving forward with the obtained iodinated tertiary aniline **169**, subjection to standard Sonogashira coupling conditions utilising $Pd(PPh_3)_2Cl_2$ and CuI in Et_3N resulted in the alkyne-linked **170** in good yields.

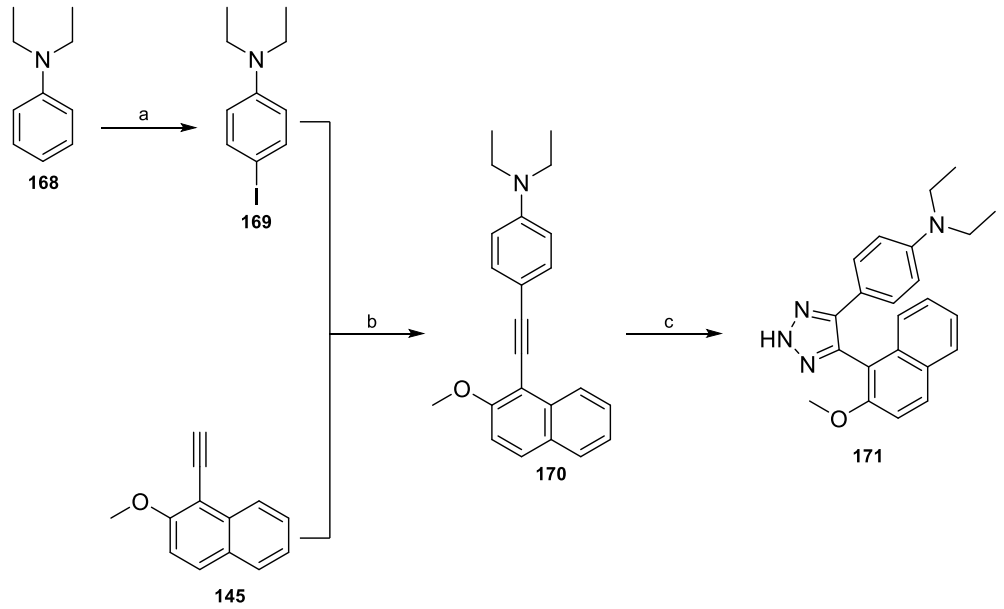

Scheme 9. Convergent synthetic pathway for accessing lead 4,5-disubstituted 1,2,3-triazole derivative **171**. *Reagents and Conditions*: a) H_5IO_6, KI, DCM:H_2O, RT, 1 h, 82% b) $PdCl_2(PPh_3)_2$, CuI, Et_3N, 40 °C, 8 h, 80% c) $(AcO)_2IPh$, NaN_3, MeCN, RT, 6 h, 27%

It is worth noting that both the iodinated derivative **169** and alkyne-linked **170** presented difficulties in purification *via* flash chromatography. Although 1% Et_3N was added to the column eluent used in either case so as to prevent interaction with the hydroxyl groups present within the silica, each derivative demonstrated a level of unwanted contact with the formed silica oxide functionalities. It may be the case that delocalised conjugation of electrons result in a positively charged tertiary amine and thus undesired polar interaction that results in long elution times. Additional attempts to purify the compounds without eluent modification with Et_3N resulted in a similar result. This would be due to tertiary amine unfavourably deprotonating the silica, thereby resulting in a protonated tertiary amine and subsequent undesired interaction with the silica oxide. If necessary, future attempts should review other purification techniques to overcome these issues.

Finally, it was found that Hu, L. *et al.* investigated the synthesis of 4,5-disubstituted 1,2,3-triazoles through an azidyl radical-based pathway.[248] This reaction proceeds through the azidyl radical **175** that is formed through oxidation *via* $(AcO)_2IPh$ (**172**, **Figure 51A**).[248–250] **172** undergoes substitution by two equivalents of N_3^- thereby resulting in the disubstituted product **173**. Homolytic cleavage follows that affords the iodanyl **174** and azidyl **175** radical species. Formation of the 4,5-disubstiuted 1,2,3-triazole radical **176** progresses through a step-wise process after intramolecular homolytic addition of **175** to the alkyne **170** (**Figure 51B**). Hydrogen atom transfer (HAT) from MeCN then affords the protonated triazole **171**. Using the optimised conditions outlined by Hu, L. *et al*, **170** was subjected to a solution of MeCN containing the oxidant $(AcO)_2IPh$ alongside NaN_3 at RT. Consequently this afforded the lead 4,5-disubstituted 1,2,3-triazole derivative **171** in poor yield. Regardless, purification *via* flash chromatography provided the compound in great purity for future *in vitro* assessment.

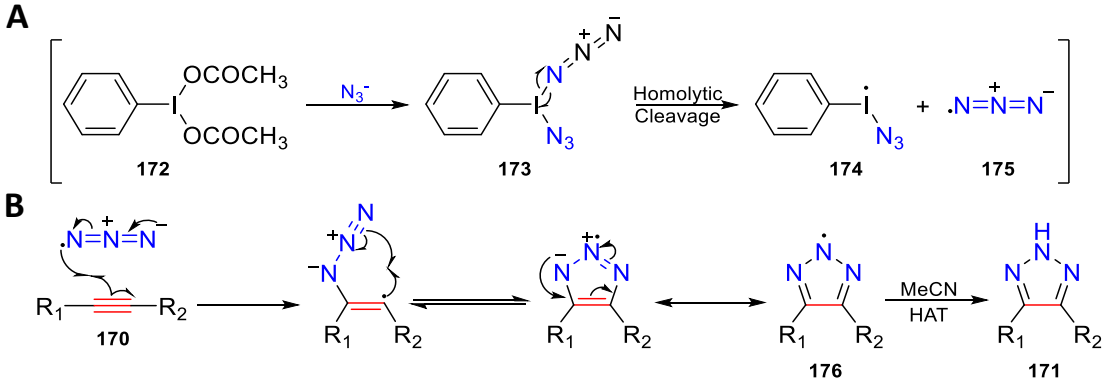

Figure 51. a) Proposed formation of the azidyl radical **175** and; b) mechanism for the formation of the 4,5-disubstituted 1,2,3-triazole **171**.[248–250]

3.4 Synthesis of 1,5-Disubstituted 1,2,3,4-Tetrazole Derivatives

Amide route

As 1,5-disubstituted 1,2,3,4-tetrazoles are a common motif in biologically active materials, it was considered an ideal functionality to pursue. It is found in several structures endemic to β-lactam antibiotics within the cephalosporin scaffold (**177**) as well as anti-hypertensive (**178**), anti-viral (**179**) and anti-tubercular agents (**180**) (**Figure 52**; tetrazole motif highlighted in BLUE).[251] The tetrazole structure has also been demonstrated to show low *in vivo* toxicity.[252] Additionally, greater opportunities for π-stacking or hydrogen bond formation can result due to the density of nitrogens within the ring. This can also result in enhanced metabolic stability leading to a lengthened half-life as well as ideal membrane permeability.[253] These perceived benefits made the exploration of 1,5-substituted 1,2,3,4-tetrazole derivative (**189**, **Scheme 10**) an interesting prospect.

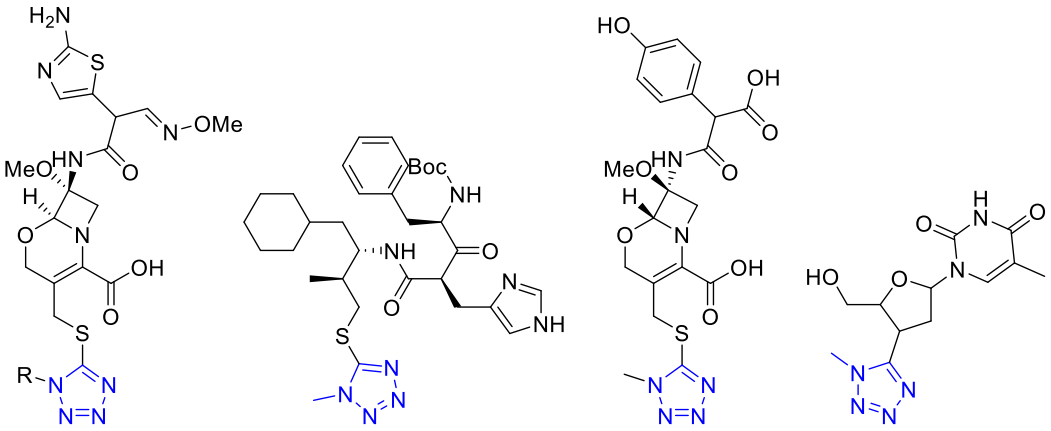

Figure 52. Examples of biologically active molecules containing the 1,5-disubstituted 1,2,3,4-tetrazole motif.[251]

To initially approach the synthesis of the 1,5-disubstituted tetrazole derivatives **189 – 192**, it was envisioned to synthetically proceed through the amides **184 – 188** (**Scheme 10**). This was considered an ideal way to obtain an additional amide linker library that could be compared to the original diazenyl motif alongside the tetrazole chemotype. Evaluating the amide library would indicate if additional non-rigid linkers may be viable. To begin the synthesis of the amides it was thought that the naphthoic acid **181** could be dialkylated under standard conditions to afford the methoxy methyl benzoate **182**. Subsequent hydrolysis of the benzoate would afford the methoxy carboxylic acid **183** that could then be subjected to acid chloride formation and subsequent amide coupling with the aniline derivatives **76**, **85 – 87** and **89**. Lastly, formation of the tetrazole derivatives **189 – 192** could then be afforded by ring

closure proceeding through nitrilium formation (**Figure 54**). Dialkylation of **181** with K_2CO_3 and MeI at reflux afforded the methoxy methyl benzoate derivative **182** in good yield. Ensuing hydrolysis of the benzoate under standard conditions resulted in a quantitative yield of the alkylated carboxylic acid **183**. With **183** in hand, the various aniline derivatives **76**, **85 – 87** and **89** were coupled to the naphthalene tail group *via* acid chloride formation in good yields. In respect to the nitrile derivative **87**, the high electronegativity of the nitrile functionality resulted in an unreactive aniline that did not proceed under the working conditions of the previous derivatives.

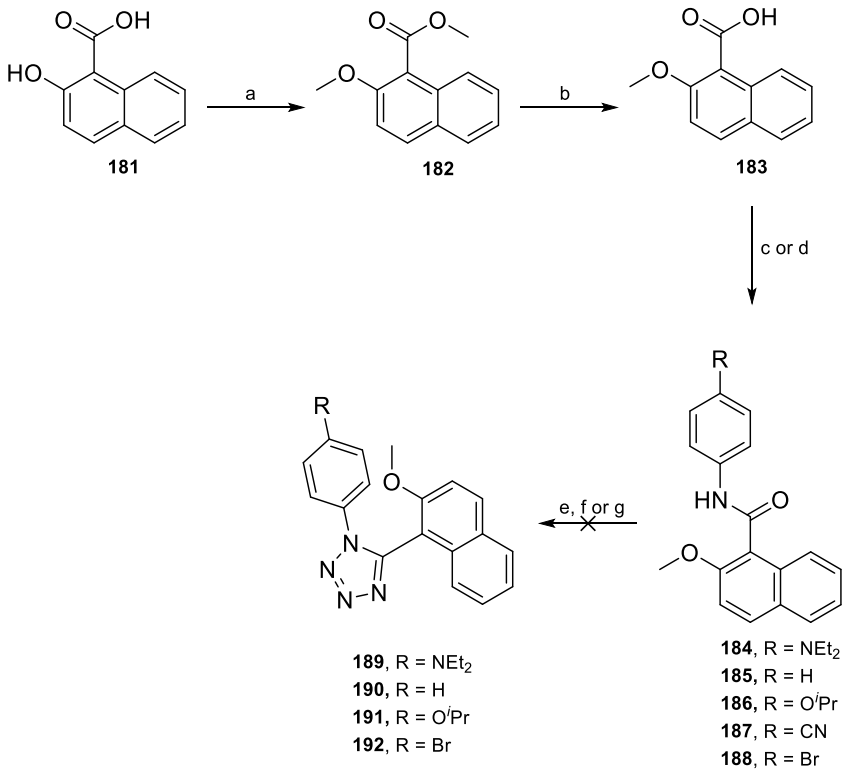

Scheme 10. Attempted synthetic pathway for 1,5-disubstituted 1,2,3,4-tetrazole derivatives **189 – 192**. *Reagents and Conditions*: a) MeI, K_2CO_3, Acetone, 50 °C, 2 h, 84% b) NaOH, MeOH:H_2O, 3 h, 80 °C, quant. c) i. $(COCl)_2$, cat. DMF, DCM, 0 °C – RT, 1 h, ii. **76**, **85** – **87**, **89**, DCM, RT, 4 h, 70 – 86% d) i. $(COCl)_2$, cat. DMF, DCM, 0 °C – RT, 1 h, ii. **87**, DMAC, DCM, RT, 4 h, 42% e) $TMSN_3$, Na_2CO_3, $(CF_3SO_2)_2O$, DCM, -40 °C – RT, 4 h f) $POCl_3$, NaN_3, MeCN, 90 °C, 12 h g) DPPA, 4-picoline, 145 °C, 16 h.

An investigation by Otsuka, R. *et al.* found that use of the latent Brønsted base DMAC as a solvent could aid formation of amides from anilines exhibiting weakly basic or even neutral properties (**Figure 53**).[254] Typically anilines with strongly electron withdrawing substituents exhibit weakly or neutral basic character. It is most likely that a derivative such as **87** does not present sufficient nucleophilicity to progress in this reaction. However, addition of a Brønsted base such as DMAC as a solvent may allow the neutral aniline to be

favoured in formation and allows the reaction to eventuate over time. Nonetheless, this method for coupling of the nitrile derivative **87** was able to proceed, albeit in average yield. It was not considered to make a phenol derivative of the amide derivative of the amide linker as this would require unnecessary protection steps and it was considered more pertinent to assess more synthetically accessible derivatives before a more diverse library was established.

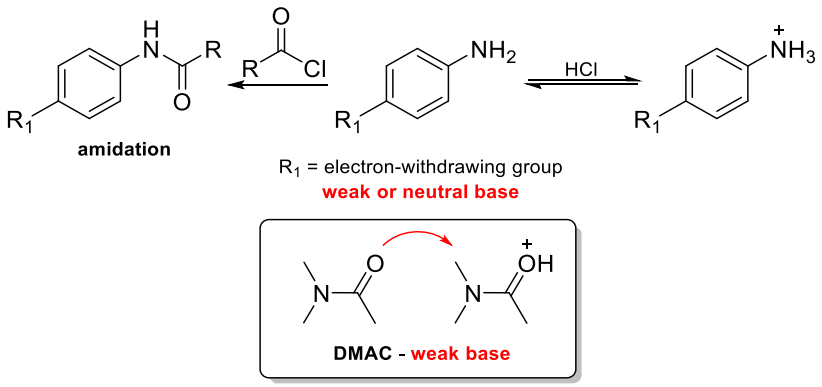

Figure 53. Proposed mechanism for DMAC-assisted amide formation.[254]

To progress forward to the tetrazole moiety, cyclisation was attempted on derivatives **185** and **186** under several conditions (**Table 9**). Unfortunately none of these conditions gave the desired tetrazole derivative. It should be noted that all the following methodologies appear to advance through a nitrilium-based intermediate **194** (**Figure 54**) although through different reagents. Formation of the iminium ester **193** proceeds by nucleophilic attack of the secondary amide carbonyl on a leaving group (LG), in this case OTf, Cl or DPP based on the reagent used. Removal of the iminium proton subsequently releases the oxygenated leaving group LGO^-, resulting in the nitrilium ion **194**. An ensuing [3+2] cycloaddition with a source of azide then results in the desired 1,5-disubstiuted 1,2,3,4-tetrazole.

Initially conditions reported by Li, L. H, *et al.* that demonstrate multinitrogenation of amides *via* [3+2] cycloaddition were trialled on the isopropoxy derivative **186** (**Table 9, Entry 1**).[255] The isopropoxy derivative **186** was initially trialled under these conditions because the scope of the paper did not demonstrate formation of a tetrazole that had any anilines present on the phenyl ring. After complete consumption of the starting materials, the significant products of the reaction were isolated *via* flash chromatography even though a complex mixture was observed. Upon assessment of the primary product *via* ESI-MS, a positive 376 *m/z* was observed alongside a 398 *m/z* with an Na^+ adduct. Conversely a negative

374 *m/z* peak could also be seen; indicating the primary material to have a 375 *m/z*. Unfortunately, this compound could not be identified *via* ^{1}H NMR as it was not discernable even after purification. Additionally the obtained *m/z*'s did not match any of the potential intermediates that resulted from the reaction (**Figure 55**). In fact, one isolated product of the reaction appeared to only contain the lower 2-methoxynaphthalene tail group. In any case, it was decided to move forward to trial additional reaction conditions.

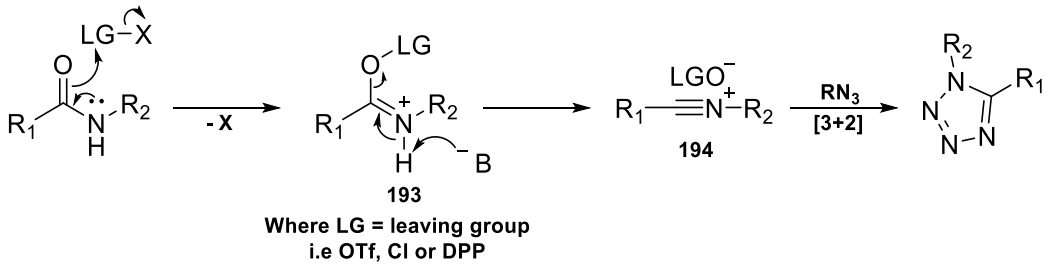

Figure 54. Proposed general mechanism for formation of nitrilium intermediate **194** and subsequent [3+2] cycloaddition to form 1,5-disubstituted 1,2,3,4-tetrazoles.[251,255]

Table 9. Reaction conditions trialled and subsequent results to obtain 1,5-disubstituted 1,2,3,4-tetrazoles **189** and **190**.

Entry	Reaction Conditions	Result
1	**186**, $TMSN_3$, Na_2CO_3, $(CF_3SO_2)O_2$, DCM, -40 °C – 90 °C	Complex mixture
2	**186**, $POCl_3$, NaN_3, MeCN, 90 °C	Complex mixture
3	**185**, $POCl_3$, NaN_3, MeCN, 90 °C	Complex mixture
4	**185**, DPPA, 4-picoline, 145 °C	No reaction

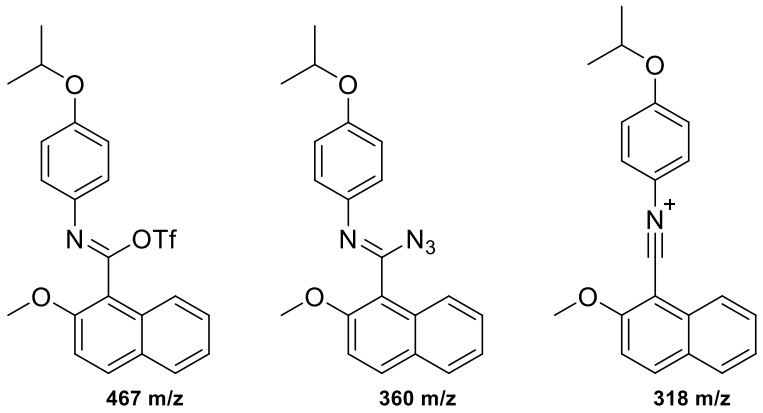

Figure 55. Potential reaction intermediates from attempted conversion to 1,5-disubstituted 1,2,3,4-tetrazole derivative **191**.[255]

Recently it had been reported by Keegan, B. *et al.* that the Hsp90-Aha 1,5-disubstituted tetrazole **66** (**Chapter 1.6.1**, **Figure 26**) was afforded through [3+2] cycloaddition of KU177 derivative **48** (**Chapter 1.6.1**, **Figure 23A**).[196] Using the reported methodology, the derivative **186** was again used for comparison to the original trial (**Table 9**, **Entry 2**). Treating the compound with $POCl_3$ and NaN_3 in a solution of MeCN at 90 °C resulted in a complex mixture being formed with full consumption of the starting material. However upon isolation of the products *via* flash chromatography, assessment of the materials by ^{1}H NMR found no discernible peaks indicating complete degradation of the derivative **186**. Furthermore, no products could be observed when analysed by ESI-MS. To evaluate whether this was a result of the electron donating properties of the isopropoxy substituent on the head group, the more neutral derivative **185** was trialled (**Table 9**, **Entry 3**). Similarly to previously trialled conditions a complex mixture was obtained on which isolation of the materials yielded unidentifiable ^{1}H-NMR spectra that implied degradation of the starting material. This result ruled out the possibility of the head group substituent playing a role in the result of the reaction. It is most likely the case that the conditions were too harsh, thereby leading to the degradation observed. Therefore, it was decided to attempt a new set of conditions in another effort to access the tetrazole derivatives.

An investigation by Ishihara, K. *et al.* evaluated the use of DPPA derivatives in pyridine-based solvents as an effective method for the formation of 1,5-disubstituted tetrazole species from secondary amides.[256] It was demonstrated that optimised conditions using either *p*-NO_2DPPA in pyridine or DPPA in 4-picoline afforded equivalent yields albeit at marginally different temperatures. Due to the accessibility of DPPA and 4-picoline, it was decided to trial the conditions on derivative **185** at 145 °C (**Table 9**, **Entry 4**). The use of the

relatively neutral phenyl headgroup would rule out the role of substituent effects if degradation was observed. Additionally, the scope reported by the authors did not assess secondary amides containing a substituted phenyl ring on either end of the amide motif. [256] This would allow for a better comparison to the results reported. In any case, no reaction was detected after a period of 16 h. Although undesirable, it indicates temperature-related degradation was not causative of the results seen in previous attempts.

Nitrile route

Due to the limited success seen in conversion of the amide derivatives to the tetrazole moiety, an alternative synthetic pathway was considered to afford the lead 1,5-disubstiuted 1,2,3,4-tetrazole derivative **189** (**Scheme 11**). Although it is possible to couple organic azides and nitriles through a [3+2] cycloaddition to afford the desired 1,5-disubstituted tetrazoles, this cycloaddition progresses at a rate that is synthetically ineffective.[251,257,258] Moreover, the scope of this reaction is limited due to the necessity of nitrile substrates to exhibit highly electron withdrawing moieties, allowing the nitrile to react as a dipolarphilic substrate.[251,257] Such examples include CF_3, C_3F_7, CCl_3 or other similar strongly electron withdrawing functionalities.[251]

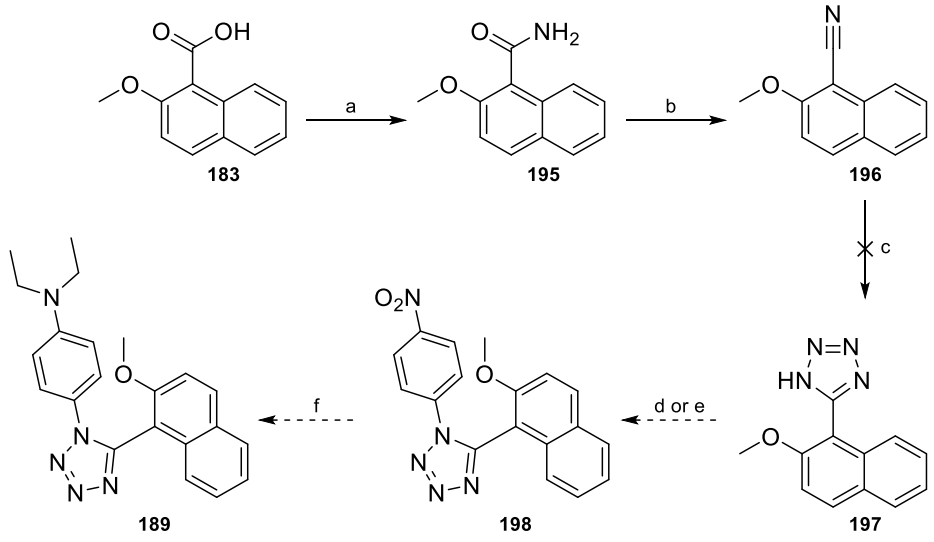

Scheme 11. Alternative synthetic pathway to access lead 1,5-disubstituted 1,2,3,4-tetrazole derivative **189**. *Reagents and Conditions*: a) i. $(COCl)_2$, cat. DMF, DCM, 0 °C – RT, 1 h, ii. 25% NH_4OH, DCM, 0 °C – RT, 1 h, quant. b) $POCl_3$, 1,2-dichloroethane, 80 °C, 3 h, 83% c) NaN_3, NH_4Cl, DMF, 120 °C d) NaH, **74**, THF, 70 °C, not attempted e) 4-iodonitrobenzene or 4-bromonitrobenzene, $Pd(dba)_2$, Xantphos, 2 M NaOH, Toluene, 110 °C, not attempted f) H_2, Pd/C, EtOAc, RT, not attempted f) EtI, K_2CO_3, Acetone, 50 °C, not attempted.

Conversely, formations of 1*H*-tetrazoles with azide salts presents a wider scope of nitriles that can act as capable dipolarophiles.[257,258] As such, it was envisioned to form the free

1*H*-tetrazole **197** on the lower naphthalene moiety which could then be subsequently coupled to the head group (**Scheme 11**). To approach the synthesis the previously synthesised carboxylic acid **183** could be used to form the required primary amide **195**. Dehydration of the primary amide **195** would then provide the nitrile derivative **196**, which could be converted to the 1*H*-tetrazole motif containing intermediate (**197**). Coupling to a nitrobenzene derivative to form the 1,5-disubstituted tetrazole **189** may be achieved through a S_NAr with **74**. Alternatively, a Buchwald-Hartwig reaction using either 4-iodo or 4-bromonitrobenzene could be a viable pathway to installation of the 4-nitrobenzene motif to the tetrazole scaffold. Subsequent reduction followed by dialkylation would then afford the lead 1,5-disubstituted tetrazole **189**.

The carboxylic acid **183** was treated with oxalyl chloride in DCM alongside cat. DMF to afford the acid chloride that subsequently underwent amidation with 25% NH_4OH solution. This resulted in the desired primary amide **195** in quantitative yield. Transformation of the amide **195** to the respective nitrile **196** *via* dehydration required several methods to be trialled to achieve a desirable yield (**Table 10**). It has been demonstrated by Ding, R. *et al.* that methodology involving a catalytic Swern oxidation is a viable pathway to formation of nitriles from primary amides.[259] It has been proposed that this mechanistically proceeds by a chloridimethylsulfonium chloride intermediate that leads to the formation of the nitrile in a similar manner to the nitrilium formation previously shown in **Figure 54**.[259] As such this was the initial method trialled in attempt to form the desired nitrile compound (**Table 10**, **Entry 1**). Following the reported optimised methodology, treatment of the amide **195** with $(COCl)_2$ alongside cat. DMSO and Et_3N in MeCN afforded **196** in a poor yield albeit as a clean reaction. Additional $(COCl)_2$, Et_3N or DMSO did not progress the reaction forward. As a result, an alternative method was sought that may provide a more ideal yield.

It has been reported by Rana, A. *et al.* that triflic anhydride can encourage the conversion of primary amides to their respective nitriles.[260] Treatment of the amide **195** with triflic anhydride as described by the optimised method proceeded in limited capacity, affording the nitrile in modest yield (**Table 10**, **Entry 2**). Although only noted to be required for highly electron withdrawn substrates, addition of Et_3N to aid the reaction at 0 °C did not appear to advance the reaction nor substantially improve the yield obtained. Nevertheless, this method did not prove satisfactory in providing an ideal amount of material for continuation. Finally, Trampota, M. and Murphy, R. B. described the conversion of primary

cubane-derived amides to their respective nitriles in excellent yields with quick reaction times utilising $POCl_3$ in 1,2-dichloroethane.[261] Due to the proposed efficiency of both the reaction rate and output, this was considered to be an ideal methodology to trial. Subjecting the amide **195** to the reported conditions afforded the desired nitrile **196** in great yield (**Table 10**, **Entry 3**). Furthermore, the reaction took place within 1 h and exhibited clean conversion of the starting material to the desired nitrile product **196**.

Table 10. Reaction conditions trialled and subsequent results to afford the nitrile derivative **196**.

Entry	Reaction Conditions	Result
1	**195**, $(COCl)_2$, 1 mol % DMSO, Et_3N, MeCN, RT	10% yield
2	**195**, $(CF_3SO_2)O_2$, DCM, 0 °C – RT	27% yield
3	**195**, $POCl_3$, 1,2-dichloroethane, 80 °C	89% yield

With the nitrile **196** in hand, synthetic conversion to the 1*H*-tetrazole **197** was attempted by treatment of the compound with an azide salt. Previously Sharon, A. *et al.* have demonstrated synthesis toward a library containing 1*H*-tetrazole motifs within their scaffolds.[262] Using the method as detailed, the nitrile **196** was subjected to a solution of NaN_3, NH_4Cl and DMF at 120 °C (**Scheme 11**). In this circumstance NH_4Cl acts as a protic ammonium salt of the azide, thus providing a competent azide donor for the reaction to occur.[257] Monitoring the reaction *via* TLC indicated complete conversion of the starting material to a new primary product. Notably there were no additional by-products present within the reaction mixture and upon purification *via* flash chromatography afforded a material that indicated formation of the 1*H*-tetrazole **197** by NMR (**Figure 56** and **Figure 57**). Comparing the ^{1}H-NMR between the nitrile (**Figure 56**; key chemical shifts highlighted in BLUE) and obtained product (**Figure 56**; key chemical shifts highlighted in RED), very clear chemical shifts between the two can be observed. The doublet at 8.10 ppm and the doublet

residing at 7.27 ppm (H_a and H_b, respectively, **Figure 56**; highlighted in BLUE) can be observed to shift to 8.03 ppm and 7.19 ppm, respectively (H_a and H_b, respectively, **Figure 56**; highlighted in RED). This clearly indicates that a new motif has been furnished, thus affecting the position of the peaks and initially suggested installation of the tetrazole moiety. These correlations were confirmed by ^{1}H-^{1}H COSY and ^{1}H-^{1}H NOESY NMR.

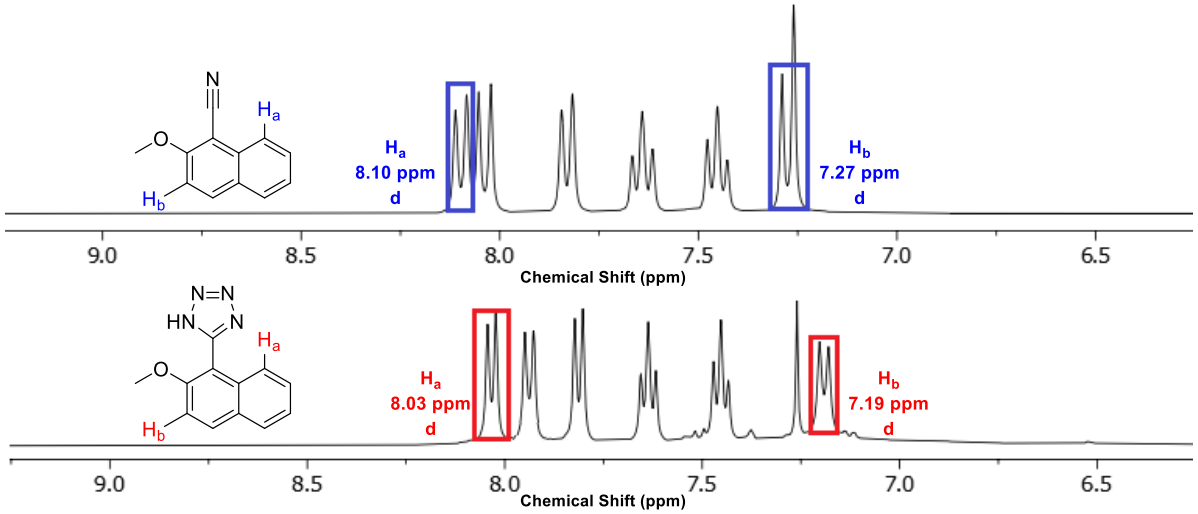

Figure 56. ^{1}H-NMR (300 MHz, $CDCl_3$) spectrum for compound **196** and ^{1}H-NMR (400 MHz, $CDCl_3$) spectra for suspected compound **197**. Key ^{1}H chemical shifts for **196** are highlighted in BLUE. Respective ^{1}H chemical shifts for suspected compound **197** are highlighted in RED. **Full spectral data in Appendix A**.

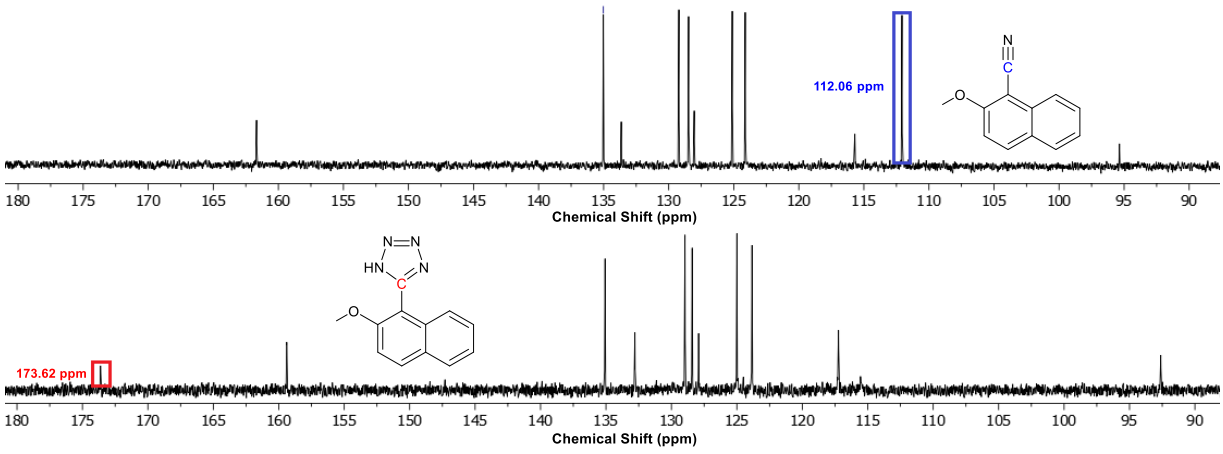

Figure 57. ^{13}C-NMR (75 MHz, $CDCl_3$) spectrum for compound **196** and ^{13}C-NMR (101 MHz, $CDCl_3$) spectra for suspected compound **197**. Key ^{13}C chemical shift for **196** is highlighted in BLUE. Respective ^{13}C chemical shift for suspected compound **197** are highlighted in RED. **Full spectral data in Appendix A**.

Additionally, ^{13}C-NMR of the nitrile presents a clear chemical shift at 112.1 ppm for the nitrile carbon (**Figure 57**; highlighted in BLUE). Conversely, the obtained product exhibits a new carbon chemical shift at 173.6 ppm (**Figure 57**; highlighted in RED) with no correlated nitrile peak to be observed. This is consistent with the highly deshielded nature of

the tertiary 1*H*-tetrazole carbon environment due to the electronegativity of the adjacent nitrogen atoms within the ring (**Figure 57**; highlighted in RED). However neither ^{1}H or ^{13}C NMR indicate the presence of a methoxy peak in the suspected **197** compound. This is unexpected as these reactions conditions would not be associated with the removal of a methoxy functionality. Additionally the major spot was observed to have a negative 473 *m/z* when assessed by atomic pressure mass spectrometry (APCI-MS) whilst assessment through ESI-MS did not detect a signal. Although consideration of dimer formation was initially proposed, this product would form a 452 *m/z* alongside a 487 *m/z* with a Cl^- adduct. This indicates the desired material was not able to be detected within the sample and unfortunately the material obtained could not be identified. Due to time restrictions, additional methodologies were not able to be trialled to obtain **197**. Such approaches that could be investigated include metal-catalysed formation using $Al_2(SO_4)_3$, $ZnBr_2$ or $CuSO_4$ alongside azide salts.[258,263,264]

3.5 Synthesis of 3,5-Disubstituted Pyrazole and Isoxazole Derivatives

Propynone route

Due to the bioisosterism both 3,5-disubstiuted pyrazole and isoxazole motifs exhibit in relation to the diazenyl scaffold, these structures were proposed as interesting linkers to explore. In approaching the synthesis of the 3,5-disubstituted pyrazole and isoxazole derivatives, it was speculated that formation of the mutual propynone intermediate **203** (**Scheme 12**) could be used to afford both scaffolds. To obtain the intermediate **203** an initial trialkylation of the amino benzoic acid **199** would afford the tertiary amino ethyl benzoate **200**. This could undergo subsequent hydrolysis to the respective benzoic acid **201**. Coupling of the previously synthesised alkyne **145** could then be conducted following conversion of the acid **201** to an acid chloride (**202**) *via* Sonogashira conditions or a standard substitution to afford the desired intermediate **203**. Lastly, addition of hydrazine to **203** and subsequent cyclisation would result in the formation of the 3,5-disubstituted pyrazole **204.** Conversely the treatment of **203** with hydroxylamine can lead to formation of both regioisomeric 3,5-disubstituted isoxazoles **205** and **206**.

To begin with the amino benzoic acid **199** successfully underwent trialkylation in a solution of EtI, K_2CO_3 and acetone at reflux to afford the tertiary amino ethyl benzoate **200** in good yield. Ensuing hydrolysis of the benzoate with NaOH in EtOH:H_2O yielded the respective benzoic acid **201** in quantitative yield. Conversion to the acid chloride **202** by

treatment with $(COCl)_2$ with cat. DMF in DCM appeared successful when assessed by TLC upon mini workup with MeOH to observe the methyl benzoate formation. As outlined above, coupling of the previously obtained alkyne **145** to the acid chloride to afford the desired propynone intermediate **203** can be potentially achieved by two paths. Substitution of acid chloride motifs with acetylene functionalities *via* Sonogashira coupling conditions has been extensively covered in the literature.[265–267] Additionally it has been demonstrated that use of *n*-Buli as a strong base to deprotonate **145** can promote nucleophilic substitution onto an acid chloride.[268]

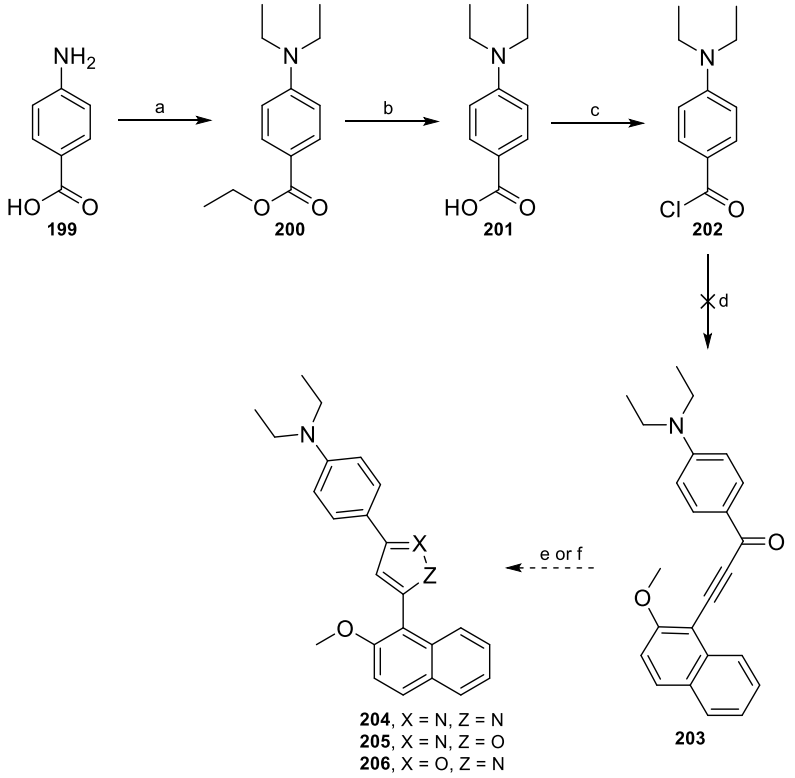

Scheme 12. Synthetic pathway to achieve lead 3,5-disubstituted pyrazole and isoxazole derivatives *via* propynone linker intermediate **203**. *Reagents and Conditions*: a) EtI, K_2CO_3, Acetone, 50 °C, 2 h, 74% b) NaOH, EtOH:H_2O, 80 °C, 3 h, quant. c) $(COCl)_2$, cat. DMF, DCM, 0 °C – RT d) conditions outlined in **Table 11** e) N_2H_4•H_2O, Toluene, 80 °C, not attempted f) KOH, $NH_2OH.HCl$, MeOH:H_2O, RT, not attempted

Both conditions were trialled (**Table 11**) in attempts to obtain the propynone linker **203**. It has been described by Zheng, S. C. *et al.* that standard Sonogashira conditions can be used for the coupling of **145** to **121** in high yields.[266] Following the reported conditions, the acid chloride **202** was treated with $Pd(PPh_3)_2Cl_2$, CuI and Et_3N in a solution of THF (**Table 11**, **Entry 1**). After allowing the reaction to stir for 30 mins, addition of the alkyne then followed and proceeded at room temperature. After several hours, monitoring *via* TLC resulted in no observed reaction between the materials. Gradually the temperature was raised to 40 °C but

no consumption of starting materials was seen by TLC. Finally the reaction was brought to 80 °C and allowed to react overnight; however, no further progression was detected. As the alkyne **145** has previously been coupled to the iodinated tertiary amine **169** (**Section 3.3.3**) under similar conditions in high yield, it was not perceived that the alkyne **145** was unable to partake in the necessary copper cycle of the Sonogashira reaction. In this case the role of the copper substrate provides the capacity to increase the acidity of the acetylide proton *via* coordination.[269] This allows for Et_3N to successfully deprotonate **145**. Because the coupling of **145** to the iodinated aniline **169** proceeded well, this would rule out the inability of the Et_3N to favourably deprotonate **145** and impede the reaction. Although one would expect the acid chloride substrate to be electrophilic enough to undergo oxidative addition to the active Pd-species, it may be the case that the substantial electron donating effect presented by the tertiary amine leads to the oxidative addition being unable to proceed. In this case, it was decided to pursue *n*-BuLi promoted nucleophilic substitution of the acid chloride.

Table 11. Reaction conditions trialled and subsequent results to afford the propynone intermediate **203**.

Entry	Reaction Conditions	Result
1	**145**, **202**, $Pd(PPh_3)_2Cl_2$, CuI, Et_3N, THF, RT – 80 °C	No reaction
2	1. **145**, n-BuLi, THF, –78 °C – RT 2. **202**, THF, –78 °C – RT	No reaction

Substitution of the alkyne **145** onto the acid chloride **121** has been previously reported by Heller, B. *et al.* through an *n*-BuLi mediated synthesis.[268] Following the methodology as detailed, **145** was treated with *n*-BuLi in THF at -78 °C and gradually allowed to come to room temperature (**Table 11**, **Entry 2**). Assessment of the conversion *via* mini workup with **202** found no indication of deprotonation at the acetylene. Leaving the reaction to stir for several more hours at room temperature again resulted in no observation of successful deprotonation or formation of the **203** coupled product. To assess if additional *n*-BuLi was required, the reaction was cooled back down to -78 °C and another equivalent of the reagent added. Upon assessment at room temperature and after stirring overnight, no deprotonation or reaction with **202** was observed. Because of the highly sensitive, basic and nucleophilic

nature of *n*-BuLi, use of an alternative solvent that may increase the acidity of the acetylene proton, such as DMSO (as discussed in **Section 3.3.2**) was not viable.

1,3-Diketone route

Due to difficulties encountered in attempting synthesis toward the propynone linker **203**, an alternative synthetic route was sought. It has been well-reported that synthesis of both 3,5-disubstituted pyrazoles and isoxazoles can be effectively obtained through 1,3-diketone intermediates such as **209** (**Scheme 13**).[270–279] This intermediate would be a mutual precursor to both chemotype scaffolds much like the previous propynone motif. It was envisioned that this key intermediate could be obtained by subjecting the previously attained ethyl benzoate **200** and ketone **105** to a Claisen condensation reaction. Alternatively switching of the ketone and benzoate functionalities between the head and tail motifs was thought also capable to afford the desired intermediate **209**. As such, both pathways were trialled (**Table 12**) in attempts to obtain the 1,3-diketone **209**.

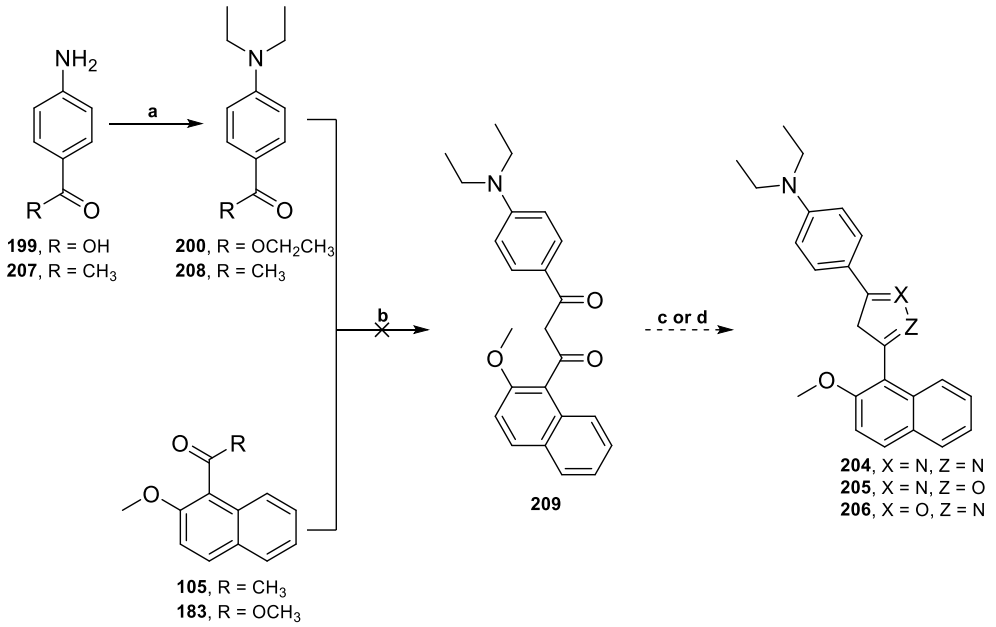

Scheme 13. Synthetic pathway to achieve lead 3,5-disubstituted pyrazole and isoxazole derivatives *via* 1,3-diketone intermediate **209**. *Reagents and Conditions*: a) EtI, K_2CO_3, Acetone, 50 °C, 74 – 86% b) NaH, THF, 80 °C c) N_2H_4•H_2O, EtOH:H_2O, 80 °C, not attempted d) KOH, NH_2OH.HCl, EtOH:H_2O, 80 °C, not attempted

Table 12. Reaction conditions trialled and subsequent results to afford the 1,3-diketone intermediate **209**.

Entry	Reaction Conditions	Result
1	1. **105**, NaH, THF, 0 °C – RT 2. **200**, THF, RT – 80 °C	No reaction
2	1. **208**, NaH, THF, 0 °C – RT 2. **183**, THF, RT – 80 °C	Complex mixture

The previously synthesised ketone **105**, was dissolved into a solution of THF, treated with NaH and allowed to stir for 1 h to provide the deprotonated species (**Table 12**, **Entry 1**). Following addition of the ethyl benzoate **200** the reaction was brought to reflux and monitored *via* TLC. However, no reaction was observed after extended reaction time. To ensure **105** had sufficiently deprotonated, an additional equivalent of NaH was supplemented to the reaction but no further progress was detected. In this case it is most likely that the benzoate **200** does not present ideal electrophilicity to undergo nucleophilic attack due to the substantial electron donating capacity the residing tertiary amine exhibits. Therefore, it was decided to swap the functionalities between the motifs as it was speculated that the electron donating effect of the tertiary amine may help to promote the Claisen condensation.

As the benzoate **183** had been previously synthesised, only additional synthesis to obtain the complementary acetophenone **208** was required. This could be readily afforded by dialkylation under standard conditions of **207** to furnish **208** in great yield. In a similar manner to the previous attempt the acetophenone **208** was treated with NaH in THF and allowed to stir to provide the deprotonated species (**Table 12**, **Entry 2**). Following addition of the benzoate **183** the solution was brought to reflux. Again no reaction was observed when left to react overnight. However, complete degradation of the materials was observed after 24 h. Interestingly no UV active spots could be detected by TLC under shortwave UV (254 nm) but a complex mixture could be seen under long wave UV (365 nm) thereby indicating the potential formation of significantly larger molecular structures. Although the initial absence of a reaction occurring could be attributed to insufficient electrophilic character at the benzoate position of **183**, subsequent formation of long wave active UV molecules may be due to the instability of **208**. Upon assessment, the molecule demonstrates the formation of degradative products *via* TLC when stored on the shelf under normal conditions after 24 h. Furthermore, the compound visually indicates degradation as it shifts from a clear yellow

crystalline solid to a dark brown solid within this period. As such it is most likely that the natural degradative products formed over this period reacted with the benzoate to form undesired by-products of the reaction. It is unfortunate that the 1,3-diketone intermediate **209** was unable to be obtained and therefore the 3,5-disubstituted chemotypes were not able to be realised. Regrettably due to time constraints additional pathways were not able to be explored that may afford the desired molecules.

In retrospect using the electron deficient nitro moiety in place of the tertiary amine functionality on the compounds **122** or **210** (**Figure 58**) would most likely provide a more favourable outcome in affording the desired molecules. For example, use of the respective 4-nitro acid chloride **122** might allow more favourable oxidative addition to occur under Sonogashira conditions. This would afford a nitrated propynone linker that can be subsequently converted to the desired chemotypes. Additionally, the acid chloride could undergo nucleophilic substitution by the acetyl position of **105** to provide a nitrated 1,3-diketone intermediate. The corresponding nitro benzoate **210** also may provide the desired precursor under Claisen conditions with **105**.

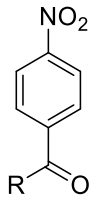

122, R = Cl
210, R = OCH_3

Figure 58. Nitro-containing derivatives **122** or **210** that may afford the desired chemotypes in future attempts.

3.6 Concluding remarks

Several chemotypes succeeding the lead diazenyl scaffold have been synthetically achieved; their synthetic approaches described and their relevant characterisations discussed within this chapter. In particular, these chemotypes have replaced the metabolically liable diazenyl motif with a rigid 5-membered ring structure thus eliminating the *cis*- and *trans*-isomerism exhibited in the original scaffold. Additionally, this has removed the diazenyl-hydrazone tautomerism discussed in **Chapter 2.2.3**. Examples include the lead 1,5-disubstiuted pyrazole (**118**), 1,4- and 1,5-regioisomeric 1,2,3-triazoles (**146** and **160**, respectively) as well as a 4,5-disubstiuted 1,2,3-triazole motif (**171**). Where synthetically applicable, various structural derivatives have also been established so as to provide

additional SAR information when evaluated for activity in future *in vitro* studies. Additionally an amide-linked framework and associated library was developed and synthesised.

Although they were not obtained, a diverse range of synthetic pathways and associated difficulties have been comprehensively reported towards achieving the 1,5-disubstituted 1,2,3,4-tetrazole motif (**189**) as well as the 3,5-disubstiuted pyrazole and isoxazole functionalities (**204 – 206**). These may assist future attempts in affording these desired chemotypes. Unfortunately, biological assessment was not carried out for the novel derivatives outlined within this chapter due to the complications noted in **Chapter 2.3.3** for the ThT assay nor their activity on the Aha1-Hsp90 complex due to accessibility issues.

Chapter 4:

Investigation of Naphthalene Group

Chapter 4: Investigation of Naphthalene Group

4.1 Introductory Remarks

Lipophilicity is an integral physicochemical parameter that can be altered so as to modulate various characteristics such absorption, distribution and pharmacological response *in vivo*. These variables affect both the solubility and permeability of a drug.[280,281] However, a balance between aqueous solubility and membrane permeability must be found for a drug candidate to succeed. Due to the highly lipophilic nature of the diazenyl compounds explored in **Chapter 2**, it was of interest to explore structural changes at the tail-end of the scaffold that would confer desirable hydrophilic properties. The bicyclic naphthalene moiety accounts for a substantial portion of the hydrophobic character exhibited by the lead scaffold (**52**; **Figure 59**). Therefore this motif provides an ideal site for adjusting the lipophilic nature of the overall framework. Variance in size and length of alkyl groups is a conventional method for modulating this physicochemical property. Replacement of the bicyclic naphthalene with a monocyclic phenol is therefore proposed. This allows additional evaluation for the necessity of a bicyclic moiety within the scaffold. Previously it has been suggested that indole is a bioisostere of the naphthalene moiety and has been described as a privileged structure for drug development.[282–284] Implementation of this motif would allow removal of a carbon atom while introducing a hydrogen bonding functionality. Investigation and application of the synthetic approaches to achieve these substitutions are discussed herein.

Chapter Aims

To conclude the investigations outlined within the thesis, this chapter presents the synthetic approaches to substitutions made at the naphthalene group residing on the tail-end of the lead diazenyl compound **52** (**Figure 59**). It was considered pertinent to assess the importance of a bicyclic entity as well as remove the metabolically liable phenolic moiety, whilst improving hydrophilic properties. Therefore both phenol and indole substitutions (**211** and **212**; **Figure 59**) were proposed and synthesised to achieve these goals. Additionally, a methylated derivative of the monocyclic derivative (**212**; **Figure 59**) was synthesised to directly compare the effect of tautomerisation at the target to the lead diazenyl molecule **52** and lead alkylated diazenyl **73**. Unfortunately, biological assessment was not carried out for the novel derivatives outlined within this chapter due to the complications previously addressed in **Chapter 2** for the ThT assay nor their activity on the Aha1-Hsp90 complex.

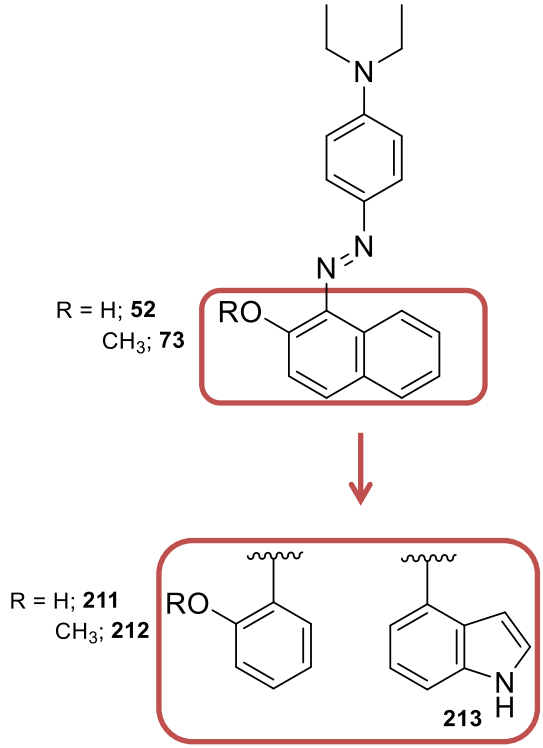

Figure 59. Lead candidate **52** and the proposed substitutions to replace the naphthalene tail group.

4.2 Synthesis of 2-((4-(Diethylamino)phenyl)diazenyl)phenol

To determine the necessity of a bicyclic moiety on the tail group, the monocylic phenol **211** was synthesised. Initial approach to the synthesis of the phenol derivative **211** was envisioned through an *in situ* diazonium coupling protection and deprotection strategy of the phenol **214** (**Scheme 14**). Because of the differing pK_a of the phenolic (pK_a ~ 10, calculated in MarvinSketch)[285] and aniline (pK_a ~ 4.5, calculated in MarvinSketch)[285] functionalities of 2-aminophenol, it was perceived there would be difficulties in pursuing a direct *in situ* diazonium coupling with **168** to afford **211**. At an alkaline pH the phenolic moiety would be deprotonated whilst in an acidic environment the aniline would be protonated. In either case this would affect the ability of the reaction to proceed. This was able to be overcome by utilising **214** through installation of a phenyl sulfonate moiety to the phenolic position. Subjecting **214** to $PhSO_2Cl$ in neat pyridine at RT afforded the sulfonate protected derivative **215** in good yields. Subsequent reduction of the nitro moiety to the respective aniline **216** was pursued under standard conditions, resulting in quantitative yield. Due to the greatly electron donating capacity of the tertiary amine moiety of **168**, it was considered that it may be reasonable to afford the protected diazenyl phenol **217** by means of nucleophilic substitution *via* the *para*-position. In fact, this has previously been reported by Griffiths and Thomasson.[286]

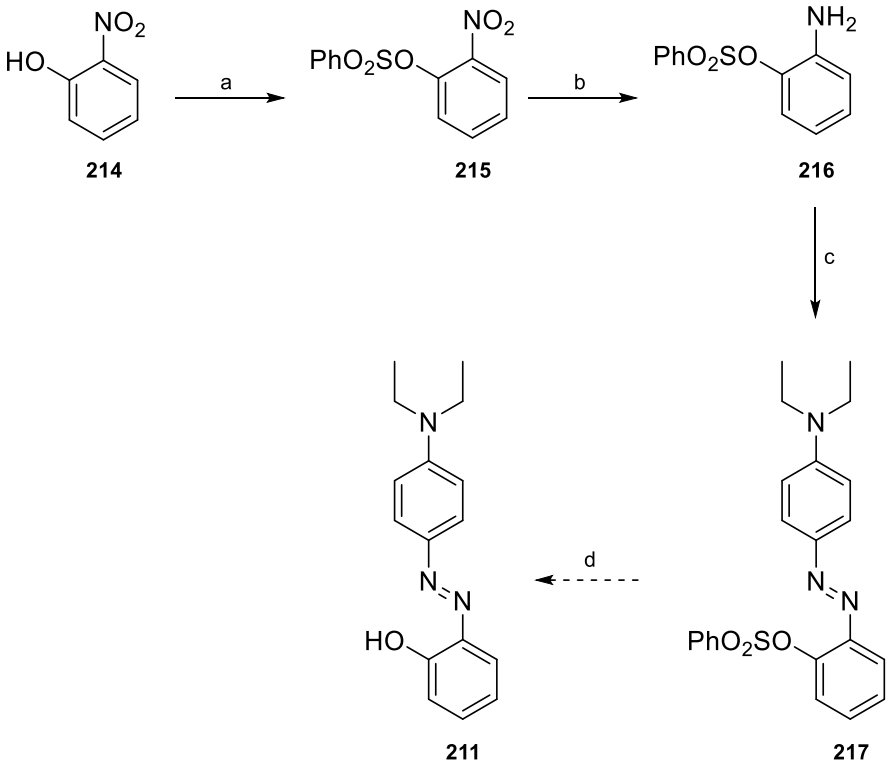

Scheme 14. Initial convergent synthesis pathway for accessing the phenol substituted derivative **211**. *Reagents and Conditions*: a) $PhSO_2Cl$, Pyridine, 0 °C – RT, 1 h, quant. b) Pd/C, H_2, EtOAc, RT, 8 h, quant. c) i. HCl, $NaNO_2$, 0 °C, 15 min ii. **168**, AcONa, 0 °C – RT, 1 h, 4% d) 30% NaOH, 100 °C, 2 h

However, because the *in situ* diazonium formation is mediated in acidic conditions it was thought that modulating of the solutions pH between 6-7 was necessary. This would allow an environment that would encourage the nucleophilic attack to occur without significant protonation of **168** or deprotonation of the phenol. Following procedures reported by Griffiths and Thomasson, the protected aniline **216** was exposed to a solution of HCl and $NaNO_2$ at 0 °C to form the diazonium *in situ*.[286] Following the formation of the diazonium, the pH of the solution was modulated by dropwise addition of aqueous NaOAc. Although the authors suggest that a nucleophilic base such as NaOH can be used, this can lead to competitive formation of hydroxyl diazene *via* addition of hydroxide to the diazonium electrophile.[210] Once at a suitable pH as indicated by litmus paper, the tertiary aniline **168** was added and the reaction allowed to proceed. On completion of the reaction a complex mixture was observed by TLC and subsequent purification *via* flash chromatography afforded the protected diazenyl phenol **217** in low yields. It is most likely that the nucleophilicity of **168** is not sufficient enough to proceed at a fast enough reaction rate, perhaps even that which exceeds the instability of chloride diazonium salts observed at temperatures greater than 5 °C.[210] As such, it was necessary to determine an alternative route of synthesis in which C-N

bond formation capability could be embellished to the *para*-position of **168**. Therefore an extensive investigation into various synthetic routes to afford the halogenated derivative **219** (**Scheme 15**; **Table 13**) was carried out. In principle this would allow the substrate to undergo metal-halogen exchange thus conferring greater nucleophilicity at the *para*-position to the tertiary amine.

Dialkylation of the 4-bromoaniline **218** was initially achieved with mild conditions consisting of EtI and K_2CO_3 in a solution of MeCN at 60 °C (**Scheme 15**, **Pathway A**; **Table 13**, **Entry 1**). After monitoring the reaction for 24 h, minor amounts of both the monoalkylated and dialkylated species were observed with notable starting material remaining. An additional equivalent of both EtI and K_2CO_3 was added to the reaction and allowed to proceed for a total of 32 h. However, this did not seemingly consume any more of the starting materials than previously seen by TLC. Upon workup and purification the reaction yielded poorly. As the addition of reagents did not seemingly increase conversion of the starting material it was considered that harsher conditions might be required to drive the reaction forward. Therefore it was decided to utilise NaH as the base for the reaction alongside a solvent switch to THF (**Table 13**, **Entry 2**). Initially the reaction was trialled at room temperature and proceeded to consume the starting material but stalled primarily at formation of the monoalkylated product. In an effort to drive additional alkylation of the monoalkylated material as well as the remaining starting material, the temperature was increased to 60 °C and monitored. Subsequent workup and purification provided better yields than the original attempt but were not adequate for the purposes necessary. It may be possible that interaction of the NaH with the EtI leads to an elimination reaction forming ethylene and thereby prevents alkylation from occurring. In either case, the long reaction times and sub optimal yields necessitated an alternative pathway to be sought.

In an investigation reported by Liu, C. *et al*, it was found that bromination of **168** to afford the halogenated derivative **219** could be done in high yields and fast reaction times (**Scheme 15**, **Pathway B**).[287] In fact, subjecting **168** to HBr in DMSO at 60 °C afforded the brominated compound in excellent yields within an hour on gram scale (**Table 13**, **Entry 3**). In this reaction, it is proposed that HBr forms bromodimethylsulfonium bromide that can then drive the electrophilic aromatic substitution.[287] It should be noted that the poor yields of both alkylation attempts may also be attributed to the electron-withdrawing properties of the bromine substituent at the *para*-position. Although considered a weak deactivator, its effect

may have been enough to prevent optimal yields from being attained. Conversely, the highly electron-donating properties of the tertiary amine would result in the far greater reaction rates observed for the electrophilic substitution reaction when **168** was subjected to the HBr-DMSO brominating conditions.

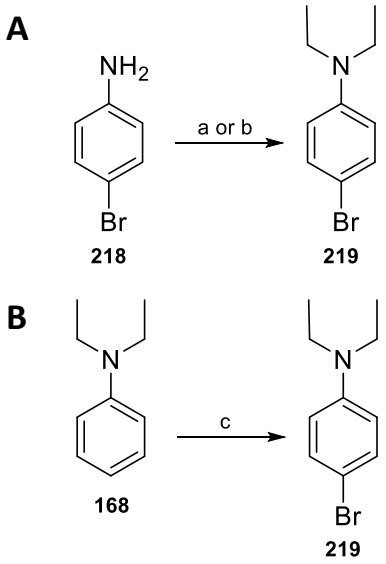

Scheme 15. Synthetic approaches to derive the brominated tertiary aniline **219**. *Reagents and Conditions*: a) EtI, K_2CO_3, MeCN, 60 °C, 32 h, 22% b) EtI, NaH, THF, RT – 78 °C , 24 h, 48% c) HBr, DMSO, 60 °C, 1 h, 90%

Table 13. Reaction conditions trialled and subsequent results for obtaining the brominated derivative **219**.

Entry	Reaction Conditions	Result
1	**218**, EtI, K_2CO_3, MeCN, 60 °C	22% yield
2	**218**, EtI, NaH, THF, 0 °C – 60 °C	48% yield
3	**168**, HBr, DMSO, 60 °C	90% yield

With **219** in hand, an alternative synthesis was devised (**Scheme 16**). It was envisaged that conversion of the brominated derivative to the Grignard reagent **221** could be carried out by metal-halogen exchange which would confer greater nucleophilic capacity to the *para*-position and allow for the desired C-N bond formation to occur. Subsequently this meant that an *in situ* diazonium reaction could not proceed due to the aqueous conditions of this conversion, as discussed previously. It was theorised that formation of the requisite diazonium tetrafluoroborate salt **220** from the protected aniline **216** could be isolated and suspended in THF solution to allow coupling to the Grignard reagent **221** under anhydrous

conditions. It has been previously reported that aryl diazoniums have capacity to undergo coupling reactions with Grignard reagents to form diazenyls, although with drastically varying yields.[288–291]

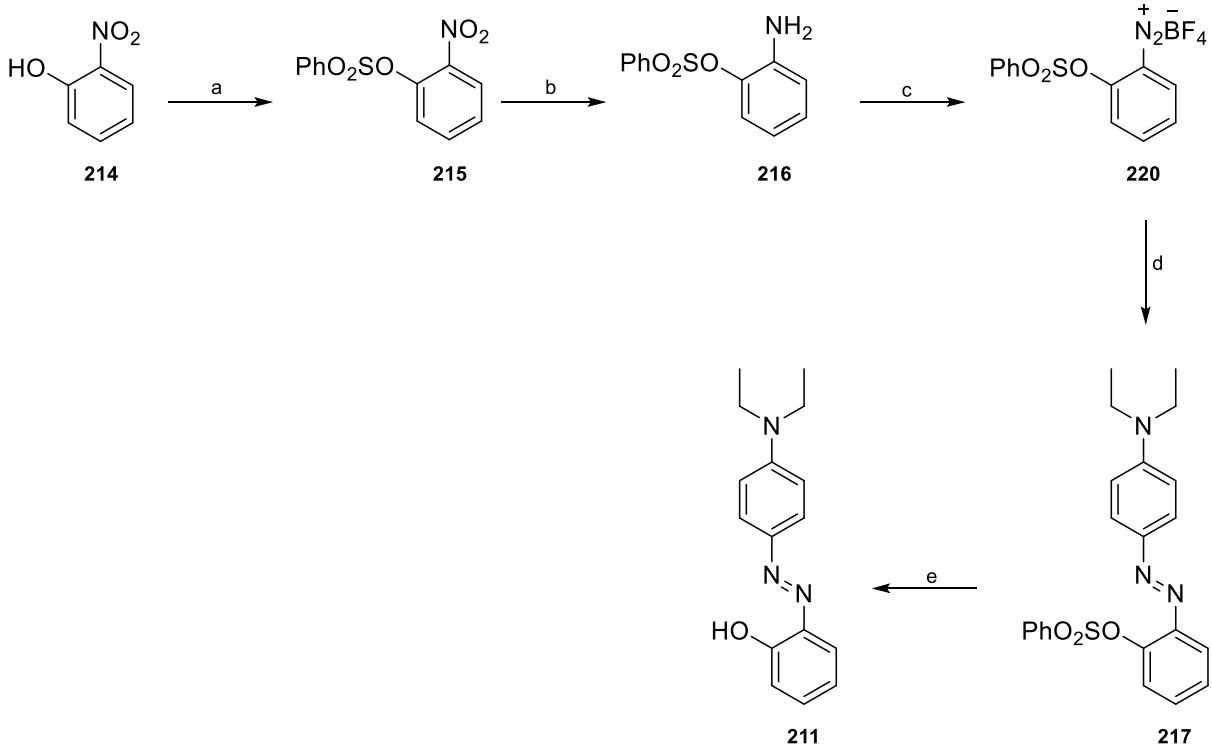

Scheme 16. Alternative convergent synthesis pathway for accessing the phenol substituted derivative **211**. *Reagents and Conditions*: a) $PhSO_2Cl$, Pyridine, 0 °C – RT, 1 h, quant. b) Pd/C, H_2, EtOAc, RT, 8 h, quant. c) i. HBF_4, Isopentyl Nitrite, AcOH, RT, 15 min ii. Et_2O, -40 °C, 81% d) **221**, THF, -78 °C – RT, 1 h, 45% e) 30% NaOH, 100 °C, 2 h, 55%

Several attempts were trialled to afford the Grignard reagent **221** from the halogenated derivative **219** (**Table 14**). Under standard Grignard conditions, the halogenated derivative was heated overnight in a solution of THF containing $Mg_{(s)}$ (**Table 14**, **Entry 1**). Subsequent addition of the Grignard reagent to the diazonium salt **220** resulted in a poor yield of the protected phenol **217**. Although the reaction proceeded cleanly, a significant portion of the unconverted halogenated derivative **219** was retrieved. One of the most widely used methods for activation of magnesium turnings is addition of the Gilman catalyst I_2.[292,293] It is proposed that addition of the iodine leads to formation of magnesium(I) iodide and thereby functions as the primary active agent in formation of the Grignard reagent. Furthermore, magnesium(I) iodide demonstrates greater solubility than magnesium metal and can additionally act as a catalyst since it is regenerated throughout the reaction.[292] Proceeding forward, a crystal of I_2 was added to a flask containing magnesium metal without any solvent

under nitrogen atmosphere (**Table 14**, **Entry 2**). To assist catalysis of the magnesium(I) iodide the flask was heated with a heat gun to vaporise the I_2 and dry stirred with the magnesium metal at room temperature. Subsequent addition of **219** dissolved in THF and refluxing overnight afforded a greater yield of the protected phenol **217** following addition of **221** to the diazonium salt **220** than the initial method trialled. However, this yield was still not acceptable given the expected mass loss after deprotection to the desired phenol **211**.

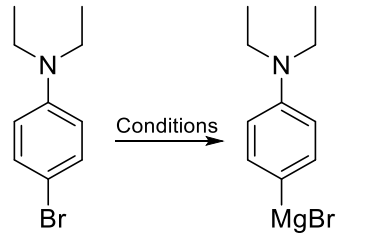

219 **221**, R = MgBr
222, R = MgCl•LiCl

Table 14. Reaction conditions trialled and subsequent results for conversion of **219** to **221** and subsequent coupling to afford **217**.

Entry	Reaction Conditions	Result
1	1. **219**, $Mg_{(s)}$, THF, 60 °C 2. **220**, THF, -78 °C – RT	4% yield
2	1. I_2, $Mg_{(s)}$, RT 2. **219**, THF, 60 °C 3. **220**, THF, -78 °C – RT	18% yield
3	1. $Mg_{(s)}$, RT 2. I_2, RT 3. **219,** THF, 60 °C 4. **220**, THF, -78 °C – RT	45% yield
4	1. **219**, *i*PropMgCl•LiCl, THF, 0 °C 2. **220**, THF, -78 °C – RT	8% yield

On further investigation, it has been reported that the compound 1-bromo-*N,N*-dimethylaniline is notoriously difficult to convert to the corresponding Grignard reagent.[292,294] Notably, electron-donating substituents present on aryl halides significantly hamper or even completely inhibit formation of Grignard reagents whilst electron-withdrawing substituents promote the formation. In this respect the electron-donating effect of the diethyl groups present on the tertiary amine of **219** would result in greater hampering of conversion than that

of its dimethyl counterpart. In any case, Mendel and co-workers reported that vigorous dry-stirring of magnesium turnings for lengthy times (>24 h) preceding addition of 1-bromo-*N,N*-dimethylaniline and subsequent heating in THF led to complete conversion to the respective Grignard reagent.[294] This procedure is on the basis that forceful stirring of the turnings results in the activation of magnesium through removal of the external oxide layer and thus facilitates more effective conversion. In an effort to substantiate conversion of the halide **219** to the Grignard reagent, magnesium turnings were vigorously stirred under nitrogen atmosphere for 24 h prior to further activation of the magnesium metal by the Gilman catalyst (**Table 14**, **Entry 3**). Subsequent addition of the aryl halide **219** in THF and overnight heating resulted in a significantly greater yield being observed of the protected phenol **217** on addition of the Grignard **221** to the diazonium salt **220**.

Although previous conditions yielded an acceptable amount of **217** to move forward, use of the turbo-Grignard reagent *i*PropMgCl•LiCl to boost conversion was attempted in a final effort to optimise the reaction (**Table 14**, **Entry 4**). It has been demonstrated that although bromine-magnesium exchanges are slow, the rate of the exchange can be considerably enhanced by addition of the turbo-Grignard reagent.[295] This was trialled in hopes that the MgCl•LiCl would insert more effectively into **219**, thus providing better conversion to a turbo-Grignard reagent **222**. Unfortunately this ultimately proved to be only slightly more efficient than the original method trialled and demonstrated a more complex mixture than the spot to spot reaction of the classic Grignard in previous attempts. However, with enough of **217** in hand, a subsequent deprotection of **217** at reflux in 30% NaOH solution afforded the final phenol **211** in moderate yields. Purification *via* flash chromatography resulted in excellent purity of the compound for future *in vitro* testing.

4.3 Synthesis of *N,N*-Diethyl-4-((2-methoxyphenyl)diazenyl)aniline

As previously discussed in **Chapter 2.2.3**, the lead derivative **52** can undergo tautomerisation to form either the hydrazone or phenolic tautomers (**93** and **52**, respectively; **Scheme 3**). Similarly this tautomerisation can occur in the azophenol **211** (**Scheme 17**). To ensure comparison can be made between the tautomers of the bicyclic and monocyclic derivatives when assessing activity at the target, alkylation of the phenolic moiety of **211** was carried out. It was envisioned this could be undertaken using the conditions for the successful alkylation of **52**. Indeed, methylation of the phenol moiety proceeded in good yields when **211** was subjected to both NaH and MeI in THF at RT.

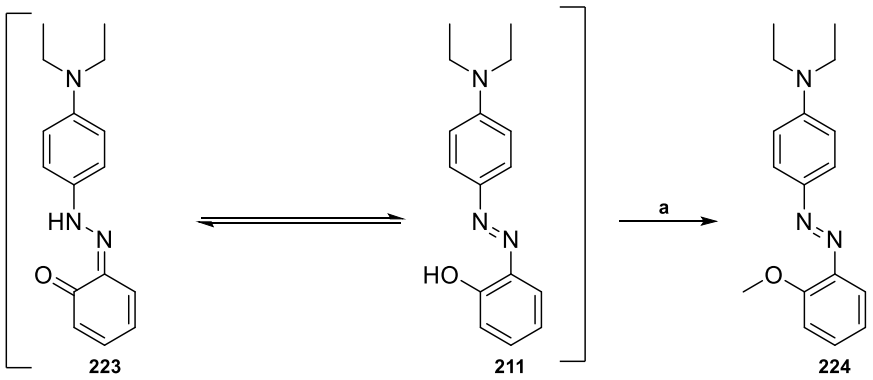

Scheme 17. The equilibrium for tautomerism can be observed alongside the general synthetic scheme to access derivative **224**. Specifically, tautomerisation occurs between the phenol and azo functionalities, leading to formation of a hydrazone moiety that may play a pivotal role in activity at the target. *Reagents and Conditions*: a) MeI, NaH, THF, 8 h, 72%.

In regards to characterisation of compound **211**, a typical chemical shift for the methoxy functionality can be observed as a singlet at 4.00 ppm (highlighted in RED) in the ^{1}H-NMR spectra displayed in **Figure 60**. Accordingly a corresponding ^{13}C-NMR carbon for the newly alkylated moiety is observed at 56.4 ppm (**Appendix A**). Although an unlikely possibility, due to the tautomeric-dependent potential of alkylation to occur at the either the phenolic moiety, thereby conferring the formation of the methoxy moiety (compound **224**), or methylation of the NH present within the hydrazone tautomer (compound **225**; **Figure 61**), 2D NMR was carried out to observe through space ^{1}H-^{1}H interactions (**Figure 61**, **224** highlighted in BLUE and **225** highlighted in RED) *via* NOESY NMR (**Figure 61**) to confirm the position of alkylation. In particular, a correlation between the methoxy peak at 4.00 ppm and doublet at 7.04 ppm can be observed (highlighted by the BLUE box in **Figure 61**; multiplet proton chemical shift is highlighted by a BLUE asterisk). As such, this confirms that the methoxy moiety has in fact been furnished to the phenolic position. Conversely, if the amino group had been alkylated then a through space correlation would be expected between the methylated amine protons and phenylic protons residing on the lower part of the ring (**225**, **Figure 61**, highlighted in RED; ^{1}H NMR chemical shifts highlighted by a RED asterisk).

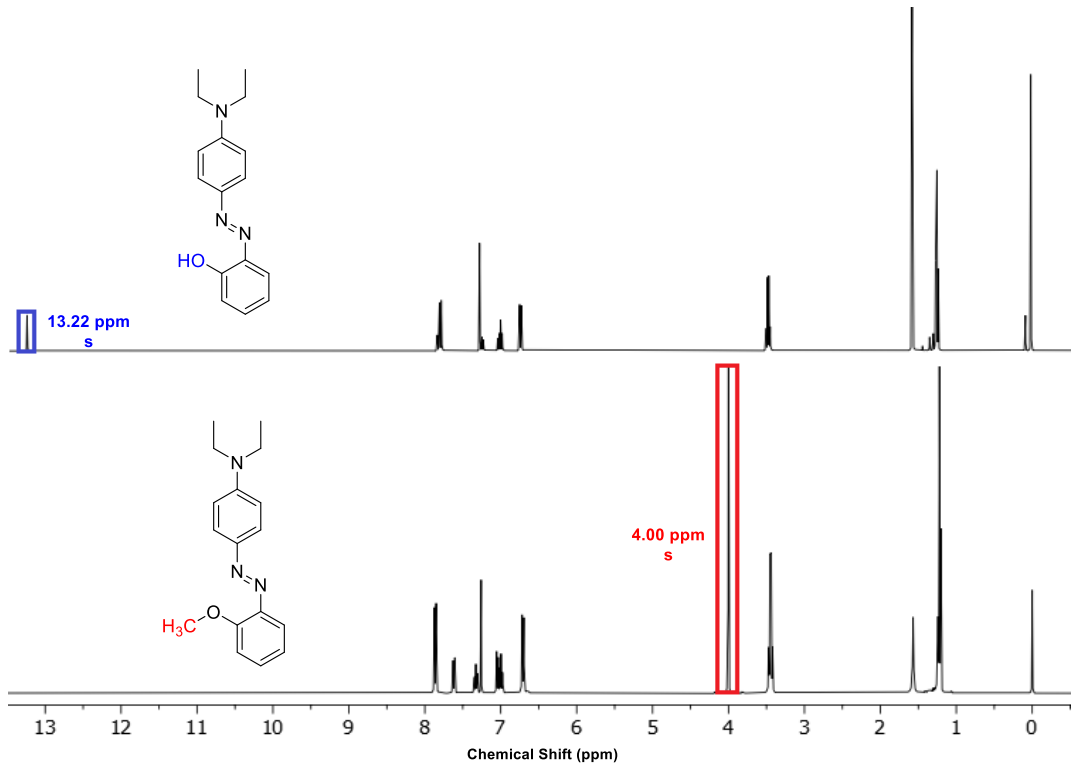

Figure 60. ^{1}H-NMR (400 MHz, $CDCl_3$) spectrum for compounds **211** and **224**. Phenol moiety for compound **211** is highlighted in BLUE. Newly conferred methoxy functionality and correlated chemical shift is highlighted in RED for compound **224**. Multiplicity and integration of each respective chemical shift can be seen in **Chapter 6**.

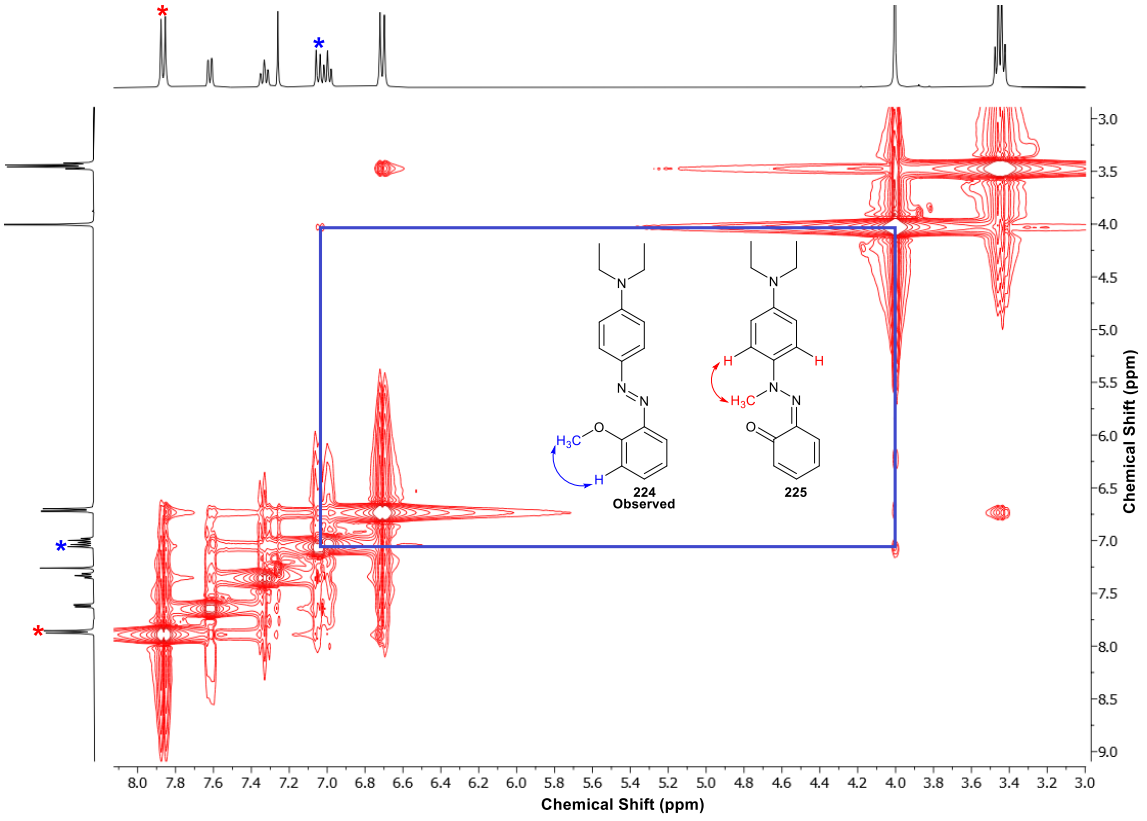

Figure 61. NOESY NMR (400 MHz, $CDCl_3$) spectrum for compound **224**. Observed through space correlations are highlighted by a BLUE box. The correlated doublet is highlighted by a BLUE asterisk. Phenylic protons on the lower portion of the ring are highlighted by a RED asterisk.

4.4 Synthesis of 4-((1*H*-Indol-4-yl)diazenyl)-*N*,*N*-diethylaniline

For the lead indole derivative **213**, introduction of a bicyclic indole in place of the naphthalene functionality was proposed to remove the metabolically liable phenol functionality whilst improving hydrophilicity through installation of a hydrogen bonding point. Formation of the 4-aminoindole **227** from the corresponding nitro derivative **226** was initially considered, as this would allow subsequent coupling of the tertiary amine **168** through an *in situ* diazonium formation (**Scheme 18**). However, attempted reduction of the nitro functionality of **226** to the respective amino moiety under standard hydrogenation conditions was unsuccessful (**Table 15, Entry 1**). Upon further investigation it was found within literature that several methods had been developed in which the reduction of **226** can be undertaken at elevated temperatures and/or pressure using rhodium, nickel or palladium catalysts.[296–300] This indicated that harsh conditions are required to drive the reduction of the nitro moiety. Therefore, a safer synthetic pathway was envisioned that did not require the use of hydrogen gas at elevated temperatures or pressure to afford the aminoindole **227**. It has been reported that standard as well as modified Bechamp processes are feasible.[301,302] However, utilisation of Bechamp conditions did not result in any observed reaction when trialled (**Table 15**, **Entry 2**).

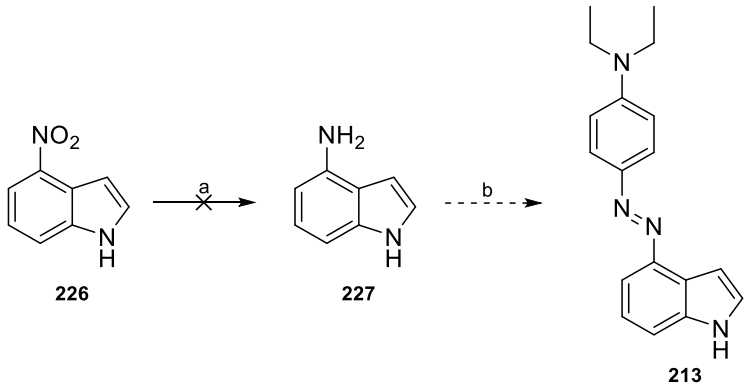

Scheme 18. Initial synthesis pathway for accessing the 4-aminoindole **213**. *Reagents and Conditions*: a) conditions outlined in **Table 15** b) i. HCl, $NaNO_2$, 0 °C, 15 min ii. **168**, AcONa, 0 °C – RT, 1 h, not attempted

Table 15. Reaction conditions trialled and subsequent results for obtaining the aniline **227**.

Entry	Reaction Conditions	Result
1	H_2, Pd/C, EtOAC, RT	No reaction
2	$Fe_{(s)}$, 6 N HCl, EtOH, 80 °C	No reaction

It was proposed that the amine **227** could be obtained beginning with the methyl benzoate derivate **228** (**Scheme 19**). Hydrolysis of the benzoate and subsequent formation of the acyl azide **230** could then be used to access the amino moiety *via* a Curtius rearrangement and subsequent decomposition to the amine **227**. The hydrolysis of the methyl ester **228** under standard conditions using NaOH in EtOH afforded the carboxylic derivative **229** in quantitative yields. Utilising DPPA as an azide source in 1,4-dioxane alongside Et_3N allowed the acyl azide **230** to be obtained in good yields, which was then subjected to a solution of HCl and H_2O at reflux so as to drive rearrangement to the isocyanate **231** (**Figure 62**) and further decomposition to the required amino derivative **227**. This reaction is surprisingly robust, leading to a quantitative yield of the amine.

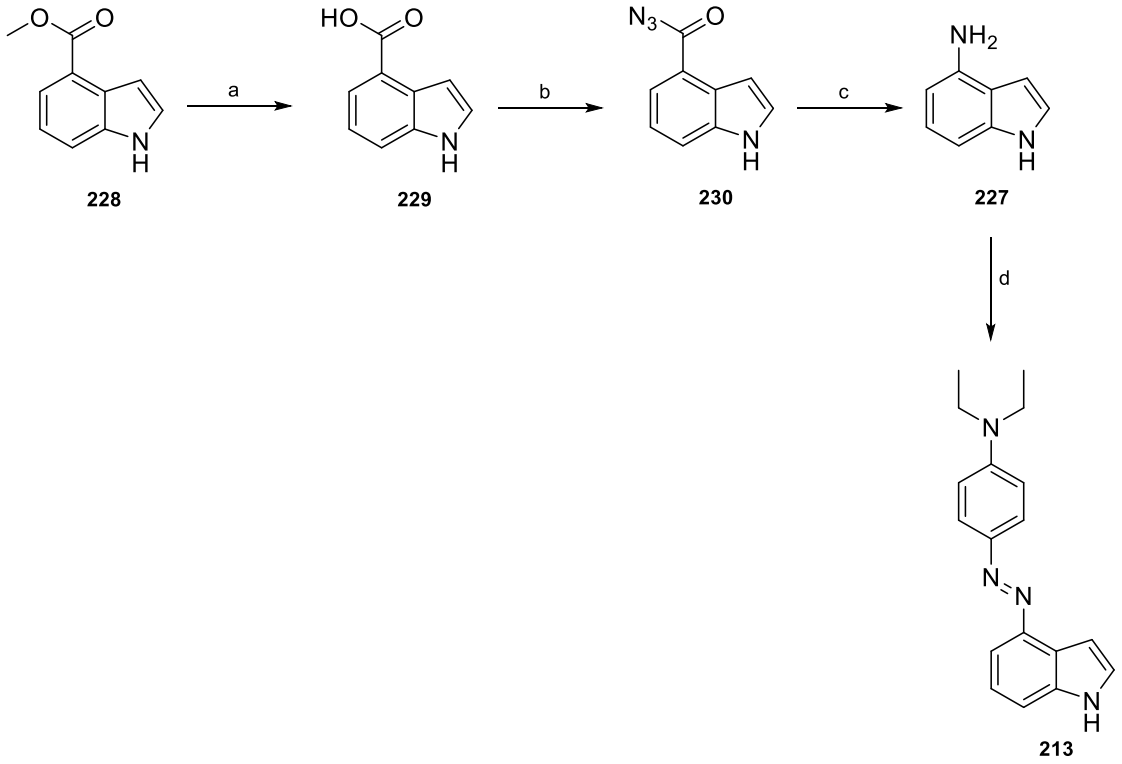

Scheme 19. Alternative convergent synthesis pathway for accessing the indole substituted derivative **213**. *Reagents and Conditions*: a) NaOH, EtOH, 80 °C, 8 h, quant. b) DPPA, 1,4-dioxane, Et_3N, RT, 30 min, 78% c) 38% HCl, H_2O, 100 °C, quant. d) i. HCl, $NaNO_2$, 0 °C , 15 min ii. **168**, AcONa, 0 °C – RT, 1 h, 10%

Mechanistically the Curtius rearrangement and decomposition to the amine **227** (**Figure 62**) is particularly interesting. Heating of the acyl azide **230** results in a concerted decomposition that leads to the formation of the corresponding isocyanate **231** with the loss of N_2. Subsequent nucleophilic attack by water followed by a proton transfer results in the formation of the unstable carbamic acid intermediate **232**. Due to the instability of carbamic acid, a spontaneous decarboxlyation occurs that leads to the desired amino product **227**. After

obtaining **227** an *in situ* diazonium formation is carried out with the previously described conditions of $NaNO_2$ and HCl, followed by addition of **168**. Similarly to the initial attempt discussed in **Section 4.2** to form the protected phenol **217**, pH of the solution was modulated with NaOAc so as to provide an environment in which **168** could act as a sufficient nucleophile without a competing nucleophilic base present. Although the yield of the reaction was poor, it afforded enough of the indole derivative **213** that it was purified *via* flash chromatography to give excellent purity for future *in vitro* assessment.

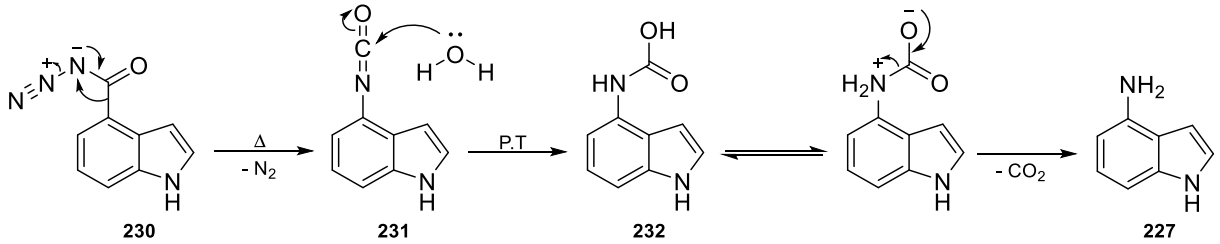

Figure 62. Proposed mechanism for the Curtius rearrangement leading to formation of the isocyanate **232** and subsequent decomposition to the aniline **227**.

It was considered to attempt Grignard coupling of **221** to the respective diazonium tetrafluoroborate salt of **227** (characterisation in **Chapter 6**). However, this compound surprisingly exhibited extremely poor solubility in all solvents including DMSO. Although the majority of the compound was able to be characterised, a suitable ^{13}C-NMR could not be obtained. In any case, the coupling may not have been viable due to the indolic nitrogen presenting an accessible proton that may have quenched the Grignard reagent **221**. If necessary to attempt in the future for the purposes of a greater yield, protection of the indolic nitrogen would most likely be necessary but would increase the number of steps to reach the title compound. One such example of a protecting group may be a fluorenylmethoxycarbonyl (FMOC) group that could be installed to the acyl azide **230**. It would not be removed by the acid-mediated decomposition step that forms **227** and can be deprotected under basic conditions using a base such as piperidine.[303]

4.5 Concluding Remarks

Synthetic approaches toward several derivatives have been discussed within this chapter. Although this is not an extensive investigation, the moieties that have been introduced to explore the naphthalene moiety present on the lead diazenyl compound **52** seek to inform the importance of multiple aspects of variability that may influence activity at the desired target. To evaluate the necessity for a bicyclic phenol, a monocyclic phenol derivative has been synthesised. Following on so as to directly compare the effect of tautomerisation of

the target between the lead diazenyl and monocyclic derivatives, the phenol derivative **211** has been successfully methylated (**224**) and the desired chemoselectivity of alkylation has been discerned (**Figure 61**). Lastly, an indole motif (**213**) has been imbued to the scaffold to remove the metabolically liable phenolic functionality. Additionally, introduction of the indolic nitrogen acts to improve hydrophilicity within the scaffold by means of a hydrogen bonding motif as well as subtle improvements through removal of a carbon atom.

Chapter 5:

Conclusions and Future Work

Chapter 5: Conclusions and Future Work

5.1 Summary and Conclusions

Within this thesis the exploration of chemotypes for potential tau aggregation therapeutics has been discussed. In particular, several pathways were compared to evaluate their capacity as promising pharmacological targets in for the reduction of tau. As a result the Hsp90-Aha1 complex was identified as a novel approach to achieve this goal and the lead candidate **52** was selected as a starting point to begin this investigation. Previously it has been mentioned that limited literature exists for this co-chaperone within literature, including a narrow scope of small molecule interactors.

Chapter 2 focused on the preparation, derivatisation and validation of the established diazenyl scaffold of **52** as the primary backbone upon which to widen the scope of chemotypes that can interact with target. Various analogues of the diazenyl scaffold were synthesised to probe the tolerability of functionalities residing on the phenyl group with additional alkylation of the lead phenolic position for assessment of the pharmacological relevance of its tautomeric forms. Evaluation of the lead candidate **52** and the derivative library in a ThT assay demonstrated promising results for novel inhibitory activity on tau aggregation directly. However, the disease-relevance of the model has been brought into question and as such these compounds will require reassessment before it can be accurately concluded that the scaffold exhibits direct inhibition on tau. Additionally, inability to access a Hsp90-Aha1 relevant assay has prevented evaluation of the lead diazenyl scaffold and associated derivatives at the target. As a consequence, future iterations could not be informed by *in vitro* testing as typically done within medicinal chemistry efforts. This highlights the difficulty of validating compounds in disease-relevant models as well as obtaining access to assays that evaluate innovative pharmacological targets.

Chapter 3 described the rational exploration, synthesis and characterisation of chemotypes that expand the chemical space surrounding the previously identified lead diazenyl scaffold. In particular several frameworks were able to be successfully furnished to the scaffold including pyrazole (**118**), triazole (**146, 160** and **171**) and amide-based (**184**) motifs. These were able to add rigidity to the overall backbone while eliminating the metabolically liable diazenyl motif and its discussed tautomeric variability. Although not all

chemotypes were successfully achieved, a diverse range of synthetic pathways and their relevant complications have been comprehensively discussed. It is indeed unfortunate that biological evaluation was not able to be conducted for these compounds. However, future study of SAR between these novel chemotypes and the Hsp90-Aha1 complex will provide a greater overall insight to the underlying pharmacology.

Finally, it was important to ascertain the significance of the naphthalene tail-group moiety in the overall pharmacophore of the diazenyl scaffold. As such, **Chapter 4** outlined the exploration, synthesis and characterisation of motif substitutions that inform the importance of a bicyclic moiety and tolerance of installing a privileged indole functionality. Additionally alkylation of the monocylic phenol position was carried out to evaluate and compare to the effect of tautomeric structures between the new motif of **224** and the methylated lead candidate **73**.

5.2 Future Work

It is imperative that the compounds described in **Chapter 2** through to **Chapter 4** can be evaluated within *in vitro* models so as to inform future iterations. In particular, a model for assessment on tau inhibition directly that contains AD-relevant recombinant tau filaments (as discussed in **Chapter 2.3.3**) as well as an assay with capacity to determine activity at the Hsp90-Aha1 complex. More information is required surrounding the SAR of these compounds at both targets before it can be considered useful to conduct additional modifications on the scaffolds. If the results from **Chapter 2** can be confirmed to demonstrate the diazenyl-based library has appreciable inhibitory activity on tau directly, it would be of great interest to assess if this is maintained by the chemotype iterations presented in **Chapter 3** and the tail-group substitutions in **Chapter 4**. Most importantly the lead candidate **52** must be validated for its reported action of inhibition on the Hsp90-Aha1 complex along with the alterations presented. This may pave the way to identifying multi-target pharmacophores provided that the lead diazenyl scaffold and associated chemotype variations can be validated in both *in vitro* models.

If the chemotypes presented in **Chapter 3** exhibit reasonable inhibitory activity on the Hsp90-Aha1 target, it would be interesting to explore additional azole-based heterocyclic linkers such as pyrimidine (**233**), piperazine (**234**), isothiazole (**235**), imidazole (**236**), 1,3-diazetidine (**237**) and aziridine (**238**) motifs (**Figure 63**). Variance in ring structure sizes would inform the tolerated atom lengths within the linker. Additionally, walking the head and

tail group substitutions around the ring structures could present useful SAR information when assessed. This can be further applied to heteroatoms within the ring structures. Non-heterocyclic bioisotere linkers such as ureas (**239**), thioamides (**240**), sulfonamides (**241**) and sulfonates (**242**) (**Figure 63**) are appealing scaffold functionalities to explore although they present a limited scope of additional substitutions that can be furnished compared to heterocyclic motifs. Further diversification of linker chemotypes greatly expands the chemical space surrounding this target and assists in probing the fundamental mechanistic components of its system. However, these future alterations must be directed by biological results.

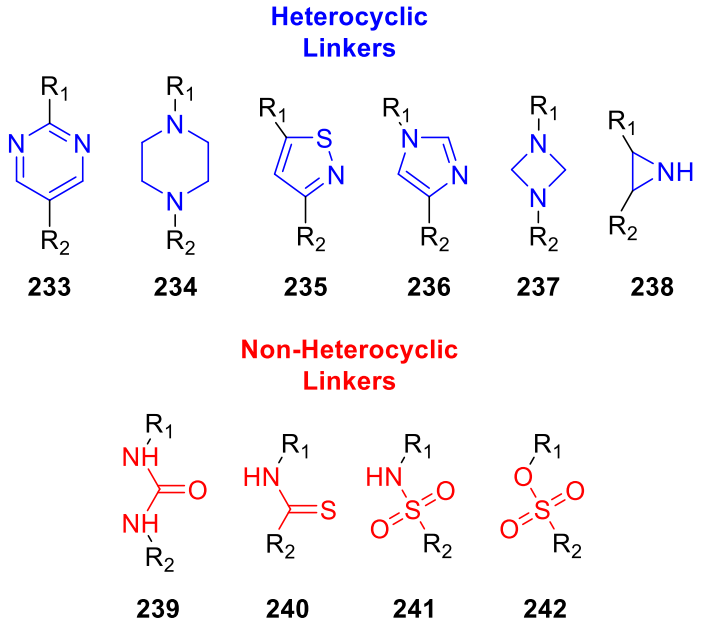

Figure 63. Examples of heterocyclic and non-heterocyclic linker motifs for future iterations.

There are several ways future modifications of the tail-group functionality can be directed, dependent on *in vitro* results obtained from the compounds in **Chapter 4**. Importance of the phenol must be discerned within the pharmacophore to inform whether its presence is necessary in additional iterations. If a bicyclic moiety required, it may be of interest to explore similar functionalities to the previously presented indole as base scaffolds. This includes benzofuran (**243**), benzimidazole (**244**), benzothiazole (**245**) and benzoxazole (**246**) structures (**Figure 64**). In the case that a monocylic moiety is tolerated, exploration of motifs such as **247**, benzene (**248**) or pyridine (**249**) could prove useful (**Figure 64**). It has been previously reported that the $–CF_2H$ functionality is a useful bioisosteric replacement of the phenolic –OH as it demonstrates similar hydrogen bond donor capacity. Additionally it is not

prone to metabolic glucuronidation.[304] A benzene motif can be used to probe the necessity of any functional group substitutions along the ring while pyridine derivatives can be used to increase hydrophilicity through introduction of nitrogen atom within the ring with capacity to hydrogen bond.

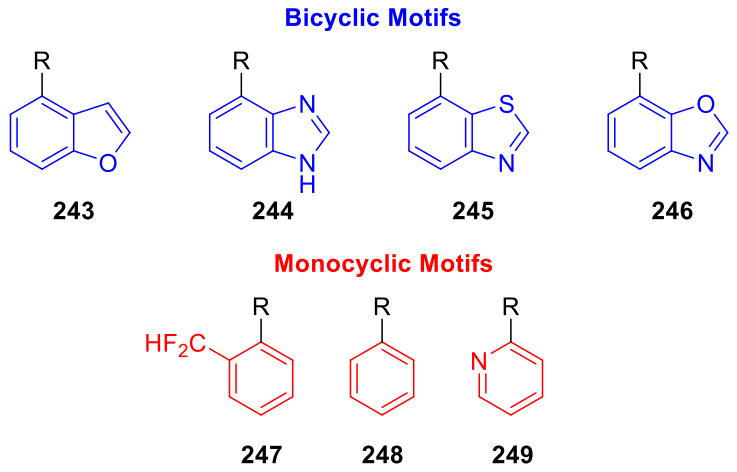

Figure 64. Examples of bicyclic and monocyclic tail-group motifs for future iterations.

Chapter 6:

Experimental and Characterisation

Chapter 6: Experimental and Characterisation

6.1 General Experimental Details

Unless otherwise stated, all solvents and reagents were purchased and used from commercial sources. Anhydrous solvents were obtained from an Innovative Technology PureSolv7 purification system. THF and DCM were dried through an alumina column. DMF was dried through a 5 Å molecular sieve column. All reagents were weighed out under ambient conditions.

All reactions were performed under a nitrogen or argon atmosphere, unless otherwise stated. Analytical thin-layer chromatography (TLC) was performed using Merck aluminium backed silica gel 60 F254 (0.2 mm) plates, which were visualised with shortwave (254 nm) ultraviolet light. Products were also visualised with potassium permanganate, vanillin, cerium molybdate, bromocresol green or ninhydrin stains where appropriate. Flash column chromatography was performed using Merck Kieselgel 60 (230-400 mesh) silica gel, with the eluent mixture reported as the volume:volume ratio.

IR spectra were recorded neat using a Bruker ALPHA FT-IR spectrometer and peaks are expressed in wavenumbers (cm^{-1}). Nuclear magnetic resonance spectra were recorded at 300 K using either a Bruker AVANCE DRX300 (300 MHz), AVANCE DRX400 (400 MHz) or AVANCE DRX500 (500 MHz) spectrometer. ^{1}H chemical shifts are expressed as parts per million (ppm) with residual chloroform (δ 7.26), methanol (δ 3.31), dimethyl sulfoxide (δ 2.50) and acetone (δ 2.05) as reference and are reported as chemical shift (δ); multiplicity (s = singlet, br s = broad singlet, d = doublet, dd = doublet of doublets, dt = doublet of triplets, dq = doublet of quartets, dp = doublet of pentets, ddd = doublet of doublets of doublets, ddt = doublet of doublets of triplets, dtd = doublet of triplets of doublets, dtt = doublet of triplets of triplets, t = triplet, td = triplet of doublets, tt = triplet of triplets, q = quartet, qd = quartet of doublets, p = pentet, hept = heptet, m = multiplet); coupling constants (*J*) reported in Hz; relative integral. ^{13}C chemical shifts are expressed as parts per million (ppm) with residual chloroform (δ 77.16), methanol (δ 49.00), dimethyl sulfoxide (δ 39.52) and acetone (δ 29.84) as reference and reported as chemical shift (δ); multiplicity (d = doublet, q = quartet); coupling constants (*J*) reported in Hz. ^{11}B chemical shifts are reported as parts per million (ppm). Proton decoupled ^{19}F chemical shifts are reported as parts per million (ppm). ^{11}B and ^{19}F NMR were not calibrated with an internal standard.

Low-resolution mass spectra (LRMS) were recorded using ESI-MS and APCI-MS recorded on a Bruker AmaZon SL ion trap spectrometer. High-resolution mass spectrometry (HRMS) was performed on a Bruker Apex Qe 7T Fourier Transform Ion Cyclotron Resonance mass spectrometer equipped with an Apollo II ESI/MALDI dual source. Samples were run with syringe infusion at 150 μL/hr on a Cole Palmer syringe pump into the ESI or APCI source. HRMS samples were run by Dr. Nicholas Proschogo. High performance liquid chromatography (HPLC) analysis of organic purity was conducted on a Waters Alliance 2695 instrument using a SunFire TM C18 column (5 μm, 2.1 × 150 mm) and detected using a Waters 2996 photodiode array detector set at 230 and 254 nm. Separation was achieved using water + 0.1% trifluoroacetic acid (solvent A) and acetonitrile + 0.1% trifluoroacetic acid(solvent B) at a flow rate of 0.2 mL/min and a gradient of 0% solvent B to 100% solvent B over 30 minutes. HPLC data is reported as percentage purity and retention time (t_R) in minutes.

UV-Vis absorption spectra were recorded using an Agilent Cary 60 UV-Vis Spectrophotometer. Compounds were dissolved in DMSO to provide stock solutions at 1.56 mM. Measurements were performed using a quartz cuvette with a 10 mm pathlength and DMSO as the baseline. Measurements were taken between 200 nm – 800 nm with a scan rate of 4800 nm/min and a data interval of 1.00 nm at an average time of 0.0125 sec.

Fluorescence spectra and quenching studies were recorded using an Agilent Cary Eclipse Fluorescence Spectrophotometer. Compounds were dissolved in DMSO to provide stock solutions at 1.56 mM. Measurements were performed using a quartz cuvette with a 10 mm pathlength and DMSO as the baseline. Measurements were taken between 450 nm – 800 nm at an excitation wavelength of 440 nm through a 5 nm slit. Additional parameters include a scan rate of 600 nm/min and a data interval of 1.00 nm at an average time of 0.1 sec.

6.2 General Synthetic Procedures

General Procedure A: Diazenyl Formations

To a concentrated aqueous solution of HCl (15 mL, 20 vol %) was added the aniline (1 eq.) and cooled down to 0 °C. $NaNO_2$ (1.1 eq.) pre-dissolved in deionised water (1 mL) was slowly added drop wise to the solution and stirred for 1 h in an ice bath. An alkaline solution of **78** (1 eq.) in 2.5 M NaOH made up in H_2O (2 mL) was then slowly added to the reaction at 0 °C with vigorous stirring for 3 h and then left to further react at room temperature for 2 –

3 h. The resulting precipitate was then filtered and washed with water. Subsequently, the residue was purified *via* recrystallization or flash chromatography (Hexane/EtOAC or Hexane/DCM as eluents) to yield the desired diazenyl compound.

General Procedure B: Diazonium Tetrafluoroborate Crystallisations

A derivative of aniline was dissolved in a solution of AcOH (3 mL) and 48% aq. HBF_4 (5 eq., 48% wt. adjusted). Subsequently, isopentyl nitrite (1.7 eq.) solution in AcOH (1 mL) was added dropwise to the reaction at room temperature over a period of 5 min and allowed to stir for another 10 min. Et_2O (10 mL) was added and the reaction temperature cooled down to -46°C in order to induce crystallisation of the product. The crystals were filtered off *in vacuo*, washed with Et_2O (3 × 5 mL) and dried on air to afford the diazonium tetrafluoroborate derivatives.

General Procedure C: Alkylation with K_2CO_3

A solution of phenol, carboxylic acid or aniline (1.0 eq.), K_2CO_3 (2.0 eq) and alkyl halide (3 eq.) in acetone or MeCN (10 mL) was stirred at room temperature or with heating at 60 °C for 3 h, until TLC indicated conversion of starting material. The reaction mixture was then diluted into H_2O (15 mL) and extracted with EtOAc (3 × 10 mL). The combined organic phases were washed with brine (1 × 15 mL), dried over $MgSO_4$, and concentrated *in vacuo*. The crude product was purified *via* flash chromatography (Hexane/EtOAc as eluents) to yield the desired product.

General Procedure D: Alkylation with NaH

A solution of phenol, carboxylic acid or aniline (1.0 eq.), alkyl halide (3 eq.) in anhydrous THF (10 mL) was cooled down to 0 °C. NaH (1.1 eq.) was added to the reaction and allowed to gradually come to room temperature. The solution was stirred at room temperature or with heating for 3 h, until TLC indicated conversion of starting material. The reaction mixture was then diluted into H_2O (15 mL) and extracted with EtOAc (3 × 10 mL). The combined organic phases were washed with brine (1 × 15 mL), dried over $MgSO_4$, and concentrated *in vacuo*. The crude product was purified *via* flash chromatography (Hexane/EtOAc as eluents) to yield desired product.

General Procedure E: Reduction with H_2 and Pd/C

A nitro derivative (1 eq.) was dissolved in a solution of EtOAc (15 mL) alongside Pd/C (10 mol %) at room temperature. The atmosphere was evacuated and charged with N_2 gas

(3 ×) before introduction of H_2. On completion as indicated by TLC, the reaction was filtered over a pad of celite and reduced *in vacuo* to provide the respective aniline derivative.

General Procedure F: Knorr-Pyrazole Formations

A solution of **105** (1 eq.) and NaH (2 eq.) in THF (10 mL) was heated to 40 °C for 1 h. Addition of methyl formate (5 eq.) followed and the reaction was monitored until TLC indicated consumption of starting material. Upon completion, the reaction was cooled down and quenched with 3 N HCl (10 mL) alongside addition of phenyl hydrazine or **111** (1 eq.). The reaction was heated to 100 °C for 2 h, until TLC indicated conversion of starting material. The reaction mixture was extracted with EtOAc (3 × 10 mL), dried over $MgSO_4$, and concentrated *in vacuo*. The crude product was purified *via* flash chromatography (Hexane/EtOAc as eluents) to yield the desired 1,3- or 1,5-1*H*-pyrazole product.

General Procedure G: Aryl Azido Substitutions

A diazonium tetrafluoroborate derivative was dissolved in a solution of THF (10 mL) alongside NaN_3 (1.1 eq.). The reaction was stirred vigorously at room temperature and monitored *via* TLC. On completion, the reaction was portioned between brine (10 mL) and hexane (10 mL). The aqueous layer was further extracted with hexane (2 × 10 mL). The organic layers were combined, dried over $MgSO_4$ and concentrated *in vacuo* to afford the crude azido products. These were carried through to the next step without further purification.

General Procedure H: CuAAC Synthesis of 1,4-disubstituted 1,2,3-triazoles

To a three-neck flask affixed with a condenser was added $CuSO_4 \cdot 5H_2O$ (10 mol %) and sodium ascorbate (1 eq.). A mixture of degassed THF and water (4:1, 10 mL) was added and the mixture was stirred under N_2 at room temperature for 45 min, giving a homogeneous solution. To this was added a solution of **145** (1 eq.) in degassed THF (5 mL), followed by a solution of an azido derivative (1 eq.) in degassed THF (5 mL) and the mixture was heated to 75 ºC and stirred for 4 h under N_2. The mixture was kept under N_2 atmosphere to cool and poured into a separatory funnel containing EtOAc (10 mL) and water (10 mL). The organic layer was collected and the aqueous layer was extracted twice more with EtOAc (2 × 10 mL). The organic phase was concentrated *in vacuo* to afford the crude product, which was then purified *via* flash chromatography (Hexane/EtOAc or DCM/EtOAc) to afford the 1*H*-1,2,3-1,4-triazole regioisomeric derivative.

General Procedure I: Base-Catalysed Synthesis of 1,5-disubstituted 1,2,3-triazoles

To a solution of **145** and an azidobenzene derivative in DMSO (5 mL) was added NMe_4OH (10 mol %, 25% wt adjusted) and the reaction mixture was stirred at room temperature under N_2 to maintain a CO_2–free atmosphere. After 20 h, the reaction was quenched by pouring into ice-cold water (15 mL). After stirring for 2 h at room temperature, the crude precipitate was filtered off *in vacuo*. It was then redissolved in EtOAc (15 mL), concentrated *in vacuo* and purified *via* flash chromatography (Hexane/EtOAc) to afford the 1*H*-1,2,3-triazole-1,5 regioisomer derivative.

General Procedure J: Base Mediated Ester Hydrolysis

A solution of ester (1.0 eq.) in MeOH or EtOH (10 mL) was treated with NaOH (3.0 eq.) and stirred at room temperature for 4 – 6 h. The reaction mixture was then poured into H_2O and acidified to pH ~ 2 by the addition of 1 M aq. HCl. The aqueous phase was then extracted with EtOAc (3 × 10 mL). The combined organic phases were then dried over $MgSO_4$, and concentrated *in vacuo* to yield the desired carboxylic acid.

General Procedure K: Amide Couplings

183 (1 eq.) was dissolved in DCM (5 mL) and cooled down to 0 ºC. Addition of $(COCl)_2$ (1.1 eq.) was followed by cat. DMF then allowed to stir for 1 h. After completion *via* TLC the solvent was removed under a stream of N_2. Subsequently the crude residue was redissolved in DCM and removed under a stream of N_2 (3 ×). After this, an aniline derivative (1 eq.) was dissolved in DCM (5 mL) alongside Et_3N (2 eq.) and allowed to stir for 15 minutes before addition to the acid chloride mixture at 0 ºC. The reaction was gradually brought to room temperature and monitored *via* TLC. On completion, the mixture was diluted with water and extracted with DCM (3 × 10 mL), washed with brine (1 × 10 mL), dried over $MgSO_4$ and concentrated *in vacuo*. The crude product was then purified *via* flash chromatography (Hexane/EtOAc) to afford the amide derivative.

6.3 Chapter 2 Experimental and Characterisation

4-(*N,N*-Diethylamino)nitrobenzene - 75

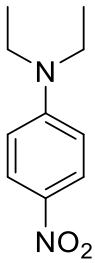

74 (752 µL, 7.08 mmol) was dissolved in DMSO (10 ml), K_2CO_3 (1.52 g, 11.0 mmol) and diethylamine (1.46 mL, 14.2 mmol) were added, and the mixture was stirred at 90 °C overnight. Then, water was added to the reaction solution and subsequently extracted with EtOAc (3 × 15 mL), washed with brine (1 × 15 mL) and dried over $MgSO_4$. The solvent was removed *in vacuo* and the compound purified *via* flash chromatography (2:1 Hexane:EtOAc) to afford the title compound as a yellow crystalline solid (1.34 g, 98%).

SMILES CODE: CCN(CC)C1=CC=C([N+]([O-])=O)C=C1 **^{1}H NMR** (400 MHz, Chloroform-*d*) δ 8.10 (d, *J* = 9.5 Hz, 2H), 6.58 (d, *J* = 9.5 Hz, 2H), 3.45 (q, *J* = 7.1 Hz, 4H), 1.23 (t, *J* = 7.1 Hz, 6H) ppm **^{13}C NMR** (101 MHz, Chloroform-*d*) δ 152.24, 136.33, 126.48, 109.85, 44.94, 12.39 ppm **LRMS (+ESI)**: *m/z* 195 $[M+H]^+$, 217 $[M+Na]^+$ **IR** (diamond cell thin film): $\tilde{\nu}$ = 2979, 1572, 1299, 1271 cm^{-1}

4-(*N,N*-Diethylamino)aniline - 76

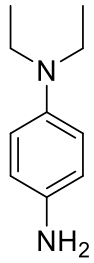

76 was prepared from **75** (500 mg, 2.57 mmol) and Pd/C (50 mg, 10 mol %) according to **general procedure E**. The product was carried through to the next step without further purification.

SMILES CODE: CCN(CC)C1=CC=C(N)C=C1 **^{1}H NMR** (300 MHz, DMSO-d_6) δ 6.74 – 6.25 (m, 4H), 4.40 (s, 2H), 3.09 (q, *J* = 7.0 Hz, 4H), 0.97 (t, *J* = 7.0 Hz, 6H) ppm **^{13}C NMR**

(75 MHz, DMSO-d_6) δ 140.83, 140.16, 117.66, 115.72, 45.66, 12.86 ppm **LRMS (+ESI)**: *m/z* 165 $[M+H]^+$ **IR** (diamond cell thin film): ṽ = 3414, 3345, 2967 cm^{-1}

1-(Phenyldiazenyl)naphthalen-2-ol - 67

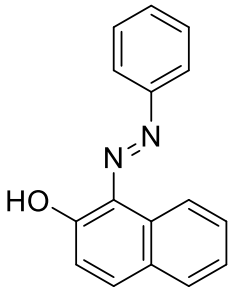

67 was prepared from aniline derivative **85** (97 μL, 1.07 mmol), $NaNO_2$ (82 mg, 1.18 mmol) and **78** (155 mg, 1.07 mmol) according to **general procedure A**. The crude product was recrystallised with MeOH to provide the title compound as needle red crystals (205 mg, 77%).

SMILES CODE: OC1=CC=C(C=CC=C2)C2=C1/N=N/C3=CC=CC=C3 **^{1}H NMR** (500 MHz, Chloroform-*d*) δ 8.57 (d, *J* = 8.2, 1.0 Hz, 1H), 7.76 – 7.72 (m, 3H), 7.71 (s, 1H), 7.60 (d, *J* = 7.9, 1.2 Hz, 1H), 7.58 – 7.53 (m, 1H), 7.51 – 7.45 (m, 2H), 7.39 (ddd, *J* = 8.1, 7.2, 1.2 Hz, 1H), 7.33 – 7.28 (m, 1H), 6.87 (d, *J* = 9.4 Hz, 1H) ppm **^{13}C NMR** (101 MHz, Chloroform-*d*) δ 171.77, 144.87, 140.04, 133.63, 130.10, 129.60, 128.87, 128.62, 128.09, 127.45, 125.72, 124.80, 121.73, 118.63 ppm **LRMS (+APCI)**: *m/z* 249 $[M+H]^+$ **HRMS (+APCI)**: *m/z* calculated $C_{16}H_{12}N_2O$ [M] 248.0950, found 248.0944, calculated $[M+H]^+$ 249.1022, found 249.1022 **IR** (diamond cell thin film): ṽ = 1616, 1548, 1492, 1319, 1204, 1135 cm^{-1} **HPLC** t_R = 31.33 min, 99.30% (254 nm), 99.25% (230 nm)

1-((4-Isopropoxyphenyl)diazenyl)naphthalen-2-ol - 68

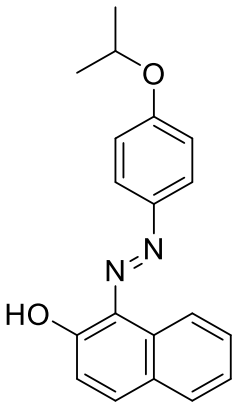

68 was prepared from aniline derivative **86** (98 μL, 0.66 mmol), $NaNO_2$ (50 mg, 0.73 mmol) and **78** (95 mg, 0.66 mmol) according to **general procedure A**. The crude product was purified *via* flash chromatography (5:1 Hexane/EtOAc) to afford the title compound as red crystalline shards (145 mg, 72%).

SMILES CODE: OC1=CC=C(C=CC=C2)C2=C1/N=N/C3=CC=C(OC(C)C)C=C3 **^{1}H-NMR** (500 MHz, Chloroform-*d*): δ 15.70 (s, 1H), 8.72 (d, *J* = 8.3 Hz, 1H), 7.84 – 7.79 (m, 2H), 7.76 (d, *J* = 9.1 Hz, 1H), 7.70 (d, *J* = 8.0, 1.2 Hz, 1H), 7.60 – 7.55 (m, 1H), 7.43 – 7.38 (m, 1H), 7.05 (d, *J* = 9.2 Hz, 1H), 7.02 – 6.99 (m, 2H), 4.64 (hept, *J* = 6.1 Hz, 1H), 1.40 (d, *J* = 6.1 Hz, 6H) ppm **^{13}C NMR** (101 MHz, Chloroform-*d*) δ 161.03, 159.18, 141.66, 136.53, 133.32, 129.53, 128.31, 128.16, 128.10, 124.75, 122.16, 122.14, 121.63, 116.48, 70.42, 22.02 ppm **LRMS (+ESI)***: m/z* 307 $[M+H]^+$, 329 $[M+Na]^+$ **LRMS (-ESI)**: *m/z* 305 $[M-H]^-$ **HRMS (+ESI)**: *m/z* calculated $C_{19}H_{18}N_2O_2$ $[M+H]^+$ 307.1441, found 307.1439 **IR** (diamond cell thin film): $\tilde{\nu}$ = 2973, 1618, 1594, 1294, 1246, 946 cm^{-1} **HPLC** t_R = 33.55 min, 100% (254 nm), 99.22% (230 nm)

4-((2-Hydroxynaphthalen-1-yl)diazenyl)benzonitrile - 69

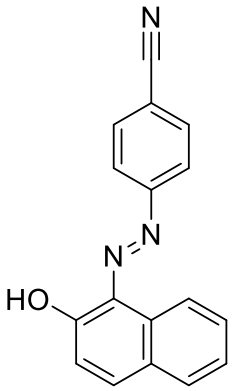

69 was prepared from aniline derivative **87** (100 mg, 0.85 mmol), $NaNO_2$ (64 mg, 0.93 mmol) and **78** (122 mg, 0.85 mmol) according to **general procedure A**. The crude product was purified *via* flash chromatography (2:1 to 1:2 Hexane/DCM) and recrystallised from *n*-BuOH to afford the title compound as an orange-red crystalline solid (218 mg, 94%).

SMILES CODE: OC(C=CC1=C2C=CC=C1)=C2/N=N/C(C=C3)=CC=C3C#N **^{1}H NMR** (400 MHz, Chloroform-*d*) δ 8.42 (d, *J* = 7.9 Hz, 1H), 7.77 – 7.65 (m, 5H), 7.61 – 7.50 (m, 2H), 7.42 (ddd, *J* = 8.2, 7.0, 1.2 Hz, 1H), 6.72 (d, *J* = 9.6 Hz, 1H), 5.30 (s, 1H) ppm **^{13}C NMR** (101 MHz, Chloroform-*d*) δ 179.00, 146.57, 143.02, 133.80, 133.18, 131.58, 129.66, 129.10,

128.55, 127.28, 126.16, 122.35, 118.82, 117.36, 108.64 ppm **LRMS (-ESI)**: *m/z* 271 $[M–H]^-$ **HRMS (+ESI)**: *m/z* calculated $C_{17}H_{11}N_3O$ $[M+H]^+$ 274.0974, found 274.0974 **IR** (diamond cell thin film): ṽ = 2216, 1602, 1550, 1497[1], 1148, 979 cm^{-1} **HPLC** t_R = 26.59 min, 100% (254 nm), 97.68% (230 nm)

1-((4-Hydroxyphenyl)diazenyl)naphthalen-2-ol - 70

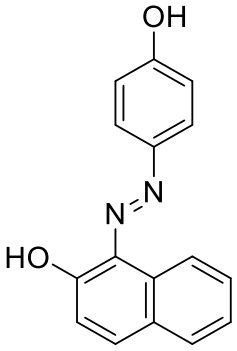

70 was prepared from aniline derivative **88** (100 mg, 0.92 mmol), $NaNO_2$ (70 mg, 1.00 mmol) and **78** (132 mg, 0.92 mmol) according to **general procedure A**. The crude product was purified *via* flash chromatography (1:1 Hexane/EtOAc) to afford the title compound as a dark purple residue (40 mg, 17%).

SMILES CODE: OC1=CC=C(C=CC=C2)C2=C1/N=N/C3=CC=C(O)C=C3 **^{1}H NMR** (400 MHz, Chloroform-*d*) δ 15.64 (s, 1H), 8.63 (d, *J* = 8.3 Hz, 1H), 7.71 (t, *J* = 8.9 Hz, 3H), 7.66 – 7.61 (m, 1H), 7.51 (ddd, *J* = 8.4, 6.8, 1.3 Hz, 1H), 7.34 (td, *J* = 7.4, 6.9, 1.2 Hz, 1H), 6.98 (d, *J* = 9.2 Hz, 1H), 6.94 – 6.87 (m, 2H), 5.20 (s, 1H) ppm **^{13}C NMR** (101 MHz, Chloroform-*d*) δ 161.47, 156.94, 141.98, 136.85, 133.35, 129.54, 128.37, 128.21, 128.18, 124.86, 122.29, 122.22, 121.62, 116.39 ppm **LRMS (-ESI)**: *m/z* 262 $[M–H]^-$ **HRMS (+ESI)**: *m/z* calculated $C_{16}H_{12}N_2O_2$ $[M+Na]^+$ 287.0791, found 287.0786 **IR** (diamond cell thin film): ṽ = ~3100, 1610, 1587, 1228, 1141 cm^{-1} **HPLC** t_R = 27.22 min, 96.51% (254 nm), 97.53% (230 nm)

1-((4-Bromophenyl)diazenyl)naphthalen-2-ol - 71

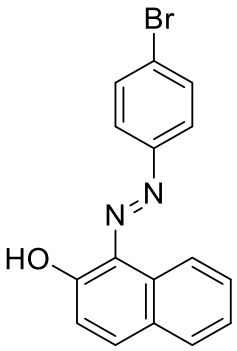

71 was prepared from aniline derivative **89** (100 mg. 0.58 mmol), $NaNO_2$ (44 mg, 0.64 mmol) and **78** (84 mg, 0.58 mmol) according to **general procedure A**. The crude product was purified *via* flash chromatography (5:1 Hexane/EtOAc) to afford the title compound as a red crystalline solid (164 mg, 86%).

SMILES CODE: OC1=CC=C(C=CC=C2)C2=C1/N=N/C3=CC=C(Br)C=C3 **^{1}H NMR** (400 MHz, Chloroform-*d*) δ 16.08 (s, 1H), 8.54 (d, *J* = 8.2 *Hz,* 1H), 7.73 (d, *J* = 9.4 Hz, 2H), 7.64 – 7.59 (m, 3H), 7.56 (ddd, *J* = 8.3, 7.1, 1.3 Hz, 1H), 7.41 (ddd, *J* = 8.1, 7.1, 1.2 Hz, 1H), 6.87 (d, *J* = 9.4 Hz, 2H) ppm **^{13}C NMR** (101 MHz, Chloroform-*d*) δ 171.26, 144.20, 140.30, 133.42, 132.71, 130.34, 129.00, 128.72, 128.23, 125.97, 124.50, 121.79, 120.83, 120.11 ppm **LRMS (-ESI)**: *m/z* 327/329 $[M-H]^-$ **HRMS (+ESI)**: *m/z* calculated $C_{16}H_{11}BrN_2O$ $[M+H]^+$ 327.0128/329.0108, found 327.0126/329.0106 **IR** (diamond cell thin film): $\tilde{\nu}$ = 1619, 1554, 1478, 1249, 1208, 493 cm^{-1} **HPLC** t_R = 31.38 min, 100% (254 nm), 99.55% (230 nm)

1-((4-Fluorophenyl)diazenyl)naphthalen-2-ol - 72

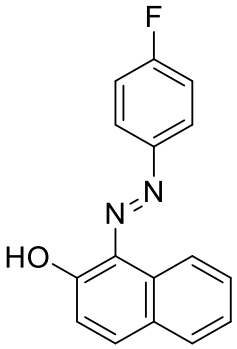

72 was prepared from **90** (85 μL, 0.90 mmol), $NaNO_2$ (68 mg, 0.99 mmol) and **78** (130 mg, 0.90 mmol) according to **general procedure A**. The crude product was purified *via* flash

chromatography (5:1 Hexane/EtOAc) to afford the title compound as a red crystalline solid (198 mg, 83%).

SMILES CODE: OC1=CC=C(C=CC=C2)C2=C1/N=N/C3=CC=C(F)C=C3 **^{1}H NMR** (500 MHz, Chloroform-*d*) δ 15.82 (s, 1H), 8.67 – 8.59 (m, 1H), 7.83 – 7.74 (m, 3H), 7.66 (dd, *J* = 7.9, 1.3 Hz, 1H), 7.60 – 7.55 (m, 1H), 7.44 – 7.39 (m, 1H), 7.23 – 7.16 (m, 2H), 6.97 (d, *J* = 9.4 Hz, 1H) ppm **^{13}C NMR** ($CDCl_3$, 101 MHz) δ 166.15, 163.72, 161.24, 143.04, 138.75, 133.40, 129.91, 128.65, 128.20, 126.99 (d, *J* = 313.7 Hz), 123.27, 121.63, 121.24 (d, *J* = 8.5 Hz), 116.55 (d, *J* = 23.2 Hz) ppm **^{19}F NMR** (376 MHz, Chloroform-*d*) δ -112.52 ppm (1F, s) **LRMS (+ESI)**: *m/z* 267 $[M+H]^+$ **HRMS (+ESI)**: *m/z* calculated $C_{16}H_{11}FN_2O$ $[M+H]^+$ 267.0928, found 267.0927 **IR** (diamond cell thin film): ῡ = 1618, 1595, 1489, 1226, 1202, 1093 cm^{-1} **HPLC** t_R = 33.88 min, 100% (254 nm), 100% (230 nm)

1-((4-Nitrophenyl)diazenyl)naphthalen-2-ol - 92

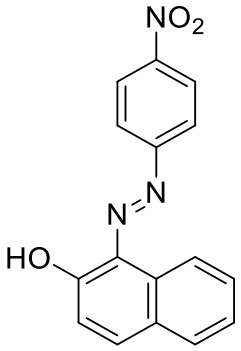

92 was prepared from **91** (100 mg. 0.72 mmol), $NaNO_2$ (55 mg, 0.80 mmol) and **78** (104 mg, 0.72 mmol) according to **general procedure A**. The crude product was purified *via* flash chromatography (2:1 to 1:2 Hexane/DCM) to afford the title compound as a dark red crystalline solid (193.2 mg, 91%).

SMILES CODE: OC1=CC=C(C=CC=C2)C2=C1/N=N/C3=CC=C([N+]([O-])=O)C=C3 **^{1}H NMR** (400 MHz, Chloroform-*d*) δ 16.15 (s, 1H), 8.42 (d, *J* = 8.0 Hz, 1H), 8.36 – 8.27 (m, 2H), 7.73 – 7.66 (m, 3H), 7.59 – 7.50 (m, 2H), 7.47 (d, *J* = 7.3 Hz, 1H), 6.70 (d, *J* = 9.6 Hz, 1H) ppm **^{13}C NMR** (101 MHz, Chloroform-*d*) δ 180.15, 147.98, 144.59, 143.51, 133.07, 132.05, 129.80, 129.19, 128.67, 127.60, 126.35, 125.75, 22.55, 116.63 ppm **LRMS (+APCI)**: *m/z* 294 $[M+H]^+$ **HRMS (+APCI)**: *m/z* calculated $C_{16}H_{11}N_3O_3$ [M] 293.0800, found 263.0798, calculated $[M+H]^+$ 294.0873, found 294.0877 **IR** (diamond cell thin film): ῡ = 3390, 1596, 1502, 1327 cm^{-1}

1-((4-(Diethylamino)phenyl)diazenyl)naphthalen-2-ol - 52

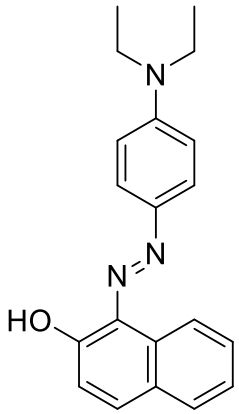

52 was prepared from aniline derivative **76** (500 mg, 3.04 mmol), $NaNO_2$ (231 mg, 3.35 mmol; dissolved in 4 mL H_2O) and **78** (439 mg, 3.04 mmol; dissolved in 7.5 mL H_2O) according to **general procedure A**. The crude product was purified *via* flash chromatography (1:1 Hexane/EtOAc) to afford the title compound as an iridescent purple crystalline solid (623 mg, 60%).

SMILES CODE: CCN(C1=CC=C(/N=N/C2=C(O)C=CC3=C2C=CC=C3)C=C1)CC **^{1}H NMR** (400 MHz, Chloroform-*d*) δ 15.49 (s, 1H), 8.81 (d, *J* = 8.5 Hz, 1H), 7.87 – 7.78 (m, 2H), 7.72 (d, *J* = 9.2, 2H), 7.55 (ddd, *J* = 8.4, 6.9, 1.3 Hz, 1H), 7.38 (ddd, *J* = 8.1, 6.9, 1.2 Hz, 1H), 7.12 (d, *J* = 9.0 Hz, 1H), 6.77 – 6.70 (m, 2H), 3.43 (q, *J* = 7.1 Hz, 4H), 1.22 (t, *J* = 7.1 Hz, 6H) ppm **^{13}C NMR** (101 MHz, Chloroform-*d*) δ 155.29, 149.46, 139.36, 133.51, 132.98, 129.37, 128.24, 128.05, 127.34, 124.06, 123.62, 121.77, 120.81, 111.55, 44.74, 12.68 ppm **LRMS (+ESI)**: *m/z* 320 $[M+H]^+$ **LRMS (-ESI)**: *m/z* 318 $[M-H]^-$ **HRMS (+ESI)**: *m/z* calculated $C_{20}H_{21}N_3O$ $[M+H]^+$ 320.1757, found 320.1752 **IR** (diamond cell thin film): $\tilde{\nu}$ = 2967, 1591, 1554, 1152, 1078 cm^{-1} **HPLC** t_R = 24.00 min, 100% (254 nm), 100% (230 nm)

N,N-Diethyl-4-((2-methoxynaphthalen-1-yl)diazenyl)aniline - 73

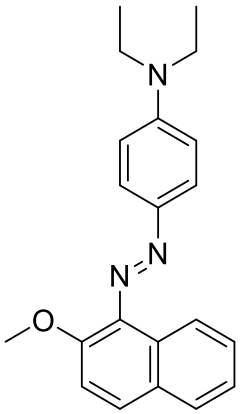

73 was prepared from **52** (57 mg, 0.178 mmol), NaH (8 mg, 0.196 mmol, 60% dispersion in oil) and MeI (111 μL, 1.78 mmol) according to **general procedure D**. The crude product was purified *via* flash chromatography (20:3 Hexane/EtOAc) to afford the title compound as red needle crystals (40 mg, 67%).

SMILES CODE: CCN(C1=CC=C(/N=N/C2=C(OC)C=CC3=C2C=CC=C3)C=C1)CC **^{1}H NMR** (400 MHz, Chloroform-*d*) δ 8.18 (d, *J* = 8.5 Hz, 1H), 8.04 – 7.91 (m, 2H), 7.85 – 7.72 (m, 2H), 7.51 – 7.31 (m, 3H), 6.85 – 6.69 (m, 2H), 3.94 (s, 3H), 3.48 (q, *J* = 7.1 Hz, 4H), 1.25 (t, *J* = 7.1 Hz, 6H) ppm **^{13}C NMR** (101 MHz, Chloroform-*d*) δ 150.23, 147.61, 144.02, 137.85, 129.46, 128.71, 128.48, 127.69, 126.78, 125.15, 124.12, 123.35, 115.26, 110.96, 57.64, 44.76, 12.68 ppm **LRMS (+ESI)**: *m/z* 334 $[M+H]^+$, 356 $[M+Na]^+$ **HRMS (+ESI)**: *m/z* calculated $C_{21}H_{23}N_3O$ $[M+H]^+$ 334.1914, found 334.1908 **IR** (diamond cell thin film): $\tilde{\nu}$ = 2959, 1589, 1533, 1352, 1175, 1136, 1079 cm^{-1} **HPLC** t_R = 23.45 min, 100% (254 nm), 99.24% (230 nm)

6.4 Chapter 3 Experimental and Characterisation

1-(2-Methoxynaphthalen-1-yl)ethan-1-one - 105

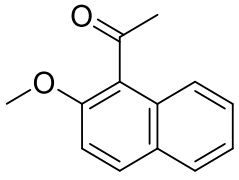

105 was prepared from **104** (1.00 g, 5.37 mmol), NaH (85 mg, 5.91 mmol, 60% dispersion in oil) and MeI (1.00 mL, 16.11 mmol) according to **general procedure D**. The crude product

was purified *via* flash chromatography (20:1 Hexane/EtOAc) to afford the title compound as pale yellow crystalline solid (882 mg, 82%).

SMILES CODE: COC1=C(C(C)=O)C2=C(C=CC=C2)C=C **^{1}H NMR** (300 MHz, Chloroform-*d*) δ 7.88 (d, *J* = 9.1 Hz, 1H), 7.82 – 7.83 (m, 2H), 7.47 (ddd, *J* = 8.4, 6.8, 1.4 Hz, 1H), 7.36 (ddd, *J* = 8.1, 6.8, 1.2 Hz, 1H), 7.27 (d, *J* = 9.1 Hz, 1H), 3.97 (s, 3H), 2.64 (s, 3H) ppm **^{13}C NMR** (75 MHz, Chloroform-*d*) δ 205.13, 153.98, 131.47, 130.33, 128.88, 128.17, 127.69, 125.16, 124.11, 123.66, 112.82, 56.44, 32.70 ppm **LRMS (+APCI)**: *m/z* 201 $[M+H]^+$ **HRMS (+APCI)**: *m/z* calculated $C_{13}H_{12}O_2$ [M] 200.0837, found 200.0832, calculated $[M+H]^+$ 201.0910, found 201.0910 **IR** (diamond cell thin film): ṽ = 1685, 1274, 1249 cm^{-1}

3-(2-Methoxynaphthalen-1-yl)-1-phenyl-1*H*-pyrazole - 114

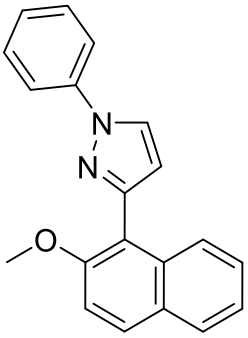

114 was prepared from **105** (100 mg, 0.50 mmol), NaH (24 mg, 1.00 mmol, 60% dispersion in oil), methyl formate (153 μL, 2.49 mmol) and phenyl hydrazine (49 μL, 0.50 mmol) according to **general procedure F**. The crude product was purified *via* flash chromatography (1:0 to 20:1 Hexane/EtOAc) to afford the title compound as an off-white crystalline solid (45 mg, 30%).

SMILES CODE: COC(C=CC1=C2C=CC=C1)=C2C3=NN(C4=CC=CC=C4)C=C3 **^{1}H NMR** (400 MHz, Chloroform-*d*) δ 8.10 (d, *J* = 2.4 Hz, 1H), 7.99 (d, *J* = 8.5 Hz, 1H), 7.90 (d, *J* = 9.1 Hz, 1H), 7.81 (m, 3H), 7.49 – 7.42 (m, 2H), 7.41 – 7.32 (m, 3H), 7.31 – 7.26 (m, 1H), 6.67 (d, *J* = 2.4 Hz, 1H), 3.91 (s, 3H) ppm **^{13}C NMR** (101 MHz, Chloroform-*d*) δ 155.34, 148.66, 140.37, 133.94, 130.17, 129.35, 129.21, 127.82, 126.96, 126.72, 126.13, 125.50, 123.68, 119.06, 117.15, 113.73, 110.62, 56.92 ppm **LRMS (+APCI)**: *m/z* 301 [M+H] **HRMS (+APCI)**: *m/z* calculated $C_{20}H_{16}N_2O$ [M] 300.1263, found 300.1256, calculated $[M+H]^+$ 301.1335, found 301.1335 **IR** (diamond cell thin film): ṽ = 1620, 1594, 1268, 1251 cm^{-1} **HPLC** t_R = 28.95 min, 98.70% (254 nm), 96.99% (230 nm)

5-(2-Methoxynaphthalen-1-yl)-1-phenyl-1*H*-pyrazole - 115

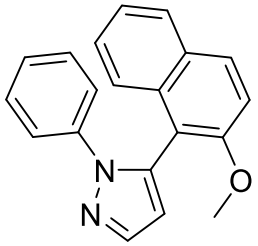

115 was prepared from **105** (100 mg, 0.50 mmol), NaH (24 mg, 1.00 mmol, 60% dispersion in oil), methyl formate (153 μL, 2.49 mmol) and phenyl hydrazine (49 μL, 0.50 mmol) according to **general procedure F**. The crude product was purified *via* flash chromatography (1:0 to 20:1 Hexane/EtOAc) to afford the title compound as an off-white crystalline solid (105 mg, 70%).

SMILES CODE: COC(C=CC1=C2C=CC=C1)=C2C3=CC=NN3C4=CC=CC=C4 **^{1}H NMR** ($CDCl_3$, 400 MHz) δ 7.92 – 7.86 (m, 2H), 7.82 (d, *J* = 8.1 Hz, 1H), 7.74 (d, *J* = 8.4 Hz, 1H), 7.44 (ddd, *J* = 8.4, 6.8, 1.4 Hz, 1H), 7.38 (ddd, *J* = 8.1, 6.8, 1.3 Hz, 1H), 7.22 – 7.11 (m, 6H), 6.53 (d, *J* = 1.8 Hz, 1H), 3.51 (s, 3H) ppm **^{13}C NMR** (101 MHz, Chloroform-*d*) δ 154.84, 140.61, 140.21 136.98, 133.65, 131.13, 128.83, 128.35, 128.07, 127.30, 126.76, 124.49, 123.96, 123.40, 113.82, 113.09, 109.97, 55.95 ppm **LRMS (+APCI)**: *m/z* 301 $[M+H]^+$, 600 [2M] **HRMS (+APCI)**: *m/z* calculated $C_{20}H_{16}N_2O$ [M] 300.1263, found 300.1256*,* calculated $[M+H]^+$ 301.1335, found 300.1335 **IR** (diamond cell thin film): ṽ = 1620, 1594, 1269, 1246 cm^{-1} **HPLC** t_R = 17.37 min, 98.46% (254 nm), 97.30% (230 nm)

5-(2-Methoxynaphthalen-1-yl)-1-(4-nitrophenyl)-1*H*-pyrazole - 116

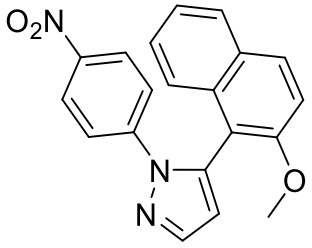

116 was prepared from **105** (200 mg, 1.00 mmol), NaH (24 mg, 2.00 mmol, 60% dispersion in oil), methyl formate (153 μL, 5.00 mmol) and **111** (185 mg, 1.00 mmol) according to **general procedure F**. The crude product was purified *via* flash chromatography (1:0 to 20:1 Hexane/EtOAc) to afford the title compound as a yellow crystalline solid (345 mg, quant.).

SMILES CODE: COC(C=CC1=C2C=CC=C1)=C2C3=CC=NN3C4=CC=CC=C4 **^{1}H NMR** (300 MHz, Chloroform-*d*) δ 8.03 (d, *J* = 9.1 Hz, 2H), 7.99 – 7.92 (m, 2H), 7.86 (d, *J* = 1.4 Hz, 1H), 7.73 – 7.64 (m, 1H), 7.51 – 7.42 (m, 2H), 7.39 (d, *J* = 9.1 Hz, 2H), 7.21 (d, *J* = 9.1 Hz, 1H), 6.58 (d, *J* = 1.7 Hz, 1H), 3.57 (s, 3H) ppm **^{13}C NMR** (75 MHz, Chloroform-*d*) δ 154.70, 145.63, 145.52, 141.70, 137.69, 133.26, 131.89, 128.93, 128.36, 127.80, 124.31, 124.20, 124.05, 122.76, 112.86, 112.75, 111.54, 55.98 ppm **LRMS (+APCI)**: *m/z* 346 $[M+H]^+$ **HRMS (+APCI)**: *m/z* calculated $C_{20}H_{15}N_3O_3$ [M] 345.1113, found 345.1106, calculated $[M+H]^+$ 346.1186, found 346.1185 **IR** (diamond cell thin film): ν̃ = 1594, 1502, 1498, 1334, 1270, 1253 cm^{-1}

4-(5-(2-Methoxynaphthalen-1-yl)-1*H*-pyrazol-1-yl)aniline - 117

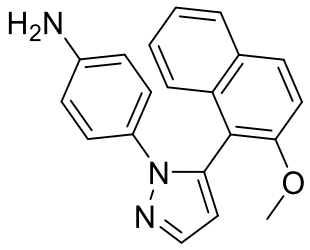

117 was prepared from **116** (173 mg, 0.50 mmol) and Pd/C (17 mg, 10 mol %) according to **general procedure E**. The crude product was purified *via* flash chromatography (5:1 Hexane/EtOAc) to afford the title compound as a light purple oil (158 mg, quant.).

SMILES CODE: COC(C=CC1=C2C=CC=C1)=C2C3=CC=NN3C4=CC=C(N)C=C4 **^{1}H NMR** (300 MHz, Chloroform-*d*) δ 7.87 (d, *J* = 9.1 Hz, 1H), 7.82 (d, *J* = 1.8 Hz, 1H), 7.80 (d, *J* = 1.4 Hz, 1H), 7.67 (d, *J* = 8.4 Hz, 1H), 7.48 – 7.30 (m, 2H), 7.17 (d, *J* = 9.1 Hz, 1H), 6.96 (d, *J* = 8.7 Hz, 2H), 6.47 (d, *J* = 1.8 Hz, 1H), 6.41 (d, *J* = 8.7 Hz, 2H), 3.60 (s, 3H) ppm, $N\underline{H_2}$ proton signals not observed **^{13}C NMR** (101 MHz, Chloroform-*d*) δ 154.93, 145.23, 139.55, 136.88, 133.82, 132.25, 130.91, 128.75, 127.98, 127.14, 124.98, 124.58, 123.84, 114.60, 114.06, 113.13, 109.17, 56.13 ppm **LRMS (+ESI)**: *m/z* 316 $[M+H]^+$, 338 $[M+Na]^+$, 653 $[2M+Na]^+$ **LRMS (-ESI)**: *m/z* 314 $[M-H]^-$ **HRMS (+ESI)**: *m/z* calculated $C_{20}H_{17}N_3O$ $[M+H]^+$ 316.1444, found 316.1446 **IR** (diamond cell thin film): ν̃ = 3340, 3264, 1623, 1593, 1270, 1251 cm^{-1}

***N,N*-Diethyl-4-(5-(2-methoxynaphthalen-1-yl)-1*H*-pyrazol-1-yl)aniline- 118**

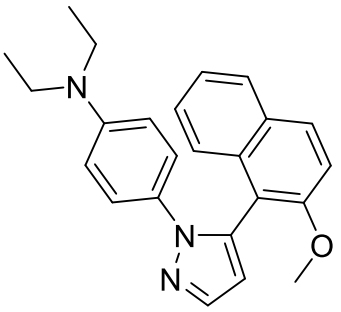

118 was prepared from **117** (158 mg, 0.50 mmol), EtI (121 μL, 1.50 mmol) and K_2CO_3 (138 mg, 1.00 mmol) in acetone according to **general procedure C**. The crude product was purified *via* flash chromatography (10:1 to 5:1 Hexane/EtOAc as eluents) to afford the title compound as an off-white crystalline solid (186 mg, 83%).

SMILES CODE: COC(C=CC1=C2C=CC=C1)=C2C3=CC=NN3C4=CC=C(N(CC)CC)C=C4 **^{1}H NMR** (400 MHz, Chloroform-*d*) δ 7.86 (d, *J* = 9.1 Hz, 1H), 7.82 (d, *J* = 1.8 Hz, 1H), 7.79 (d, *J* = 8.1 Hz, 1H), 7.68 (d, *J* = 8.4 Hz, 1H), 7.41 (ddd, *J* = 8.4, 6.8, 1.4 Hz, 1H), 7.35 (ddd, *J* = 8.0, 6.8, 1.3 Hz, 1H), 7.18 (d, *J* = 9.1 Hz, 1H), 7.02 (d, *J* = 9.1 Hz, 2H), 6.46 (d, *J* = 1.8 Hz, 1H), 6.44 – 6.35 (m, 2H), 3.60 (s, 3H), 3.23 (q, *J* = 7.1 Hz, 4H), 1.05 (t, *J* = 7.0 Hz, 6H) ppm **^{13}C NMR** (101 MHz, Chloroform-*d*) δ 155.02, 146.77, 139.34, 136.71, 133.97, 130.76, 129.60, 128.77, 127.91, 127.06, 124.80, 124.72, 123.79, 114.43, 113.29, 111.36, 108.98, 56.21, 44.37, 12.41 ppm **LRMS (+ESI)**: *m/z* 372 $[M+H]^+$, 394 $[M+Na]^+$, 742 $[2M+H]^+$, 765 $[2M+Na]^+$ **HRMS (+ESI)**: *m/z* calculated $C_{24}H_{25}N_3O$ $[M+H]^+$ 372.2070, found 372.2071 **IR** (diamond cell thin film): $\tilde{\nu}$ = 2963, 2920, 2861, 1616, 1592, 1266, 1249 cm^{-1} **HPLC** t_R = 12.48 min, 99.29% (254 nm), 97.93% (230 nm)

***N,N*-(Diethylamino)benzenediazonium tetrafluoroborate - 128**

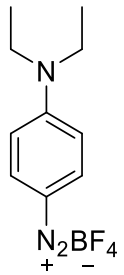

128 was prepared from aniline derivative **76** (169 mg, 1.03 mmol), aq. HBF_4 (672 μL, 5.14 mmol, 48% wt adjusted) and isopentyl nitrite (235 μL, 1.75 mmol) in AcOH according

to **general procedure B**. The crystals were filtered off *in vacuo*, washed with Et_2O and dried on air to afford the title compound as a green crystalline solid (222 mg, 82%).

SMILES CODE: CCN(CC)C1=CC=C([N+]#N)C=C1.F[B-](F)(F)F **^{1}H NMR** (400 MHz, DMSO-d_6) δ 8.22 (d, J = 9.7 Hz, 2H), 7.09 (d, J = 9.7 Hz, 2H), 3.64 (q, J = 7.1 Hz, 4H), 1.18 (t, J = 7.1 Hz, 6H) ppm **^{13}C NMR** (101 MHz, DMSO-d_6) δ 155.08, 134.86, 114.31, 89.08, 45.83, 12.62 ppm **^{19}F NMR** (376 MHz, DMSO-d_6) δ -148.29, -148.34 (d, J = 2.3 Hz) ppm **^{11}B NMR** (128 MHz, DMSO-d_6) δ -1.27 ppm **IR** (diamond cell thin film): $\tilde{\nu}$ = 2945, 1551, 1027 cm^{-1}

Benzenediazonium tetrafluoroborate - 129

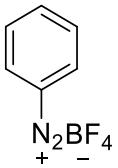

129 was prepared from aniline derivative **85** (147 μL, 1.61 mmol), aq. HBF_4 (1.05 mL, 8.05 mmol, 48% wt adjusted) and isopentyl nitrite (368 μL, 2.74 mmol) in AcOH according to **general procedure B**. The crystals were filtered off *in vacuo*, washed with Et_2O and dried on air to afford the title compound as an off-white crystalline solid (271 mg, 88%).

SMILES CODE: N#[N+]C1=CC=CC=C1.F[B-](F)(F)F **^{1}H NMR** (400 MHz, DMSO-d_6) δ 8.67 (d, J = 1.5 Hz, 2H), 8.26 (t, J = 1.2 Hz, 1H), 7.98 (t, J = 2.2 Hz, 3H) ppm **^{13}C NMR** (101 MHz, DMSO-d_6) δ 141.31, 133.12, 131.70, 129.74 ppm **^{19}F NMR** (376 MHz, DMSO-d_6) δ -148.22, -148.28 (d, J = 2.4 Hz) ppm **^{11}B NMR** (128 MHz, DMSO-d_6) δ -1.25 ppm **IR** (diamond cell thin film): $\tilde{\nu}$ = 1569, 1462, 1026 cm^{-1}

4-Isopropoxybenzenediazonium tetrafluoroborate - 130

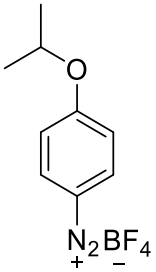

130 was prepared from the aniline derivative **86** (100 μL, 0.67 mmol), aq. HBF_4 (439 μL, 3.36 mmol, 48% wt adjusted) and isopentyl nitrite (153 μL, 1.14 mmol) in AcOH according

to **general procedure B**. The crystals were filtered off *in vacuo*, washed with Et_2O and dried on air to afford the title compound as a light pink crystalline solid (153 mg, 93%).

SMILES CODE: CC(C)OC1=CC=C([N+]#N)C=C1.F[B-](F)(F)F **^{1}H NMR** (400 MHz, DMSO-d_6) δ 8.59 (d, J = 9.4 Hz, 2H), 7.47 (d, J = 9.4 Hz, 2H), 5.00 (hept, J = 6.1 Hz, 1H), 1.36 (d, J = 6.0 Hz, 6H) ppm **^{13}C NMR** (101 MHz, DMSO-d_6) δ 167.83, 136.72, 118.53, 102.94, 73.46, 21.80 ppm **^{19}F NMR** (376 MHz, DMSO-d_6) δ -148.27, -148.33 (d, J = 2.1 Hz) ppm **^{11}B NMR** (128 MHz, DMSO-d_6) δ -1.29 ppm **IR** (diamond cell thin film): $\tilde{\nu}$ = 3120, 3106, 2996, 2983, 2249, 1578, 1282, 1086, 1030 cm^{-1}

4-Cyanobenzenediazonium tetrafluoroborate - 131

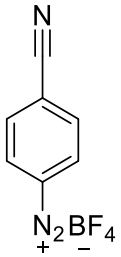

131 was prepared from aniline derivative **87** (150 mg, 1.27 mmol), aq. HBF_4 (830 μL, 6.35 mmol, 48% wt adjusted) and isopentyl nitrite (206 μL, 1.53 mmol) in AcOH according to **general procedure B**. The crystals were filtered off *in vacuo*, washed with Et_2O and dried on air to afford the title compound as a white crystalline solid (247 mg, 90%).

SMILES CODE: N#CC1=CC=C([N+]#N)C=C1. [B-](F)(F)F **^{1}H NMR** (400 MHz, DMSO-d_6) δ 8.85 (d, J = 9.0 Hz, 2H), 8.47 (d, J = 9.0 Hz, 2H) ppm **^{13}C NMR** (101 MHz, DMSO-d_6) δ 135.28, 133.49, 122.25, 121.50, 116.80 ppm **^{19}F NMR** (376 MHz, DMSO-d_6) δ -148.20, -148.25 (d, J = 2.2 Hz) ppm **^{11}B** NMR (128 MHz, DMSO-d_6) δ -1.32 ppm **IR** (diamond cell thin film): $\tilde{\nu}$ = 2289, 1587, 1297, 1031 cm^{-1}

4-Hydroxybenzenediazonium tetrafluroborate - 132

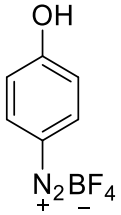

132 was prepared from aniline derivative **88** (152 mg, 1.40 mmol), aq. HBF_4 (910 μL, 6.96 mmol, 48% wt adjusted) and isopentyl nitrite (318 μL, 2.37 mmol) in AcOH according to **general procedure B**. The crude product was carried through to the next reaction without further purification.

SMILES CODE: OC1=CC=C([N+]#N)C=C1.F[B-](F)(F)F

4-Bromobenzenediazonium tetrafluoroborate - 133

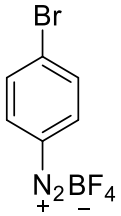

133 was prepared from aniline derivative **89** (104 mg, 0.75 mmol), 48% aq. HBF_4 (492 μL, 3.76 mmol) and isopentyl nitrite (172 μL, 1.28 mmol) in AcOH according to **general procedure B**. The crystals were filtered off *in vacuo*, washed with Et_2O and dried on air to afford the title compound as a white crystalline solid (131 mg, 64%).

SMILES CODE: BrC1=CC=C([N+]#N)C=C1.F[B-](F)(F)F **^{1}H NMR** (400 MHz, DMSO-d_6) δ 8.59 (d, J = 9.0 Hz, 2H), 8.27 (2H, J = 9.0 Hz, d) ppm **^{13}C NMR** (101 MHz, DMSO-d_6) δ 137.01, 135.00, 134.43, 115.63 ppm **^{19}F NMR** (376 MHz, DMSO-d_6) δ -148.26, -148.31 (d, J = 2.4 Hz) ppm **^{11}B NMR** (128 MHz, DMSO-d_6) δ -1.31 ppm **IR** (diamond cell thin film): $\tilde{\nu}$ = 3002, 2289, 1554, 1032, 521 cm^{-1}

4-Azido-*N,N*-diethylaniline - 134

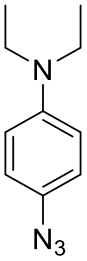

134 was prepared from diazonium tetrafluoroborate salt derivative **128** (222 mg, 0.84 mmol) and NaN_3 (60 mg, 0.93 mmol) according to **general procedure G**. The crude product was carried through to the next reaction without further purification.

SMILES CODE: CCN(CC)C1=CC=C(N=[N+]=[N-])C=C1

Azidobenzene - 135

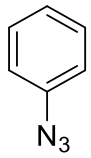

135 was prepared from the diazonium tetrafluoroborate salt derivative **129** (271 mg, 1.41 mmol) and NaN_3 (101 mg, 1.55 mmol) according to **general procedure G**. The crude product was carried through to the next reaction without further purification.

SMILES CODE: [N-]=[N+]=NC1=CC=CC=C1

1-Azido-4-isopropoxybenzene - 136

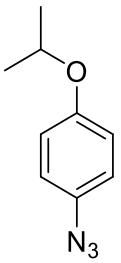

136 was prepared from the diazonium tetrafluoroborate salt derivative **130** (153 mg, 0.61 mmol) and NaN_3 (44 mg, 0.67 mmol) according to **general procedure G**. The crude product was carried through to the next reaction without further purification.

SMILES CODE: CC(C)OC1=CC=C(N=[N+]=[N-])C=C1

4-Azidobenzonitrile - 137

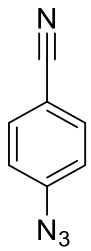

137 was prepared from diazonium tetrafluoroborate salt derivative **131** (247 mg, 1.14 mmol) and NaN_3 (81 mg, 1.25 mmol) according to **general procedure G**. The crude product was carried through to the next reaction without further purification.

SMILES CODE: N#CC1=CC=C(N=[N+]=[N-])C=C1

4-Azidophenol - 138

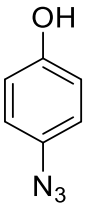

138 was prepared from diazonium tetrafluoroborate salt derivative **132** (210 mg, 1.01 mmol) and NaN_3 (72 mg, 1.11 mmol) according to **general procedure G**. The crude product was carried through to the next reaction without further purification.

SMILES CODE: OC1=CC=C(N=[N+]=[N-])C=C1

1-Azido-4-bromobenzene - 139

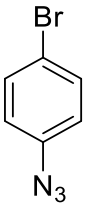

139 was prepared from diazonium tetrafluoroborate salt derivative **133** (131 mg, 0.48 mmol) and NaN_3 (35 mg, 0.53 mmol) according to **general procedure G**. The crude product was carried through to the next reaction without further purification.

SMILES CODE: BrC1=CC=C(N=[N+]=[N-])C=C1

1-Bromonaphthalen-2-ol - 140

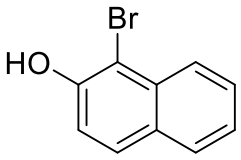

78 (1.00 g, 6.94 mmol) was dissolved in $CHCl_3$ (20 mL). NBS was then added (1.24 g, 6.94 mmol) and stirred at room temperature for 24 h. The resultant solution was filtered to remove NBS precipitate. Subsequently, the filtrate washed with sodium thiosulphate (1 × 15 mL), extracted with $CHCl_3$ (3 × 15 mL), dried over $MgSO_4$ and concentrated *in vacuo*.

The crude product was purified *via* flash chromatography (19:1 Hexane/EtOAc) to afford the title compound as a brown crystalline solid (1.45 g, 94%).

SMILES CODE: BrC1=C2C(C=CC=C2)=CC=C1 **^{1}H NMR** (300 MHz, Chloroform-*d*) δ 8.06 (d, *J* = 8.5 Hz, 1H), 7.89 – 7.74 (m, 2H), 7.60 (ddd, *J* = 8.4, 6.9, 1.3 Hz, 1H), 7.42 (ddd, *J* = 8.1, 6.9, 1.2 Hz, 1H), 7.31 (d, *J* = 5.3 Hz, 1H), 5.96 (s, 1H) ppm **^{13}C NMR** (101 MHz, Chloroform-*d*) δ 150.62, 132.33, 129.71, 129.34, 128.22, 127.85, 125.34, 124.15, 117.18, 106.15 ppm **LRMS (-ESI)**: *m/z* 220/222 $[M-H]^-$ **IR** (diamond cell thin film): ṽ = 3264, 517 cm^{-1}

1-Bromo-2-methoxynaphthalene - 141

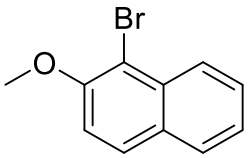

141 was prepared from **140** (1.00 g, 4.48 mmol), NaH (326 mg, 7.6 mmol, 60% dispersion in oil) and MeI (474 μL, 7.6 mmol) according to **general procedure D**. The crude product was purified *via* flash chromatography (19:1 Hexane/EtOAc) to afford the title compound as a brown crystalline solid (1.06 g, quant.).

SMILES CODE: BrC1=C2C(C=CC=C2)=CC=C1OC **^{1}H NMR** (400 MHz, Chloroform-*d*) δ 8.22 (d, *J* = 8.6 Hz, 1H), 7.85 – 7.77 (m, 2H), 7.56 (ddd, *J* = 8.2, 6.8, 1.2 Hz, 1H), 7.39 (ddd, *J* = 8.0, 6.8, 1.1 Hz, 1H), 7.26 (d, *J* = 5.3 Hz, 1H), 4.04 (s, 3H) ppm **^{13}C NMR** (101 MHz, Chloroform-*d*) δ 153.81, 133.18, 129.87, 128.98, 128.05, 127.75, 126.17, 124.35, 113.71, 108.76, 57.11 ppm **LRMS (+APCI)**: *m/z* 237/239 $[M+H]^+$ **IR** (diamond cell thin film): ṽ = 2922, 1268, 1060, 516 cm^{-1}

1-Iodonaphthalen-2-ol - 142

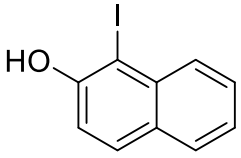

78 (500 mg, 3.47 mmol) was dissolved in MeCN (50 mL). NIS was then added (780 mg, 3.47 mmol) alongside TsOH (600 mg, 3.47 mmol) and stirred at room temperature for 6 h. Upon completion, the solvent was removed under a stream of N_2. The crude residue was washed with sodium thiosulphate (1 × 15 mL) extracted with EtOAc (3 × 15 mL), and dried over $MgSO_4$ and concentrated *in vacuo*. The crude product was purified *via* flash chromatography (19:1 Hexane/EtOAc) to afford the title compound as an off-white crystalline solid (889 mg, 95%).

SMILES CODE: OC1=CC=C(C=CC=C2)C2=C1I **^{1}H NMR** (400 MHz, Chloroform-*d*) δ 7.92 (d, *J* = 8.5, 1H), 7.78 – 7.70 (m, 2H), 7.54 (ddd, *J* = 8.2, 6.9, 1.3 Hz, 1H), 7.38 (ddd, *J* = 8.0, 6.9, 1.1 Hz, 1H), 7.25 (d, *J* = 6.1 Hz, 1H), 5.78 (s, 1H) ppm **^{13}C NMR** (101 MHz, Chloroform-*d*) δ 153.78, 134.81, 130.61, 130.26, 129.70, 128.29, 128.21, 124.18, 116.45, 86.21 ppm **LRMS (-ESI)**: *m/z* 268 $[M-H]^-$ **IR** (diamond cell thin film): ṽ = 3221, 511 cm^{-1}

1-Iodo-2-methoxynaphthalene - 143

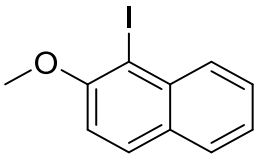

143 was prepared from **142** (500 mg, 1.85 mmol), NaH (135 mg, 3.14 mmol, 60% dispersion in oil) and MeI (196 μL, 3.14 mmol) according to **general procedure D**. The crude product was purified *via* flash chromatography (19:1 Hexane/EtOAc) to afford the title compound as an off-white crystalline solid (525 mg, quant.).

SMILES CODE: COC1=CC=C(C=CC=C2)C2=C1I **^{1}H NMR** (400 MHz, Chloroform-*d*) δ 8.14 (d, *J* = 8.6, 1H), 7.82 (d, *J* = 8.9 Hz, 1H), 7.73 (d, *J* = 8.2, 1H), 7.53 (ddd, *J* = 8.3, 6.8, 1.3 Hz, 1H), 7.37 (ddd, *J* = 8.0, 6.8, 1.1 Hz, 1H), 7.20 (d, *J* = 8.9 Hz, 1H), 4.02 (s, 3H) ppm **^{13}C NMR** (101 MHz, Chloroform-*d*) δ 156.69, 135.67, 131.21, 130.36, 129.94, 128.19, 128.11, 124.36, 113.00, 87.77, 57.26 ppm **LRMS (+APCI)**: *m/z* 284 $[M+H]^+$ **HRMS (+APCI)**: *m/z* calculated $C_{11}H_9IO$ [M] 283.9698, found 283.9692, calculated $[M+H]^+$ 284.9771, found 284.9770 **IR** (diamond cell thin film): ṽ = 2955, 1263, 1058, 510 cm^{-1}

((2-Methoxynaphthalen-1-yl)ethynyl)trimethylsilane) - 144

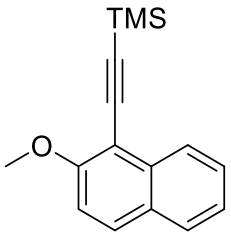

Method 1:

141 (106 mg, 0.45 mmol), Pd_2dba_3 (21 mg, 0.02 mmol), XPhos (42 mg, 0.08 mmol), CuI (4 mg, 0.02 mmol) and $(i\text{-prop})_2NH_2$ (286 μL, 2.04 mmol) were dissolved in toluene (5 mL) under stirring and degassed with N_2 for 30 mins. Following this, TMS-acetylene (62 μL, 0.45 mmol) was added and the solution heated at 40 °C. The reaction was monitored *via* TLC and upon completion the solvent was removed under a stream of N_2 overnight. The crude residue was then up taken in water (1 × 15 mL), extracted with EtOAc (3 × 15 mL), dried over $MgSO_4$ and concentrated *in vacuo.* The crude product was purified *via* flash chromatography (Hexane) to afford the title compound as an off-white crystalline solid (91 mg, 80%).

Method 2:

143 (1.00 g, 3.52 mmol), $PdCl_2(PPh_3)_2$ (247 mg, 0.35 mmol) and CuI (40 mg, 0.21 mmol) were dissolved in Et_3N (10 mL) with stirring and degassed with N_2 for 30 mins. Following this, TMS-acetylene (1.00 mL, 7.04 mmol) was added and the solution heated at 40 °C. The reaction was monitored *via* TLC and upon completion the solvent was removed under a stream of N_2 overnight. The crude residue was then up taken in water (1 × 30 mL), extracted with EtOAc (3 × 30 mL), dried over $MgSO_4$ and concentrated *in vacuo.* The crude product was purified *via* flash chromatography (Hexane) to afford the title compound as an off-white crystalline solid (842 mg, 94%).

SMILES CODE: COC1=CC=C(C=CC=C2)C2=C1C#C[Si](C)(C)C **^{1}H NMR** (300 MHz, DMSO-d_6) δ 8.09 (d, J = 8.5 Hz, 1H), 8.00 (d, J = 9.1 Hz, 1H), 7.91 (d, J = 8.2 Hz, 1H), 7.60 (t, J = 7.7 Hz, 1H), 7.47 – 7.37 (m, 2H), 3.97 (s, 3H), 0.31 (s, 9H) ppm **^{13}C NMR** (75 MHz, DMSO-d_6) δ 160.11, 134.63, 131.64, 129.15, 128.68, 128.54, 124.92, 114.06, 105.26, 104.47, 100.60, 64.23, 57.14, 0.93 ppm **LRMS (+APCI)**: *m/z* 255 $[M+H]^+$ **HRMS (+APCI)**: *m/z*

calculated $C_{16}H_{18}OSi$ [M] 254.1127, found 254.1121, calculated $[M+H]^+$ 255.1200, found 255.1196 **IR** (diamond cell thin film): $\tilde{\nu}$ = 2140, 1272, 1246, 838 cm^{-1}

1-Ethynyl-2-methoxynaphthalene - 145

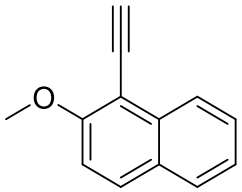

144 (842 mg, 3.32 mmol) was dissolved in MeOH (10 mL) alongside TBAF (4.98 mL, 4.98 mmol, 1.0 M in THF) and stirred at room temperature. The reaction was monitored *via* TLC and upon completion the solvent was removed under a stream of N_2 overnight. The crude residue was then up taken in water (1 × 15 mL), extracted with EtOAC (3 × 30 mL), washed with brine (1 × 15 mL), dried over $MgSO_4$ and concentrated *in vacuo.* The crude product was purified *via* flash chromatography (19:1 Hexane/EtOAc) to afford the title compound as an off-white crystalline solid (555 mg, 92%).

SMILES CODE: COC1=CC=C(C=CC=C2)C2=C1C#C **^{1}H NMR** (400 MHz, DMSO-d_6) δ 8.27 (d, *J* = 8.5 Hz, 1H), 7.85 (d, *J* = 9.1 Hz, 1H), 7.79 (d, *J* = 8.2 Hz, 1H), 7.55 (ddd, *J* = 8.3, 6.8, 1.3 Hz, 1H), 7.38 (ddd, *J* = 8.1, 6.8, 1.2 Hz, 1H), 7.25 (d, *J* = 3.3 Hz, 1H), 4.05 (s, 3H), 3.75 (s, 1H) ppm **^{13}C NMR** (101 MHz, DMSO-d_6) δ 160.13, 134.44, 131.17, 128.82, 128.40, 128.17, 124.65, 124.63, 113.78, 104.52, 90.27, 78.55, 56.78 ppm **LRMS (+APCI)**: *m/z* 183 $[M+H]^+$, 365 $[2M+H]^+$, 547 $[3M+H]^+$ **HRMS (+APCI)**: *m/z* calculated $C_{13}H_{10}O$ [M] 182.0732, found 182.0726, calculated $[M+H]^+$ 183.0804, found 183.0803 **IR** (diamond cell thin film): $\tilde{\nu}$ = 3257, 2359, 1272, 1253 cm^{-1}

***N,N*-Diethyl-4-(4-(2-methoxynaphthalen-1-yl)-1*H*-1,2,3-triazol-1-yl)aniline - 146**

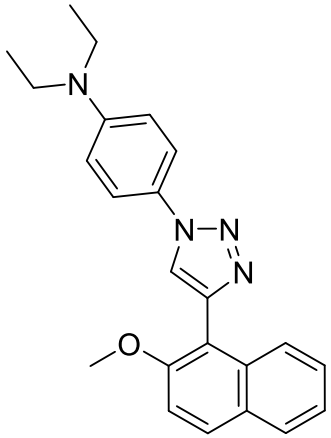

To a three-neck flask affixed with a condenser was added CuI (8 mg, 0.042 mmol), sodium ascorbate (84 mg, 0.42 mmol) and **158** (20 mg, 0.038 mmol). A mixture of degassed THF and water (4:1, 5 mL) was added and the mixture was stirred under N_2 at rt for 45 min, giving a homogeneous solution. To this was added **145** (77 mg, 0.42 mmol) followed by the azido derivative **134** (80 mg, 0.42 mmol). The mixture was heated to 75 ºC and stirred for 8 h under N_2. The mixture was allowed to cool to room temperature under N_2 and quickly poured into a separatory funnel containing EtOAc (10 mL), brine (10 mL) and a solution of 50 mM EDTA in NH_3/NH_4Cl buffer (2 M, pH 9.5, 10 mL). The aqueous layer was collected and the organic layer was extracted twice more with an identical brine/buffer mixture (20 mL). The organic phase was dried over MgSO4 and concentrated *in vacuo*. The crude product was purified *via* flash chromatography (20:1 to 20:3 Hexane/EtOAc) give the title compound as a brown crystalline solid (101 mg, 64%).

SMILES CODE: CN(CC)C(C=C1)=CC=C1N2N=NC(C3=C(OC)C=CC4=C3C=CC=C4)=C2 **^{1}H NMR** (400 MHz, Chloroform-*d*) δ 8.28 (d, *J* = 8.5 Hz, 1H), 8.12 (s, 1H), 7.91 (d, *J* = 9.1 Hz, 1H), 7.82 (d, *J* = 8.1 Hz, 1H), 7.65 (d, *J* = 9.1 Hz, 2H), 7.46 (ddd, *J* = 8.5, 6.8, 1.4 Hz, 1H), 7.40 – 7.35 (m, 2H), 6.78 (d, *J* = 9.0 Hz, 2H), 3.92 (s, 3H), 3.43 (q, *J* = 7.1 Hz, 4H), 1.22 (t, *J* = 7.1 Hz, 6H) ppm **^{13}C NMR** (101 MHz, Chloroform-*d*) δ 154.80, 147.93, 141.99, 133.47, 130.41, 129.26, 127.88, 126.99, 125.66, 123.86, 122.92, 122.29, 113.79, 113.29, 111.76, 56.75, 44.60, 30.90, 12.49 ppm **LRMS (+ESI)**: *m/z* 373 $[M+H]^+$, 395 $[M+Na]^+$, 767 $[2M+Na]^+$ **HRMS (+ESI)**: *m/z* calculated $C_{23}H_{24}N_4O$ $[M+H]^+$ 373.2023, found 373.2023 **IR** (diamond cell thin film): $\tilde{\nu}$ = 2976, 2964, 2901, 1610, 1590, 1248, 1215 cm^{-1} **HPLC** t_R = 20.00 min, 100% (254 nm), 97.90% (230 nm)

4-(2-Methoxynaphthalen-1-yl)-1-phenyl-1*H*-1,2,3-triazole - 147

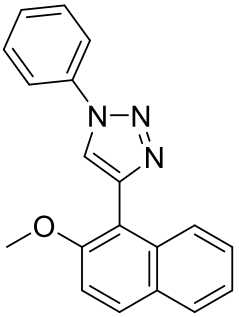

147 was prepared from the azido derivative **135** (84 mg, 0.70 mmol), $CuSO_4 \bullet 5H_2O$ (18 mg, 0.070 mmol), sodium ascorbate (140 mg, 0.70 mmol) and **145** (130 mg, 0.9 mmol) according to **general procedure H**. The crude product was purified *via* flash chromatography (1:0 to 10:1 Hexane/EtOAc) to afford the title compound as a beige crystalline solid (110 mg, 52%).

SMILES CODE: COC(C=CC1=C2C=CC=C1)=C2C3=CN(C4=CC=CC=C4)N=N3 **^{1}H NMR** ($CDCl_3$, 400 MHz) δ 8.27 (s, 1H), 8.25 (d, *J* = 8.5 Hz, 1H), 7.93 (d, *J* = 9.1 Hz, 1H), 7.88 (d, *J* = 7.3 Hz, 2H), 7.83 (d, *J* = 8.1 Hz, 1H), 7.57 (ddd, *J* = 8.5, 6.8, 1.4 Hz, 2H), 7.51 – 7.43 (m, 2H), 7.42 – 7.35 (m, 2H), 3.94 (s, 3H) ppm **^{13}C NMR** ($CDCl_3$, 101 MHz) δ 154.85, 142.66, 137.33, 133.38, 130.69, 129.75, 129.24, 128.55, 127.97, 127.13, 125.47, 123.93, 122.84, 120.56, 113.23, 113.16, 56.71 ppm **LRMS (+APCI)**: *m/z* 302 $[M+H]^+$ **HRMS (+APCI)**: *m/z* calculated $C_{19}H_{15}N_3O$ $[M+H]^+$ 302.1288, found 302.1287 **IR** (diamond cell thin film): $\tilde{\nu}$ = 1267, 1225 cm^{-1} **HPLC** t_R = 26.75 min, 97.33% (254 nm), 95.68% (230 nm)

1-(4-Isopropoxyphenyl)-4-(2-methoxynaphthalen-1-yl)-1*H*-1,2,3-triazole - 148

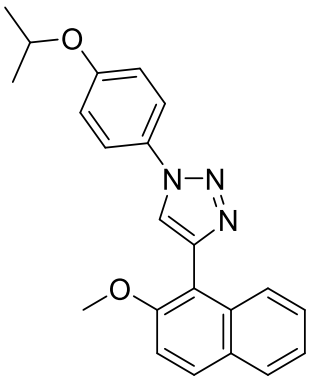

148 was prepared from the azido derivative **136** (54 mg, 0.30 mmol), $CuSO_4 \bullet 5H_2O$ (8 mg, 0.030 mmol), sodium ascorbate (60 mg, 0.30 mmol) and **145** (56 mg, 0.30 mmol) according

to **general procedure H**. The crude product was purified *via* flash chromatography (1:0 to 10:1 Hexane/EtOAc) to afford the title compound as a red oily residue (198 mg, 83%).

SMILES CODE: COC(C=CC1=C2C=CC=C1)=C2C3=CN(C4=CC=C(OC(C)C)C=C4)N=N3 **^{1}H NMR** (400 MHz, Chloroform-*d*) δ 8.25 (d, *J* = 8.6 Hz, 1H), 8.17 (s, 1H), 7.92 (d, *J* = 9.0 Hz, 1H), 7.82 (d, *J* = 8.2 Hz, 1H), 7.76 (d, *J* = 1.5 Hz, 2H), 7.49 – 7.43 (ddd, *J* = 8.5, 6.8, 1.4 Hz, 1H), 7.38 (m, 2H), 7.04 (d, *J* = 1.5 Hz, 2H), 4.63 (hept, *J* = 6.0 Hz, 1H), 3.93 (s, 3H), 1.39 (d, *J* = 6.0 Hz, 6H) ppm **^{13}C NMR** (101 MHz, Chloroform-*d*) δ 158.11, 154.82, 142.37, 133.41, 130.59, 130.54, 129.24, 127.94, 127.08, 125.53, 123.91, 123.00, 122.21, 116.63, 113.42, 113.19, 70.50, 56.71, 21.97 ppm **LRMS (+ESI)**: *m/z* 360 $[M+H]^+$, 382 $[M+Na]^+$, 718 $[2M+H]^+$, 741 $[2M+Na]^+$ **HRMS (+ESI)**: *m/z* calculated $C_{22}H_{21}N_3O_2$ $[M+H]^+$ 360.1707, found 360.1702 **IR** (diamond cell thin film): $\tilde{\nu}$ = 2965, 2935, 2910, 1653, 1558, 1294, 1246 cm^{-1} **HPLC** t_R = 27.03 min, 98.94% (254 nm), 98.64% (230 nm)

4-(4-(2-Methoxynaphthalen-1-yl)-1*H*-1,2,3-triazol-1-yl)benzonitrile - 149

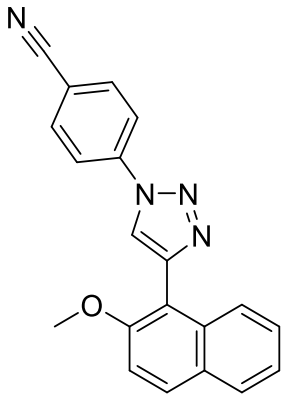

149 was prepared from the azido derivative **137** (82 mg, 0.57 mmol), $CuSO_4 \cdot 5H_2O$ (14 mg, 0.057 mmol), sodium ascorbate (113 mg, 0.57 mmol) and **145** (104 mg, 0.57 mmol) according to **general procedure H**. The crude product was purified *via* flash chromatography (1:0 to 10:1 Hexane/EtOAc) to afford the title compound as a red oily residue (59 mg, 37%).

SMILES CODE: COC(C=CC1=C2C=CC=C1)=C2C3=CN(C4=CC=C(OC(C)C)C=C4)N=N3 **^{1}H NMR** ($CDCl_3$, 300 MHz) δ 8.34 (s, 1H), 8.20 (d, *J* = 8.5 Hz, 1H), 8.04 (d, *J* = 8.5 Hz, 2H), 7.95 (d, *J* = 9.1 Hz, 1H), 7.91 – 7.82 (m, 3H), 7.48 (ddd, *J* = 8.5, 6.8, 1.4 Hz, 1H), 7.42 – 7.35 (m, 2H), 3.94 (s, 3H) ppm **^{13}C NMR** (101 MHz, Chloroform-*d*) δ 154.88, 143.49, 140.07, 133.94, 133.18, 131.10, 129.21, 128.10, 127.32, 125.19, 124.06, 122.45, 120.54, 117.83, 112.95, 112.37, 112.19, 56.65 ppm **LRMS (+APCI)**: *m/z* 327 $[M+H]^+$, 653 $[2M+H]^+$ **HRMS**

(+APCI): *m/z* calculated $C_{20}H_{14}N_4O$ $[M+H]^+$ 327.1240, found 327.1239 **IR** (diamond cell thin film): $\tilde{\nu}$ = 2229, 1228, 1213 cm^{-1} **HPLC** t_R = 16.93 min, 96.96% (254 nm), 98.35% (230 nm)

4-(4-(2-Methoxynaphthalen-1-yl)-1*H*-1,2,3-triazol-1-yl)phenol - 150

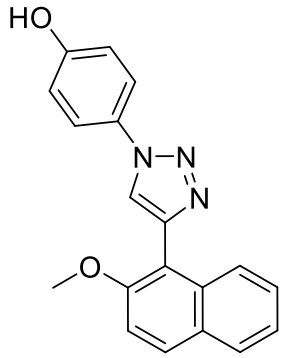

150 was prepared from the azido derivative **138** (68 mg, 0.51 mmol), $CuSO_4 \bullet 5H_2O$ (13 mg, 0.051 mmol), sodium ascorbate (100 mg, 0.51 mmol) and **145** (92 mg, 0.51 mmol) according to **general procedure H**. The crude product was purified *via* flash chromatography (1:0 to 20:1 DCM/EtOAc) to afford the title compound as a beige crystalline solid (69 mg, 43%).

SMILES CODE: OC(C=C1)=CC=C1N2N=NC(C3=C(OC)C=CC4=C3C=CC=C4)=C2 **^{1}H NMR** ($CDCl_3$, 400 MHz) δ 8.17 – 8.13 (m, 2H), 7.93 (d, *J* = 9.1 Hz, 1H), 7.83 (d, *J* = 8.1 Hz, 1H), 7.66 (d, *J* = 8.4 Hz, 2H), 7.46 (ddd, *J* = 8.5, 6.8, 1.4 Hz, 1H), 7.41 – 7.35 (m, 2H), 7.01 (d, *J* = 8.5 Hz, 2H), 3.92 (s, 3H) ppm, OH proton signal not observed **^{13}C NMR** ($CDCl_3$, 101 MHz) δ 156.69, 154.93, 142.29, 133.40, 130.80, 130.37, 129.18, 128.02, 127.16, 125.24, 123.95, 123.10, 122.33, 116.50, 113.13, 112.99, 56.67 ppm **LRMS (+ESI)**: *m/z* 318 $[M+H]^+$, 340 $[M+Na]^+$ **LRMS (-ESI)**: *m/z* 316 $[M-H]^-$ **HRMS (-ESI)**: *m/z* calculated $C_{19}H_{15}N_3O_2$ $[M-H]^-$ 316.1092, found 316.1091 **IR** (diamond cell thin film): $\tilde{\nu}$ = ~3131, 1249, 1229 cm^{-1} **HPLC** t_R = 23.45 min, 99.31% (254 nm), 96.93% (230 nm)

1-(4-Bromophenyl)-4-(2-methoxynaphthalen-1-yl)-1*H*-1,2,3-triazole - 151

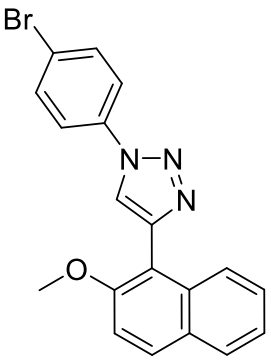

151 was prepared from the azido derivative **139** (48 mg, 0.24 mmol), $CuSO_4 \cdot 5H_2O$ (6 mg, 0.024 mmol), sodium ascorbate (48 mg, 0.24 mmol) and **145** (44 mg, 0.24 mmol) according to **general procedure H**. The crude product was purified *via* flash chromatography (1:0 to 10:1 Hexane/EtOAc) to afford the title compound as a white crystalline solid (30 mg, 33%).

SMILES CODE: BrC(C=C1)=CC=C1N2N=NC(C3=C(OC)C=CC4=C3C=CC=C4)=C2 **^{1}H NMR** (400 MHz, Chloroform-*d*) δ 8.23 (m, 2H), 7.94 (d, *J* = 9.1 Hz, 1H), 7.83 (d, *J* = 8.1 Hz, 1H), 7.77 (d, *J* = 8.6 Hz, 2H), 7.70 (d, *J* = 8.9 Hz, 2H), 7.47 (ddd, *J* = 8.4, 6.9, 1.4 Hz, 1H), 7.38 (m, 2H), 3.93 (s, 3H) ppm **^{13}C NMR** (101 MHz, Chloroform-*d*) δ 154.84, 142.95, 136.27, 133.29, 132.91, 130.84, 129.22, 128.01, 127.19, 125.35, 123.97, 122.63, 122.14, 121.92, 113.06, 112.88, 56.68 ppm **LRMS (+ESI)**: *m/z* 380/382 $[M+H]^+$, 402/404 $[M+Na]^+$ **HRMS (+ESI)**: *m/z* calculated $C_{19}H_{14}BrN_3O$ $[M+H]^+$ 380.0393/382.0373, found 380.0388/382.0368 **IR** (diamond cell thin film): ṽ = 1268, 1252, 508 cm^{-1} **HPLC** t_R = 26.92 min, 100% (254 nm), 97.81% (230 nm)

***N,N*-Diethyl-4-(5-(2-methoxynaphthalen-1-yl)-1*H*-1,2,3-triazol-1-yl)aniline - 160**

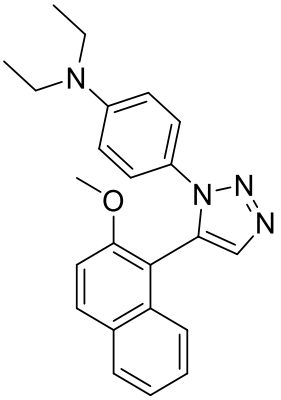

160 was prepared from the azido derivative **134** (111 mg, 0.42 mmol), NMe_4OH (15 μL, 0.042 mmol, 25% wt adjusted) and **145** (77 mg, 0.42 mmol) according to **general procedure I**. The crude product was purified *via* flash chromatography (10:1 to 10:3 Hexane/EtOAc) to afford the title compound as a transparent oily residue (39 mg, 25%).

SMILES CODE: COC(C=CC1=C2C=CC=C1)=C2C3=CN=NN3C4=CC=C(N(CC)CC)C=C4 **^{1}H NMR** (400 MHz, Chloroform-*d*) δ 7.92 (d, *J* = 9.0 Hz, 1H), 7.84 – 7.79 (m, 2H), 7.53 (d, 1H), 7.43 (ddd, *J* = 8.5, 6.7, 1.5 Hz, 1H), 7.37 (ddd, *J* = 8.0, 6.7, 1.3 Hz, 1H), 7.21 (d, *J* = 9.1 Hz, 1H), 7.07 (d, *J* = 9.1 Hz, 2H), 6.44 (d, *J* = 9.1 Hz, 2H), 3.64 (s, 3H), 3.26 (q, *J* = 7.1 Hz, 4H), 1.08 (t, *J* = 7.1 Hz, 6H) ppm **^{13}C NMR** (101 MHz, Chloroform-*d*) δ 155.34,

147.79, 135.24, 133.70, 132.02, 131.64, 128.69, 128.13, 127.57, 127.44, 124.82, 124.04, 124.00, 112.97, 111.09, 110.25, 56.11, 44.36, 12.39 ppm **LRMS (+APCI)**: *m/z* 373 $[M+H]^+$ **HRMS (+APCI)**: *m/z* calculated $C_{23}H_{24}N_4O$ [M] 372.1950, found 372.1947, calculated $[M+H]^+$ 373.2023, found 373.2024 **IR** (diamond cell thin film): $\tilde{\nu}$ = 2964, 2930, 2892, 1608, 1588, 1258, 1239 cm^{-1} **HPLC** t_R = 20.90 min, 98.16% (254 nm), 98.44% (230 nm)

5-(2-Methoxynaphthalen-1-yl)-1-phenyl-1*H*-1,2,3-triazole - 161

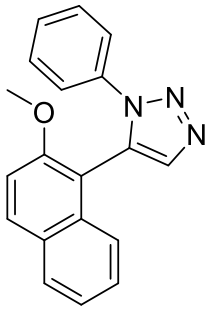

161 was prepared from the azido derivative **135** (135 mg, 0.71 mmol), NMe_4OH (25 μL, 0.071 mmol, 25% wt adjusted) and **145** (129 mg, 0.71 mmol) according to **general procedure I**. The crude product was purified *via* flash chromatography (1:0 to 10:1 Hexane/EtOAc) to afford the title compound as a white crystalline solid (70 mg, 33%).

SMILES CODE: COC(C=CC1=C2C=CC=C1)=C2C3=CN=NN3C4=CC=CC=C4 **^{1}H NMR** (400 MHz, DMSO-d_6) δ 8.10 (d, J = 9.1 Hz, 1H), 8.05 (s, 1H), 7.94 (d, J = 8.2 Hz, 1H), 7.47 (d, J = 1.2 Hz, 2H), 7.44 – 7.33 (m, 5H), 7.28 – 7.20 (m, 2H), 3.64 (s, 3H) ppm **^{13}C NMR** (101 MHz, DMSO-d_6) δ 155.65, 136.99, 135.78, 133.17, 132.69, 132.58, 129.65, 129.48, 128.81, 128.67, 128.33, 124.52, 124.04, 123.58, 113.94, 108.91, 56.52 ppm **LRMS (+APCI)**: *m/z* 302 $[M+H]^+$, 603 $[2M+Na]^+$ **HRMS (+APCI)**: *m/z* calculated $C_{19}H_{15}N_3O$ [M] 301.1215, found 301.1208, calculated $[M+H]^+$ 302.1288, found 302.1287 **IR** (diamond cell thin film): $\tilde{\nu}$ = 1248, 1229 cm^{-1} **HPLC** t_R = 15.97 min, 99.31% (254 nm), 100% (230 nm)

1-(4-Isopropoxyphenyl)-5-(2-methoxynaphthalen-1-yl)-1*H*-1,2,3-triazole - 162

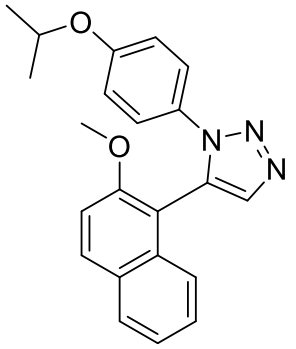

162 was prepared from the azido derivative **136** (76 mg, 0.31 mmol), NMe_4OH (11 μL, 0.031 mmol, 25% wt adjusted) and **145** (55 mg, 0.31 mmol) according to **general procedure I**. The crude product was purified *via* flash chromatography (1:0 to 10:1 Hexane/EtOAc) to afford the title compound as a white crystalline solid (16 mg, 15%).

SMILES CODE: CC(C)OC(C=C1)=CC=C1N2N=NC=C2C3=C(OC)C=CC4=C3C=CC=C4 **^{1}H NMR** (400 MHz, Chloroform-*d*) δ 7.93 (d, *J* = 9.0 Hz, 1H), 7.85 (s, 1H), 7.82 (d, *J* = 8.5 Hz, 1H), 7.55 (d, *J* = 8.5 Hz, 1H), 7.45 (ddd, *J* = 8.4, 6.7, 1.5 Hz, 1H), 7.38 (ddd, *J* = 8.4, 6.7, 1.5 Hz, 1H), 7.16 (m, 3H), 6.71 (d, *J* = 8.0 Hz, 2H), 4.45 (p, *J* = 5.8 Hz, 1H), 3.60 (s, 3H), 1.26 (d, *J* = 6.0 Hz, 6H) ppm **^{13}C NMR** (101 MHz, Chloroform-*d*) δ 158.42, 155.65, 135.92, 133.96, 132.70, 132.37, 130.51, 129.17, 128.72, 128.21, 125.49, 124.62, 124.24, 116.24, 113.25, 110.13, 70.67, 56.42, 22.33 ppm **LRMS (+ESI)**: *m/z* 360 $[M+H]^+$, 382 $[M+Na]^+$, 718 $[2M+H]^+$, 741 $[2M+Na]^+$ **HRMS (+ESI)**: *m/z* calculated $C_{22}H_{21}N_3O_2$ $[M+H]^+$ 360.1707, found 360.1711, calculated $[M+Na]^+$ 382.1526, found 382.1531 **IR** (diamond cell thin film): $\tilde{\nu}$ = 2947, 2921, 2850, 1516, 1507, 1257, 1244 cm^{-1} **HPLC** t_R = 18.08 min, 99.88% (254 nm), 98.50% (230 nm)

4-(5-(2-Methoxynaphthalen-1-yl)-1*H*-1,2,3-triazol-1-yl)benzonitrile - 163

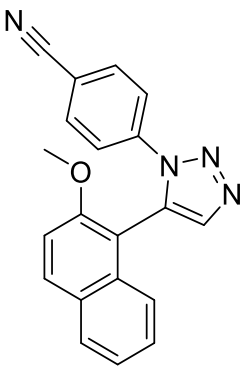

163 was prepared from the azido derivative **137** (123 mg, 0.59 mmol), NMe_4OH (20 μL, 0.059 mmol, 25% wt adjusted) and **145** (103 mg, 0.59 mmol) according to **general procedure I**. The crude product was purified *via* flash chromatography (1:0 to 10:1 Hexane/EtOAc) to afford the title compound as a white crystalline solid (63 mg, 34%).

SMILES CODE: COC(C=CC1=C2C=CC=C1)=C2C3=CN=NN3C4=CC=C(C#N)C=C4 **^{1}H NMR** (400 MHz, Chloroform-*d*) δ 8.00 (d, *J* = 9.1 Hz, 1H), 7.90 (s, 1H), 7.87 (d, *J* = 8.5 Hz, 1H), 7.56 (m, 3H), 7.49 (ddd, *J* = 8.4, 6.7, 1.5 Hz, 1H), 7.44 (m, 3H), 7.21 (d, *J* = 9.1 Hz, 1H), 3.58 (s, 3H) ppm **^{13}C NMR** (101 MHz, Chloroform-*d*) δ 154.94, 140.64, 136.29, 133.07, 133.02, 132.66, 132.35, 128.85, 128.56, 128.27, 124.55, 123.65, 123.36, 117.80, 112.60, 112.36, 108.57, 55.89 ppm **LRMS (+APCI)**: *m/z* 327 $[M+H]^+$ **HRMS (+APCI)**: *m/z* calculated $C_{20}H_{14}N_4O$ [M] 326.1168, found 326.1161, calculated $[M+H]^+$ 327.1240, found 327.1239 **IR** (diamond cell thin film): $\tilde{\nu}$ = 2225, 1258, 1213, 1244 cm^{-1} **HPLC** t_R = 15.85 min, 100% (254 nm), 99.62% (230 nm)

1-(4-Bromophenyl)-5-(2-methoxynaphthalen-1-yl)-1*H*-1,2,3-triazole - 164

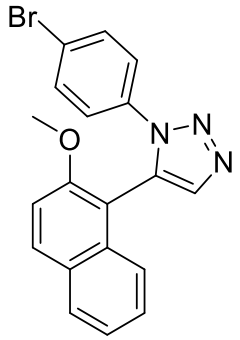

164 was prepared from the azido derivative **139** (65 mg, 0.24 mmol), NMe_4OH (9 μL, 0.024 mmol, 25% wt adjusted) and **145** (44 mg, 0.24 mmol) according to **general procedure I**. The crude product was purified *via* flash chromatography (1:1 Hexane/EtOAc) to afford the title compound as a white crystalline solid (28 mg, 30%).

SMILES CODE: BrC(C=C1)=CC=C1N2N=NC=C2C3=C(OC)C=CC4=C3C=CC=C4 **^{1}H NMR** (400 MHz, Chloroform-*d*) δ 7.96 (d, *J* = 8.9 Hz, 1H), 7.87 (s, 1H), 7.85 (d, *J* = 7.9 Hz, 1H), 7.55 (d, *J* = 8.5 Hz, 1H), 7.47 (ddd, *J* = 8.4, 6.7, 1.5 Hz, 1H), 7.42 (ddd, *J* = 8.4, 6.7, 1.5 Hz, 1H), 7.38 (d, *J* = 8.8 Hz, 2H), 7.20 (d, *J* = 9.1 Hz, 1H), 7.16 (d, *J* = 8.8 Hz, 2H), 3.60 (s, 3H) ppm **^{13}C NMR** (101 MHz, Chloroform-*d*) δ 155.05, 136.26, 135.86, 133.27, 132.27, 132.21, 132.07, 128.75, 128.40, 128.01, 124.98, 124.33, 123.52, 122.46, 112.68, 109.04, 55.90 ppm **LRMS (+APCI)**: *m/z* 380/382 $[M+H]^+$ **HRMS (+APCI)**: *m/z* calculated

$C_{19}H_{14}BrN_3O$ $[M+H]^+$ 380.0393/382.0373, found 380.0395/382.0375 **IR** (diamond cell thin film): $\tilde{\nu}$ = 1259, 1228, 501 cm^{-1} **HPLC** t_R= 18.07 min, 97.36% (254 nm), 98.54% (230 nm)

4-Iodo-*N,N*-diethylaniline - 169

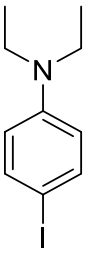

To a solution of **168** (538 μL, 3.35 mmol) in DCM:H_2O (1:1, 10 mL) was added KI (667 mg, 4.02 mmol) alongside H_5IO_6 (916 mg, 4.02 mmol) and stirred at room temperature for 15 min or until completion as indicated by TLC. The crude mixture was washed with sodium thiosulphate (1 × 15 mL), extracted with $CHCl_3$ (3 × 15 mL), dried over $MgSO_4$ and concentrated *in vacuo*. The crude product was purified *via* flash chromatography (Hexane) to afford the title compound as a dark purple oil (756 mg, 82%).

SMILES CODE: CCN(CC)C1=CC=C(I)C=C1 **^{1}H NMR** (400 MHz, Chloroform-*d*) δ 7.41 (d, *J* = 9.0 Hz, 2H), 6.44 (d, *J* = 9.0 Hz, 2H), 3.30 (q, *J* = 7.1 Hz, 4H), 1.13 (t, *J* = 7.1 Hz, 6H) ppm **^{13}C NMR** (101 MHz, Chloroform-*d*) δ 147.29, 137.76, 114.17, 75.69, 44.38, 12.44 ppm **LRMS (+ESI)**: *m/z* 276 $[M+H]^+$ **IR** (diamond cell thin film): $\tilde{\nu}$ = 2963, 2922, 2910, 554 cm^{-1}

***N,N*-Diethyl-4-((2-methoxynaphthalen-1-yl)ethynyl)aniline - 170**

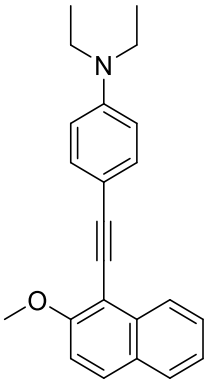

169 (50 mg, 0.18 mmol), $PdCl_2(PPh_3)_2$ (13 mg, 0.018 mmol), CuI (2 mg, 0.011 mmol) were dissolved in Et_3N (5 mL) with stirring and degassed with N_2 for 30 mins. Following this, **145**

(33 mg, 0.18 mmol) was added and the solution heated at 40 °C. The reaction was monitored *via* TLC and upon completion the solvent was removed under a stream of N_2 overnight. The crude reaction residue was then up taken in water (1 × 10 mL), extracted with EtOAc (3 × 10 mL), dried over $MgSO_4$ and concentrated *in vacuo.* The crude product was purified *via* flash chromatography (1:0 to 20:1 Hexane/EtOAc) to afford the title compound as a beige oily residue (48 mg, 80%).

SMILES CODE: COC(C=CC1=C2C=CC=C1)=C2C#CC3=CC=C(N(CC)CC)C=C3 **^{1}H NMR** (400 MHz, Chloroform-*d*) δ 8.30 (d, *J* = 8.4 Hz, 1H), 7.69 (d, *J* = 8.8 Hz, 2H), 7.49 – 7.41 (m, 3H), 7.29 (ddd, *J* = 8.4, 6.7, 1.5 Hz, 1H), 7.17 (d, *J* = 7.9 Hz, 1H), 6.58 (d, *J* = 8.8 Hz, 2H), 3.97 (s, 3H), 3.31 (q, *J* = 7.1 Hz, 4H), 1.11 (t, *J* = 7.0 Hz, 6H) ppm **^{13}C NMR** (101 MHz, Chloroform-*d*) δ 157.21, 146.53, 133.57, 131.99, 128.05, 127.72, 126.96, 125.94, 124.61, 123.04, 112.11, 110.27, 108.67, 106.66, 99.61, 80.36, 55.80, 43.36, 11.57 ppm **LRMS (+ESI)**: *m/z* 330 $[M+H]^+$ **HRMS (+ESI)**: *m/z* calculated $C_{23}H_{23}NO$ [M] 329.1780, found 329.1780, calculated $[M+H]^+$ 330.1852, found 330.1857 **IR** (diamond cell thin film): $\tilde{\nu}$ = 2921, 2198, 1268, 1181 cm^{-1}

***N,N*-Diethyl-4-(5-(naphthalen-1-yl)-2*H*-1,2,3-triazol-4-yl)aniline - 171**

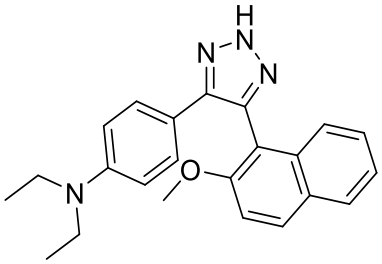

170 (48 mg, 0.15 mmol), NaN_3 (10 mg, 0.16 mmol) and $(AcO)_2IPh$ (52 mg, 0.16 mmol) were dissolved in MeCN (5 mL) and stirred at room termperature for 6 h. The reaction was monitored *via* TLC and upon completion the solvent was removed under a stream of N_2. The crude reaction residue was then up taken in water (1 × 5 mL), extracted with EtOAc (3 × 5 mL), dried over $MgSO_4$ and concentrated *in vacuo.* The crude product was purified *via* flash chromatography (1:0 to 20:1 Hexane/EtOAc) to afford the title compound as an orange oily residue (15 mg, 27%).

SMILES CODE: CCN(CC)C(C=C1)=CC=C1C2=NNN=C2C3=CC=CC4=C3C=CC=C4 **^{1}H NMR** (400 MHz, Acetonitrile-*d*$_3$) δ 8.14 (d, *J* = 8.5 Hz, 1H), 7.76 – 7.66 (m, 2H), 7.41 (ddd, *J* = 8.3, 6.8, 1.3 Hz, 1H), 7.29 – 7.19 (m, 4H), 6.52 – 6.41 (m, 2H), 4.52 (s, 1H), 3.86 (s, 3H),

2.99 (q, *J* = 7.2 Hz, 4H), 1.06 (t, *J* = 7.1 Hz, 6H) ppm **^{13}C NMR** (101 MHz, Acetonitrile-*d*$_3$) δ 159.09, 149.93, 134.75, 133.16, 130.05, 129.23, 128.80, 127.90, 125.53, 124.77, 113.90, 112.73, 110.83, 107.18, 100.85, 81.94, 56.81, 38.21, 14.33 ppm **LRMS (-ESI)**: *m/z* 371 $[M-H]^-$ **HRMS (-ESI)**: *m/z* calculated $C_{23}H_{24}N_4O$ $[M-H]^-$ 371.1877, found 371.1878 **IR** (diamond cell thin film): $\tilde{\nu}$ = 3392, 1268, 1181 cm^{-1} **HPLC** t_R = 21.78 min, 97.57% (254 nm), 97.02% (230 nm)

Methyl 2-methoxy-1-naphthoate benzoate - 182

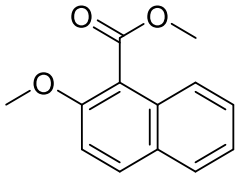

181 (1.00 g, 5.31 mmol) was prepared from K_2CO_3 (1.47 g, 10.62 mmol) and MeI (992 μL, 15.94 mmol) in acetone according to **general procedure C**. The crude residue was purified *via* flash chromatography (40:1 to 40:3 Hexane/EtOAc) to afford the title compound as a bright yellow oil (1.03 g, 90%).

SMILES CODE: COC(C=CC1=C2C=CC=C1)=C2C(OC)=O **^{1}H NMR** (300 MHz, Chloroform-*d*) δ 7.89 (d, *J* = 9.1 Hz, 1H), 7.83 – 7.68 (m, 2H), 7.49 (ddd, *J* = 8.5, 6.8, 1.4 Hz, 1H), 7.36 (ddd, *J* = 8.1, 6.8, 1.2 Hz, 1H), 7.26 (d, *J* = 9.1 Hz, 1H), 4.03 (s, 3H), 3.96 (s, 3H) ppm **^{13}C NMR** (75 MHz, Chloroform-*d*) δ 168.54, 154.46, 131.70, 131.03, 128.56, 128.12, 127.65, 124.16, 123.79, 117.51, 113.12, 56.81, 52.44 ppm **LRMS (+APCI)**: *m/z* 217 $[M+H]^+$ **HRMS (+APCI)**: *m/z* calculated $C_{13}H_{12}O_3$ [M] 216.0786, found 216.0781, calculated $[M+H]^+$ 217.0859, found 217.0859 **IR** (diamond cell thin film): $\tilde{\nu}$ = 1720, 1254, 1229 cm^{-1}

2-Methoxy-1-naphthoic acid - 183

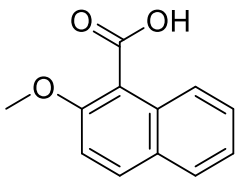

183 was prepared from **182** (1.03 g, 4.76 mmol), NaOH (572 mg, 1.43 mmol) in MeOH according to **general procedure J**. This afforded the pure title compound as a white crystalline solid (925 mg, 96%).

SMILES CODE: COC(C=CC1=C2C=CC=C1)=C2C(O)=O **^{1}H NMR** (300 MHz, Chloroform-*d*) δ 8.46 (d, *J* = 8.7 Hz, 1H), 7.99 (d, *J* = 9.1 Hz, 1H), 7.87 – 7.79 (m, 1H), 7.59 (ddd, *J* = 8.5, 6.8, 1.4 Hz, 1H), 7.43 (ddd, *J* = 8.0, 6.8, 1.1 Hz, 1H), 7.33 (d, *J* = 9.1 Hz, 1H), 4.09 (s, 3H) ppm, OH proton signal not observed **^{13}C NMR** (75 MHz, Chloroform-*d*) δ 169.46, 155.93, 133.67, 131.77, 129.06, 128.39, 128.24, 124.85, 124.62, 114.78, 112.78, 57.25 **LRMS (-ESI)**: *m/z* 201 $[M-H]^-$ **HRMS (+ESI)**: *m/z* calculated $C_{12}H_{10}O_3$, $[M+Na]^+$ 225.0522, found 225.0524 **IR** (diamond cell thin film): $\tilde{\nu}$ = 1680, 1286, 1252 cm^{-1}

***N,N*-(4-(Diethylamino)phenyl)-2-methoxy-1-naphthamide - 184**

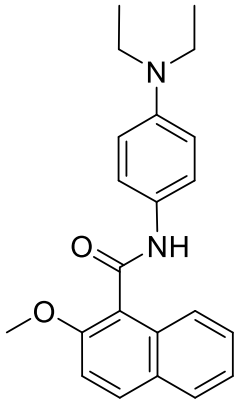

184 was prepared from **183** (123 mg, 0.61 mmol), $(COCl)_2$ (57 μL, 0.67 mmol), **76** (100 mg, 0.61 mmol) and Et_3N (170 μL, 1.22 mmol) according to **general procedure K**. The crude residue was purified *via* flash chromatography (20:3 to 4:1 Hexane/EtOAc) to afford the title compound as an off-white crystalline solid (182 mg, 86%).

SMILES CODE: COC(C=CC1=C2C=CC=C1)=C2C(NC3=CC=C(N(CC)CC)C=C3)=O **^{1}H NMR** (400 MHz, Chloroform-*d*) δ 8.06 (d, *J* = 8.6 Hz, 1H), 7.89 (d, *J* = 9.4 Hz, 1H), 7.79 (d, *J* = 8.2 Hz, 1H), 7.57 – 7.44 (m, 4H), 7.37 (ddd, *J* = 8.5, 6.8, 1.4 Hz, 1H), 7.29 (d, *J* = 9.1 Hz, 1H), 6.71 (d, *J* = 9.0 Hz, 2H), 3.97 (s, 3H), 3.36 (q, *J* = 7.1 Hz, 4H), 1.16 (t, *J* = 7.0 Hz, 6H) ppm **^{13}C NMR** (101 MHz, Chloroform-*d*) δ 153.70, 145.35, 131.66, 131.31, 129.15, 128.90, 127.95, 127.56, 127.11, 124.56, 124.20, 122.02, 120.98, 113.26, 112.55, 56.87, 44.66, 12.55 ppm **LRMS (+ESI)**: *m/z* 349 $[M+H]^+$, 371 $[M+Na]^+$, 697 $[2M+H]^+$ **LRMS (-ESI)**: *m/z* 347 $[M-H]^-$ **HRMS (+ESI)**: *m/z* calculated $C_{22}H_{24}N_2O_2$ $[M+H]^+$ 349.1911, found 349.1912 **IR** (diamond cell thin film): $\tilde{\nu}$ = 1646, 1273, 1251 cm^{-1} **HPLC** t_R = 17.35 min, 99.64% (254 nm), 97.57% (230 nm)

2-Methoxy-*N*-phenyl-1-naphthamide - 185

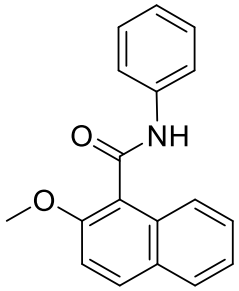

185 was prepared from **183** (109 mg, 0.54 mmol), $(COCl)_2$ (51 μL, 0.59 mmol), **85** (49 μL, 0.54 mmol) and Et_3N (150 μL, 1.07 mmol) according to **general procedure K**. The crude residue was purified *via* flash chromatography (20:3 to 4:1 Hexane/EtOAc) to afford the title compound as a white crystalline solid (105 mg, 70%).

SMILES CODE: COC1=CC=C(C=CC=C2)C2=C1C(NC3=CC=CC=C3)=O **^{1}H NMR** (400 MHz, Chloroform-*d*) δ 8.06 (d, *J* = 1.1 Hz, 1H), 7.93 (d, *J* = 9.1 Hz, 1H), 7.81 (d, *J* = 8.2 Hz, 1H), 7.72 (m, 3H), 7.51 (ddd, *J* = 8.4, 6.8, 1.4 Hz, 1H), 7.39 (m, 3H), 7.32 (d, *J* = 9.1 Hz, 1H), 7.17 (t, *J* = 7.4 Hz, 1H), 4.00 (s, 3H) ppm **^{13}C NMR** (101 MHz, Chloroform-*d*) δ 165.48, 153.78, 138.27, 131.71, 131.57, 129.11, 128.91, 128.04, 127.77, 124.45, 124.36, 124.34, 120.47, 119.85, 113.11, 56.86 ppm **LRMS (+APCI)**: *m/z* 278 $[M+H]^+$ **HRMS (+ESI)**: *m/z* calculated $C_{18}H_{15}NO_2$ [M] 277.1103, found 277.1097, calculated $[M+H]^+$ 278.1176, found 278.1175 **IR** (diamond cell thin film): $\tilde{\nu}$ = 1664, 1276, 1254 cm^{-1} **HPLC** t_R = 15.00 min, 99.23% (254 nm), 98.66% (230 nm)

***N*-(4-Isopropoxyphenyl)-2-methoxy-1-naphthamide - 186**

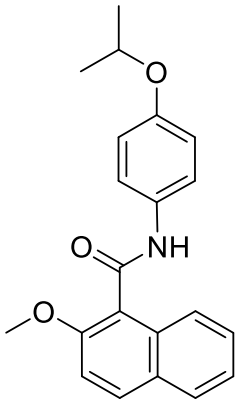

185 was prepared from **183** (67 mg, 0.33 mmol), $(COCl)_2$ (31 μL, 0.36 mmol), **86** (49 μL, 0.33 mmol) and Et_3N (92 μL, 0.66 mmol) according to **general procedure K**. The crude residue was purified *via* flash chromatography (20:3 to 4:1 Hexane/EtOAc) to afford the title compound as a white crystalline solid (88 mg, 79%).

SMILES CODE: COC(C=CC1=C2C=CC=C1)=C2C(NC3=CC=C(OC(C)C)C=C3)=O **^{1}H NMR** (400 MHz, Chloroform-*d*) δ 8.06 (d, *J* = 8.6 Hz, 1H), 7.91 (d, *J* = 9.1 Hz, 1H), 7.84 – 7.77 (m, 1H), 7.60 (m, 3H), 7.50 (ddd, *J* = 8.4, 6.8, 1.4 Hz, 1H), 7.38 (ddd, *J* = 8.0, 6.8, 1.2 Hz, 1H), 7.30 (d, *J* = 9.1 Hz, 1H), 6.92 (d, *J* = 8.9 Hz, 2H), 4.54 (hept, *J* = 6.1 Hz, 1H), 3.99 (s, 3H), 1.35 (d, *J* = 6.0 Hz, 6H) ppm **^{13}C NMR** (101 MHz, Chloroform-*d*) δ 165.24, 154.84, 153.74, 131.61, 131.55, 131.33, 128.91, 128.00, 127.67, 124.43, 124.28, 121.63, 120.62, 116.58, 113.15, 70.46, 56.86, 22.07 ppm **LRMS (+ESI)**: *m/z* 336 $[M+H]^+$, 358 $[M+Na]^+$ **HRMS (+ESI)**: *m/z* calculated $C_{21}H_{21}NO_3$ $[M+H]^+$ 336.1594, found 336.1596 **IR** (diamond cell thin film): $\tilde{\nu}$ = 3041, 2972, 1648, 1254, 1233 cm^{-1} **HPLC** t_R = 16.83 min, 99.94% (254 nm), 97.90% (230 nm)

***N*-(4-Cyanophenyl)-2-methoxy-1-naphthamide - 187**

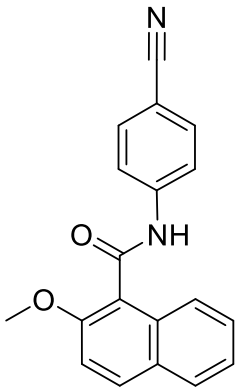

183 (85 mg, 0.42 mmol) was dissolved in DCM (5 mL) and cooled down to 0 ºC. Addition of $(COCl)_2$ (40 μL, 4.7 mmol) was followed by cat. DMF then allowed to stir for 1 h. After completion *via* TLC the solvent was removed under a stream of N_2. Subsequently the crude residue was redissolved in DCM and removed under a stream of N_2 (3 ×). After this, **87** (50 mg, 0.42 mmol) was dissolved in DMAC (5 mL) and then added to the acid chloride mixture at 0 ºC. The reaction was gradually brought to room temperature and monitored *via* TLC. On completion, the mixture was diluted with water and extracted with DCM (3 × 10 mL), washed with brine, dried over $MgSO_4$ and concentrated *in vacuo*. The subsequent

crude product was then purified *via* flash chromatography (20:3 to 4:1 Hexane/EtOAc) to afford the title compound as a white crystalline solid (53 mg, 42%).

SMILES CODE: COC(C=CC1=C2C=CC=C1)=C2C(NC3=CC=C(C#N)C=C3)=O **^{1}H NMR** (400 MHz, Chloroform-*d*) δ 8.04 (d, *J* = 8.6 Hz, 1H), 8.00 (s, 1H), 7.95 (d, *J* = 9.1 Hz, 1H), 7.82 (m, 3H), 7.65 (d, *J* = 8.6 Hz, 2H), 7.52 (ddd, *J* = 8.4, 6.8, 1.4 Hz, 1H), 7.41 (ddd, *J* = 8.1, 6.8, 1.2 Hz, 1H), 7.31 (d, *J* = 9.1 Hz, 1H), 4.00 (s, 3H) ppm **^{13}C NMR** (101 MHz, Chloroform-*d*) δ 165.81, 154.02, 142.21, 133.36, 132.44, 131.48, 128.94, 128.21, 128.09, 124.55, 124.11, 119.62, 119.25, 118.87, 112.81, 107.27, 56.85 ppm **LRMS (+APCI)**: *m/z* 303 $[M+H]^+$ **HRMS (+APCI)**: *m/z* calculated $C_{19}H_{14}N_2O_2$ $[M+H]^+$ 303.1128, found 303.1127 **IR** (diamond cell thin film): $\tilde{\nu}$ = 3333, 2227, 1653, 1252, 1216 cm^{-1} **HPLC** t_R = 15.22 min, 100% (254 nm), 99.66% (230 nm)

***N*-(4-Bromophenyl)-2-methoxy-1-naphthamide - 188**

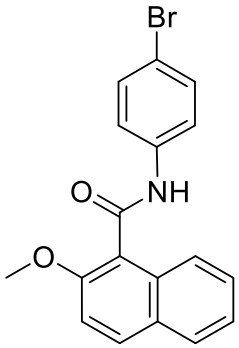

185 was prepared from **183** (59 mg, 0.29 mmol), $(COCl)_2$ (27 μL, 0.32 mmol), **89** (50 mg, 0.29 mmol) and Et_3N (81 μL, 0.58 mmol) according to **general procedure K**. The crude residue was purified *via* flash chromatography (20:3 to 4:1 Hexane/EtOAc) to afford the title compound as a white crystalline solid (77 mg, 74%).

SMILES CODE: COC(C=CC1=C2C=CC=C1)=C2C(NC3=CC=C(Br)C=C3)=O **^{1}H NMR** (400 MHz, Chloroform-*d*) δ 8.04 (d, *J* = 8.5 Hz, 1H), 7.93 (d, *J* = 9.1 Hz, 1H), 7.81 (d, *J* = 8.2 Hz, 1H), 7.74 (s, 1H), 7.61 (d, *J* = 8.9 Hz, 2H), 7.55 – 7.46 (m, 3H), 7.39 (ddd, *J* = 8.1, 6.8, 1.2 Hz, 1H), 7.31 (d, *J* = 9.1 Hz, 1H), 3.99 (s, 3H) ppm **^{13}C NMR** (101 MHz, Chloroform-*d*) δ 165.48, 153.84, 137.34, 132.04, 131.96, 131.53, 128.91, 128.10, 127.88, 124.41, 124.26, 121.38, 119.98, 116.94, 112.98, 56.85 ppm **LRMS (+ESI)**: *m/z* 356/358 $[M+H]^+$, 378/380 $[M+Na]^+$ **LRMS (-ESI)**: *m/z* 354/356 $[M-H]^-$ **HRMS (+ESI)**: *m/z* calculated $C_{18}H_{14}BrNO_2$

$[M+Na]^+$ 378.0100/380.0079, found 378.0095/380.0075 **IR** (diamond cell thin film): $\tilde{\nu}$ = 1654, 1253, 1213, 506 cm^{-1} **HPLC** t_R = 17.50 min, 99.23% (254 nm), 97.12% (230 nm)

2-Methoxy-1-naphthamide - 195

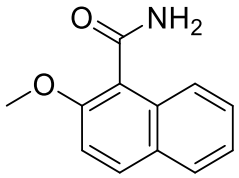

183 (200 mg, 0.99 mmol) was dissolved in DCM (10 mL) and cooled down to 0 ºC. Addition of $(COCl)_2$ (93 μL, 1.09 mmol) was followed by cat. DMF then allowed to stir for 1 h. After completion *via* TLC the solvent was removed under a stream of N_2. Subsequently the crude residue was redissolved in DCM and removed under a stream of N_2 (3 ×). The acid chloride was then redissolved in DCM (10 mL) followed by addition of aqueous NH_4OH (308 uL, 1.98 mmol, 25% wt adjusted). The mixture was stirred for 1.5 h at room temperature, the precipitate was collected by filtration and subsequently recrystallised from EtOH to obtain the title compound as a white crystalline solid (199 mg, quant.).

SMILES CODE: COC(C=CC1=C2C=CC=C1)=C2C(N)=O **^{1}H NMR** (400 MHz, Chloroform-*d*) δ 8.09 (d, *J* = 8.6 Hz, 1H), 7.90 (d, *J* = 9.1 Hz, 1H), 7.78 (d, *J* = 8.3 Hz, 1H), 7.52 (ddd, *J* = 8.4, 6.8, 1.4 Hz, 1H), 7.38 (ddd, *J* = 8.1, 6.8, 1.2 Hz, 1H), 7.29 (d, *J* = 9.1 Hz, 1H), 6.05 (s, 2H), 4.00 (s, 3H) ppm **^{13}C NMR** (101 MHz, Chloroform-*d*) δ 169.48, 153.70, 131.62, 131.41, 128.90, 127.97, 127.67, 124.50, 124.25, 119.35, 112.96, 56.77 ppm **LRMS (-ESI)**: *m/z* 202 $[M-H]^-$ **HRMS (+ESI)**: *m/z* calculated $C_{12}H_{11}NO_2$ $[M+H]^+$ 202.0863, found 202.0864 **IR** (diamond cell thin film): $\tilde{\nu}$ = 3320, 3150, 1717, 1265, 1250 cm^{-1}

2-Methoxy-1-naphthonitrile - 196

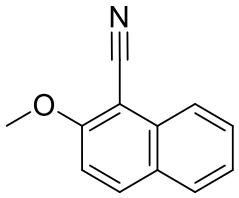

195 (199 mg, 0.99 mmol) was dissolved in 1,2-dichloroethane (5 mL) followed by the addition of $POCl_3$ (461 uL, 4.95 mmol) and subsequently heated to 80 °C. After completion of reaction as indicated by TLC, the solvent was removed under a stream of N_2. Sat. $NaHCO_3$

(10 mL) was added to the residue, the mixture was extracted with CH_2Cl_2 (3 × 10 mL). The organic layers were combined and washed with brine (1 × 10 mL), dried over anhydrous $MgSO_4$, filtered, and concentrated *in vacuo*. The crude product was purified *via* flash chromatography (9:1 Hexane/EtOAc) to afford the title compound as a white crystalline solid (163 mg, 90%).

SMILES CODE: COC(C=CC1=C2C=CC=C1)=C2C#N **^{1}H NMR** ($CDCl_3$, 400 MHz) δ 8.09 (d, *J* = 8.4 Hz, 1H), 8.03 (d, *J* = 9.2 Hz, 1H), 7.83 (d, *J* = 8.2 Hz, 1H), 7.64 (ddd, *J* = 8.3, 6.8, 1.3 Hz, 1H), 7.45 (ddd, *J* = 8.1, 6.9, 1.2 Hz, 1H), 7.27 (d, *J* = 9.1 Hz, 1H), 4.07 (3H, s) ppm **^{13}C NMR** (101 MHz, Chloroform-*d*) δ 161.68, 135.02, 133.65, 129.22, 128.47, 128.04, 125.12, 124.12, 115.69, 112.07, 95.34, 56.65 ppm **LRMS (+APCI)**: *m/z* 184 $[M+H]^+$ **HRMS (+APCI)**: *m/z* calculated $C_{12}H_9NO$ [M] 183.0684, found 183.0681, calculated $[M+H]^+$ 184.0757, found 184.0759 **IR** (diamond cell thin film): $\tilde{\nu}$ = 2208, 1281, 1258 cm^{-1}

Ethyl 4-(diethylamino)benzoate - 200

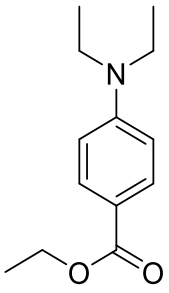

200 was prepared from **199** (1.00 g, 7.29 mmol), K_2CO_3 (2.02 g, 14.58 mmol) and EtI (1.76 mL, 21.88 mmol) in acetone according to **general procedure C**. The crude residue was purified *via* flash chromatography (20:1 to 20:3 Hexane/EtOac) to afford the title compound as a light yellow oil (1.19 g, 74%).

SMILES CODE: CCN(CC)C1=CC=C(C(OCC)=O)C=C1 **^{1}H NMR** (300 MHz, Chloroform-*d*) δ 7.89 (d, *J* = 9.1 Hz, 2H), 6.61 (d, *J* = 9.1 Hz, 2H), 4.31 (q, *J* = 7.1 Hz, 2H), 3.40 (q, *J* = 7.1 Hz, 4H), 1.36 (t, *J* = 7.1 Hz, 3H), 1.19 (t, *J* = 7.1 Hz, 6H) ppm **^{13}C NMR** (75 MHz, Chloroform-*d*) δ 167.04, 150.92, 131.49, 116.47, 110.15, 60.01, 44.47, 14.51, 12.49 ppm **LRMS (+ESI)**: *m/z* 222 $[M+H]^+$, 244 $[M+Na]^+$, 465 $[2M+Na]^+$ **HRMS (+ESI)**: *m/z* calculated $C_{13}H_{19}NO_2$ $[M+Na]^+$ 244.1308, found 244.1306 **IR** (diamond cell thin film): $\tilde{\nu}$ = 2973, 2931, 2901, 1697, 1601, 1283, 1263 cm^{-1}

4-(Diethylamino)benzoic acid - 201

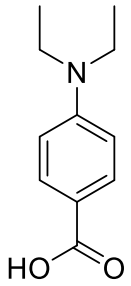

201 was prepared from **200** (537 mg, 2.43 mmol) and NaOH (291 mg, 7.38 mmol) in EtOH according to **general procedure J**. This afforded the pure title compound as a white crystalline solid (468 mg, quant.).

SMILES CODE: CCN(CC)C1=CC=C(C(O)=O)C=C1 **^{1}H NMR** (300 MHz, Chloroform-*d*) δ 7.94 (d, *J* = 9.1 Hz, 2H), 6.63 (d, *J* = 9.1 Hz, 2H), 3.42 (q, *J* = 7.1 Hz, 4H), 1.20 (t, *J* = 7.1 Hz, 6H) ppm, O<u>H</u> proton signal not observed **^{13}C NMR** (75 MHz, Chloroform-*d*) δ 171.86, 151.55, 132.32, 115.03, 110.18, 44.53, 12.49 ppm **LRMS (+ESI)**: *m/z* 194 $[M+H]^+$, 216 $[M+Na]^+$ **HRMS (+ESI)**: *m/z* calculated $C_{11}H_{15}NO_2$ $[M+Na]^+$ 216.0995, found 216.0991 **IR** (diamond cell thin film): $\tilde{\nu}$ = 2974, 2965, 2905, 1653 cm^{-1}

4-(Diethylamino)benzoyl chloride - 202

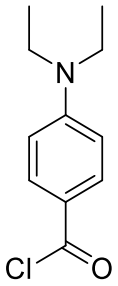

201 (50 mg, 0.26 mmol) was dissolved in DCM (5 mL) and cooled down to 0 ºC. Addition of $(COCl)_2$ (24 μL, 0.28 mmol) was followed by cat. DMF then allowed to stir for 1 h. After completion *via* TLC the solvent was removed under a stream of N_2. Subsequently the crude residue was redissolved in DCM and removed under a stream of N_2 (3 ×). The crude product was carried through to the next reaction without further purification.

SMILES CODE: CCN(CC)C1=CC=C(C(Cl)=O)C=C1

N,N-Diethylaminoacetophenone – 208

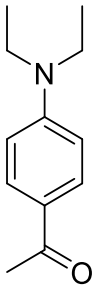

208 was prepared from **207** (500 mg, 3.70 mmol), K_2CO_3 (1.02 g, 7.40 mmol) and EtI (892 μL, 1.11 mmol) in acetone according to **general procedure C**. The crude residue was purified *via* flash chromatography (20:1 to 20:3 Hexane/EtOac) to afford the title compound as a yellow oily solid (524 mg, 74%).

SMILES CODE: CCN(CC)C1=CC=C(C(C)=O)C=C1 **^{1}H NMR** (300 MHz, Chloroform-*d*) δ 7.85 (d, *J* = 9.1 Hz, 2H), 6.63 (d, *J* = 9.1 Hz, 2H), 3.42 (q, *J* = 7.1 Hz, 4H), 2.51 (s, 3H), 1.22 (t, *J* = 7.1 Hz, 6H) ppm **^{13}C NMR** (75 MHz, Chloroform-*d*) δ 196.10, 151.15, 130.85, 124.71, 110.11, 44.53, 25.88, 12.51 ppm **LRMS (+ESI)**: *m/z* 192 $[M+H]^+$, 214 $[M+Na]^+$ **IR** (diamond cell thin film): $\tilde{\nu}$ = 2966, 2921, 2870, 1651 cm^{-1}

6.5 Chapter 4 Experimental and Characterisation

4-Bromo-*N,N*-diethylaniline - 219

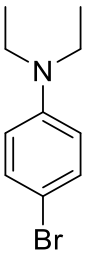

Method 1:

219 was prepared from **218** (2.00 g, 11.6 mmol), K_2CO_3 (3.21 g, 23.3 mmol) and EtI (2.80 mL, 34.88 mmol) in MeCN according to **general procedure C**. The crude product was purified *via* flash chromatography (19:1 DCM/Hexane) to afford the title compound as a yellow-brown crystalline solid (578 mg, 22%).

Method 2:

219 was prepared from **218** (2.00 g, 11.63 mmol), EtI (2.80 mL, 34.88 mmol) and NaH (512 mg, 12.79 mmol, 60% dispersion in oil) in THF according to **general procedure D**. The crude product was purified *via* flash chromatography (19:1 DCM/Hexane) to afford the title compound as a yellow-brown crystalline solid (1.27 g, 48%).

Method 3:

To a stirred solution of **168** (2.13 mL, 13.4 mmol) in DMSO (13 mL) was added HBr (5 mL, 92 mmol) and heated to 60 °C for 1 h. The reaction was monitored *via* TLC until completion, after which the solution was subsequently cooled to room temperature and pH adjusted to 7 – 8 with 4 M aq. NaOH. Following this, the mixture was extracted with EtOAc (3 × 30 mL), dried over $MgSO_4$ and concentrated *in vacuo.* The crude product was purified *via* flash chromatography (19:1 DCM/Hexane) to afford the title compound as a brown crystalline solid (2.75 g, 90%).

SMILES CODE: CCN(CC)C1=CC=C(Br)C=C1 **^{1}H NMR** (400 MHz, Chloroform-*d*) δ 7.28 (d, *J* = 9.1 Hz, 2H), 6.53 (d, *J* = 9.1 Hz, 2H), 3.31 (q, *J* = 7.1 Hz, 4H), 1.14 (t, *J* = 7.1 Hz, 6H) ppm **^{13}C NMR** (101 MHz, Chloroform-*d*) δ 146.78, 131.86, 113.50, 107.06, 44.46, 12.39 ppm **LRMS (+ESI)**: *m/z* 228/230 $[M+H]^+$ **IR** (diamond cell thin film): $\tilde{\nu}$ = 2966, 2927, 2892, 570 cm^{-1}

2-Nitrophenyl benzenesulfonate - 215

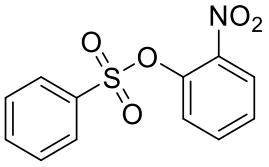

214 (1.19 g, 8.56 mmol) was dissolved in pyridine (8 mL) and cooled to 0 °C. Benzenesulfonyl chloride (1.09 mL, 8.56 mmol,) was then added dropwise and stirred at room temperature for 1 h, giving a white precipitate. The solvent was removed under a stream of N_2 and the subsequent residue extracted with HCl (1 M, 3 × 20 mL) and EtOAc (3 × 20 mL), washed with brine (1 × 20 mL) and dried over $MgSO_4$. The crude product was purified *via* flash chromatography (5:1 Hexane/EtOAc) to afford the title compound as a pale yellow crystalline solid (2.37 g, quant.).

SMILES CODE: O=S(C1=CC=CC=C1)(OC2=CC=CC=C2[N+]([O-])=O)=O **^{1}H NMR** (400 MHz, Chloroform-*d*) δ 7.91 (dd, *J* = 8.4, 1.5 Hz, 3H), 7.76 – 7.70 (m, 1H), 7.67 – 7.53 (m, 3H), 7.44 (ddd, *J* = 15.9, 8.3, 1.3 Hz, 2H) ppm **^{13}C NMR** (101 MHz, Chloroform-*d*) δ 142.86, 141.41, 134.93, 134.75, 134.22, 129.43, 128.67, 127.63, 125.87, 125.39 ppm **LRMS (+ESI)**: *m/z* 301.96 $[M+Na]^+$ **HRMS (+ESI)**: *m/z* calculated $C_{12}H_9NO_5S$ $[M+Na]^+$ 302.0094, found 302.0088 **IR** (diamond cell thin film): ṽ = 1585, 1376, 1354, 1237, 1166, 1080 cm^{-1}

2-Aminophenyl benzenesulfonate - 216

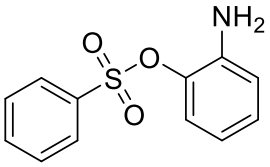

216 was prepared from **215** (290 mg, 1.03 mmol) and Pd/C (29 mg, 10 mol %) according to **general procedure E**. The product was carried through to the next step without further purification.

SMILES CODE: O=S(C1=CC=CC=C1)(OC2=CC=CC=C2N)=O **^{1}H NMR** (300 MHz, DMSO-d_6) δ 7.99 – 7.87 (m, 2H), 7.80 (td, *J* = 7.5, 1.4 Hz, 1H), 7.70 – 7.58 (m, 2H), 6.95 (t, *J* = 7.7 Hz, 1H), 6.87 (dd, *J* = 8.1, 1.7 Hz, 1H), 6.68 (dd, *J* = 8.0, 1.7 Hz, 1H), 6.47 (td, *J* = 7.8, 1.7 Hz, 1H), 4.99 (s, 2H) ppm **^{13}C NMR** (75 MHz, DMSO-d_6) δ 141.38, 135.87, 135.45, 135.31, 129.98, 128.79, 128.18, 122.54, 116.85, 116.19 ppm **LRMS (+ESI)**: *m/z* 250 $[M+H]^+$, 272 $[M + Na]^+$, 499 $[2M+H]^+$ **HRMS (+ESI)**: *m/z* calculated $C_{12}H_{11}NO_3S$ $[M+Na]^+$ 272.0352, found 272.0347 **IR** (diamond cell thin film): ṽ = 3475, 3382, 1628, 1358, 1193, 1150, 1088 cm^{-1}

2-((Phenylsulfonyl)oxy)benzenediazonium tetrafluoroborate - 220

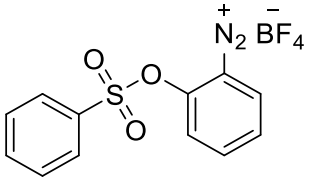

220 was prepared from **216** (257 mg, 1.03 mmol), aq. HBF_4 (673 uL, 5.15 mmol, 48% wt adjusted) and isopentyl nitrite (121 μL, 1.75 mmol) in AcOH according to **general procedure**

B. The crystals were filtered off *in vacuo*, washed with Et_2O and dried on air to afford the title compound as off-white crystals (290 mg, 81%).

SMILES CODE: O=S(OC1=CC=CC=C1[N+]#N)(C2=CC=CC=C2)=O.F[B-](F)(F)F **^{1}H NMR** (400 MHz, DMSO-d_6) δ 7.72 (d, J = 8.7 Hz, 1H), 7.61 (dd, J = 7.6, 2.3 Hz, 2H), 7.50 (td, J = 8.3, 7.4, 4.0 Hz, 1H), 7.38 – 7.29 (m, 3H), 6.69 (d, J = 9.4 Hz, 1H), 6.58 – 6.41 (m, 1H) ppm **^{13}C NMR** (101 MHz, DMSO-d_6) δ 172.28 148.55, 140.67, 128.99, 128.14, 128.06, 125.94, 121.54, 117.21, 117.12 ppm **^{19}F NMR** (DMSO-d_6, 376 MHz) δ -148.24, -148.29 (d, J = 2.2 Hz) ppm **^{11}B NMR** (128 MHz, DMSO-d6) δ -1.29 ppm **IR** (diamond cell thin film): $\tilde{\nu}$ = 2285, 1394, 1230, 1191, 1030, 1001 cm^{-1}

2-((4-(Diethylamino)phenyl)diazenyl)phenyl benzenesulfonate - 217

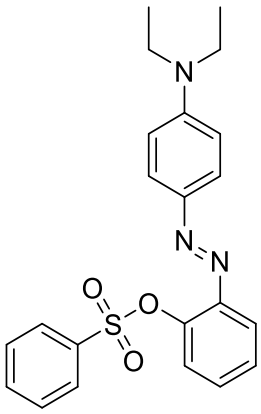

To a dried flask was added magnesium chips (24 mg, 0.98 mmol) and a crystal of I_2. The flask was flushed with argon and briefly heated *via* heat gun before being placed in an oil bath. A solution of **219** (190 mg, 0.83 mmol) in THF (5 mL) was made up, followed by addition (1 mL) to the flask containing magnesium and I_2. After the iodine colour disappeared, the remaining solution was added dropwise and the mixture heated to 60 °C overnight. The resulting mixture was allowed to cool, obtaining the formed product of **221** in THF (0.17 mmol / mL).

Following the above, a suspension of **220** (290 mg, 0.83 mmol) in THF (3 mL) was vigorously stirred and cooled to –78°C under N_2 flow. The solution of **221** in THF (5 mL, from above) was added dropwise using a syringe, over a period of 10 min. Stirring at -78 °C was continued for 1 h until the coupling reaction with **220** was completed *via* TLC. The mixture was poured into water (3 mL), extracted with Et_2O (3 × 15 mL), dried over $MgSO_4$

and concentrated *in vacuo*. The crude product was purified *via* flash chromatography (20:1 to 20:3 Hexane/EtOAc) to afford title compound as a red oily residue (169 mg, 45%).

SMILES CODE: O=S(C1=CC=CC=C1)(OC2=CC=CC=C2/N=N/C3=CC=C(N(CC)CC)C=C3)=O **^{1}H NMR** (400 MHz, Chloroform-*d*) δ 7.78 (d, *J* = 7.5 Hz, 2H), 7.62 (d, *J* = 9.2 Hz, 2H), 7.56 (dd, *J* = 7.9, 1.9 Hz, 1H), 7.44 – 7.26 (m, 6H), 6.66 (d, *J* = 9.2 Hz, 2H), 3.48 (q, *J* = 7.1 Hz, 4H), 1.26 (t, *J* = 7.1 Hz, 6H) ppm **^{13}C NMR** (101 MHz, Chloroform-*d*) δ 150.52, 146.22, 145.57, 143.37, 135.61, 133.67, 129.65, 128.67, 128.55, 127.64, 126.07, 124.32, 117.36, 110.72, 44.77, 12.68 ppm **LRMS (+ESI)**: *m/z* 410 $[M+H]^+$, 432 $[M+Na]^+$ **HRMS (+ESI)**: *m/z* calculated $C_{22}H_{23}N_3O_3S$ $[M+H]^+$ 410.1533, found 410.1529 **IR** (diamond cell thin film): $\tilde{\nu}$ = 2922, 1596, 1368, 1190, 1137, 1085 cm^{-1}

2-((4-(Diethylamino)phenyl)diazenyl)phenol - 211

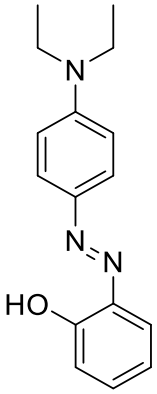

216 (169 mg, 0.41 mmol) was dissolved in an aqueous solution of 30% NaOH and heated at 100 °C. The reaction was monitored *via* TLC and after completion was neutralised with HCl to give an oily product which solidified upon standing. Subsequently it was extracted with EtOAc (3 × 15 mL), washed with brine (1 × 15 mL), dried over $MgSO_4$ and concentrated *in vacuo*. The crude product was then purified *via* flash chromatography (1:1 Hexane/EtOAc) to afford the title compound as orange-yellow crystalline plates (61 mg, 55%).

SMILES CODE: CCN(C1=CC=C(/N=N/C2=C(O)C=CC=C2)C=C1)CC **^{1}H NMR** (400 MHz, Chloroform-*d*) δ 13.22 (s, 1H), 7.93 – 7.64 (m, 3H), 7.23 (ddd, *J* = 8.7, 7.4, 1.8 Hz, 1H), 7.04 – 6.94 (m, 2H), 6.75 – 6.67 (m, 2H), 3.45 (t, *J* = 7.1 Hz, 4H), 1.24 (t, *J* = 7.1 Hz, 6H) ppm **^{13}C NMR** (101 MHz, Chloroform-*d*) δ 152.70, 150.24, 140.45, 137.54, 131.52, 130.90, 124.53, 119.55, 117.79, 111.30, 44.78, 12.67 ppm **LRMS (+ESI)**: *m/z* 260 $[M+H]^+$, 292 $[M+Na]^+$ **HRMS (+ESI)**: *m/z* calculated $C_{16}H_{19}N_3$ $[M+H]^+$ 270.1601, found 270.1597, calculated

$[M+Na]^+$ 292.1420, found 292.1416 **IR** (diamond cell thin film): $\tilde{\nu}$ = 2962, 1594, 1264, 1153, 1070, 1028 cm^{-1} **HPLC** t_R = 27.40 min, 99.22% (254 nm), 98.98% (230 nm)

N,N-Diethyl-4-((2-methoxyphenyl)diazenyl)aniline - 224

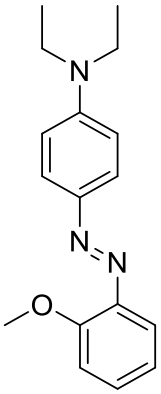

224 was prepared from **211** (20 mg, 0.074 mmol), NaH (3 mg, 0.082 mmol, 60% dispersion in oil) and MeI (14 μL, 0.22 mmol) according to **general procedure D**. The crude product was purified *via* flash chromatography (20:3 Hexane/EtOAc) to afford the title compound as an orange crystalline solid (40 mg, 72%).

SMILES CODE: CCN(CC)C(C=C1)=CC=C1/N=N/C2=CC=CC=C2OC **^{1}H NMR** (400 MHz, Chloroform-*d*) δ 7.86 (d, *J* = 9.2 Hz, 2H), 7.62 (dd, *J* = 8.0, 1.7 Hz, 1H), 7.33 (ddd, *J* = 8.7, 7.3, 1.7 Hz, 1H), 7.08 – 6.95 (m, 2H), 6.71 (d, *J* = 9.2 Hz, 2H), 4.00 (s, 3H), 3.45 (q, *J* = 7.1 Hz, 4H), 1.22 (t, *J* = 7.1 Hz, 6H) ppm **^{13}C NMR** (101 MHz, Chloroform-*d*) δ 156.01, 150.06, 143.80, 143.11, 130.31, 125.50, 120.91, 117.07, 112.60, 110.96, 56.44, 44.69, 12.68 ppm **LRMS (+ESI)**: *m/z* 284 $[M+H]^+$, 306 $[M+Na]^+$ **HRMS (+ESI)**: *m/z* calculated $C_{17}H_{21}N_3O$ $[M+H]^+$ 284.1757, found 284.1757 **IR** (diamond cell thin film): $\tilde{\nu}$ = 2970, 1595, 1270, 1244 cm^{-1} **HPLC** t_R = 22.17 min, 96.72% (254 nm), 98.46% (230 nm)

1*H*-Indole-4-carboxylic acid - 229

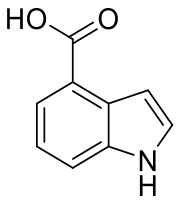

229 was prepared from **228** (638 mg, 3.64 mmol) and NaOH (437 mg, 11.0 mmol) in MeOH according to **general procedure J**. This afforded the pure title compound as a violet crystalline solid (588 mg, quant.).

SMILES CODE: OC(C1=C2C(NC=C2)=CC=C1)=O **^{1}H NMR** (400 MHz, DMSO-*d*6) δ 12.52 (s, 1H), 11.37 (s, 1H), 7.71 (dd, *J* = 7.5, 3.2 Hz, 1H), 7.65 (d, *J* = 8.0 Hz, 1H), 7.49 (t, *J* = 2.8 Hz, 1H), 7.17 (t, *J* = 7.7 Hz, 1H), 6.96 (q, *J* = 2.5 Hz, 1H) ppm **^{13}C NMR** (101 MHz, DMSO-*d*6) δ 168.97, 137.23, 127.78, 127.67, 122.80, 121.93, 120.59, 116.68, 102.82 ppm **LRMS (-ESI)**: *m/z* 160 $[M-H]^-$ **IR** (diamond cell thin film): ṽ = 3319, 1641, 1501, 1294, 1184 cm^{-1}

1*H*-Indole-4-carbonyl azide - 230

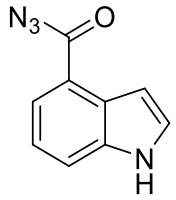

229 (100 mg, 0.62 mmol) was dissolved in 1,4-dioxane (2.5 mL) alongside DPPA (123 uL, 0.62 mmol) and Et_3N (93.5 uL, 0.671 mmol). The reaction mixture was stirred at room temperature for 30 min. Then, the solution was poured into water, extracted with hexane (3 × 10 mL), washed with brine (1 × 10 mL) and dried over $MgSO_4$ then concentrated *in vacuo*. Following this, the crude product was purified *via* flash chromatography (1:5 Hexane/EtOAc) to afford the title compound as a brown crystalline solid (89 mg, 78%).

SMILES CODE: O=C(N=[N+]=[N-])C1=C2C(NC=C2)=CC=C1 **^{1}H NMR** (400 MHz, Chloroform-*d*) δ 8.42 (s, 1H), 7.89 (dd, *J* = 7.6, 0.9 Hz, 1H), 7.70 – 7.62 (m, 1H), 7.41 (t, *J* = 2.9 Hz, 1H), 7.34 – 7.31 (m, 1H), 7.25 – 7.21 (m, 1H) ppm **^{13}C NMR** (101 MHz, Chloroform-*d*) δ 172.78, 136.61, 127.53, 127.14, 123.93, 122.07, 121.17, 117.41, 104.10 ppm **LRMS (-ESI)**: *m/z* 185 $[M-H]^-$ **IR** (diamond cell thin film): ṽ = 3338, 2257, 2150, 1661, 1608, 1343, 1262, 1178 cm^{-1}

1*H*-Indol-4-amine - 227

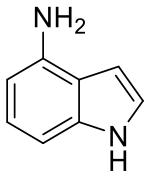

230 (89 mg, 0.48 mmol) was dissolved in H_2O (25 mL) alongside subsequent addition of 38% HCl (2 mL). The solution was set to reflux for 2 h, after which the solution was made alkaline with sat. $NaHCO_3$ (15 mL). Subsequently it was extracted with EtOAc (3 × 5 mL), washed with brine (1 × 5 mL), dried over $MgSO_4$ and concentrated *in vacuo* to provide the title compound as blue/green oil (64 mg, quant).

SMILES CODE: NC1=C2C(NC=C2)=CC=C1 **^{1}H NMR** (300 MHz, DMSO-d_6) δ 10.70 (s, 1H), 7.06 (q, J = 2.6 Hz, 1H), 6.76 (t, J = 7.7 Hz, 1H), 6.60 (d, J = 8.0 Hz, 1H), 6.51 – 6.45 (m, 1H), 6.12 (dd, J = 7.4, 0.8 Hz, 1H), 5.10 (s, 2H) ppm **^{13}C NMR** (101 MHz, DMSO-d_6) δ 141.63, 137.36, 137.00, 122.64, 106.22, 102.04, 100.49, 99.43 ppm **LRMS (+ESI)**: *m/z* 133 $[M+H]^+$ **IR** (diamond cell thin film): $\tilde{\nu}$ = 3380, 1655, 1618, 1361, 1244 cm^{-1}

1*H*-Indole-4-diazonium tetrafluoroborate salt - 250

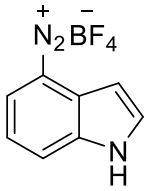

250 was prepared from **230** (64 mg, 0.48 mmol), aq. HBF_4 (316 uL, 2.42 mmol, 48% wt adjusted) and isopentyl nitrite (111 μL, 0.82 mmol) in AcOH according to **general procedure B**. The crystals were filtered off *in vacuo*, washed with Et_2O and dried on air to afford the title compound as a dark blue crystalline solid (81 mg, 72%).

SMILES CODE: N#[N+]C1=C2C(NC=C2)=CC=C1 **^{1}H NMR** (400 MHz, D_2O) δ 8.51 (d, J = 8.4 Hz, 1H), 8.29 (d, J = 8.3 Hz, 1H), 7.94 (s, 1H), 7.73 (d, J = 8.8 Hz, 1H), 7.49 (t, J = 8.0 Hz, 1H), 7.11 (d, J = 3.1 Hz, 1H) ppm **^{19}F NMR** (376 MHz, D_2O) δ -150.43, -150.48 (d, J = 3.1 Hz) ppm **^{11}B NMR** (128 MHz, D_2O) δ 0.30 (q, J = 15.1 Hz) ppm **IR** (diamond cell thin film): $\tilde{\nu}$ = 1601, 1236, 1003 cm^{-1}

4-((1*H*-Indol-4-yl)diazenyl)-*N*,*N*-diethylaniline - 213

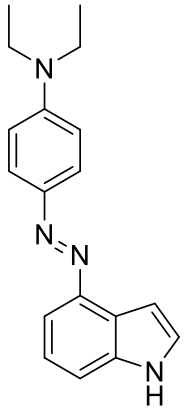

213 was prepared from aniline derivative **227** (54 mg, 0.41 mmol), $NaNO_2$ (31 mg, 0.45 mmol) and **168** (66 μL, 0.41 mmol) according to **general procedure A**. The crude product was purified *via* flash chromatography (20:3 Hexane/EtOAc) to afford the title compound as a red oily residue (12 mg, 10%).

SMILES CODE: CCN(CC)C(C=C1)=CC=C1/N=N/C2=C3C(NC=C3)=CC=C2 **^{1}H NMR** (400 MHz, Chloroform-*d*) δ 8.31 (s, 1H), 7.94 (d, *J* = 9.0 Hz, 2H), 7.68 (d, *J* = 7.5 Hz, 1H), 7.42 (d, *J* = 8.0 Hz, 1H), 7.38 – 7.31 (m, 3H), 6.76 (d, *J* = 9.0 Hz, 2H), 3.46 (q, *J* = 7.1 Hz, 4H), 1.26 (t, *J* = 7.1 Hz 6H) ppm **^{13}C NMR** (101 MHz, Chloroform-*d*) δ 150.07, 146.17, 144.32, 137.81, 125.86, 125.19, 122.45, 121.14, 117.77, 112.60, 111.39, 103.66, 45.00, 13.02 ppm **LRMS (+ESI)**: *m/z* 293 $[M+H]^+$, 315 $[M+Na]^+$ **HRMS (+ESI)**: *m/z* calculated $C_{18}H_{20}N_4$ $[M+H]^+$ 293.1761, found 293.1755 **IR** (diamond cell thin film): $\tilde{\nu}$ = 2984, 2963, 2920, 2851, 1598, 1514 cm^{-1} **HPLC** t_R = 12.25 min, 100% (254 nm), 98.02% (230 nm)

Chapter 7:

References

Chapter 7: References

(1) Australian Institute of Health and Welfare. *Dementia in Australia*; **2022**.

(2) Australian Institute of Health and Welfare. *Dementia in Australia*; **2012**.

(3) Ljubenkov, P.; Geschwind, M. Dementia. *Semin. Neurol.* **2016**, *36* (04), 397–404.

(4) Busche, M. A.; Konnerth, A. Impairments of Neural Circuit Function in Alzheimer's Disease. *Philos. Trans. R. Soc. B Biol. Sci.* **2016**, *371* (1700), 20150429.

(5) Mullane, K.; Williams, M. Alzheimer's Therapeutics: Continued Clinical Failures Question the Validity of the Amyloid Hypothesis - But What Lies Beyond? *Biochem. Pharmacol.* **2013**, *85* (3), 289–305.

(6) Mangialasche, F.; Solomon, A.; Winblad, B.; Mecocci, P.; Kivipelto, M. Alzheimer's Disease: Clinical Trials and Drug Development. *Lancet Neurol.* **2010**, *9* (7), 702–716.

(7) Chang, E.; Honson, N. S.; Bandyopadhyay, B.; Funk, K. E.; Jensen, J. R.; Kim, S.; Naphade, S.; Kuret, J. Modulation and Detection of Tau Aggregation with Small-Molecule Ligands. *Curr. Alzheimer Res.* **2009**, *6* (5), 409–414.

(8) Cisek, K.; Cooper, G. L.; Huseby, C. J.; Kuret, J. Structure and Mechanism of Action of Tau Aggregation Inhibitors. *Curr. Alzheimer Res.* **2014**, *11* (10), 918–927.

(9) Panza, F.; Solfrizzi, V.; Seripa, D.; Imbimbo, B. P.; Lozupone, M.; Santamato, A.; Zecca, C.; Barulli, M. R.; Bellomo, A.; Pilotto, A.; Daniele, A.; Greco, A.; Logroscino, G. Tau-Centric Targets and Drugs in Clinical Development for the Treatment of Alzheimer's Disease. *Biomed Res. Int.* **2016**, 1–15.

(10) Stokin, G. B.; Lillo, C.; Falzone, T. L.; Brusch, R. G.; Rockenstein, E.; Mount, S. L.; Raman, R.; Davies, P.; Masliah, E.; Williams, D. S.; Goldstein, L. S. B. Axonopathy and Transport Deficits Early in the Pathogenesis of Alzheimer's Diseases. *Science* **2005**, *307* (5713), 1282–1288.

(11) Stelzmann, R. A.; Norman Schnitzlein, H.; Reed Murtagh, F. An English Translation of Alzheimer's 1907 Paper, "Uber Eine Eigenartige Erkankung Der Hirnrinde?" *Clin. Anat.* **1995**, *8* (6), 429–431.

(12) Kidd, M. Paired Helical Filaments in Electron Microscopy of Alzheimer's Disease. *Nature* **1963**, *197* (4863), 192–193.

(13) Martinho, M.; Allegro, D.; Huvent, I.; Chabaud, C.; Etienne, E.; Kovacic, H.; Guigliarelli, B.; Peyrot, V.; Landrieu, I.; Belle, V.; Barbier, P. Two Tau Binding Sites on Tubulin Revealed by Thiol-Disulfide Exchanges. *Sci. Rep.* **2018**, *8* (1), 1–11.

(14) Zweckstetter, M.; Mandelkow, E.; Tepper, K.; Hofele, R. V.; Biernat, J.; Kumar, S.; Kadavath, H.; Urlaub, H. Tau Stabilizes Microtubules by Binding at the Interface between Tubulin Heterodimers. *Proc. Natl. Acad. Sci.* **2015**, *112* (24), 7501–7506.

(15) Mietelska-Porowska, A.; Wasik, U.; Goras, M.; Filipek, A.; Niewiadomska, G. Tau Protein Modifications and Interactions: Their Role in Function and Dysfunction. *Int. J. Mol. Sci.* **2014**, *15* (3), 4671–4713.

(16) Noble, W.; Hanger, D. P.; Miller, C. C. J. J.; Lovestone, S. The Importance of Tau Phosphorylation for Neurodegenerative Diseases. *Front. Neurol.* **2013**, *4* (July), 1–11.

(17) Iqbal, K.; Liu, F.; Gong, C-X.; Grundke-Iqbal, I. Tau in Alzheimer Disease and Related Tauopathies. *Curr. Alzheimer Res.* **2010**, *7* (8), 656–664.

(18) Gorantla, N. V.; Chinnathambi, S. Tau Protein Squired by Molecular Chaperones During Alzheimer's Disease. *J. Mol. Neurosci.* **2018**, *66* (3), 356–368.

(19) Santa-Maria, I.; Varghese, M.; Ksiezak -Reding, H.; Dzhun, A.; Wang, J.; Pasinetti, G. M. Paired Helical Filaments from Alzheimer Disease Brain Induce Intracellular Accumulation of Tau Protein in Aggresomes. *J. Biol. Chem.* **2012**, *287* (24), 20522–20533.

(20) Irwin, D. J. Tauopathies as Clinicopathological Entities. *Park. Relat. Disord.* **2016**, *22*, S29–S33.

(21) Holmes, B. B.; Diamond, M. I. Prion-like Properties of Tau Protein: The Importance of Extracellular Tau as a Therapeutic Target. *J. Biol. Chem.* **2014**, *289* (29), 19855–19861.

(22) Braak, H.; Thal, D. R.; Ghebremedhin, E.; Del Tredici, K. Stages of the Pathologic Process in Alzheimer Disease: Age Categories From 1 to 100 Years. *J. Neuropathol.*

Exp. Neurol. **2011**, *70* (11), 960–969.

(23) Andorfer, C.; Kress, Y.; Espinoza, M.; De Silva, R.; Tucker, K. L.; Barde, Y. A.; Duff, K.; Davies, P.; Silva, R. De; Tucker, K. L.; Barde, Y. A.; Duff, K.; Davies, P. Hyperphosphorylation and Aggregation of Tau in Mice Expressing Normal Human Tau Isoforms. *J. Neurochem.* **2003**, *86* (3), 582–590.

(24) Montejo de Garcini, E.; Serrano, L.; Avila, J. Self Assembly of Microtubule Associated Protein Tau into Filaments Resembling Those Found in Alzheimer Disease. *Biochem. Biophys. Res. Commun.* **1986**, *141* (2), 790–796.

(25) Wischik, C. M.; Novak, M.; Thøgersen, H. C.; Edwards, P. C.; Runswick, M. J.; Jakes, R.; Walker, J. E.; Milstein, C.; Roth, M.; Klug, A. Isolation of a Fragment of Tau Derived from the Core of the Paired Helical Filament of Alzheimer Disease. *Proc. Natl. Acad. Sci.* **1988**, *85* (12), 4506–4510.

(26) Jinwal, U. K.; Miyata, Y.; Koren, J.; Jones, J. R.; Trotter, J. H.; Chang, L.; O'Leary, J.; Morgan, D.; Lee, D. C.; Shults, C. L.; Rousaki, A.; Weeber, E. J.; Zuiderweg, E. R. P.; Gestwicki, J. E.; Dickey, C. A. Chemical Manipulation of Hsp70 ATPase Activity Regulates Tau Stability. *J. Neurosci.* **2009**, *29* (39), 12079–12088.

(27) Hardy, J.; Orr, H. The Genetics of Neurodegenerative Diseases. *J. Neurochem.* **2006**, *97* (6), 1690–1699.

(28) Blair, L. J.; Zhang, B.; Dickey, C. A. Potential Synergy between Tau Aggregation Inhibitors and Tau Chaperone Modulators. *Alzheimer's Res. Ther.* **2013**, *5* (5), 41.

(29) Churcher, I. Tau Therapeutic Strategies for the Treatment of Alzheimers Disease. *Curr. Top. Med. Chem.* **2006**, *6* (6), 579–595.

(30) Wischik, C. M.; Harrington, C. R.; Storey, J. M. D. Tau-Aggregation Inhibitor Therapy for Alzheimer's Disease. *Biochem. Pharmacol.* **2014**, *88* (4), 529–539.

(31) Kopeikina, K. J.; Hyman, B. J.; Spires-Jones, T. L. Soluble Forms of Tau Are Toxic in Alzheimer's Disease. *Transl. Neurosci.* **2012**, *3* (3), 223–233.

(32) Cowan, C. M.; Mudher, A. Are Tau Aggregates Toxic or Protective in Tauopathies? *Front. Neurol.* **2013**, *4* (August), 1–14.

(33) de Calignon, A.; Fox, L. M.; Pitstick, R.; Carlson, G. A.; Bacskai, B. J.; Spires-Jones, T. L.; Hyman, B. T. Caspase Activation Precedes and Leads to Tangles. *Nature* **2010**, *464* (7292), 1201–1204.

(34) Calcul, L.; Zhang, B.; Jinwal, U. K.; Dickey, C. A.; Baker, B. J. Natural Products as a Rich Source of Tau-Targeting Drugs for Alzheimer's Disease. *Future Med. Chem.* **2012**, *4* (13), 1751–1761.

(35) Coria, F.; Castaño, E. M.; Frangione, B. Brain Amyloid in Normal Aging and Cerebral Amyloid Angiopathy Is Antigenically Related to Alzheimer's Disease Beta-Protein. *Am. J. Pathol.* **1987**, *129* (3), 422–428.

(36) Levy, E.; Carman, M.; Fernandez-Madrid, I.; Power, M.; Lieberburg, I.; van Duinen, S.; Bots, G.; Luyendijk, W.; Frangione, B. Mutation of the Alzheimer's Disease Amyloid Gene in Hereditary Cerebral Hemorrhage, Dutch Type. *Science* **1990**, *248* (4959), 1124–1126.

(37) Ovchinnikov, D. A.; Korn, O.; Virshup, I.; Wells, C. A.; Wolvetang, E. J. The Impact of APP on Alzheimer-like Pathogenesis and Gene Expression in Down Syndrome IPSC-Derived Neurons. *Stem Cell Reports* **2018**, *11* (1), 32–42.

(38) Liu, P-P.; Xie, Y.; Meng, X-Y.; Kang, J-S. History and Progress of Hypotheses and Clinical Trials for Alzheimer's Disease. *Signal Transduct. Target. Ther.* **2019**, *4* (1).

(39) Huang, L. K.; Chao, S. P.; Hu, C. J. Clinical Trials of New Drugs for Alzheimer Disease. *J. Biomed. Sci.* **2020**, *27* (1), 1–13.

(40) Campanella, C.; Pace, A.; Bavisotto, C. C.; Marzullo, P.; Gammazza, A. M.; Buscemi, S.; Piccionello, A. P. Heat Shock Proteins in Alzheimer's Disease: Role and Targeting. *Int. J. Mol. Sci.* **2018**, *19* (9).

(41) Soeda, Y.; Saito, M.; Maeda, S.; Ishida, K.; Nakamura, A.; Kojima, S.; Takashima, A. Methylene Blue Inhibits Formation of Tau Fibrils but Not of Granular Tau Oligomers: A Plausible Key to Understanding Failure of a Clinical Trial for Alzheimer's Disease. *J. Alzheimer's Dis.* **2019**, *68* (4), 1677–1686.

(42) Cummings, J.; Lee, G.; Ritter, A.; Sabbagh, M.; Zhong, K. Alzheimer's Disease Drug Development Pipeline: 2019. *Alzheimer's Dement. Transl. Res. Clin. Interv.* **2019**, *5*,

272–293.

(43) Knopman, D. S.; Jones, D. T.; Greicius, M. D. Failure to Demonstrate Efficacy of Aducanumab: An Analysis of the EMERGE and ENGAGE Trials as Reported by Biogen, December 2019. *Alzheimer's Dement.* **2021**, *17* (4), 696–701.

(44) Tampi, R. R.; Forester, B. P.; Agronin, M. Aducanumab: Evidence from Clinical Trial Data and Controversies. *Drugs Context* **2021**, *10*, 1–9.

(45) Cummings, J. L.; Morstorf, T.; Zhong, K. Alzheimer's Disease Drug-Development Pipeline: Few Candidates, Frequent Failures. *Alzheimer's Res. Ther.* **2014**, *6* (4), 1–7.

(46) Šimic, G.; Babic Leko, M.; Wray, S.; Harrington, C.; Delalle, I.; Jovanov-Miloševic, N.; Bažadona, D.; Buée, L.; de Silva, R.; Di Giovanni, G.; Wischik, C.; Hof, P. Tau Protein Hyperphosphorylation and Aggregation in Alzheimer's Disease and Other Tauopathies, and Possible Neuroprotective Strategies. *Biomolecules* **2016**, *6* (1), 6.

(47) Crowe, A.; James, M. J.; Lee, V. M-Y.; Smith, A. B.; Trojanowski, J. Q.; Ballatore, C.; Brunden, K. R. Aminothienopyridazines and Methylene Blue Affect Tau Fibrillization via Cysteine Oxidation. *J. Biol. Chem.* **2013**, *288* (16), 11024–11037.

(48) Monti, M. C.; Margarucci, L.; Riccio, R.; Casapullo, A. Modulation of Tau Protein Fibrillization by Oleocanthal. *J. Nat. Prod.* **2012**, *75* (9), 1584–1588.

(49) Li, W.; Sperry, J. B.; Crowe, A.; Trojanowski, J. Q.; Smith III, A. B.; Lee, V. M-Y. Inhibition of Tau Fibrillization by Oleocanthal via Reaction with the Amino Groups of Tau. *J. Neurochem.* **2009**, *110* (4), 1339–1351.

(50) Zhu, M.; Rajamani, S.; Kaylor, J.; Han, S.; Zhou, F.; Fink, A. L. The Flavonoid Baicalein Inhibits Fibrillation of α-Synuclein and Disaggregates Existing Fibrils. *J. Biol. Chem.* **2004**, *279* (26), 26846–26857.

(51) Sonawane, S. K.; Uversky, V. N.; Chinnathambi, S. Baicalein Inhibits Heparin-Induced Tau Aggregation by Initializing Non-Toxic Tau Oligomer Formation. *Cell Commun. Signal.* **2021**, *19* (1), 16.

(52) Tai, H-C.; Serrano-Pozo, A.; Hashimoto, T.; Frosch, M. P.; Spires-Jones, T. L.; Hyman, B. T. The Synaptic Accumulation of Hyperphosphorylated Tau Oligomers in

Alzheimer Disease Is Associated With Dysfunction of the Ubiquitin-Proteasome System. *Am. J. Pathol.* **2012**, *181* (4), 1426–1435.

(53) George, R. C.; Lew, J.; Graves, D. J. Interaction of Cinnamaldehyde and Epicatechin with Tau: Implications of Beneficial Effects in Modulating Alzheimer's Disease Pathogenesis. *J. Alzheimer's Dis.* **2013**, *36* (1), 21–40.

(54) Sahara, N.; Maeda, S.; Murayama, M.; Suzuki, T.; Dohmae, N.; Yen, S-H.; Takashima, A. Assembly of Two Distinct Dimers and Higher-Order Oligomers from Full-Length Tau. *Eur. J. Neurosci.* **2007**, *25* (10), 3020–3029.

(55) Crowe, A.; Huang, W.; Ballatore, C.; Johnson, R. L.; Hogan, A-M. L.; Huang, R.; Wichterman, J.; McCoy, J.; Huryn, D.; Auld, D. S.; Smith, A. B.; Inglese, J.; Trojanowski, J. Q.; Austin, C. P.; Brunden, K. R.; Lee, V. M-Y. Identification of Aminothienopyridazine Inhibitors of Tau Assembly by Quantitative High-Throughput Screening. *Biochemistry* **2009**, *48* (32), 7732–7745.

(56) Barghorn, S.; Mandelkow, E. Toward a Unified Scheme for the Aggregation of Tau into Alzheimer Paired Helical Filaments. *Biochemistry* **2002**, *41* (50), 14885–14896.

(57) Schweers, O.; Mandelkow, E. M.; Biernat, J.; Mandelkow, E. Oxidation of Cysteine-322 in the Repeat Domain of Microtubule-Associated Protein Tau Controls the in Vitro Assembly of Paired Helical Filaments. *Proc. Natl. Acad. Sci.* **1995**, *92* (18), 8463–8467.

(58) Walker, S.; Ullman, O.; Stultz, C. M. Using Intramolecular Disulfide Bonds in Tau Protein to Deduce Structural Features of Aggregation-Resistant Conformations. *J. Biol. Chem.* **2012**, *287* (12), 9591–9600.

(59) Singh, J.; Petter, R. C.; Baillie, T. A.; Whitty, A. The Resurgence of Covalent Drugs. *Nat. Rev. Drug Discov.* **2011**, *10* (4), 307–317.

(60) Uetrecht, J. Immune-Mediated Adverse Drug Reactions. *Chem. Res. Toxicol.* **2009**, *22* (1), 24–34.

(61) Kumar, S.; Kassahun, K.; Tschirret-Guth, R. A.; Mitra, K.; Baillie, T. A. Minimizing Metabolic Activation during Pharmaceutical Lead Optimization: Progress, Knowledge Gaps and Future Directions. *Curr. Opin. Drug Discov. Devel.* **2008**, *11* (1), 43–52.

(62) Bulic, B.; Pickhardt, M.; Mandelkow, E. Progress and Developments in Tau Aggregation Inhibitors for Alzheimer Disease. *J. Med. Chem.* **2013**, *56* (11), 4135–4155.

(63) Chang, E.; Congdon, E. E.; Honson, N. S.; Duff, K. E.; Kuret, J. Structure−Activity Relationship of Cyanine Tau Aggregation Inhibitors. *J. Med. Chem.* **2009**, *52* (11), 3539–3547.

(64) Dwyer, D. S. Electronic Properties of Amino Acid Side Chains: Quantum Mechanics Calculation of Substituent Effects. *BMC Chem. Biol.* **2005**, *5*, 2.

(65) Parsegian, V. A. *Van Der Waals Forces: A Handbook for Biologists, Chemists, Engineers and Physicists*; Cambridge University Press: Maryland, 2005.

(66) Nayeem, A.; Krystek, S.; Stouch, T. An Assessment of Protein-Ligand Binding Site Polarizability. *Biopolymers* **2003**, *70* (2), 201–211.

(67) Zhao, L. N.; Chiu, S-W.; Benoit, J.; Chew, L. Y.; Mu, Y. The Effect of Curcumin on the Stability of Aβ Dimers. *J. Phys. Chem. B* **2012**, *116* (25), 7428–7435.

(68) Akoury, E.; Gajda, M.; Pickhardt, M.; Biernat, J.; Soraya, P.; Griesinger, C.; Mandelkow, E.; Zweckstetter, M. Inhibition of Tau Filament Formation by Conformational Modulation. *J. Am. Chem. Soc.* **2013**, *135* (7), 2853–2862.

(69) Lapidus, L. J. Understanding Protein Aggregation from the View of Monomer Dynamics. *Mol. BioSyst.* **2013**, *9* (1), 29–35.

(70) Calderón, M.; Weitzel, T.; Rodriguez, M. F.; Ciapponi, A. Methylene Blue for Treating Malaria. *Cochrane Database Syst. Rev.* **2017**, *2022* (6).

(71) Dominguez-Meijide, A.; Vasili, E.; Outeiro, T. F. Pharmacological Modulators of Tau Aggregation and Spreading. *Brain Sci.* **2020**, *10* (11), 1–29.

(72) Panza, F.; Seripa, D.; Solfrizzi, V.; Imbimbo, B. P.; Santamato, A.; Lozupone, M.; Capozzo, R.; Prete, C.; Pilotto, A.; Greco, A.; Logroscino, G. Tau Aggregation Inhibitors: The Future of Alzheimers Pharmacotherapy? *Expert Opin. Pharmacother.* **2016**, *17* (4), 457–461.

(73) Peter, C.; Hongwan, D.; Küpfer, A.; Lauterburg, B. H. Pharmacokinetics and Organ

Distribution of Intravenous and Oral Methylene Blue. *Eur. J. Clin. Pharmacol.* **2000**, *56* (3), 247–250.

(74) Khlistunova, I.; Biernat, J.; Wang, Y.; Pickhardt, M.; von Bergen, M.; Gazova, Z.; Mandelkow, E.; Mandelkow, E-M. Inducible Expression of Tau Repeat Domain in Cell Models of Tauopathy. *J. Biol. Chem.* **2006**, *281* (2), 1205–1214.

(75) Wischik, C. M.; Edwards, P. C.; Lai, R. Y.; Roth, M.; Harrington, C. R. Selective Inhibition of Alzheimer Disease-like Tau Aggregation by Phenothiazines. *Proc. Natl. Acad. Sci.* **1996**, *93* (20), 11213–11218.

(76) Harrington, C. R.; Storey, J. M. D.; Clunas, S.; Harrington, K. A.; Horsley, D.; Ishaq, A.; Kemp, S. J.; Larch, C. P.; Marshall, C.; Nicoll, S. L.; Rickard, J. E.; Simpson, M.; Sinclair, J. P.; Storey, L. J.; Wischik, C. M. Cellular Models of Aggregation-Dependent Template-Directed Proteolysis to Characterize Tau Aggregation Inhibitors for Treatment of Alzheimer Disease. *J. Biol. Chem.* **2015**, *290* (17), 10862–10875.

(77) Taniguchi, S.; Suzuki, N.; Masuda, M.; Hisanaga, S.; Iwatsubo, T.; Goedert, M.; Hasegawa, M. Inhibition of Heparin-Induced Tau Filament Formation by Phenothiazines, Polyphenols, and Porphyrins. *J. Biol. Chem.* **2005**, *280* (9), 7614–7623.

(78) Congdon, E. E.; Wu, J. W.; Myeku, N.; Figueroa, Y. H.; Herman, M.; Marinec, P. S.; Gestwicki, J. E.; Dickey, C. A.; Yu, W. H.; Duff, K. E. Methylthioninium Chloride (Methylene Blue) Induces Autophagy and Attenuates Tauopathy in Vitro and in Vivo. *Autophagy* **2012**, *8* (4), 609–622.

(79) Hosokawa, M.; Arai, T.; Masuda-Suzukake, M.; Nonaka, T.; Yamashita, M.; Akiyama, H.; Hasegawa, M. Methylene Blue Reduced Abnormal Tau Accumulation in P301L Tau Transgenic Mice. *PLoS One* **2012**, *7* (12), e52389.

(80) Zakaria, A.; Hamdi, N.; Abdel-Kader, R. M. Methylene Blue Improves Brain Mitochondrial ABAD Functions and Decreases Aβ in a Neuroinflammatory Alzheimer's Disease Mouse Model. *Mol. Neurobiol.* **2016**, *53* (2), 1220–1228.

(81) Gauthier, S.; Feldman, H. H.; Schneider, L. S.; Wilcock, G. K.; Frisoni, G. B.; Hardlund, J. H.; Moebius, H. J.; Bentham, P.; Kook, K. A.; Wischik, D. J.; Schelter, B.

O.; Davis, C. S.; Staff, R. T.; Bracoud, L.; Shamsi, K.; Storey, J. M. D.; Harrington, C. R.; Wischik, C. M. Efficacy and Safety of Tau-Aggregation Inhibitor Therapy in Patients with Mild or Moderate Alzheimer's Disease: A Randomised, Controlled, Double-Blind, Parallel-Arm, Phase 3 Trial. *Lancet* **2016**, *388* (10062), 2873–2884.

(82) Kimura, T.; Yamashita, S.; Fukuda, T.; Park, J-M.; Murayama, M.; Mizoroki, T.; Yoshiike, Y.; Sahara, N.; Takashima, A. Hyperphosphorylated Tau in Parahippocampal Cortex Impairs Place Learning in Aged Mice Expressing Wild-Type Human Tau. *EMBO J.* **2007**, *26* (24), 5143–5152.

(83) Kimura, T.; Fukuda, T.; Sahara, N.; Yamashita, S.; Murayama, M.; Mizoroki, T.; Yoshiike, Y.; Lee, B.; Sotiropoulos, I.; Maeda, S.; Takashima, A. Aggregation of Detergent-Insoluble Tau Is Involved in Neuronal Loss but Not in Synaptic Loss. *J. Biol. Chem.* **2010**, *285* (49), 38692–38699.

(84) Rane, J. S.; Bhaumik, P.; Panda, D. Curcumin Inhibits Tau Aggregation and Disintegrates Preformed Tau Filaments in Vitro. *J. Alzheimer's Dis.* **2017**, *60* (3), 999–1014.

(85) Lo Cascio, F.; Marzullo, P.; Kayed, R.; Palumbo Piccionello, A. Curcumin as Scaffold for Drug Discovery against Neurodegenerative Diseases. *Biomedicines* **2021**, *9* (2), 173.

(86) Vareed, S. K.; Kakarala, M.; Ruffin, M. T.; Crowell, J. A.; Normolle, D. P.; Djuric, Z.; Brenner, D. E. Pharmacokinetics of Curcumin Conjugate Metabolites in Healthy Human Subjects. *Cancer Epidemiol. Biomarkers Prev.* **2008**, *17* (6), 1411–1417.

(87) Prasad, S.; Tyagi, A. K.; Aggarwal, B. B. Recent Developments in Delivery, Bioavailability, Absorption and Metabolism of Curcumin: The Golden Pigment from Golden Spice. *Cancer Res. Treat.* **2014**, *46* (1), 2–18.

(88) Yang, K-Y.; Lin, L-C.; Tseng, T-Y.; Wang, S-C.; Tsai, T-H. Oral Bioavailability of Curcumin in Rat and the Herbal Analysis from Curcuma Longa by LC–MS/MS. *J. Chromatogr. B* **2007**, *853* (1–2), 183–189.

(89) Pradhan, A.; Mishra, S.; Surolia, A.; Panda, D. C1 Inhibits Liquid–Liquid Phase Separation and Oligomerization of Tau and Protects Neuroblastoma Cells against

Toxic Tau Oligomers. *ACS Chem. Neurosci.* **2021**, *12* (11), 1989–2002.

(90) Priyadarsini, K. I. Photophysics, Photochemistry and Photobiology of Curcumin: Studies from Organic Solutions, Bio-Mimetics and Living Cells. *J. Photochem. Photobiol. C Photochem. Rev.* **2009**, *10* (2), 81–95.

(91) Lo Cascio, F.; Puangmalai, N.; Ellsworth, A.; Bucchieri, F.; Pace, A.; Palumbo Piccionello, A.; Kayed, R. Toxic Tau Oligomers Modulated by Novel Curcumin Derivatives. *Sci. Rep.* **2019**, *9* (1), 19011.

(92) Vyas, A.; Dandawate, P.; Padhye, S.; Ahmad, A.; Sarkar, F. Perspectives on New Synthetic Curcumin Analogs and Their Potential Anticancer Properties. *Curr. Pharm. Des.* **2013**, *19* (11), 2047–2069.

(93) Luo, W.; Dou, F.; Rodina, A.; Chip, S.; Kim, J.; Zhao, Q.; Moulick, K.; Aguirre, J.; Wu, N.; Greengard, P.; Chiosis, G. Roles of Heat-Shock Protein 90 in Maintaining and Facilitating the Neurodegenerative Phenotype in Tauopathies. *Proc. Natl. Acad. Sci.* **2007**, *104* (22), 9511–9516.

(94) Dickey, C. A.; Burrows, F.; Petrucelli, L.; Dickey, C. A.; Kamal, A.; Lundgren, K.; Klosak, N.; Bailey, R. M.; Dunmore, J.; Ash, P.; Shoraka, S.; Zlatkovic, J.; Eckman, C. B.; Patterson, C.; Dickson, D. W.; Jr, N. S. N.; Hutton, M.; Burrows, F.; Petrucelli, L. The High-Affinity HSP90-CHIP Complex Recognizes and Selectively Degrades Phosphorylated Tau Client Proteins. *J. Clin. Invest.* **2007**, *117* (3), 648–658.

(95) Jinwal, U. K.; Koren, J.; Borysov, S. I.; Schmid, A. B.; Abisambra, J. F.; Blair, L. J.; Johnson, A. G.; Jones, J. R.; Shults, C. L.; O'Leary, J. C.; Jin, Y.; Buchner, J.; Cox, M. B.; Dickey, C. A. The Hsp90 Cochaperone, FKBP51, Increases Tau Stability and Polymerizes Microtubules. *J. Neurosci.* **2010**, *30* (2), 591–599.

(96) Mcalpine, S. R. *Heat Shock Protein Inhibitors*; McAlpine, S. R., Edkins, A. L., Eds.; Topics in Medicinal Chemistry; Springer International Publishing: Cham, **2016**; Vol. 19.

(97) Almasoud, N. N. *Heat Shock Protein-Based Therapies*; Asea, A. A. A., Almasoud, N. N., Krishnan, S., Kaur, P., Eds.; Heat Shock Proteins; Springer International Publishing: Cham, **2015**; Vol. 9.

(98) Hall, J. A.; Forsberg, L. K.; Blagg, B. S. J. Alternative Approaches to Hsp90 Modulation for the Treatment of Cancer. *Future Med. Chem.* **2014**, *6* (14), 1587–1605.

(99) Ihrig, V.; Obermann, W. M. J. Identifying Inhibitors of the Hsp90-Aha1 Protein Complex, a Potential Target to Drug Cystic Fibrosis, by Alpha Technology. *SLAS Discov.* **2017**, *22* (7), 923–928.

(100) Blair, L. J.; Sabbagh, J. J.; Dickey, C. A. Targeting Hsp90 and Its Co-Chaperones to Treat Alzheimer's Disease. *Expert Opin. Ther. Targets* **2014**, *18* (10), 1219–1232.

(101) Ou, J-R.; Tan, M-S.; Xie, A-M.; Yu, J-T.; Tan, L. Heat Shock Protein 90 in Alzheimer's Disease Jiang-Rong. *Biomed Res. Int.* **2014**, *2014*, 6–8.

(102) Jinwal, U. K.; Koren, J.; O'Leary, J. C.; Jones, J. R.; Abisambra, J. F.; Dickey, C. A. Hsp70 ATPase Modulators as Therapeutics for Alzheimer's and Other Neurodegenerative Diseases. *Mol. Cell. Pharmacol.* **2010**, *2* (2), 43–46.

(103) Dou, F.; Yuan, L. Di; Zhu, J. J. Heat Shock Protein 90 Indirectly Regulates ERK Activity by Affecting Raf Protein Metabolism. *Acta Biochim. Biophys. Sin. (Shanghai).* **2005**, *37* (7), 501–505.

(104) Evans, C. G.; Chang, L.; Gestwicki, J. E. Heat Shock Protein 70 (Hsp70) as an Emerging Drug Target. *Med. Chem.* **2010**, *70* (12), 4585–4602.

(105) Lackie, R. E.; Maciejewski, A.; Ostapchenko, V. G.; Marques-Lopes, J.; Choy, W. Y.; Duennwald, M. L.; Prado, V. F.; Prado, M. A. M. The Hsp70/Hsp90 Chaperone Machinery in Neurodegenerative Diseases. *Front. Neurosci.* **2017**, *11* (MAY), 1–23.

(106) Shelton, L. B.; Koren, J.; Blair, L. J. Imbalances in the Hsp90 Chaperone Machinery: Implications for Tauopathies. *Front. Neurosci.* **2017**, *11* (DEC), 1–12.

(107) Young, Z. T.; Rauch, J. N.; Assimon, V. A.; Jinwal, U. K.; Ahn, M.; Li, X.; Dunyak, B. M.; Ahmad, A.; Carlson, G. A.; Srinivasan, S. R.; Zuiderweg, E. R. P.; Dickey, C. A.; Gestwicki, J. E. Stabilizing the Hsp70-Tau Complex Promotes Turnover in Models of Tauopathy. *Cell Chem. Biol.* **2016**, *23* (8), 992–1001.

(108) Thompson, A. D.; Scaglione, K. M.; Prensner, J.; Gillies, A. T.; Chinnaiyan, A.; Paulson, H. L.; Jinwal, U. K.; Dickey, C. A.; Gestwicki, J. E. Analysis of the Tau-

Associated Proteome Reveals That Exchange of Hsp70 for Hsp90 Is Involved in Tau Degradation. *ACS Chem. Biol.* **2012**, *7* (10), 1677–1686.

(109) Voss, K.; Combs, B.; Patterson, K. R.; Binder, L. I.; Gamblin, T. C. Hsp70 Alters Tau Function and Aggregation in an Isoform Specific Manner. *Biochemistry* **2012**, *51* (4), 888–898.

(110) Gestwicki, J. E.; Shao, H. Inhibitors and Chemical Probes for Molecular Chaperone Networks. *J. Biol. Chem.* **2019**, *294* (6), 2151–2161.

(111) Zaiter, S. S.; Huo, Y.; Tiew, F. Y.; Gestwicki, J. E.; McAlpine, S. R. Designing de Novo Small Molecules That Control Heat Shock Protein 70 (Hsp70) and Heat Shock Organizing Protein (HOP) within the Chaperone Protein-Folding Machinery. *J. Med. Chem.* **2019**, *62* (2), 742–761.

(112) Thompson, A. D.; Dugan, A.; Gestwicki, J. E.; Mapp, A. K. Fine-Tuning Multiprotein Complexes Using Small Molecules. *ACS Chem. Biol.* **2012**, *7* (8), 1311–1320.

(113) Ran, X.; Gestwicki, J. E. Inhibitors of Protein–Protein Interactions (PPIs): An Analysis of Scaffold Choices and Buried Surface Area. *Curr. Opin. Chem. Biol.* **2018**, *44* (1), 75–86.

(114) Cesa, L. C.; Mapp, A. K.; Gestwicki, J. E. Direct and Propagated Effects of Small Molecules on Protein–Protein Interaction Networks. *Front. Bioeng. Biotechnol.* **2015**, *3* (AUG), 1–18.

(115) Wang, Y.; McAlpine, S. R. N-Terminal and C-Terminal Modulation of Hsp90 Produce Dissimilar Phenotypes. *Chem. Commun.* **2015**, *51* (8), 1410–1413.

(116) Chakafana, G.; Zininga, T.; Shonhai, A. The Link That Binds: The Linker of Hsp70 as a Helm of the Protein's Function. *Biomolecules* **2019**, *9* (10), 543.

(117) Umezawa, H.; Kondo, S.; Inuma, H.; Kunimoto, S.; Ikeda, Y.; Iwasawa, H.; Ikeda, D.; Takeuchi, T. Structure of an Antitumor Antibiotic, Spergualin. *J. Antibiot. (Tokyo).* **1981**, *34*, 1622–1624.

(118) Nishizawa, R.; Takei, Y.; Yoshida, M.; Tomiyoshi, T.; Saino, T.; Nishikawa, K.; Nemoto, K.; Takahashi, K.; Fujii, A.; Nakamura, T.; Takita, T.; Takeuchi, T. Synthesis

and Biological Activity of Spergualin Analogues. I. *J. Antibiot. (Tokyo).* **1988**, *41* (11), 1629–1643.

(119) Umeda, Y.; Moriguchi, M.; Ikai, K.; Kuroda, H.; Nakamura, T.; Fujii, A.; Takeuchi, T.; Umezawa, H. Synthesis and Antitumor Activity of Spergualin Analogues. III. Novel Method for Synthesis of Optically Active 15-Deoxyspergualin and 15-Deoxy-11-O-Methylspergualin. *J. Antibiot. (Tokyo).* **1987**, *40* (9), 1316–1324.

(120) Nadeau, K.; Nadler, S. G.; Saulnier, M.; Tepper, M. A.; Walsh, C. T. Quantitation of the Interaction of the Immunosuppressant Deoxyspergualin and Analogs with Hsc70 and Hsp90. *Biochemistry* **1994**, *33* (9), 2561–2567.

(121) Komesli, S.; Dumas, C.; Dutartre, P. Analysis of in Vivo Immunosuppressive and in Vitro Interaction with Constitutive Heat Shock Protein 70 Activity of LF08-0299 (Tresperimus) and Analogues. *Int. J. Immunopharmacol.* **1999**, *21* (5), 349–358.

(122) Evans, C. G.; Chang, L.; Gestwicki, J. E. Heat Shock Protein 70 (Hsp70) as an Emerging Drug Target. *J. Med. Chem.* **2010**, *53* (12), 4585–4602.

(123) Fewell, S. W.; Day, B. W.; Brodsky I, J. L. Identification of an Inhibitor of Hsc70-Mediated Protein Translocation and ATP Hydrolysis. *J. Biol. Chem.* **2001**, *276* (2), 910–914.

(124) Powers, M. V.; Jones, K.; Barillari, C.; Westwood, I.; Van Montfort, R. L. M.; Workman, P. Targeting HSP70: The Second Potentially Druggable Heat Shock Protein and Molecular Chaperone? *Cell Cycle* **2010**, *9* (8), 1542–1550.

(125) Fewell, S. W.; Smith, C. M.; Lyon, M. A.; Dumitrescu, T. P.; Wipf, P.; Day, B. W.; Brodsky, J. L. Small Molecule Modulators of Endogenous and Co-Chaperone-Stimulated Hsp70 ATPase Activity. *J. Biol. Chem.* **2004**, *279* (49), 51131–51140.

(126) Wisén, S.; Androsavich, J.; Evans, C. G.; Chang, L.; Gestwicki, J. E. Chemical Modulators of Heat Shock Protein 70 (Hsp70) by Sequential, Microwave-Accelerated Reactions on Solid Phase. *Bioorganic Med. Chem. Lett.* **2008**, *18* (1), 60–65.

(127) Wadhwa, R.; Sugihara, T.; Yoshida, A.; Nomura, H.; Reddel, R. R.; Simpson, R.; Maruta, H.; Kaul, S. C. Selective Toxicity of MKT-077 to Cancer Cells Is Mediated by Its Binding to the Hsp70 Family Protein Mot-2 and Reactivation of P53 Function.

Cancer Res. **2000**, *60* (24), 6818–6821.

(128) Deocaris, C. C.; Widodo, N.; Shrestha, B. G.; Kaur, K.; Ohtaka, M.; Yamasaki, K.; Kaul, S. C.; Wadhwa, R. Mortalin Sensitizes Human Cancer Cells to MKT-077-Induced Senescence. *Cancer Lett.* **2007**, *252* (2), 259–269.

(129) Rousaki, A.; Miyata, Y.; Jinwal, U. K.; Dickey, C. A.; Gestwicki, J. E.; Zuiderweg, E. R. P. Allosteric Drugs: The Interaction of Antitumor Compound MKT-077 with Human Hsp70 Chaperones. *J. Mol. Biol.* **2011**, *411* (3), 614–632.

(130) Propper, D. J.; Braybrooke, J. P.; Taylor, D. J.; Lodi, R.; Styles, P.; Cramer, J. A.; Collins, W. C. J.; Levitt, N. C.; Talbot, D. C.; Ganesan, T. S.; Harris, A. L. Phase I Trial of the Selective Mitochondrial Toxin MKT 077 in Chemo-Resistant Solid Tumours. *Ann. Oncol.* **1999**, *10* (8), 923–927.

(131) Britten, C. D.; Rowinsky, E. K.; Baker, S. D.; Weiss, G. R.; Smith, L.; Stephenson, J.; Rothenberg, M.; Smetzer, L.; Cramer, J.; Collins, W.; Von Hoff, D. D.; Eckhardt, S. G. A Phase I and Pharmacokinetic Study of the Mitochondrial-Specific Rhodacyanine Dye Analog MKT 077. *Clin. Cancer Res.* **2000**, *6* (1), 42–49.

(132) Koren, J.; Miyata, Y.; Kiray, J.; O'Leary, J. C.; Nguyen, L.; Guo, J.; Blair, L. J.; Li, X.; Jinwal, U. K.; Cheng, J. Q.; Gestwicki, J. E.; Dickey, C. A. Rhodacyanine Derivative Selectively Targets Cancer Cells and Overcomes Tamoxifen Resistance. *PLoS One* **2012**, *7* (4), e35566.

(133) Abisambra, J.; Jinwal, U. K.; Miyata, Y.; Rogers, J.; Blair, L.; Li, X.; Seguin, S. P.; Wang, L.; Jin, Y.; Bacon, J.; Brady, S.; Cockman, M.; Guidi, C.; Zhang, J.; Koren, J.; Young, Z. T.; Atkins, C. A.; Zhang, B.; Lawson, L. Y.; Weeber, E. J.; Brodsky, J. L.; Gestwicki, J. E.; Dickey, C. A. Allosteric Heat Shock Protein 70 Inhibitors Rapidly Rescue Synaptic Plasticity Deficits by Reducing Aberrant Tau. *Biol. Psychiatry* **2013**, *74* (5), 367–374.

(134) Miyata, Y.; Li, X.; Lee, H-F.; Jinwal, U. K.; Srinivasan, S. R.; Seguin, S. P.; Young, Z. T.; Brodsky, J. L.; Dickey, C. A.; Sun, D.; Gestwicki, J. E. Synthesis and Initial Evaluation of YM-08, a Blood-Brain Barrier Permeable Derivative of the Heat Shock Protein 70 (Hsp70) Inhibitor MKT-077, Which Reduces Tau Levels. *ACS Chem. Neurosci.* **2013**, *4* (6), 930–939.

(135) Tatsuta, N.; Suzuki, N.; Mochizuki, T.; Koya, K.; Kawakami, M.; Shishido, T.; Motoji, N.; Kuroiwa, H.; Shigematsu, A.; Chen, L. B. Pharmacokinetic Analysis and Antitumor Efficacy of MKT-077, a Novel Antitumor Agent. *Cancer Chemother. Pharmacol.* **1999**, *43* (4), 295–301.

(136) Koay, Y. C.; Wahyudi, H.; McAlpine, S. R. Reinventing Hsp90 Inhibitors: Blocking C-Terminal Binding Events to Hsp90 by Using Dimerized Inhibitors. *Chem. - A Eur. J.* **2016**, *22* (51), 18572–18582.

(137) Wolmarans, A.; Lee, B.; Spyracopoulos, L.; LaPointe, P. The Mechanism of Hsp90 ATPase Stimulation by Aha1. *Sci. Rep.* **2016**, *6* (1), 33179.

(138) Li, J.; Soroka, J.; Buchner, J. The Hsp90 Chaperone Machinery: Conformational Dynamics and Regulation by Co-Chaperones. *Biochim. Biophys. Acta - Mol. Cell Res.* **2012**, *1823* (3), 624–635.

(139) Zhao, R.; Houry, W. A. Molecular Interaction Network of the Hsp90 Chaperone System. *Adv. Exp. Med. Biol.* **2007**, *594*, 27–36.

(140) Piper, P. W.; Millson, S. H. Mechanisms of Resistance to Hsp90 Inhibitor Drugs: A Complex Mosaic Emerges. *Pharmaceuticals* **2011**, *4* (11), 1400–1422.

(141) Salminen, A.; Ojala, J.; Kaarniranta, K.; Hiltunen, M.; Soininen, H. Hsp90 Regulates Tau Pathology through Co-Chaperone Complexes in Alzheimer's Disease. *Prog. Neurobiol.* **2011**, *93* (1), 99–110.

(142) Bickel, D.; Gohlke, H. C-Terminal Modulators of Heat Shock Protein of 90 KDa (HSP90): State of Development and Modes of Action. *Bioorg. Med. Chem.* **2019**, 115080.

(143) Taldone, T.; Chiosis, G. Purine-Scaffold Hsp90 Inhibitors. *Curr. Top. Med. Chem.* **2009**, *9* (15), 1436–1446.

(144) Röhl, A.; Rohrberg, J.; Buchner, J. The Chaperone Hsp90: Changing Partners for Demanding Clients. *Trends Biochem. Sci.* **2013**, *38* (5), 253–262.

(145) Holmes, J. L.; Sharp, S. Y.; Hobbs, S.; Workman, P. Silencing of Hsp90 Cochaperone Aha1 Expression Decreases Client Protein Activation and Increases Cellular

Sensitivity to the Hsp90 Inhibitor 17-Allylamino-17-Demethoxygeldanamycin. *Cancer Res.* **2008**, *68* (4), 1188–1197.

(146) Kataria, N.; Kerr, B.; Zaiter, S. S.; Mcalpine, S. R.; Cook, K. M. C-Terminal Hsp90 Inhibitors Block the HIF-1 Hypoxic Response by Degrading HIF-1α through the Oxygen-Dependent Degradation Pathway. *Cell. Physiol. Biochem.* **2019**, *53* (3), 480–495.

(147) Bhatia, S.; Diedrich, D.; Frieg, B.; Ahlert, H.; Stein, S.; Bopp, B.; Lang, F.; Zang, T.; Kröger, T.; Ernst, T.; Kögler, G.; Krieg, A.; Lüdeke, S.; Kunkel, H.; Rodrigues Moita, A. J.; Kassack, M. U.; Marquardt, V.; Opitz, F. V.; Oldenburg, M.; Remke, M.; Babor, F.; Grez, M.; Hochhaus, A.; Borkhardt, A.; Groth, G.; Nagel-Steger, L.; Jose, J.; Kurz, T.; Gohlke, H.; Hansen, F. K.; Hauer, J. Targeting Hsp90 Dimerization via the C Terminus Is Effective in Imatinib-Resistant CML and Lacks the Heat Shock Response. *Blood* **2018**, *132* (3), 307–320.

(148) Echeverría, P. C.; Bernthaler, A.; Dupuis, P.; Mayer, B.; Picard, D. An Interaction Network Predicted from Public Data as a Discovery Tool: Application to the Hsp90 Molecular Chaperone Machine. *PLoS One* **2011**, *6* (10), e26044.

(149) Sidera, K.; Patsavoudi, E. HSP90 Inhibitors: Current Development and Potential in Cancer Therapy. *Recent Pat. Anticancer. Drug Discov.* **2014**, *9* (1), 1–20.

(150) Donnelly, A.; Blagg, B. Novobiocin and Additional Inhibitors of the Hsp90 C-Terminal Nucleotide- Binding Pocket. *Curr. Med. Chem.* **2008**, *15* (26), 2702–2717.

(151) Ghosh, S.; Shinogle, H. E.; Garg, G.; Vielhauer, G. A.; Holzbeierlein, J. M.; Dobrowsky, R. T.; Blagg, B. S. J. Hsp90 C-Terminal Inhibitors Exhibit Antimigratory Activity by Disrupting the Hsp90α/Aha1 Complex in PC3-MM2 Cells. *ACS Chem. Biol.* **2015**, *10* (2), 577–590.

(152) Dickey, C.; Eriksen, J.; Kamal, A.; Burrows, F.; Kasibhatla, S.; Eckman, C.; Hutton, M.; Petrucelli, L. Development of a High Throughput Drug Screening Assay for the Detection of Changes in Tau Levels - Proof of Concept with Hsp90 Inhibitors. *Curr. Alzheimer Res.* **2005**, *2* (2), 231–238.

(153) Vilenchik, M.; Solit, D.; Basso, A.; Huezo, H.; Lucas, B.; He, H.; Rosen, N.;

Spampinato, C.; Modrich, P.; Chiosis, G. Targeting Wide-Range Oncogenic Transformation via PU24FCl, a Specific Inhibitor of Tumor Hsp90. *Chem. Biol.* **2004**, *11* (6), 787–797.

(154) Tortosa, E.; Santa-Maria, I.; Moreno, F.; Lim, F.; Perez, M.; Avila, J. Binding of Hsp90 to Tau Promotes a Conformational Change and Aggregation of Tau Protein. *J. Alzheimer's Dis.* **2009**, *17* (2), 319–325.

(155) Ou, J-R.; Tan, M-S.; Xie, A-M.; Yu, J-T.; Tan, L. Heat Shock Protein 90 in Alzheimer's Disease. *Biomed Res. Int.* **2014**, *2014*, 1–7.

(156) Singh, J. K.; Hutt, D. M.; Tait, B.; Guy, N. C.; Sivils, J. C.; Ortiz, N. R.; Payan, A. N.; Komaragiri, S. K.; Owens, J. J.; Culbertson, D.; Blair, L. J.; Dickey, C.; Kuo, S. Y.; Finley, D.; Dyson, H. J.; Cox, M. B.; Chaudhary, J.; Gestwicki, J. E.; Balch, W. E. Management of Hsp90-Dependent Protein Folding by Small Molecules Targeting the Aha1 Co-Chaperone. *Cell Chem. Biol.* **2020**, *27* (3), 292-305.e6.

(157) Shelton, L. B.; Baker, J. D.; Zheng, D.; Sullivan, L. E.; Solanki, P. K.; Webster, J. M.; Sun, Z.; Sabbagh, J. J.; Nordhues, B. A.; Koren, J.; Ghosh, S.; Blagg, B. S. J.; Blair, L. J.; Dickey, C. A. Hsp90 Activator Aha1 Drives Production of Pathological Tau Aggregates. *Proc. Natl. Acad. Sci.* **2017**, *114* (36), 9707–9712.

(158) Sanchez, J.; Carter, T. R.; Cohen, M. S.; Blagg, B. S. J. Old and New Approaches to Target the Hsp90 Chaperone. *Curr. Cancer Drug Targets* **2020**, *20* (4), 253–270.

(159) Zhang, H.; Neely, L.; Lundgren, K.; Yang, Y. C.; Lough, R.; Timple, N.; Burrows, F. BIIB021, a Synthetic Hsp90 Inhibitor, Has Broad Application against Tumors with Acquired Multidrug Resistance. *Int. J. Cancer* **2010**, *126* (5), 1226–1234.

(160) Chiosis, G.; Timaul, M. N.; Lucas, B.; Munster, P. N.; Zheng, F. F.; Sepp-Lorenzino, L.; Rosen, N. A Small Molecule Designed to Bind to the Adenine Nucleotide Pocket of Hsp90 Causes Her2 Degradation and the Growth Arrest and Differentiation of Breast Cancer Cells. *Chem. Biol.* **2001**, *8* (3), 289–299.

(161) Deboer, C.; Meulman, P. A.; Wnuk, R. J.; Peterson, D. H. Geldanamycin, A New Antibiotic. *J. Antibiot. (Tokyo).* **1970**, *23* (9), 442–447.

(162) Whitesell, L.; Mimnaugh, E. G.; De Costa, B.; Myers, C. E.; Neckers, L. M. Inhibition

of Heat Shock Protein Hsp90-Pp60v-Src Heteroprotein Complex Formation by Benzoquinone Ansamycins: Essential Role for Stress Proteins in Oncogenic Transformation. *Proc. Natl. Acad. Sci.* **1994**, *91* (18), 8324–8328.

(163) Solit, D. B.; Ivy, S. P.; Kopil, C.; Sikorski, R.; Morris, M. J.; Slovin, S. F.; Kelly, W. K.; DeLaCruz, A.; Curley, T.; Heller, G.; Larson, S.; Schwartz, L.; Egorin, M. J.; Rosen, N.; Scher, H. I. Phase I Trial of 17-Allylamino-17-Demethoxygeldanamycin in Patients with Advanced Cancer. *Clin. Cancer Res.* **2007**, *13* (6), 1775–1782.

(164) Shin, S. C.; El-Damasy, A. K.; Lee, J. H.; Seo, S. H.; Kim, J. H.; Seo, Y. H.; Lee, Y.; Yu, J. H.; Bang, E. K.; Kim, E. E.; Keum, G. Structural Basis for Design of New Purine-Based Inhibitors Targeting the Hydrophobic Binding Pocket of Hsp90. *Int. J. Mol. Sci.* **2020**, *21* (24), 1–21.

(165) Samuni, Y.; Ishii, H.; Hyodo, F.; Samuni, U.; Krishna, M. C.; Goldstein, S.; Mitchell, J. B. Reactive Oxygen Species Mediate Hepatotoxicity Induced by the Hsp90 Inhibitor Geldanamycin and Its Analogs. *Free Radic. Biol. Med.* **2010**, *48* (11), 1559–1563.

(166) Chiosis, G.; Lucas, B.; Huezo, H.; Solit, D.; Basso, A.; Rosen, N. Development of Purine-Scaffold Small Molecule Inhibitors of Hsp90. *Curr. Cancer Drug Targets* **2003**, *3* (5), 371–376.

(167) Kasibhatla, S. R.; Hong, K.; Biamonte, M. A.; Busch, D. J.; Karjian, P. L.; Sensintaffar, J. L.; Kamal, A.; Lough, R. E.; Brekken, J.; Lundgren, K.; Grecko, R.; Timony, G. A.; Ran, Y.; Mansfield, R.; Fritz, L. C.; Ulm, E.; Burrows, F. J.; Boehm, M. F. Rationally Designed High-Affinity 2-Amino-6-Halopurine Heat Shock Protein 90 Inhibitors That Exhibit Potent Antitumor Activity. *J. Med. Chem.* **2007**, *50* (12), 2767–2778.

(168) Saif, M. W.; Takimoto, C.; Mita, M.; Banerji, U.; Lamanna, N.; Castro, J.; O'Brien, S.; Stogard, C.; Von Hoff, D. A Phase 1, Dose-Escalation, Pharmacokinetic and Pharmacodynamic Study of BIIB021 Administered Orally in Patients with Advanced Solid Tumors. *Clin. Cancer Res.* **2014**, *20* (2), 445–455.

(169) Dickson, M. A.; Okuno, S. H.; Keohan, M. L.; Maki, R. G.; D'Adamo, D. R.; Akhurst, T. J.; Antonescu, C. R.; Schwartz, G. K. Phase II Study of the Hsp90-Inhibitor BIIB021 in Gastrointestinal Stromal Tumors. *Ann. Oncol.* **2013**, *24* (1), 252–257.

(170) Jhaveri, K.; Taldone, T.; Modi, S.; Chiosis, G. Advances in the Clinical Development of Heat Shock Protein 90 (Hsp90) Inhibitors in Cancers. *Biochim. Biophys. Acta - Mol. Cell Res.* **2012**, *1823* (3), 742–755.

(171) Magwenyane, A. M.; Ugbaja, S. C.; Amoako, D. G.; Somboro, A. M.; Khan, R. B.; Kumalo, H. M. Heat Shock Protein 90 (HSP90) Inhibitors as Anticancer Medicines: A Review on the Computer-Aided Drug Discovery Approaches over the Past Five Years. *Comput. Math. Methods Med.* **2022**, *2022*, 1–20.

(172) Fabio Falsone, S.; Leptihn, S.; Osterauer, A.; Haslbeck, M.; Buchner, J. Oncogenic Mutations Reduce the Stability of Src Kinase. *J. Mol. Biol.* **2004**, *344* (1), 281–291.

(173) Salinas-Garcia, M. C.; Plaza-Garrido, M.; Camara-Artigas, A. The Impact of Oncogenic Mutations of the Viral Src Kinase on the Structure and Stability of the SH3 Domain. *Acta Crystallogr. Sect. D Struct. Biol.* **2021**, *77* (6), 854–866.

(174) Yu, J.; Zhang, C.; Song, C. Pan- and Isoform-Specific Inhibition of Hsp90: Design Strategy and Recent Advances. *Eur. J. Med. Chem.* **2022**, *238* (June), 114516.

(175) Soti, C.; Vermes, A.; Haystead, T. A. J.; Csermely, P. Comparative Analysis of the ATP-Binding Sites of Hsp90 by Nucleotide Affinity Cleavage: A Distinct Nucleotide Specificity of the C-Terminal ATP-Binding Site. *Eur. J. Biochem.* **2003**, *270* (11), 2421–2428.

(176) Söti, C.; Rácz, A.; Csermely, P. A Nucleotide-Dependent Molecular Switch Controls ATP Binding at the C-Terminal Domain of Hsp90. *J. Biol. Chem.* **2002**, *277* (9), 7066–7075.

(177) Marcu, M. G.; Schulte, T. W.; Neckers, L. Novobiocin and Related Coumarins and Depletion of Heat Shock Protein 90- Dependent Signaling Proteins. *J. Natl. Cancer Inst.* **2000**, *92* (3), 242–248.

(178) Burlison, J. A.; Lubbers, D. J.; Blagg, B. S. J.; Avila, C.; Vielhauer, G.; Holzbeierlein, J. Development of Novobiocin Analogues That Manifest Anti-Proliferative Activity against Several Cancer Cell Lines. *J. Org. Chem.* **2008**, *73* (6), 2130–2137.

(179) Marcu, M. G.; Chadli, A.; Bouhouche, I.; Catelli, M.; Neckers, L. M. The Heat Shock Protein 90 Antagonist Novobiocin Interacts with a Previously Unrecognized ATP-

Binding Domain in the Carboxyl Terminus of the Chaperone. *J. Biol. Chem.* **2000**, *275* (47), 37181–37186.

(180) Allan, R. K.; Mok, D.; Ward, B. K.; Ratajczak, T. Modulation of Chaperone Function and Cochaperone Interaction by Novobiocin in the C-Terminal Domain of Hsp90. *J. Biol. Chem.* **2006**, *281* (11), 7161–7171.

(181) Vígh, L.; Literáti, P. N.; Horváth, I.; Török, Z.; Balogh, G.; Glatz, A.; Kovács, E.; Boros, I.; Ferdinándy, P.; Parkas, B.; Jaszlits, L.; Jednákovits, A.; Korányi, L.; Maresca, B. Bimoclomol: A Nontoxic, Hydroxylamine Derivative with Stress Protein-Inducing Activity and Cytoprotective Effects. *Nat. Med.* **1997**, *3* (10), 1150–1154.

(182) Fülöp, F.; Vigh, L.; Török, Z.; Penke, B.; Horváth, I.; Balogh, G.; Bernáth, S.; Hunya, Á. 1,4-Dihydropyridine Derivatives with Hsp Modulating Activity. WO2013/076516 A1, 2012.

(183) Kasza, Á.; Hunya, Á.; Frank, Z.; Fülöp, F.; Török, Z.; Balogh, G.; Sántha, M.; Bálind, Á.; Bernáth, S.; Blundell, K. L. I. M.; Prodromou, C.; Horváth, I.; Zeiler, H. J.; Hooper, P. L.; Vigh, L.; Penke, B.; Abisambra, J. Dihydropyridine Derivatives Modulate Heat Shock Responses and Have a Neuroprotective Effect in a Transgenic Mouse Model of Alzheimer's Disease. *J. Alzheimer's Dis.* **2016**, *53* (2), 557–571.

(184) Roe, M. S.; Wahab, B.; Török, Z.; Horváth, I.; Vigh, L.; Prodromou, C. Dihydropyridines Allosterically Modulate Hsp90 Providing a Novel Mechanism for Heat Shock Protein Co-Induction and Neuroprotection. *Front. Mol. Biosci.* **2018**, *5* (JUN), 1–14.

(185) Lamech, L. T.; Haynes, C. M. The Unpredictability of Prolonged Activation of Stress Response Pathways. *J. Cell Biol.* **2015**, *209* (6), 781–787.

(186) Kovacech, B.; Skrabana, R.; Novak, M. Transition of Tau Protein from Disordered to Misordered in Alzheimer's Disease. *Neurodegener. Dis.* **2010**, *7* (1–3), 24–27.

(187) Dunker, A. K.; Oldfield, C. J.; Meng, J.; Romero, P.; Yang, J. Y.; Chen, J. W.; Vacic, V.; Obradovic, Z.; Uversky, V. N. The Unfoldomics Decade: An Update on Intrinsically Disordered Proteins. *BMC Genomics* **2008**, *9* (Suppl 2), S1.

(188) Criado-Marrero, M.; Gebru, N. T.; Blazier, D. M.; Gould, L. A.; Baker, J. D.;

Beaulieu-Abdelahad, D.; Blair, L. J. Hsp90 Co-Chaperones, FKBP52 and Aha1, Promote Tau Pathogenesis in Aged Wild-Type Mice. *Acta Neuropathol. Commun.* **2021**, *9* (1), 1–16.

(189) Panaretou, B.; Siligardi, G.; Meyer, P.; Maloney, A.; Sullivan, J. K.; Singh, S.; Millson, S. H.; Clarke, P. A.; Naaby-Hansen, S.; Stein, R.; Cramer, R.; Mollapour, M.; Workman, P.; Piper, P. W.; Pearl, L. H.; Prodromou, C. Activation of the ATPase Activity of Hsp90 by the Stress-Regulated Cochaperone Aha1. *Mol. Cell* **2002**, *10* (6), 1307–1318.

(190) Eskew, J. D.; Sadikot, T.; Morales, P.; Duren, A.; Dunwiddie, I.; Swink, M.; Zhang, X.; Hembruff, S.; Donnelly, A.; Rajewski, R. A.; Blagg, B. S. J.; Manjarrez, J. R.; Matts, R. L.; Holzbeierlein, J. M.; Vielhauer, G. A. Development and Characterization of a Novel C-Terminal Inhibitor of Hsp90 in Androgen Dependent and Independent Prostate Cancer Cells. *BMC Cancer* **2011**, *11*, 1–16.

(191) Augustinack, J. C.; Schneider, A.; Mandelkow, E-M.; Hyman, B. T. Specific Tau Phosphorylation Sites Correlate with Severity of Neuronal Cytopathology in Alzheimer's Disease. *Acta Neuropathol.* **2002**, *103* (1), 26–35.

(192) Luna-Muñoz, J.; Chávez-Macías, L.; García-Sierra, F.; Mena, R. Earliest Stages of Tau Conformational Changes Are Related to the Appearance of a Sequence of Specific Phospho-Dependent Tau Epitopes in Alzheimer's Disease1. *J. Alzheimer's Dis.* **2007**, *12* (4), 365–375.

(193) Naserkhaki, R.; Zamanzadeh, S.; Baharvand, H.; Nabavi, S. M.; Pakdaman, H.; Shahbazi, S.; Vosough, M.; Ghaedi, G.; Barzegar, A.; Mirtorabi, D.; Hedayatshodeh, M.; Ehsani, E.; Falahati, M.; Hajipour, M. J.; Shahpasand, K. Cis PT231-Tau Drives Neurodegeneration in Bipolar Disorder. *ACS Chem. Neurosci.* **2019**, *10* (3), 1214–1221.

(194) Criado-Marrero, M.; Shelton, L. B.; Blair, L. J. Reduction in Aha1 Chaperone Preserves Hippocampal Neurons and Prevents Tau-related Pathology in RTg4510 Tau Transgenic Mice. *Alzheimer's Dement.* **2022**, *17* (S3), e054082.

(195) Stiegler, S. C.; Rübbelke, M.; Korotkov, V. S.; Weiwad, M.; John, C.; Fischer, G.; Sieber, S. A.; Sattler, M.; Buchner, J. A Chemical Compound Inhibiting the Aha1–

Hsp90 Chaperone Complex. *J. Biol. Chem.* **2017**, *292* (41), 17073–17083.

(196) Keegan, B. M.; Catalfano, K. C.; Banerjee, M.; Blagg, B. S. J. Synthesis and Evaluation of Small Molecule Disruptors of the Aha1/Hsp90 Complex for the Reduction of Tau Aggregation. *ACS Med. Chem. Lett.* **2022**, 1–6.

(197) Wang, L.; Bharti; Kumar, R.; Pavlov, P. F.; Winblad, B. Small Molecule Therapeutics for Tauopathy in Alzheimer's Disease: Walking on the Path of Most Resistance. *Eur. J. Med. Chem.* **2021**, *209*, 112915.

(198) Kim, J.; Battsengel, O.; Liu, Y.; Chae, J. Reaction of 1,2-Difunctionalized Ethanes with Aryl Iodides in Copper-Catalyzed Cross-Coupling: Application to Synthesis of Phenols. *Bull. Korean Chem. Soc.* **2015**, *36* (12), 2833–2840.

(199) Job, G. E.; Buchwald, S. L. Copper-Catalyzed Arylation of β-Amino Alcohols. *Org. Lett.* **2002**, *4* (21), 3703–3706.

(200) Liu, Y.; Park, S. K.; Xiao, Y.; Chae, J. Copper(Ii)-Catalyzed C–O Coupling of Aryl Bromides with Aliphatic Diols: Synthesis of Ethers, Phenols, and Benzo-Fused Cyclic Ethers. *Org. Biomol. Chem.* **2014**, *12* (26), 4747.

(201) Payne, G. B. Epoxide Migrations with α,β-Epoxy Alcohols. *J. Org. Chem.* **1962**, *27* (11), 3819–3822.

(202) Mai, T. V-T.; Nguyen, T. T-D.; Nguyen, H. T.; Nguyen, T. T.; Huynh, L. K. New Mechanistic Insights into Atmospheric Oxidation of Aniline Initiated by OH Radicals. *Environ. Sci. Technol.* **2021**, *55* (12), 7858–7868.

(203) Morávková, Z.; Dmitrieva, E. The First Products of Aniline Oxidation – SERS Spectroelectrochemistry. *ChemistrySelect* **2019**, *4* (30), 8847–8854.

(204) Konaka, R.; Kuruma, K.; Terabe, S. Mechanisms of Oxidation of Aniline and Related Compounds in Basic Solution. *J. Am. Chem. Soc.* **1968**, *90* (7), 1801–1806.

(205) Bhattacharyya, D.; Hamrin, C. E.; Northey, R. P. Oxidation of Hazardous Organics in a Two-Phase Fluorocarbon-Water System. *Hazard. Waste Hazard. Mater.* **1986**, *3* (4), 405–427.

(206) Ferreira, G. R.; Garcia, H. C.; Couri, M. R. C.; Dos Santos, H. F.; De Oliveira, L. F. C.

On the Azo/Hydrazo Equilibrium in Sudan i Azo Dye Derivatives. *J. Phys. Chem. A* **2013**, *117* (3), 642–649.

(207) Spagnolo, P.; Tundo, A.; Zanirato, P. Intramolecular Addition of Aryl Azides to the Azo Group. 2. Synthesis and Properties of Benz[Cd]Indazole N-Arylimines. *J. Org. Chem.* **1978**, *43* (12), 2508–2513.

(208) Wang, Z. Irvine-Purdie Methylation. In *Comprehensive Organic Name Reactions and Reagents*; John Wiley & Sons, Inc.: Hoboken, NJ, USA, **2010**; pp 1526–1529.

(209) Dhakal, S.; Schmidt, W. F.; Kim, M.; Tang, X.; Peng, Y.; Chao, K. Detection of Additives and Chemical Contaminants in Turmeric Powder Using FT-IR Spectroscopy. *Foods* **2019**, *8* (5), 143.

(210) Merino, E. Synthesis of Azobenzenes: The Coloured Pieces of Molecular Materials. *Chem. Soc. Rev.* **2011**, *40* (7), 3835–3853.

(211) Chua, S. W.; Cornejo, A.; van Eersel, J.; Stevens, C. H.; Vaca, I.; Cueto, M.; Kassiou, M.; Gladbach, A.; Macmillan, A.; Lewis, L.; Whan, R.; Ittner, L. M. The Polyphenol Altenusin Inhibits in Vitro Fibrillization of Tau and Reduces Induced Tau Pathology in Primary Neurons. *ACS Chem. Neurosci.* **2017**, *8* (4), 743–751.

(212) Meanwell, N. A. Fluorine and Fluorinated Motifs in the Design and Application of Bioisosteres for Drug Design. *J. Med. Chem.* **2018**, *61* (14), 5822–5880.

(213) Biancalana, M.; Koide, S. Molecular Mechanism of Thioflavin-T Binding to Amyloid Fibrils. *Biochim. Biophys. Acta - Proteins Proteomics* **2010**, *1804* (7), 1405–1412.

(214) Sui, D.; Liu, M.; Kuo, M-H. In Vitro Aggregation Assays Using Hyperphosphorylated Tau Protein. *J. Vis. Exp.* **2015**, No. 95.

(215) Zhang, W.; Falcon, B.; Murzin, A. G.; Fan, J.; Crowther, R. A.; Goedert, M.; Scheres, S. H. Heparin-Induced Tau Filaments Are Polymorphic and Differ from Those in Alzheimer's and Pick's Diseases. *Elife* **2019**, *8*.

(216) Lövestam, S.; Koh, F. A.; van Knippenberg, B.; Kotecha, A.; Murzin, A. G.; Goedert, M.; Scheres, S. H. Assembly of Recombinant Tau into Filaments Identical to Those of Alzheimer's Disease and Chronic Traumatic Encephalopathy. *Elife* **2022**, *11*.

(217) Brüschweiler, B. J.; Merlot, C. Azo Dyes in Clothing Textiles Can Be Cleaved into a Series of Mutagenic Aromatic Amines Which Are Not Regulated Yet. *Regul. Toxicol. Pharmacol.* **2017**, *88*, 214–226.

(218) Chung, K-T.; Cerniglia, C. E. Mutagenicity of Azo Dyes: Structure-Activity Relationships. *Mutat. Res. Genet. Toxicol.* **1992**, *277* (3), 201–220.

(219) Ahlström, L-H.; Sparr Eskilsson, C.; Björklund, E. Determination of Banned Azo Dyes in Consumer Goods. *TrAC Trends Anal. Chem.* **2005**, *24* (1), 49–56.

(220) Chung, K-T.; Stevens, S. E.; Cerniglia, C. E. The Reduction of Azo Dyes by the Intestinal Microflora. *Crit. Rev. Microbiol.* **1992**, *18* (3), 175–190.

(221) Jacob, N.; Guillemard, L.; Wencel-Delord, J. Highly Efficient Synthesis of Hindered 3-Azoindoles via Metal-Free C–H Functionalization of Indoles. *Synthesis (Stuttg).* **2020**, *52* (04), 574–580.

(222) Frahn, J.; Illman, R. Preparation of a 4-Methoxyphenylhydrazine and Some Other Arylhydrazines. *Aust. J. Chem.* **1974**, *27* (6), 1361.

(223) Bartwal, G.; Saroha, M.; Khurana, J. M. Nickel Boride Mediated Chemoselective Reduction of Aryldiazonium Tetrafluoroborates to Corresponding Aryl Hydrazines and Aryl Amines at Ambient Temperature. *ChemistrySelect* **2018**, *3* (44), 12600–12602.

(224) Bandgar, B. P.; Uppalla, L. S. Novel Chemoselective Reduction of Aryldiazonium Fluoroborates with Zn–NiCl2•6H2O–THF. *J. Chem. Res.* **1999**, No. 12, 714–715.

(225) Roberts, D. J.; Caserio, C. M. *Basic Principles of Organic Chemistry*, 2nd ed.; Addison-Wesley, **1977**.

(226) Harikrishna, N.; Isloor, A. M.; Ananda, K.; Obaid, A.; Fun, H-K. 1,3,4-Trisubstituted Pyrazole Bearing a 4-(Chromen-2-One) Thiazole: Synthesis, Characterization and Its Biological Studies. *RSC Adv.* **2015**, *5* (54), 43648–43659.

(227) Lirag, R. C.; Miljanić, O. Š. Four Acid-Catalysed Dehydration Reactions Proceed without Interference. *Chem. Commun.* **2014**, *50* (66), 9401–9404.

(228) Knorr, L. Einwirkung von Acetessigester Auf Phenylhydrazin. *Berichte der Dtsch.*

Chem. Gesellschaft **1883**, *16* (2), 2597–2599.

(229) Creary, X.; Anderson, A.; Brophy, C.; Crowell, F.; Funk, Z. Method for Assigning Structure of 1,2,3-Triazoles. *J. Org. Chem.* **2012**, *77* (19), 8756–8761.

(230) v. Auwers, K.; Schmidt, W. Über Die Isomerie-Verhältnisse in Der Pyrazol Reihe, II: Über Das 3(5)-Phenyl-pyrazol Und Seine Derivate. *Berichte der Dtsch. Chem. Gesellschaft (A B Ser.* **1925**, *58* (3), 528–543.

(231) Rull, T.; Le Stroll, G. Sur Les Intermédiaries de Synthèse Isolés Lors de La Préparation Des Diphényl-1,3 et 1,5 Pyrazoles. *Bull. Soc. Chim. Fr.* **1975**, No. 5–6, 1375–1379.

(232) Evans, P. A. Acylation of Alcohols and Amines. In *Stereoselective Synthesis 3*; Evans, Ed.; Georg Thieme Verlag: Stuttgart, **2011**; pp 829–849.

(233) Auwers, K. V.; Mauss, H. Über Die Umsetzung von Hydrazinen Mit Oxymethylen-Ketonen Und Deren Derivaten. I. *Justus Liebig's Ann. der Chemie* **1927**, *452* (1), 182–210.

(234) Surry, D. S.; Buchwald, S. L. Dialkylbiaryl Phosphines in Pd-Catalyzed Amination: A User's Guide. *Chem. Sci.* **2011**, *2* (1), 27–50.

(235) Dobrounig, P.; Trobe, M.; Breinbauer, R. Sequential and Iterative Pd-Catalyzed Cross-Coupling Reactions in Organic Synthesis. *Monatshefte für Chemie - Chem. Mon.* **2017**, *148* (1), 3–35.

(236) Reeves, E. K.; Entz, E. D.; Neufeldt, S. R. Chemodivergence between Electrophiles in Cross-Coupling Reactions. *Chem. – A Eur. J.* **2021**, *27* (20), 6161–6177.

(237) Rousseaux, S.; García-Fortanet, J.; Del Aguila Sanchez, M. A.; Buchwald, S. L. Palladium(0)-Catalyzed Arylative Dearomatization of Phenols. *J. Am. Chem. Soc.* **2011**, *133* (24), 9282–9285.

(238) Martin, R.; Buchwald, S. L. Palladium-Catalyzed Suzuki−Miyaura Cross-Coupling Reactions Employing Dialkylbiaryl Phosphine Ligands. *Acc. Chem. Res.* **2008**, *41* (11), 1461–1473.

(239) Łączkowski, K. Z.; García, D.; Peña, D.; Cobas, A.; Pérez, D.; Guitián, E. Highly

Selective Insertion of Arynes into a C(Sp)−O(Sp 3) σ Bond. *Org. Lett.* **2011**, *13* (5), 960–963.

(240) Himo, F.; Lovell, T.; Hilgraf, R.; Rostovtsev, V. V.; Noodleman, L.; Sharpless, K. B.; Fokin, V. V. Copper(I)-Catalyzed Synthesis of Azoles. DFT Study Predicts Unprecedented Reactivity and Intermediates. *J. Am. Chem. Soc.* **2005**, *127* (1), 210–216.

(241) Worrell, B. T.; Malik, J. A.; Fokin, V. V. Direct Evidence of a Dinuclear Copper Intermediate in Cu(I)-Catalyzed Azide-Alkyne Cycloadditions. *Science* **2013**, *340* (6131), 457–460.

(242) Chan, T. R.; Hilgraf, R.; Sharpless, K. B.; Fokin, V. V. Polytriazoles as Copper(I)-Stabilizing Ligands in Catalysis. *Org. Lett.* **2004**, *6* (17), 2853–2855.

(243) Qiu, G.; Nava, P.; Martinez, A.; Colomban, C. A Tris(Benzyltriazolemethyl)Amine-Based Cage as a CuAAC Ligand Tolerant to Exogeneous Bulky Nucleophiles. *Chem. Commun.* **2021**, *57* (18), 2281–2284.

(244) Boren, B. C.; Narayan, S.; Rasmussen, L. K.; Zhang, L.; Zhao, H.; Lin, Z.; Jia, G.; Fokin, V. V. Ruthenium-Catalyzed Azide−Alkyne Cycloaddition: Scope and Mechanism. *J. Am. Chem. Soc.* **2008**, *130* (28), 8923–8930.

(245) Kwok, S. W.; Fotsing, J. R.; Fraser, R. J.; Rodionov, V. O.; Fokin, V. V. Transition-Metal-Free Catalytic Synthesis of 1,5-Diaryl-1,2,3-Triazoles. *Org. Lett.* **2010**, *12* (19), 4217–4219.

(246) Bordwell, F. G.; Algrim, D.; Fried, H. E. The Equilibrium Acidity of Phenylacetylene. *J. Chem. Soc. Perkin Trans. 2* **1979**, No. 6, 726.

(247) Ishikawa, T.; Mizuta, T.; Hagiwara, K.; Aikawa, T.; Kudo, T.; Saito, S. Catalytic Alkynylation of Ketones and Aldehydes Using Quaternary Ammonium Hydroxide Base. *J. Org. Chem.* **2003**, *68* (9), 3702–3705.

(248) Hu, L.; Mück-Lichtenfeld, C.; Wang, T.; He, G.; Gao, M.; Zhao, J. Reaction between Azidyl Radicals and Alkynes: A Straightforward Approach to NH -1,2,3-Triazoles. *Chem. - A Eur. J.* **2016**, *22* (3), 911–915.

(249) Kita, Y.; Tohma, H.; Takada, T.; Mitoh, S.; Fujita, S.; Gyoten, M. A Novel and Direct Alkyl Azidation of p -Alkylanisoles Using Phenyl Iodine(III) Bis(Trifluoroacetate) (PIFA) and Trimethylsilyl Azide. *Synlett* **1994**, *1994* (06), 427–428.

(250) Lemieux, R. U.; Ratcliffe, R. M. The Azidonitration of Tri-O-Acetyl-D-Galactal. *Can. J. Chem.* **1979**, *57* (10), 1244–1251.

(251) Sarvary, A.; Maleki, A. A Review of Syntheses of 1,5-Disubstituted Tetrazole Derivatives. *Mol. Divers.* **2015**, *19* (1), 189–212.

(252) Nohara, A.; Kuriki, H.; Ishiguro, T.; Saijo, T.; Ukawa, K.; Maki, Y.; Sanno, Y. Studies on Antianaphylactic Agents. 6. Synthesis of Some Metabolites of 6-Ethyl-3-(1H-Tetrazol-5-Yl)Chromone and Their Analogs. *J. Med. Chem.* **1979**, *22* (3), 290–295.

(253) Neochoritis, C. G.; Zhao, T.; Dömling, A. Tetrazoles via Multicomponent Reactions. *Chem. Rev.* **2019**, *119* (3), 1970–2042.

(254) Otsuka, R.; Maruhashi, K.; Ohwada, T. Latent Brønsted Base Solvent-Assisted Amide Formation from Amines and Acid Chlorides. *Synthesis (Stuttg).* **2018**, *50* (10), 2041–2057.

(255) Li, L-H.; Niu, Z-J.; Li, Y-X.; Liang, Y-M. Transition-Metal-Free Multinitrogenation of Amides by C–C Bond Cleavage: A New Approach to Tetrazoles. *Chem. Commun.* **2018**, *54* (79), 11148–11151.

(256) Ishihara, K.; Ishihara, K.; Tanaka, Y.; Shioiri, T.; Matsugi, M. Practical Synthesis of Tetrazoles from Amides and Phosphorazidates in the Presence of Aromatic Bases. *Tetrahedron* **2022**, *108*, 132642.

(257) Himo, F.; Demko, Z. P.; Noodleman, L.; Sharpless, K. B. Mechanisms of Tetrazole Formation by Addition of Azide to Nitriles. *J. Am. Chem. Soc.* **2002**, *124* (41), 12210–12216.

(258) Himo, F.; Demko, Z. P.; Noodleman, L.; Sharpless, K. B. Why Is Tetrazole Formation by Addition of Azide to Organic Nitriles Catalyzed by Zinc(II) Salts? *J. Am. Chem. Soc.* **2003**, *125* (33), 9983–9987.

(259) Ding, R.; Liu, Y.; Han, M.; Jiao, W.; Li, J.; Tian, H.; Sun, B. Synthesis of Nitriles

from Primary Amides or Aldoximes under Conditions of a Catalytic Swern Oxidation. *J. Org. Chem.* **2018**, *83* (20), 12939–12944.

(260) Rana, A.; Kumar, V.; Tiwari, L.; Thakur, A.; Meena, C.; Mahajan, D. Triflic Anhydride Promoted Synthesis of Primary Amides and Their Conversion into Nitriles. *SynOpen* **2018**, *02* (02), 0180–0191.

(261) Trampota, M.; Murphy, Randall, B. Cubane Nucleoside Analogs. WO2007059330, **2007**.

(262) Sharon, A.; Pratap, R.; Tiwari, P.; Srivastava, A.; Maulik, P. R.; Ram, V. J. Synthesis and in Vivo Antihyperglycemic Activity of 5-(1H-Pyrazol-3-Yl)Methyl-1H-Tetrazoles. *Bioorg. Med. Chem. Lett.* **2005**, *15* (8), 2115–2117.

(263) Karimian, A.; Emarloo, N.; Salari, S. The Mineral Alum: An Effective and Low-Cost Heterogeneous Catalyst for the Successful Synthesis of 5-Substituted-1 H -Tetrazoles. *Inorg. Nano-Metal Chem.* **2021**, *51* (1), 91–100.

(264) Akhlaghinia, B.; Rezazadeh, S. A Novel Approach for the Synthesis of 5-Substituted-1H-Tetrazoles. *J. Braz. Chem. Soc.* **2012**, *23* (12), 2197–2203.

(265) Qi, H.; Chi, D.; Chen, S. Pd-Catalyzed C–H Functionalization of Indole-Containing Alkene-Tethered Aryl Halides with Alkynes To Construct Indole Alkaloid Scaffolds. *Org. Lett.* **2022**, *24* (15), 2910–2914.

(266) Zheng, S-C.; Wang, Q.; Zhu, J. Catalytic Atropenantioselective Heteroannulation between Isocyanoacetates and Alkynyl Ketones: Synthesis of Enantioenriched Axially Chiral 3-Arylpyrroles. *Angew. Chemie Int. Ed.* **2019**, *58* (5), 1494–1498.

(267) Karpavičienė, I.; Jonušis, M.; Leduskrasts, K.; Misiūnaitė, I.; Suna, E.; Čikotienė, I. Synthesis and Photophysical Properties of 3,5-Diaryl-2-Heteroarylthiophenes. *Dye. Pigment.* **2019**, *170*, 107646.

(268) Heller, B.; Gutnov, A.; Fischer, C.; Drexler, H-J.; Spannenberg, A.; Redkin, D.; Sundermann, C.; Sundermann, B. Phosphorus-Bearing Axially Chiral Biaryls by Catalytic Asymmetric Cross-Cyclotrimerization and a First Application in Asymmetric Hydrosilylation. *Chem. - A Eur. J.* **2007**, *13* (4), 1117–1128.

(269) Chinchilla, R.; Nájera, C. The Sonogashira Reaction: A Booming Methodology in Synthetic Organic Chemistry. *Chem. Rev.* **2007**, *107* (3), 874–922.

(270) Gamage, D. W.; Li, Q.; Ranaweera, R. A. A. U.; Sarkar, S. K.; Weragoda, G. K.; Carr, P. L.; Gudmundsdottir, A. D. Vinylnitrene Formation from 3,5-Diphenyl-Isoxazole and 3-Benzoyl-2-Phenylazirine. *J. Org. Chem.* **2013**, *78* (22), 11349–11356.

(271) Simm, P. E.; Sekar, P.; Richardson, J.; Davies, P. W. Gold(I)-Catalyzed Synthesis of 3-Sulfenyl Pyrroles and Indoles by a Regioselective Annulation of Alkynyl Thioethers. *ACS Catal.* **2021**, *11* (11), 6357–6362.

(272) Takikawa, H.; Takada, A.; Hikita, K.; Suzuki, K. Formation of A-Hydroxy-β-diketones through Hydroxylation of Isoxazolium Salts: Stereoselective Approach to Angular Cis- Diols in Polycyclic Systems. *Angew. Chemie Int. Ed.* **2008**, *47* (39), 7446–7449.

(273) Griesbeck, A. G.; Franke, M.; Neudörfl, J.; Kotaka, H. Photocycloaddition of Aromatic and Aliphatic Aldehydes to Isoxazoles: Cycloaddition Reactivity and Stability Studies. *Beilstein J. Org. Chem.* **2011**, *7*, 127–134.

(274) Pusch, S.; Opatz, T. A Photochemical One-Pot Three-Component Synthesis of Tetrasubstituted Imidazoles. *Org. Lett.* **2014**, *16* (20), 5430–5433.

(275) Ilangovan, A.; Sakthivel, P.; Zipse, H. An Unusual Grob-Type C-C/C-O Bond Cleavage of 5-Acyl-2,3-Dihydro-4 H -Pyran-4-One Derivatives. *ChemistrySelect* **2016**, *1* (5), 1109–1116.

(276) Wu, F.; Tong, H.; Wang, K.; Zhang, X.; Zhang, J.; Wong, W-K.; Zhu, X. Synthesis, Crystal Structure and Photophysical Study of Luminescent Three-Coordinate Cuprous Bromide Complexes Based on Pyrazole Derivatives. *J. Coord. Chem.* **2016**, *69* (6), 926–933.

(277) Jia, L.; Gao, S.; Zhang, Y-Y.; Zhao, L-X.; Fu, Y.; Ye, F. Fragmenlt Recombination Design, Synthesis, and Safener Activity of Novel Ester-Substituted Pyrazole Derivatives. *J. Agric. Food Chem.* **2021**, *69* (30), 8366–8379.

(278) Fullam, E.; Talbot, J.; Abuhammed, A.; Westwood, I.; Davies, S. G.; Russell, A. J.; Sim, E. Design, Synthesis and Structure–Activity Relationships of 3,5-Diaryl-1H-

Pyrazoles as Inhibitors of Arylamine N-Acetyltransferase. *Bioorg. Med. Chem. Lett.* **2013**, *23* (9), 2759–2764.

(279) Tan, K.; Jäger, C.; Körschgen, H.; Geissler, S.; Schlenzig, D.; Buchholz, M.; Stöcker, W.; Ramsbeck, D. Heteroaromatic Inhibitors of the Astacin Proteinases Meprin α, Meprin β and Ovastacin Discovered by a Scaffold-Hopping Approach. *ChemMedChem* **2021**, *16* (6), 976–988.

(280) Freeman-Cook, K. D.; Hoffman, R. L.; Johnson, T. W. Lipophilic Efficiency: The Most Important Efficiency Metric in Medicinal Chemistry. *Future Med. Chem.* **2013**, *5* (2), 113–115.

(281) Meanwell, N. A. Improving Drug Candidates by Design: A Focus on Physicochemical Properties As a Means of Improving Compound Disposition and Safety. *Chem. Res. Toxicol.* **2011**, *24* (9), 1420–1456.

(282) Yous, S.; Depreux, P.; Renard, P. Synthesis of the Naphthalenic Bioisostere of Indorenate. *Arch. Pharm. (Weinheim).* **1993**, *326* (2), 119–120.

(283) Yous, S.; Andrieux, J.; Howell, H. E.; Morgan, P. J.; Renard, P.; Pfeiffer, B.; Lesieur, D.; Guardiola-Lemaitre, B. Novel Naphthalenic Ligands with High Affinity for the Melatonin Receptor. *J. Med. Chem.* **1992**, *35* (8), 1484–1486.

(284) Sravanthi, T. V.; Manju, S. L. Indoles — A Promising Scaffold for Drug Development. *Eur. J. Pharm. Sci.* **2016**, *91*, 1–10.

(285) MarvinSketch. ChemAxon.

(286) Griffiths, J.; Thomasson, J. The Effects of Intramolecular Hydrogen Bonding on the Color Properties of 4-*N*,*N*-Dialkylaminoazobenzenes. *Adv. Colour Sci. Technol.* **2000**, *3* (2), 32–40.

(287) Liu, C.; Dai, R.; Yao, G.; Deng, Y. Selective Bromination of Pyrrole Derivatives, Carbazole and Aromatic Amines with DMSO/HBr under Mild Conditions. *J. Chem. Res.* **2014**, *38* (10), 593–596.

(288) Ciganek, E. Electrophilic Amination of Carbanions, Enolates, and Their Surrogates. In *Organic Reactions*; John Wiley & Sons, Inc.: Hoboken, NJ, USA, **2009**; pp 1–366.

(289) Barbero, M.; Degani, I.; Dughera, S.; Fochi, R.; Perracino, P. Preparation of Diazenes by Electrophilic C-Coupling Reactions of Dry Arenediazonium o-Benzenedisulfonimides with Grignard Reagents. *Synthesis (Stuttg).* **1998**, *1998* (9), 1235–1237.

(290) Garst, M. E.; Lukton, D. Phenyldiazenes from Phenyl Diazonium Fluoborate and Carbanions. *Synth. Commun.* **1980**, *10* (2), 155–160.

(291) Nomura, Y.; Anzai, H. Syntheses and Ultraviolet Spectra of Aromatic Azo Compounds. IV. Naphthylazobenzene Derivatives. *Bull. Chem. Soc. Jpn.* **1964**, *37* (7), 970–973.

(292) Silverman, G. S.; Rakita, P. E. *Handbook of Grignard Reagents*; **1996**.

(293) Gilman, H.; Peterson, J. M.; Schulze, F. An Improved Activated Magnesium for the Preparation of the Grignard Reagent, and a Comparative Study of Various Catalysts. *Recl. des Trav. Chim. des Pays-Bas* **1928**, *47* (1), 19–27.

(294) Mendel, A. Reaction of P-(Dimethylamino)Bromobenzene with "activated" Magnesium. *J. Organomet. Chem.* **1966**, *6* (1), 97–99.

(295) Ziegler, D. S.; Wei, B.; Knochel, P. Improving the Halogen–Magnesium Exchange by Using New Turbo-Grignard Reagents. *Chem. - A Eur. J.* **2019**, *25* (11), 2695–2703.

(296) Furukawa, S.; Yoshida, Y.; Komatsu, T. Chemoselective Hydrogenation of Nitrostyrene to Aminostyrene over Pd- and Rh-Based Intermetallic Compounds. *ACS Catal.* **2014**, *4* (5), 1441–1450.

(297) Li, L.; Zhao, H.; Wang, J.; Wang, R. Facile Fabrication of Ultrafine Palladium Nanoparticles with Size- and Location-Control in Click-Based Porous Organic Polymers. *ACS Nano* **2014**, *8* (5), 5352–5364.

(298) Advani, J. H.; Ravi, K.; Naikwadi, D. R.; Bajaj, H. C.; Gawande, M. B.; Biradar, A. V. Bio-Waste Chitosan-Derived N-Doped CNT-Supported Ni Nanoparticles for Selective Hydrogenation of Nitroarenes. *Dalt. Trans.* **2020**, *49* (30), 10431–10440.

(299) Swanger, S. A.; Vance, K. M.; Acker, T. M.; Zimmerman, S. S.; DiRaddo, J. O.; Myers, S. J.; Bundgaard, C.; Mosley, C. A.; Summer, S. L.; Menaldino, D. S.; Jensen,

H. S.; Liotta, D. C.; Traynelis, S. F. A Novel Negative Allosteric Modulator Selective for GluN2C/2D-Containing NMDA Receptors Inhibits Synaptic Transmission in Hippocampal Interneurons. *ACS Chem. Neurosci.* **2018**, *9* (2), 306–319.

(300) Suárez, A. I.; García, M. C.; Compagnone, R. S. A Regioselective Acylation of N -Substituted-4-Aminoindole. Its Application to the Synthesis of Indolactam V. *Synth. Commun.* **2004**, *34* (3), 523–531.

(301) Hu, T. Method for Preparing 4-Aminoindole from 2-Methyl-3-Nitroaniline. CN103420895, **2013**.

(302) Ramakrishna, N. V. S.; Shinde, A. K.; Kambhampati, R. S.; Jasti, V. Substituted Indolyl Compounds as 5-HT6 Ligands and Their Preparation, and Use in the Treatment of Diseases. WO2009034581, **2009**.

(303) Fields, G. B. Methods for Removing the Fmoc Group. In *Peptide Synthesis Protocols*; Humana Press: New Jersey, **1995**; pp 17–28.

(304) Sessler, C. D.; Rahm, M.; Becker, S.; Goldberg, J. M.; Wang, F.; Lippard, S. J. CF_2H, a Hydrogen Bond Donor. *J. Am. Chem. Soc.* **2017**, *139* (27), 9325–9332.

Appendix A:

Selected Spectra

IR Spectrum of **52** demonstrating presence of phenol tautomer

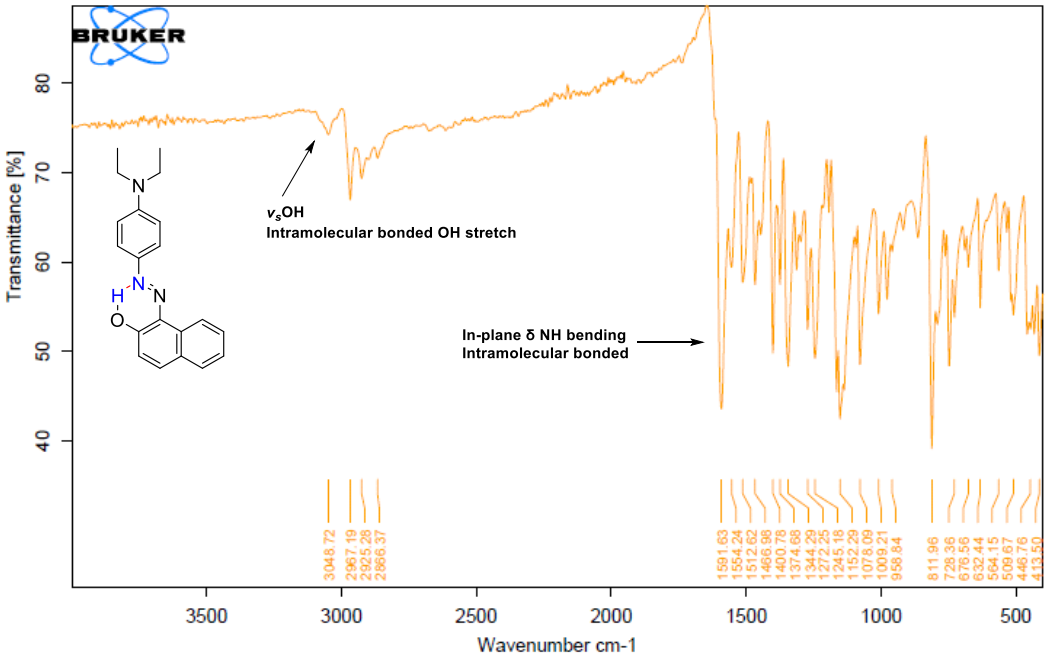

^{1}H-NMR (400 MHz, $CDCl_3$) of **52**

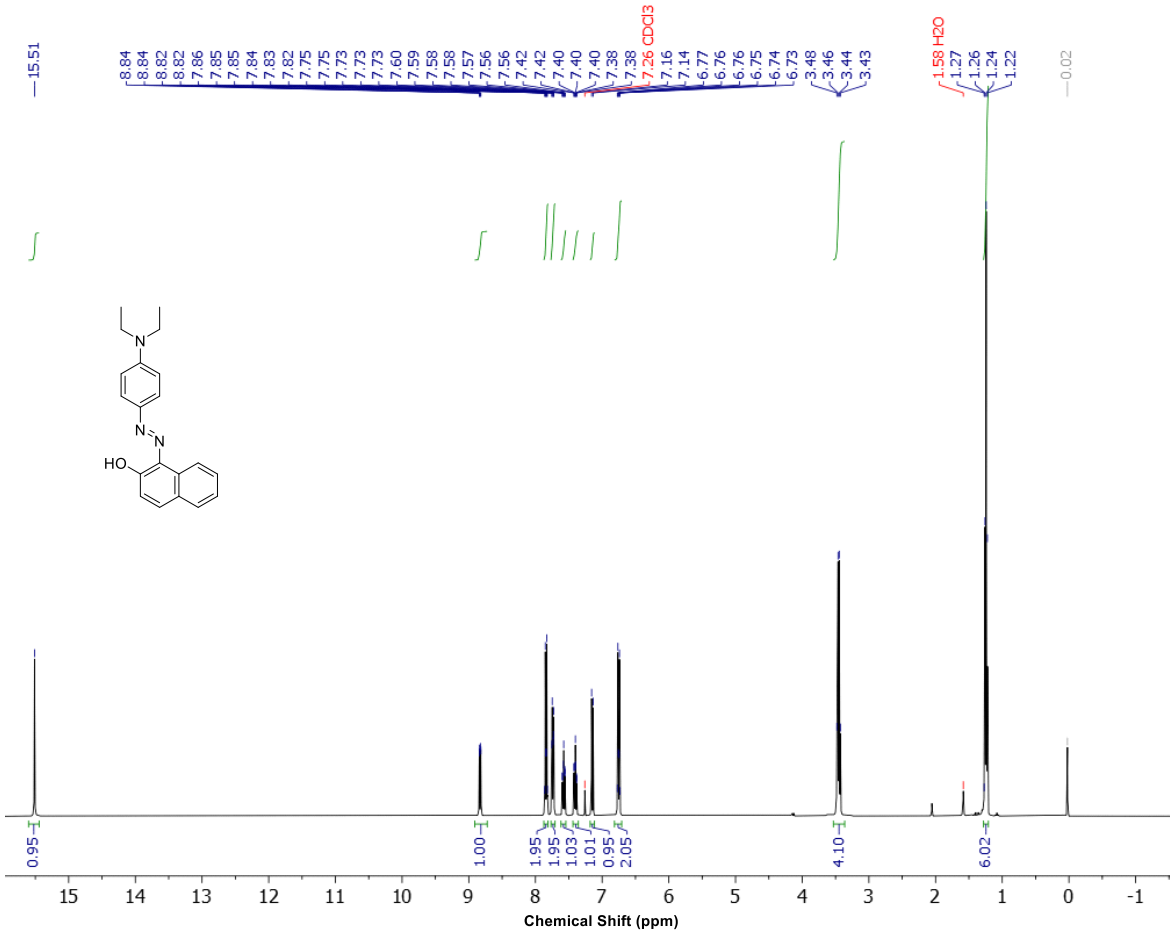

^{13}C-NMR (400 MHz, $CDCl_3$) of **52**

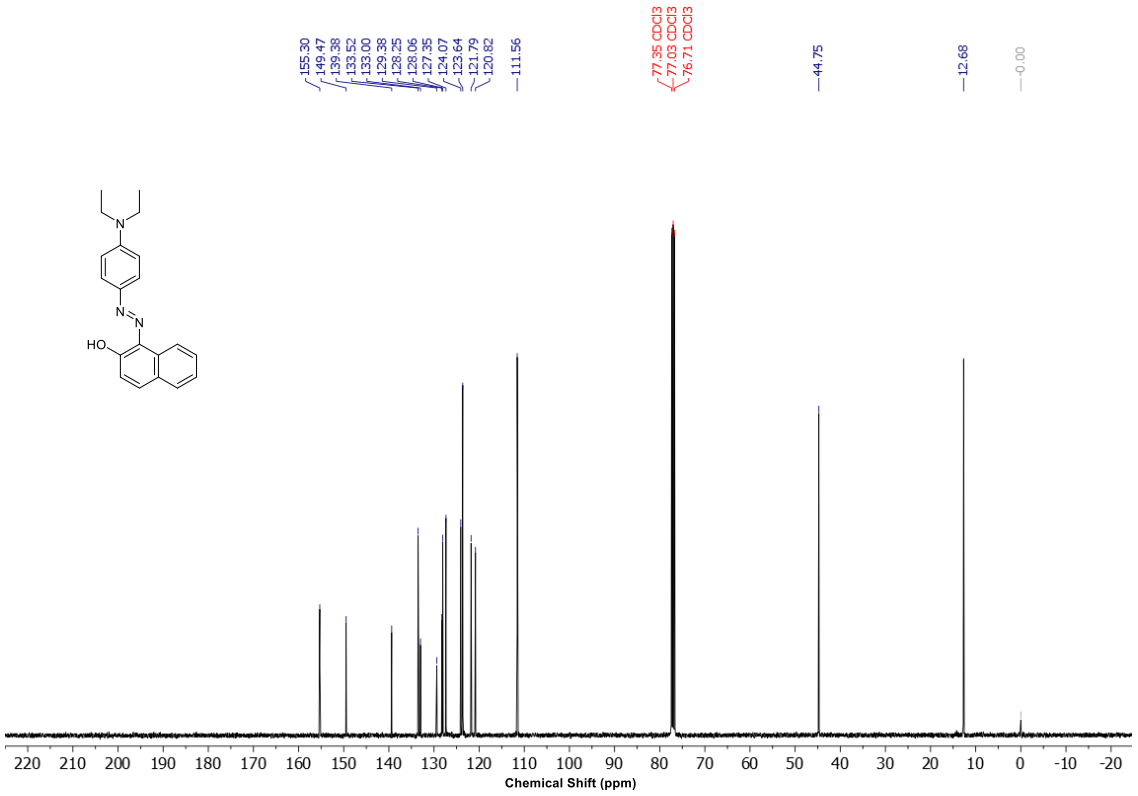

^{1}H-NMR (400 MHz, $CDCl_3$) of **73**

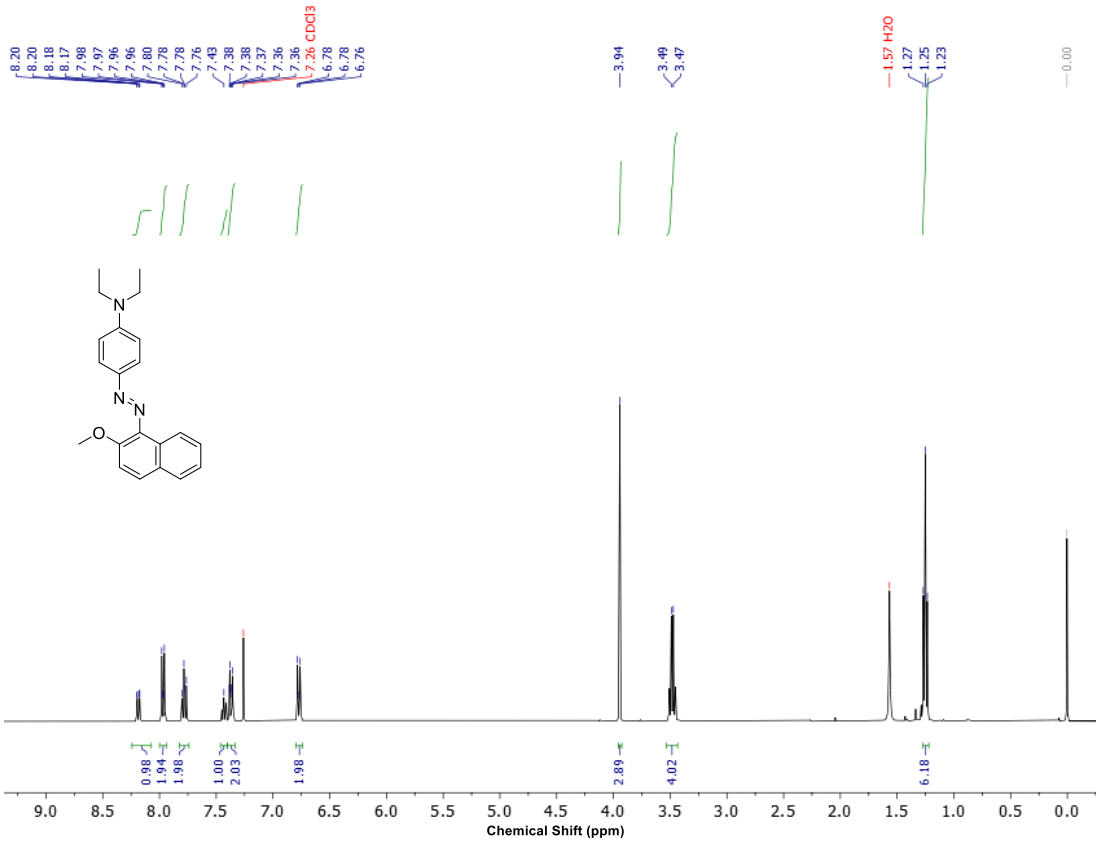

^{13}C-NMR (400 MHz, $CDCl_3$) of **73**

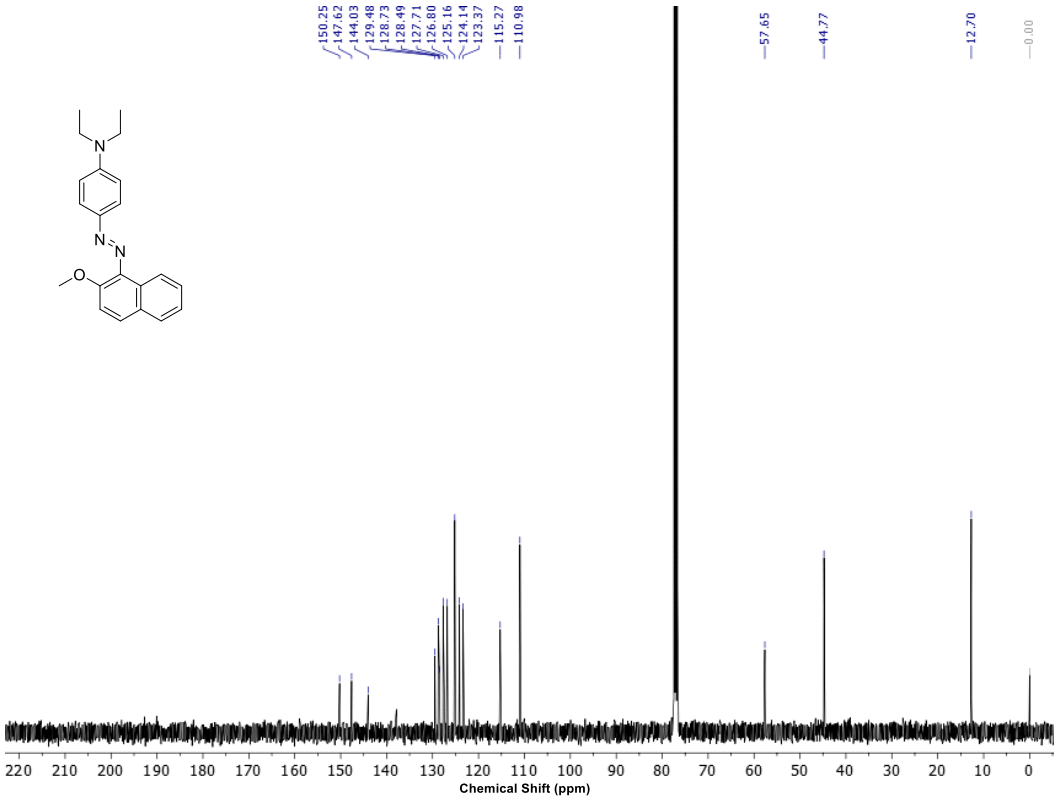

^{1}H-^{1}H NOESY NMR (400 MHz, $CDCl_3$) of **73**

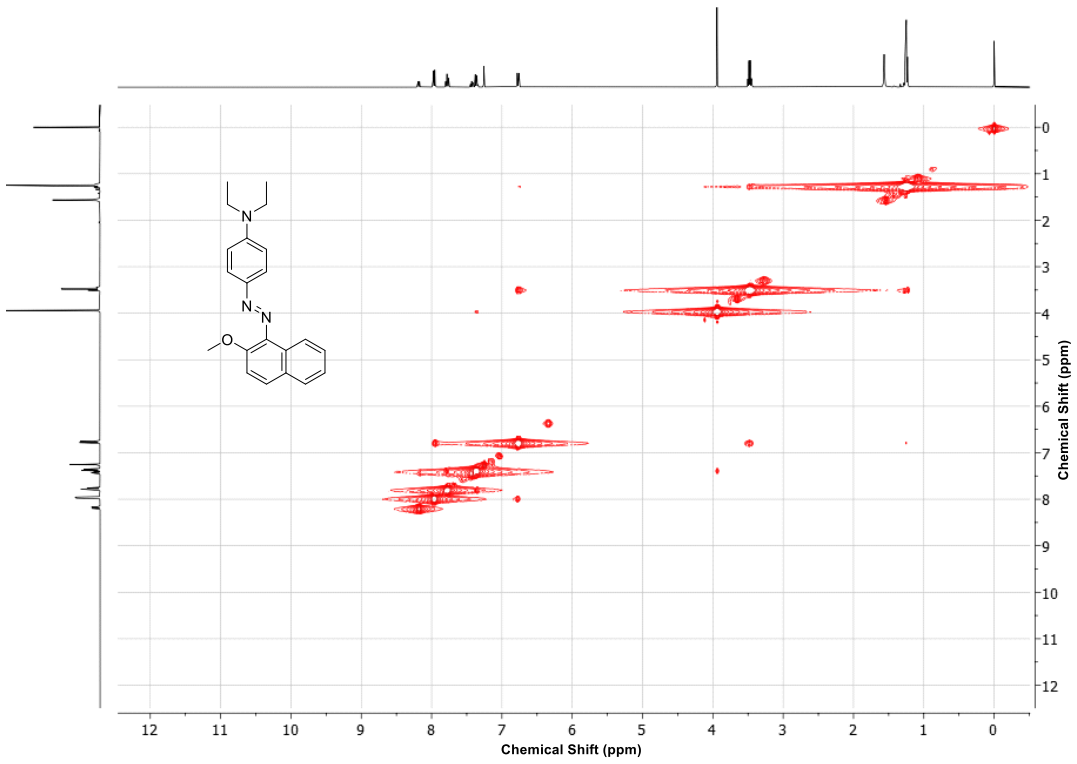

^{1}H-NMR (400 MHz, $CDCl_3$) of **114**

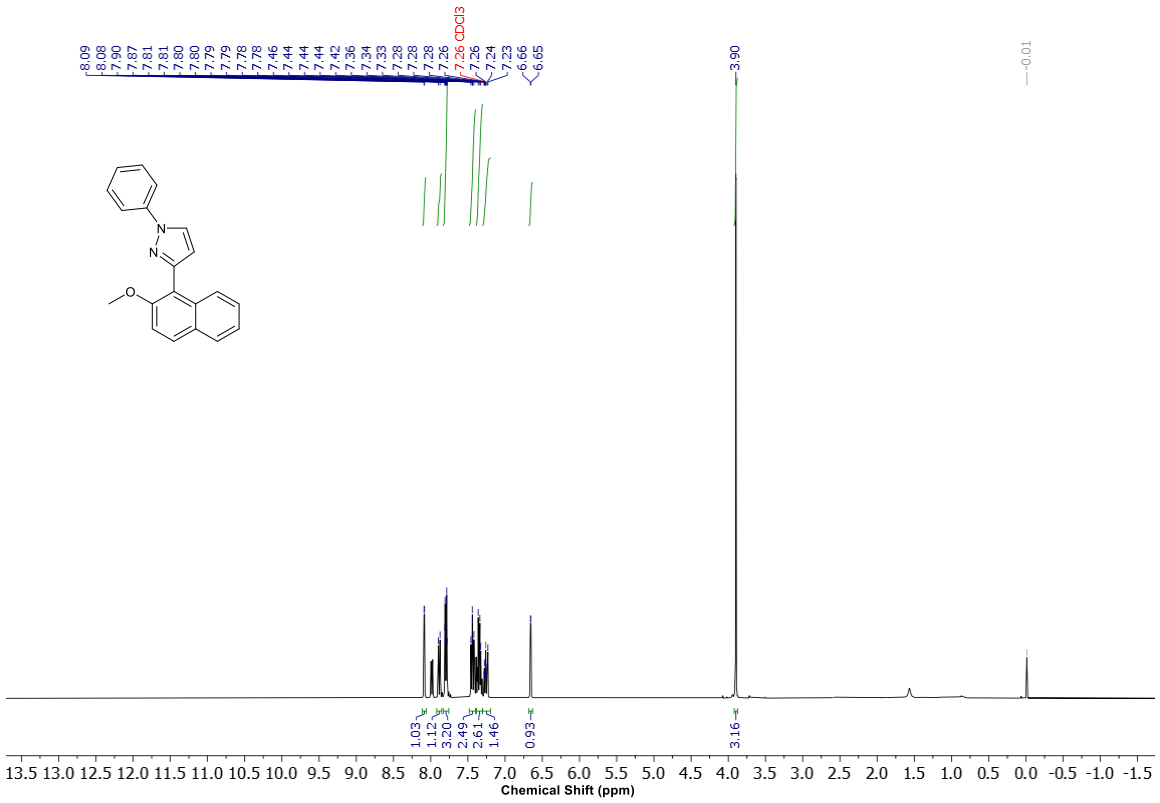

^{13}C-NMR (101 MHz, $CDCl_3$) of **114**

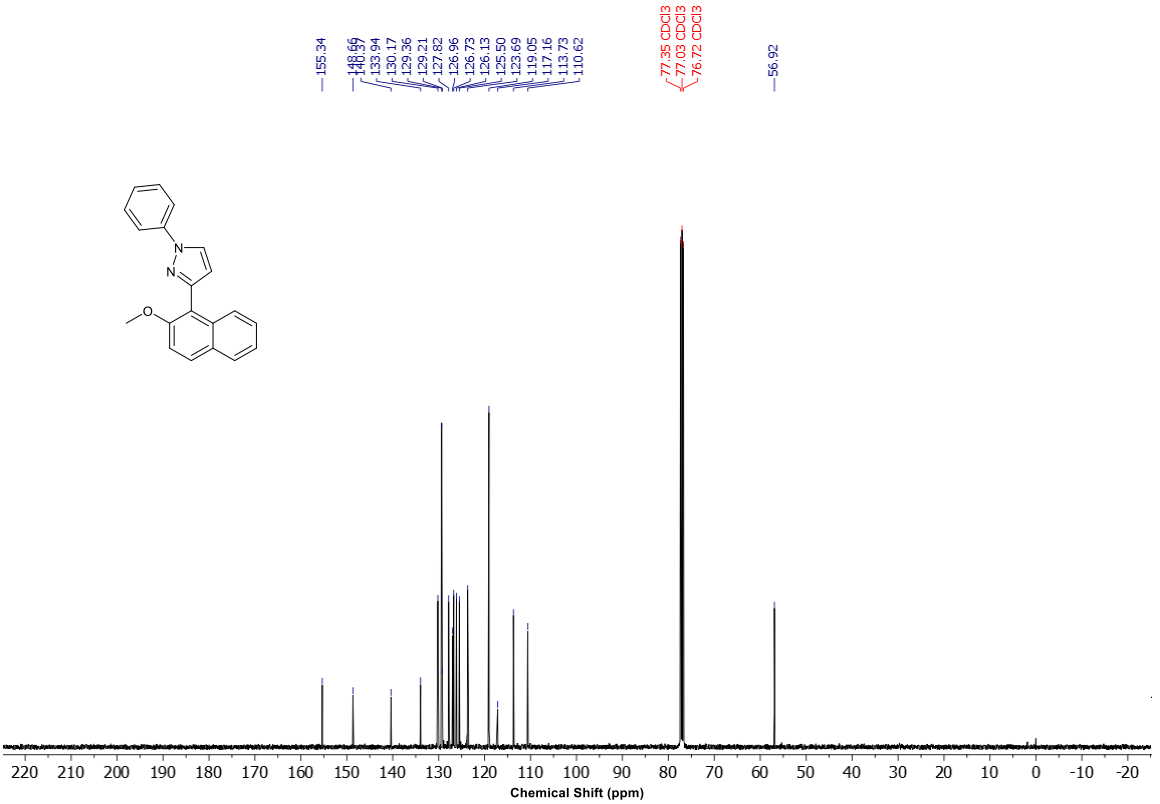

^{1}H-^{13}C HSQC NMR (400 MHz, $CDCl_3$) of **114**

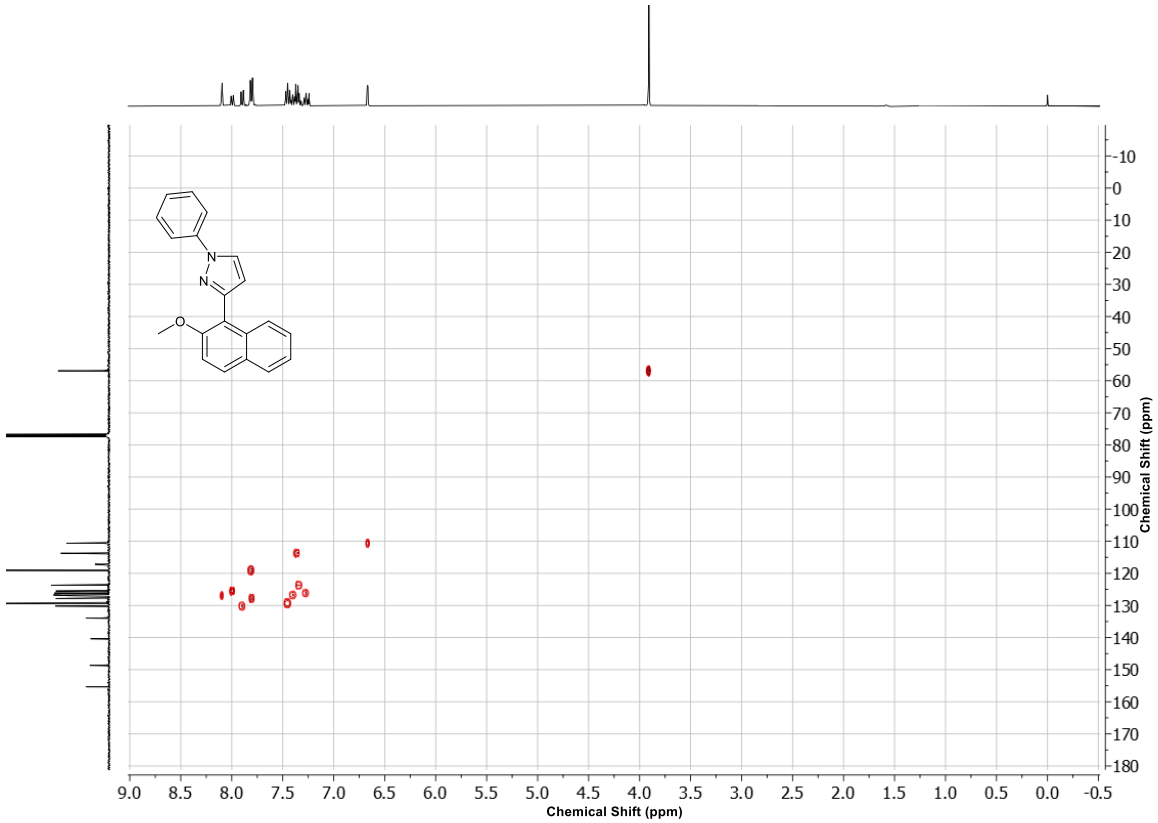

^{1}H-^{13}C HMBC NMR (400 MHz, $CDCl_3$) of **114**

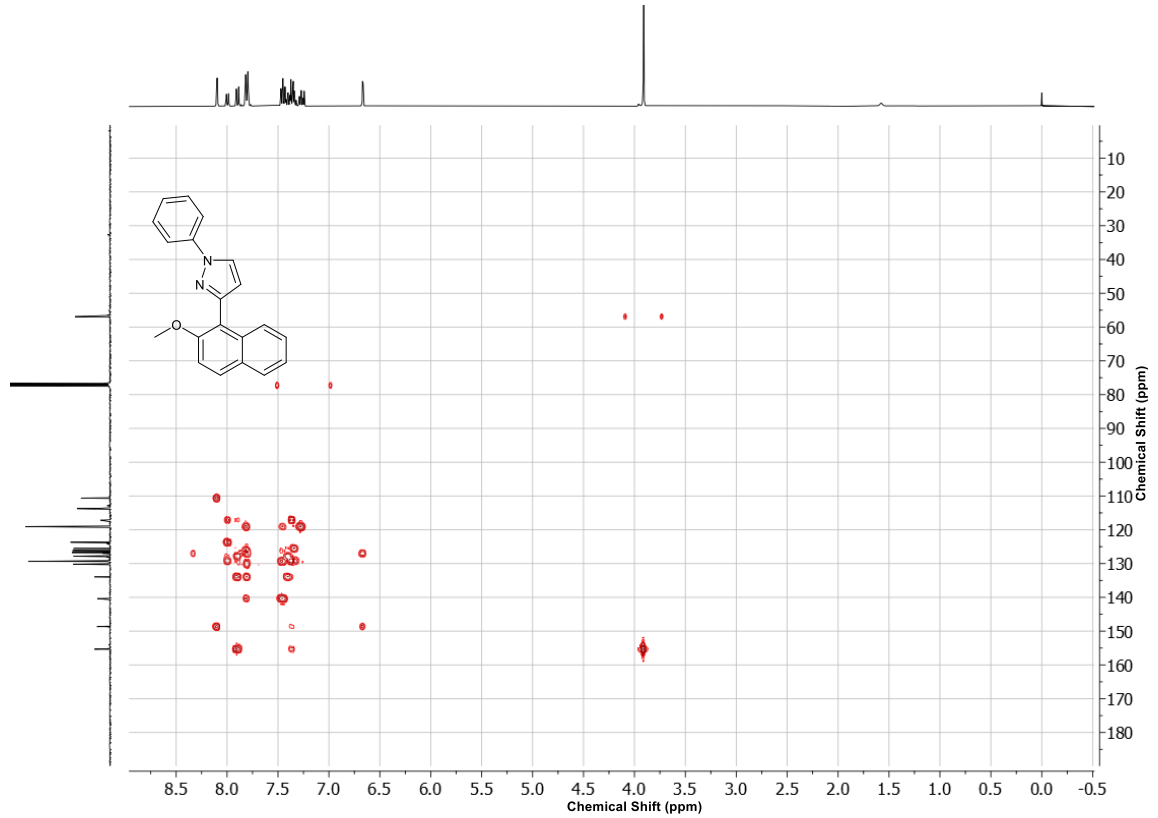

^{1}H-NMR (400 MHz, $CDCl_3$) of **115**

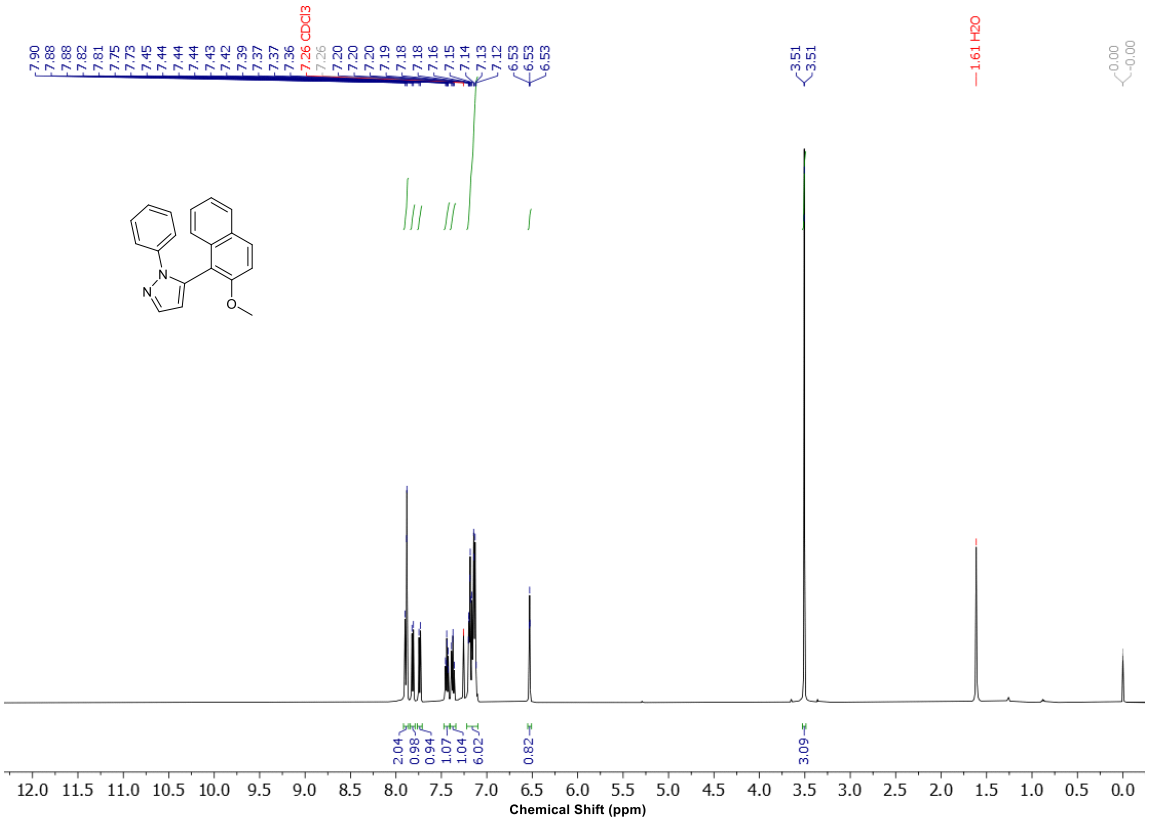

^{13}C-NMR (101 MHz, $CDCl_3$) of **115**

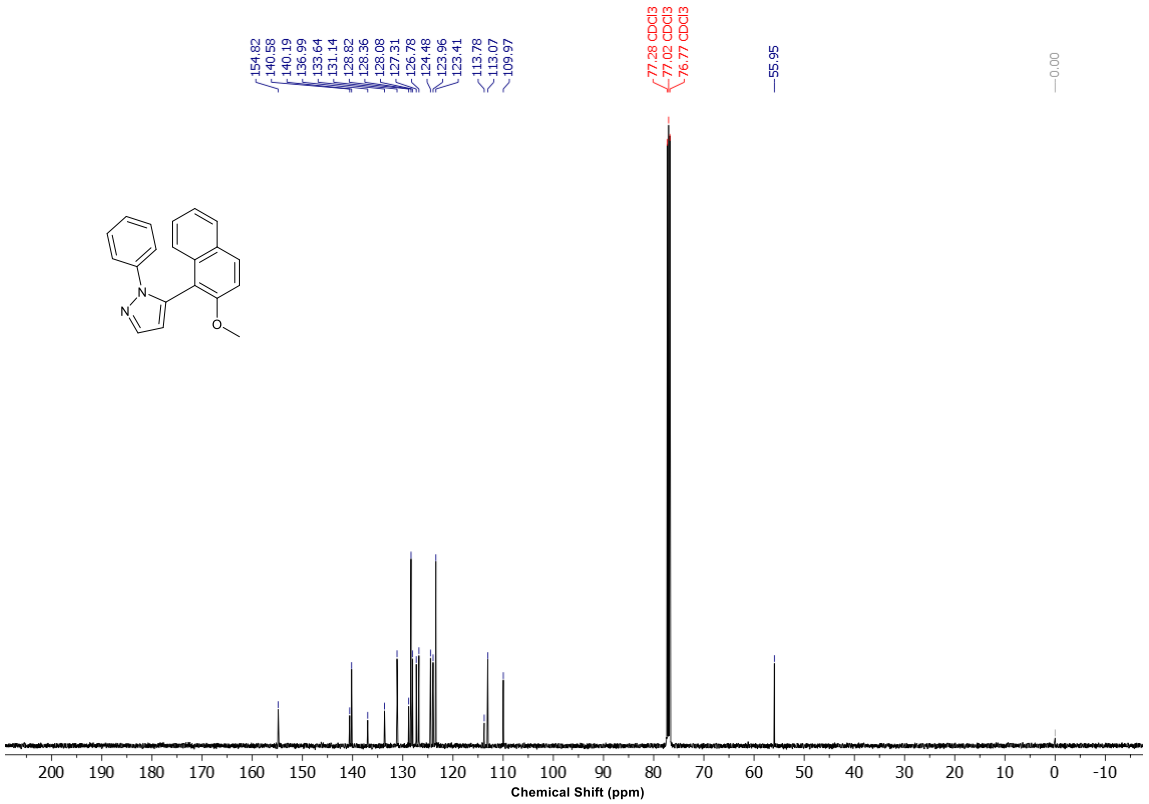

^{1}H-^{13}C HSQC NMR (400 MHz, $CDCl_3$) of **115**

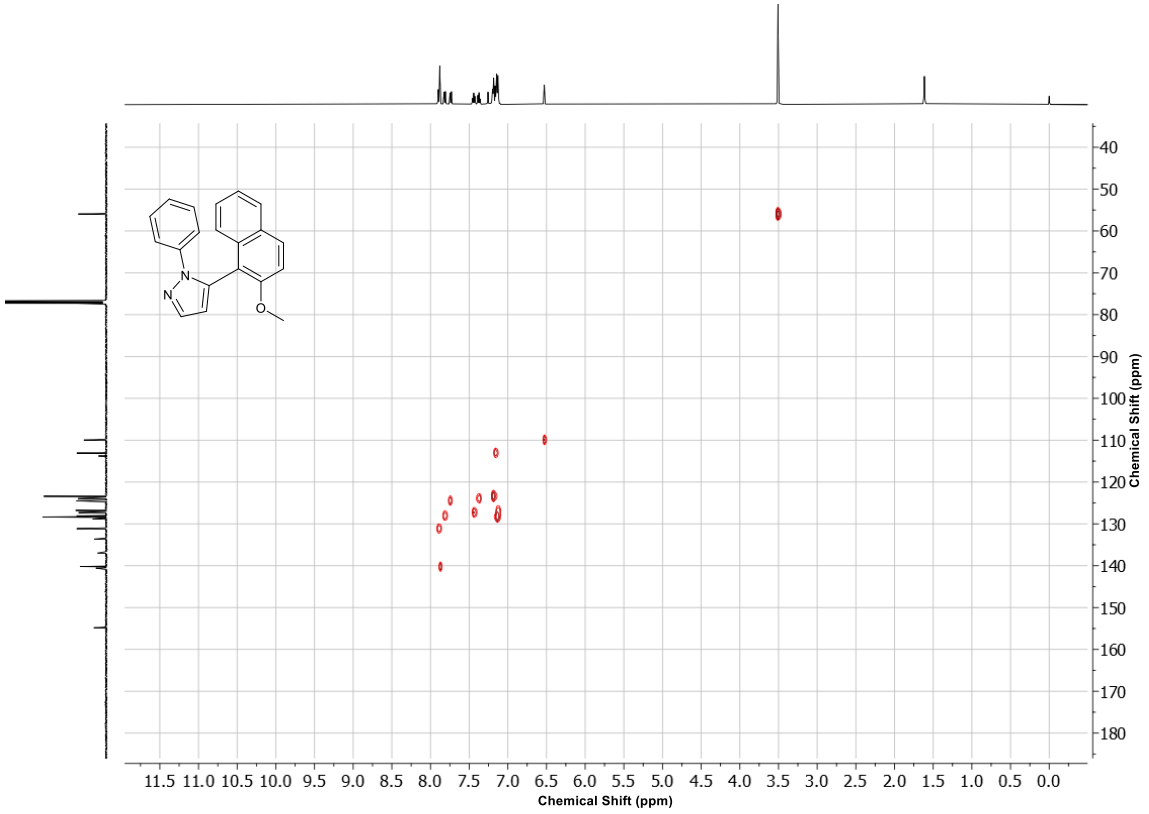

^{1}H-^{13}C HMBC NMR (400 MHz, $CDCl_3$) of **115**

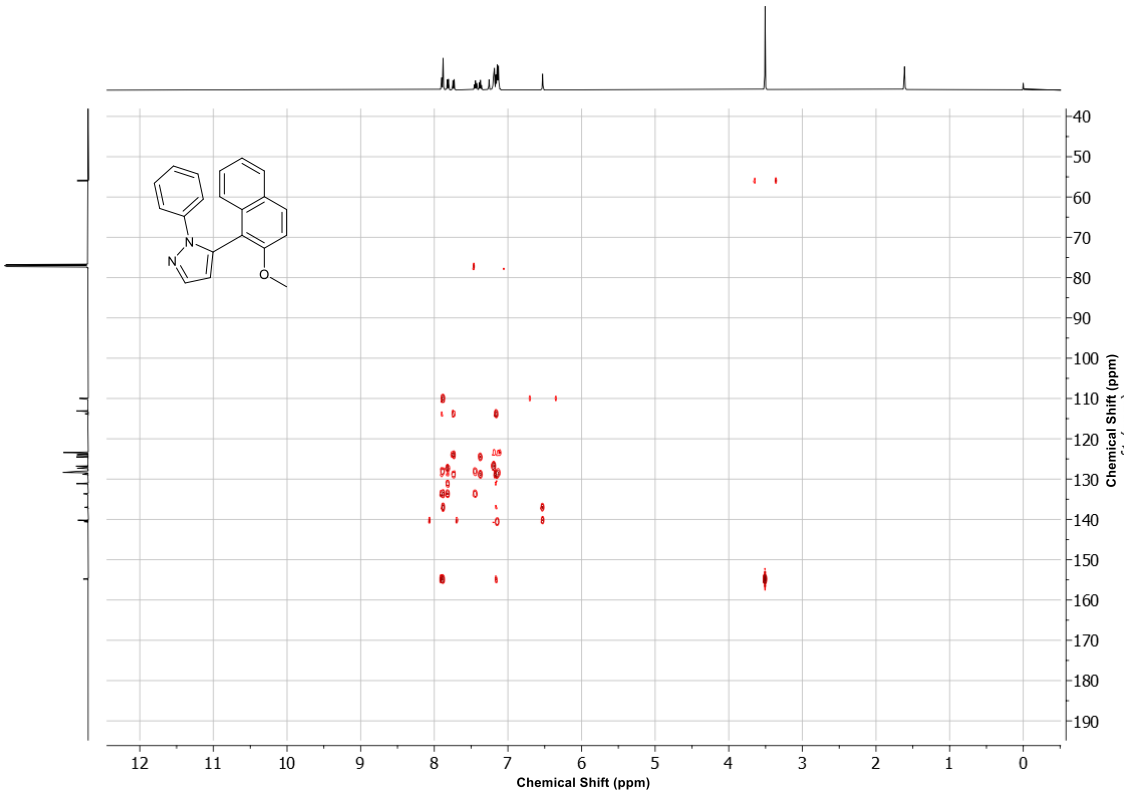

^{1}H-NMR (400 MHz, $CDCl_3$) of **118**

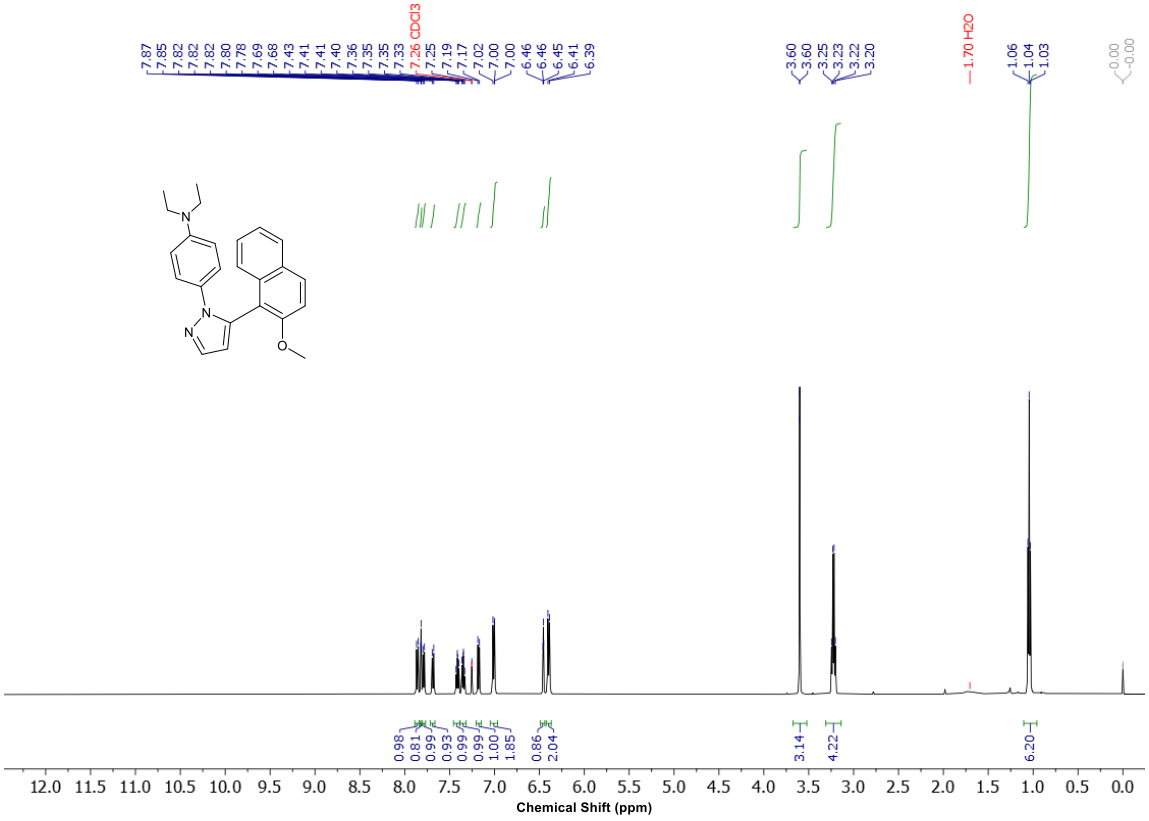

^{13}C-NMR (101 MHz, $CDCl_3$) of **118**

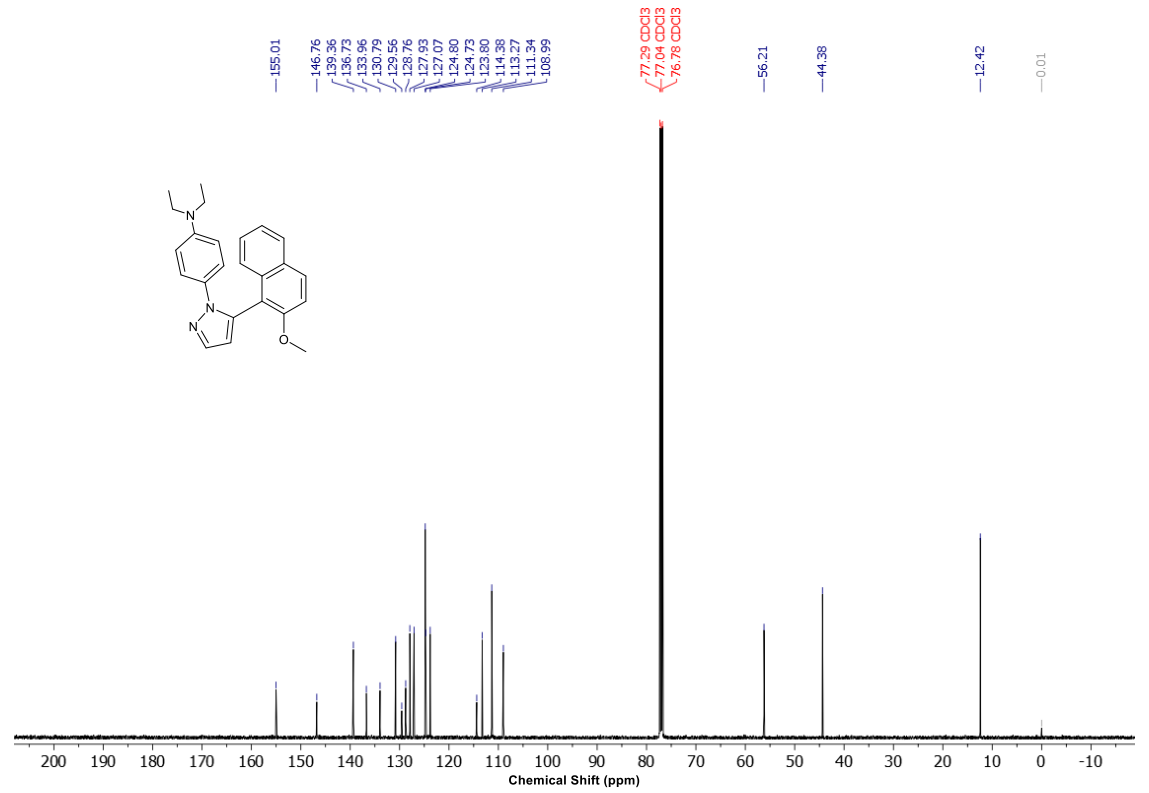

^{1}H-^{13}C HSQC NMR (400 MHz, $CDCl_3$) of **118**

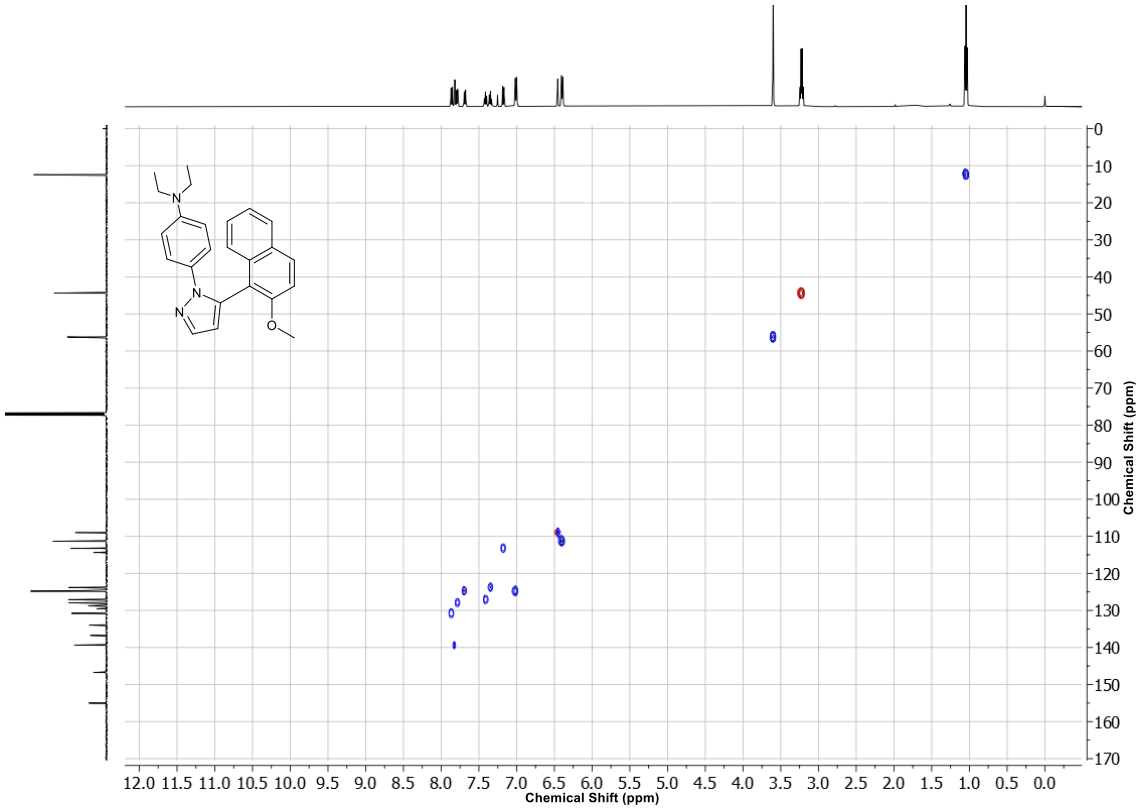

^{1}H-^{13}C HMBC NMR (400 MHz, $CDCl_3$) of **118**

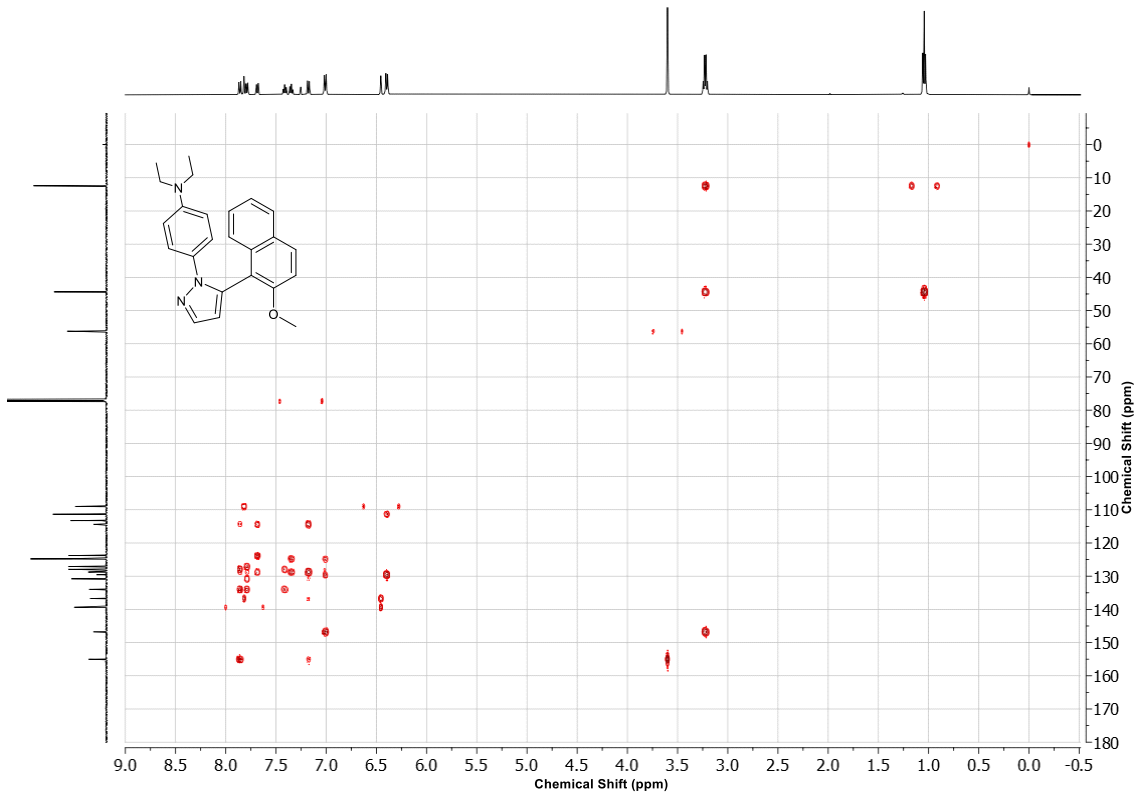

^{1}H-NMR (400 MHz, $CDCl_3$) of **146**

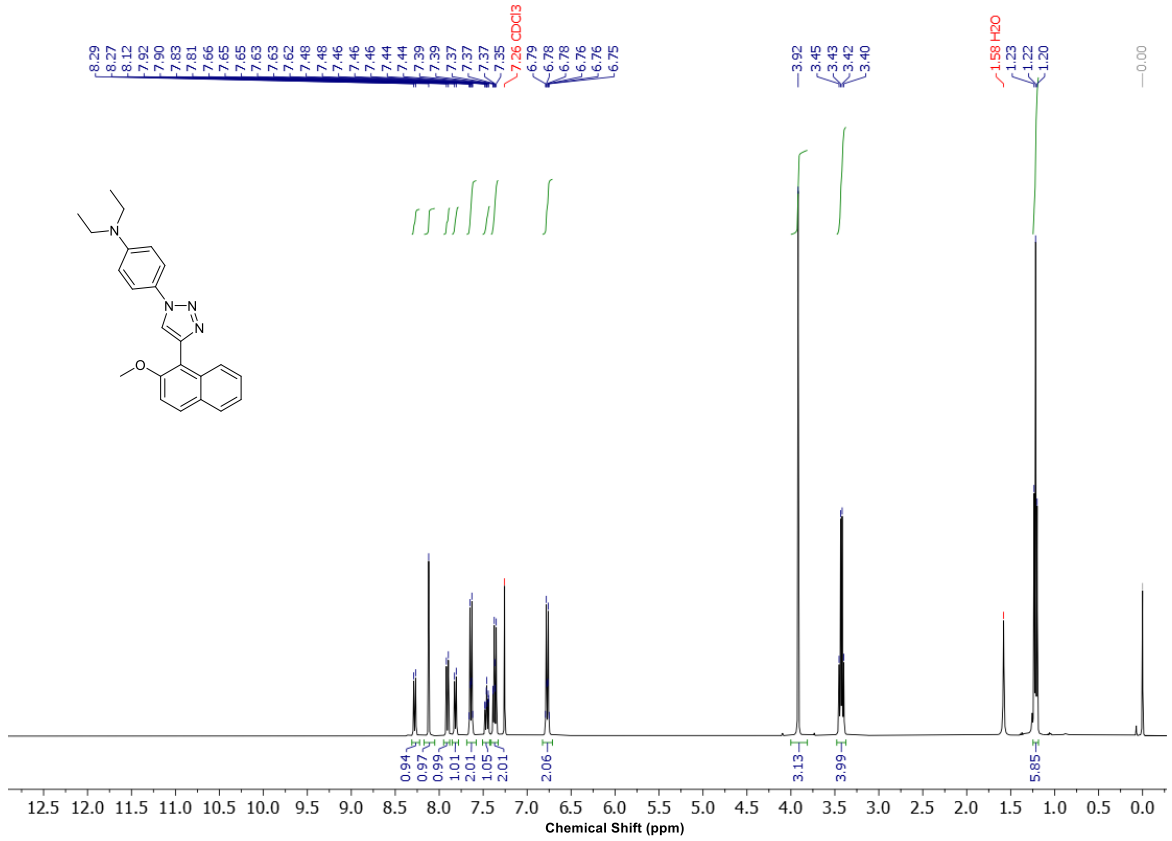

^{13}C-NMR (101 MHz, $CDCl_3$) of **146**

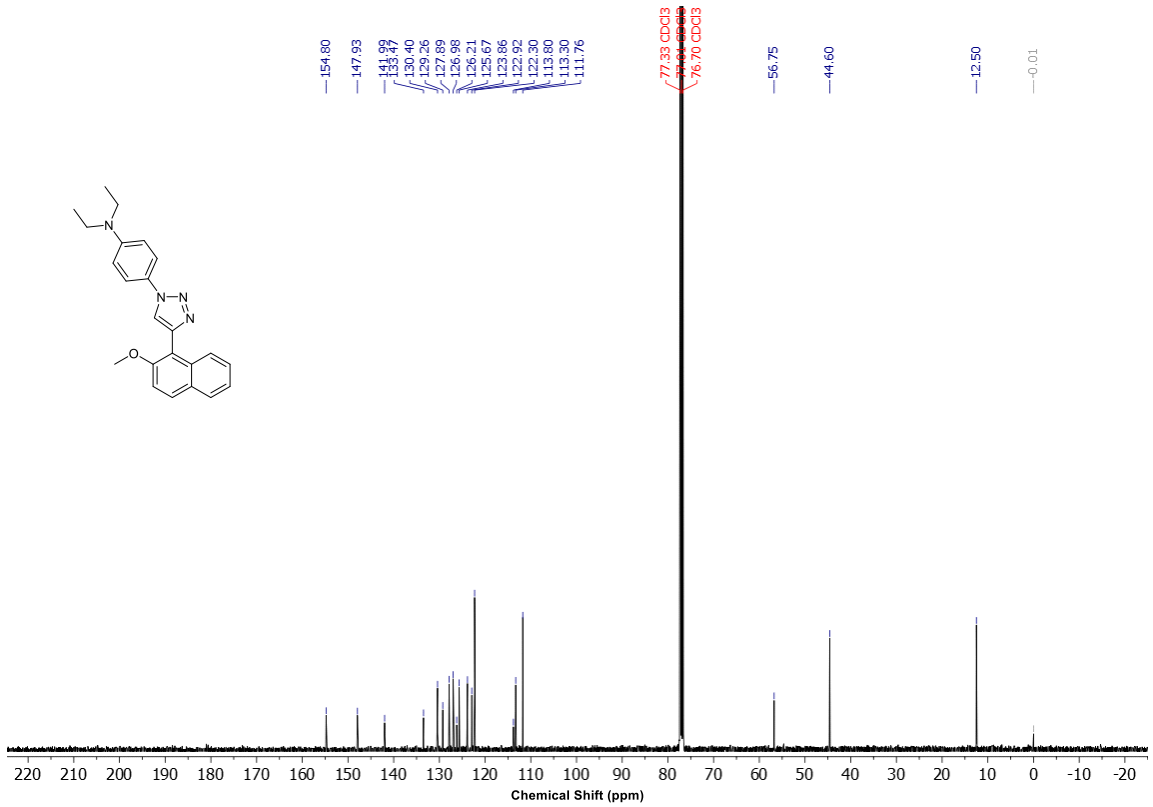

^{1}H-^{13}C HSQC NMR (400 MHz, $CDCl_3$) of **146**

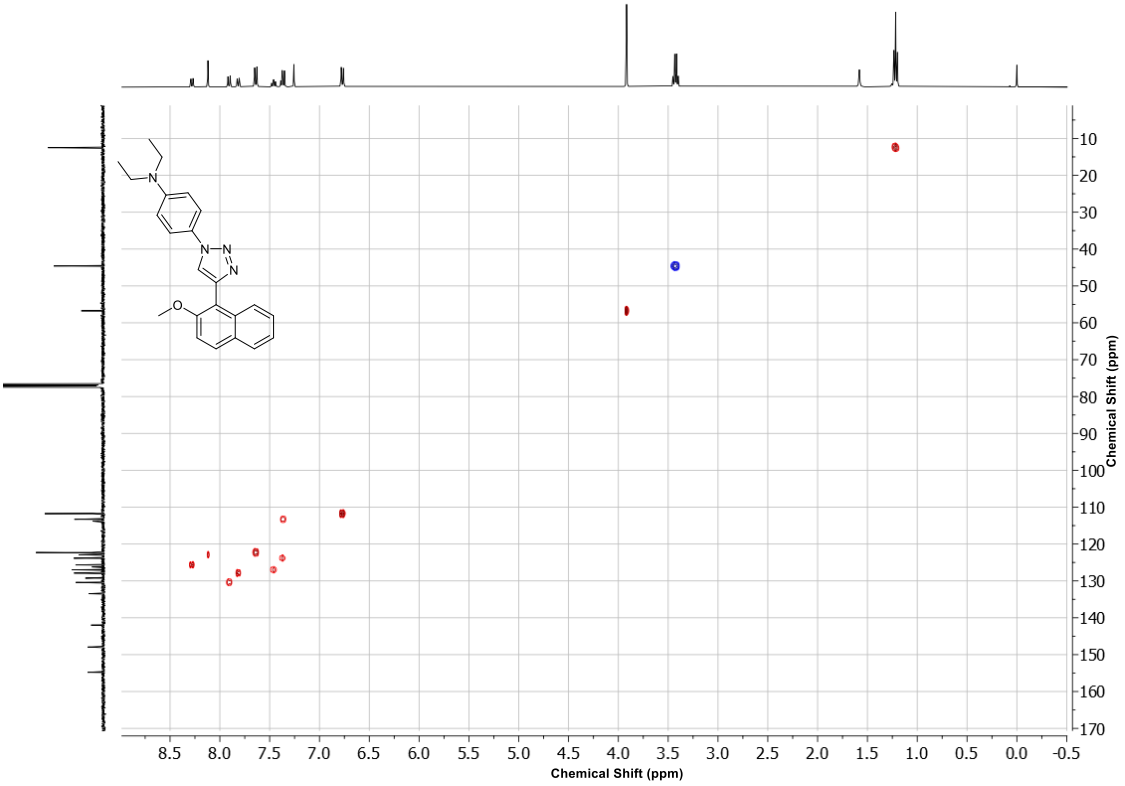

^{1}H-^{13}C HMBC NMR (400 MHz, $CDCl_3$) of **146**

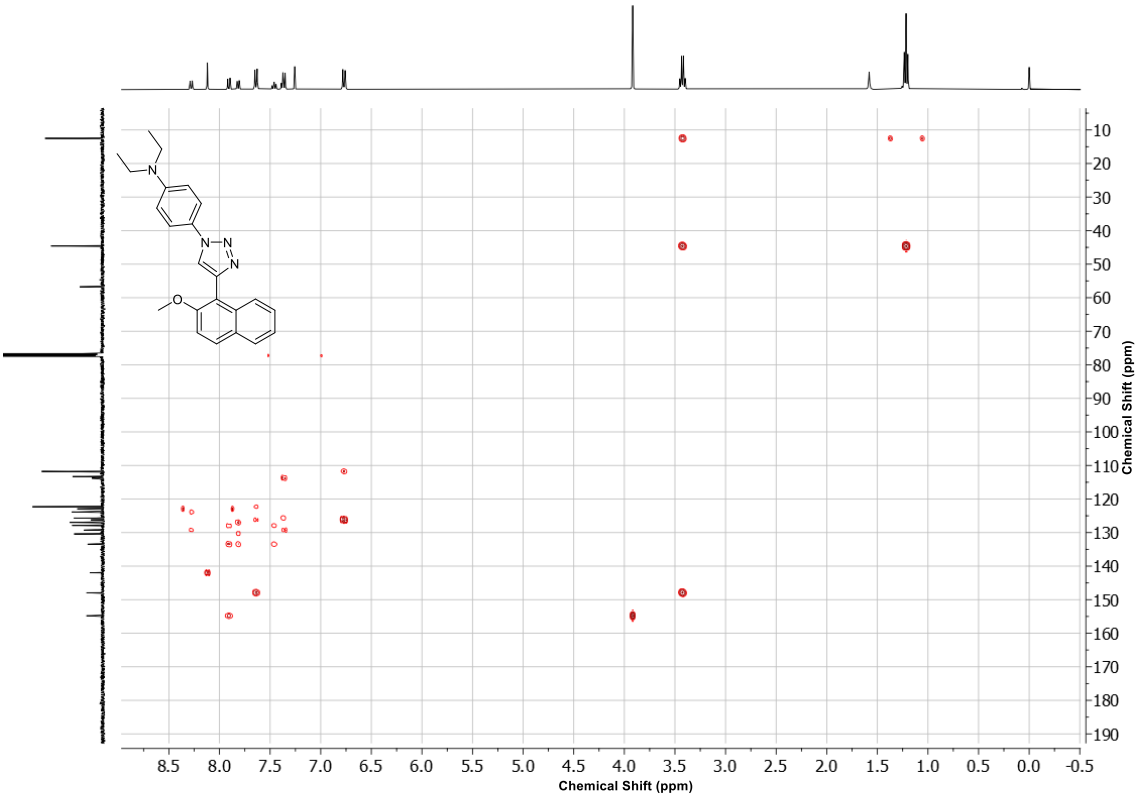

^{1}H-NMR (400 MHz, $CDCl_3$) of **160**

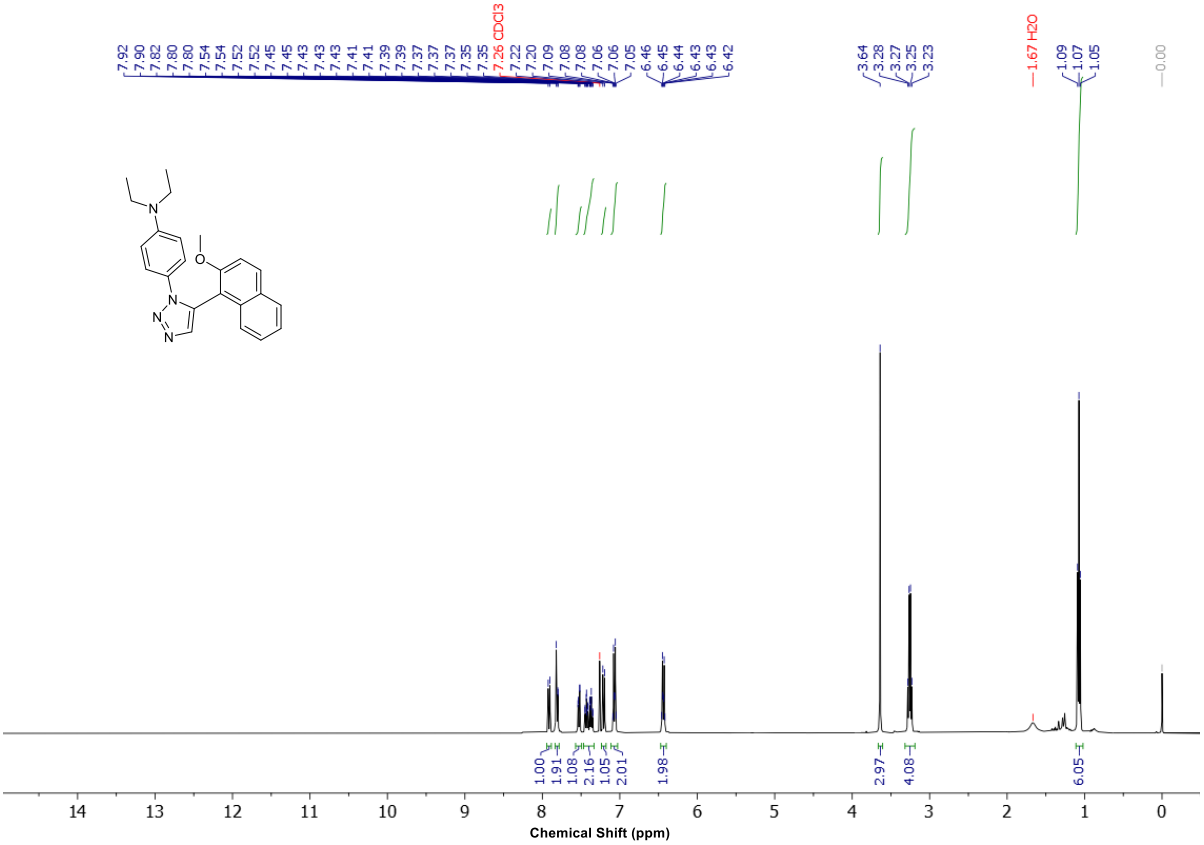

^{13}C-NMR (101 MHz, $CDCl_3$) of **160**

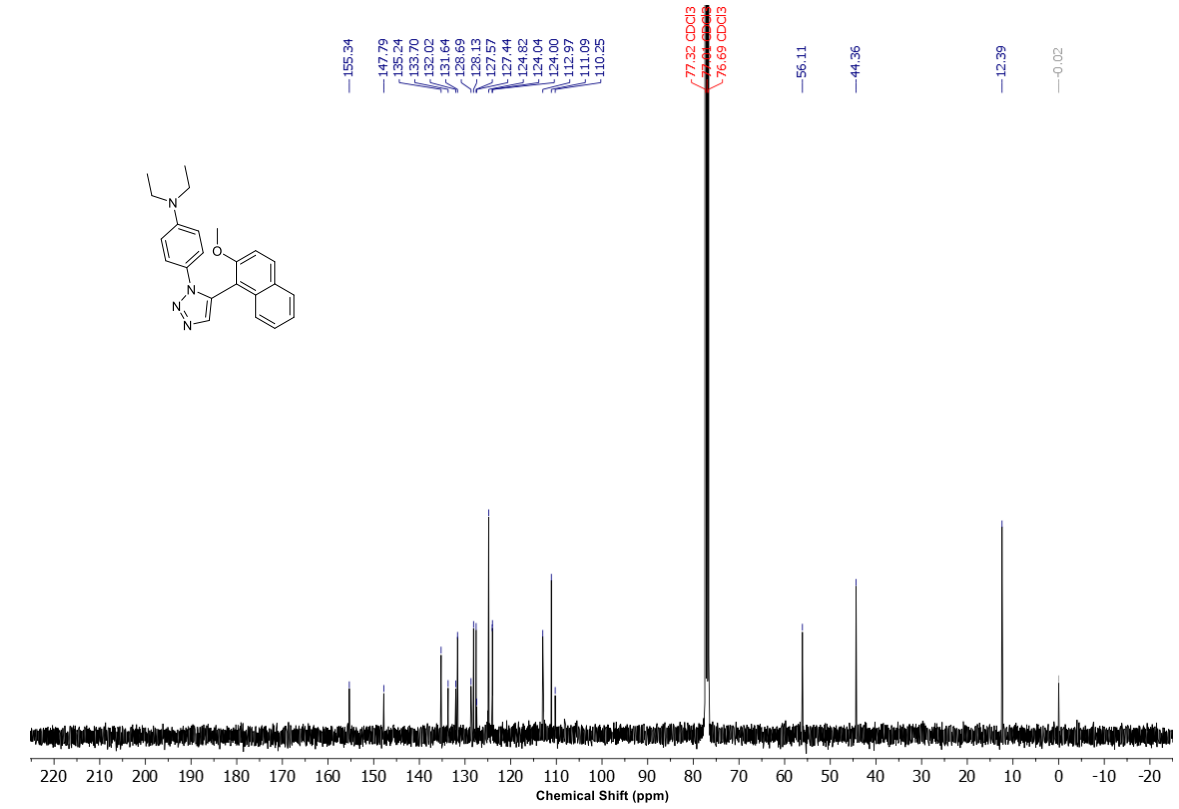

^{1}H-^{1}H NOESY NMR (400 MHz, $CDCl_3$) of **160**

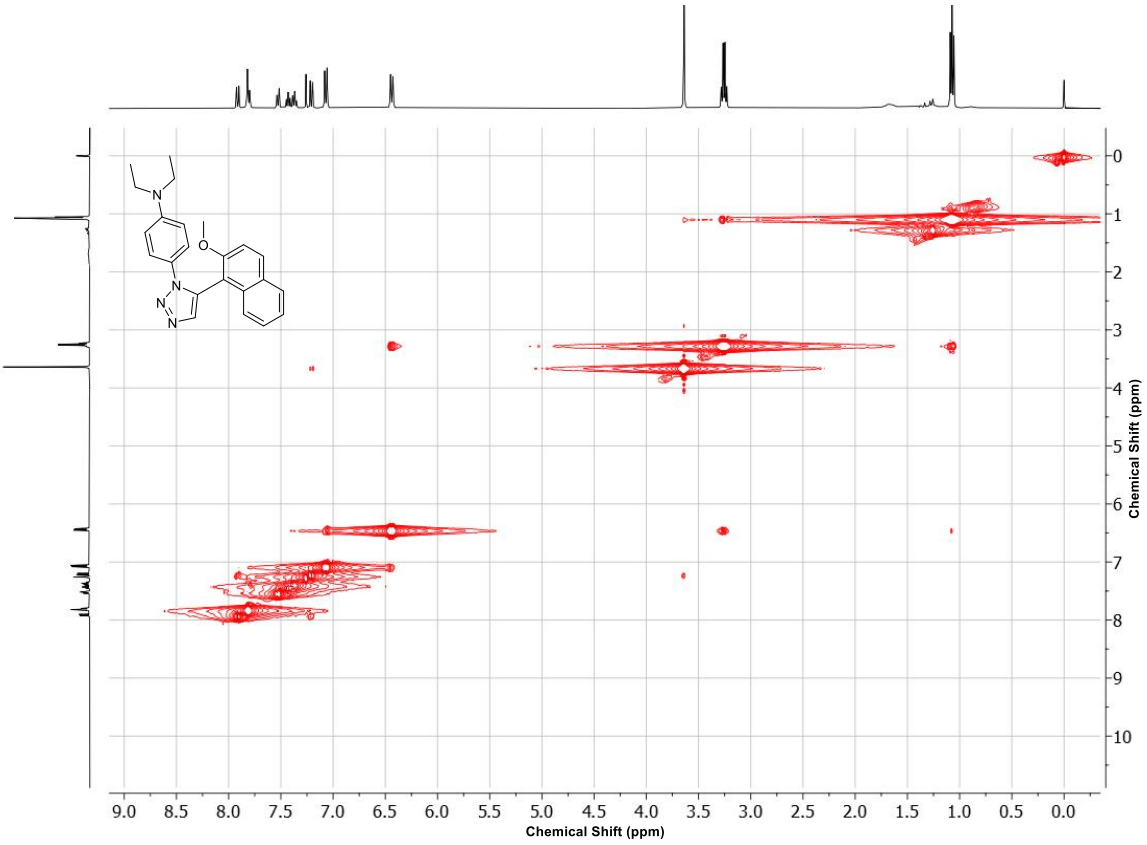

^{1}H-^{1}H COSY NMR (400 MHz, $CDCl_3$) of **160**

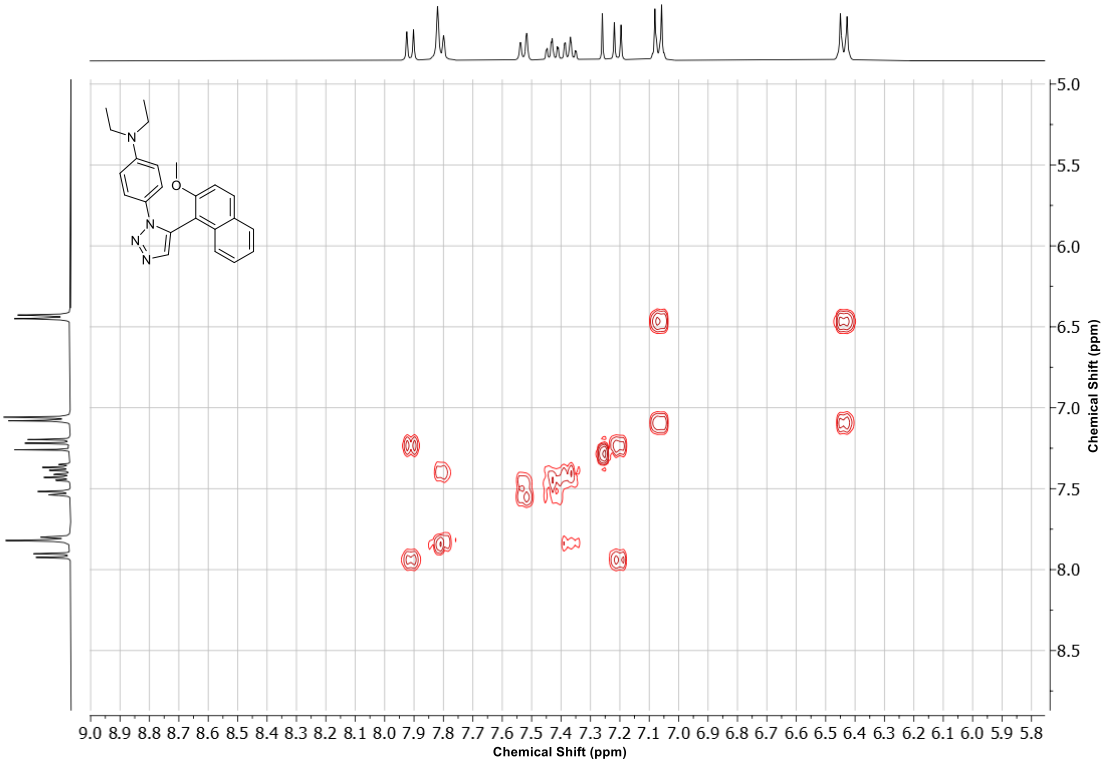

^{1}H-^{13}C HSQC NMR (400 MHz, $CDCl_3$) of **160**

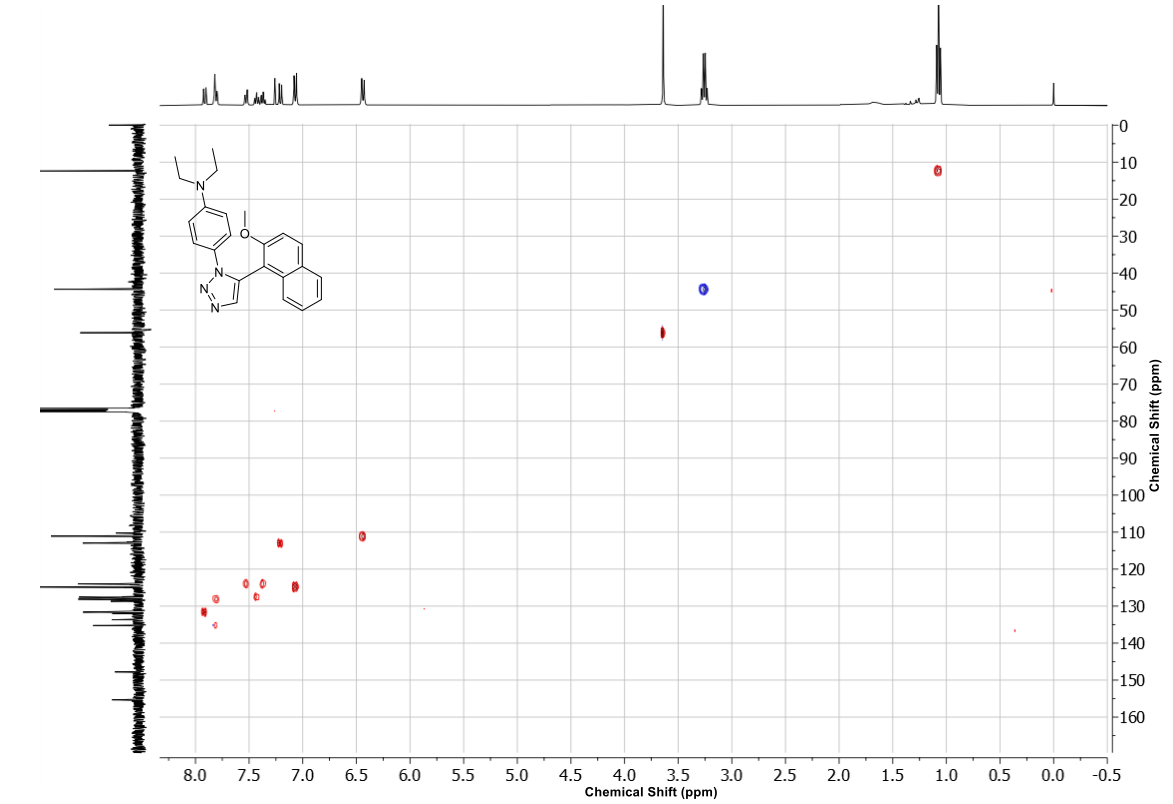

^{1}H-^{13}C HMBC NMR (400 MHz, $CDCl_3$) of **160**

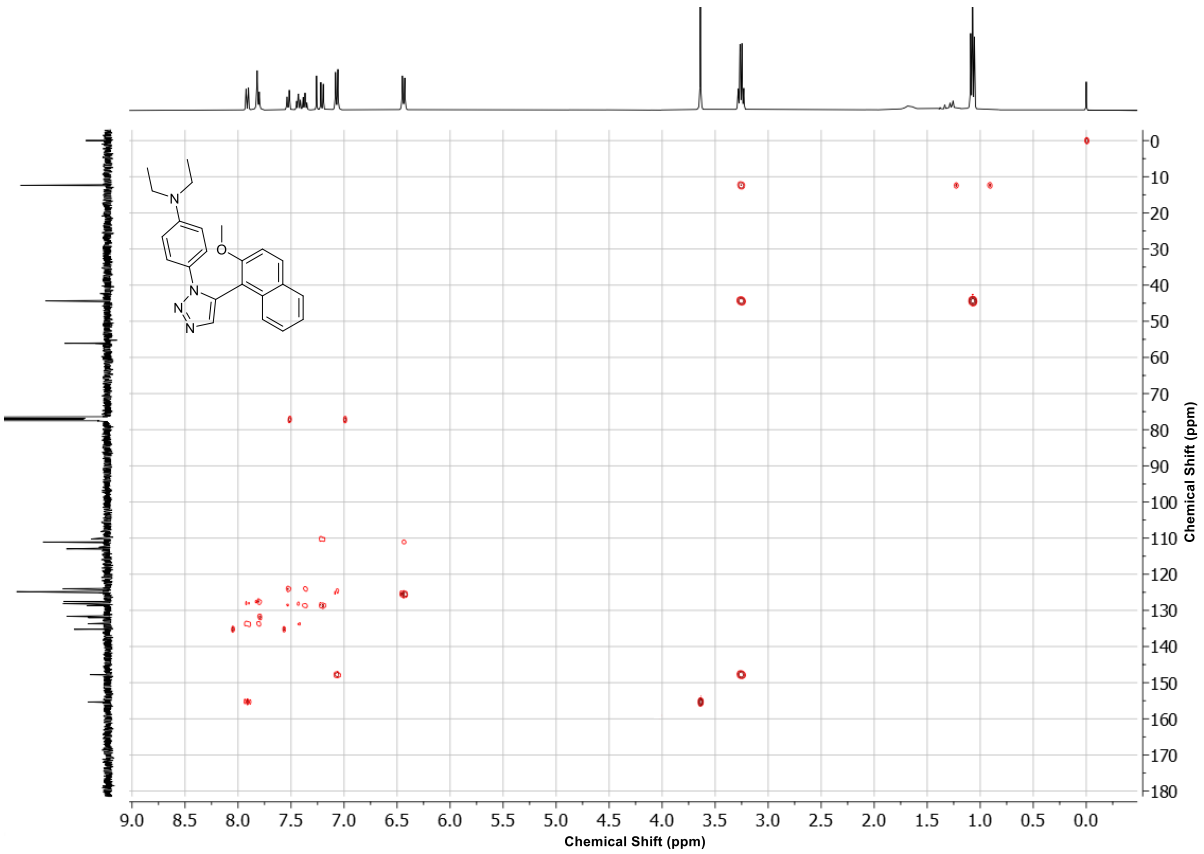

^{1}H-NMR (400 MHz, $CDCl_3$) of **196**

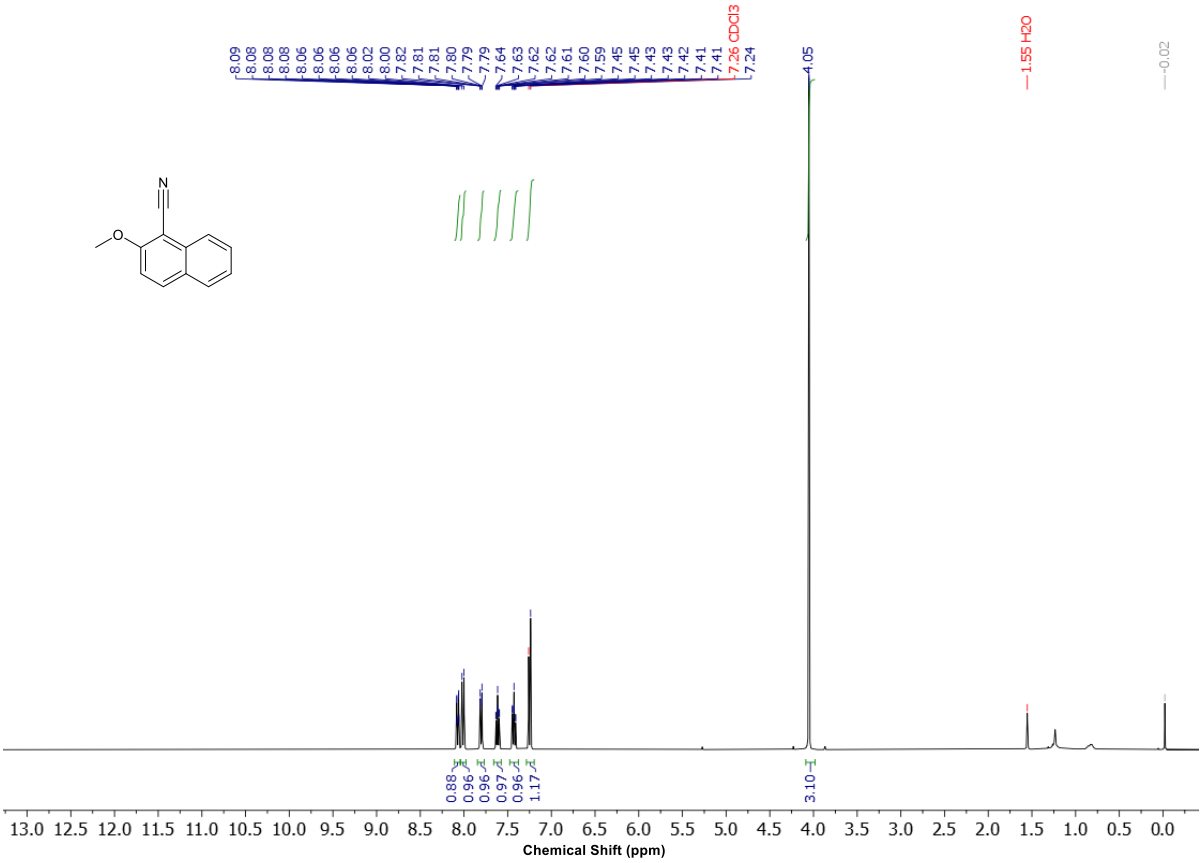

^{13}C-NMR (101 MHz, $CDCl_3$) of **196**

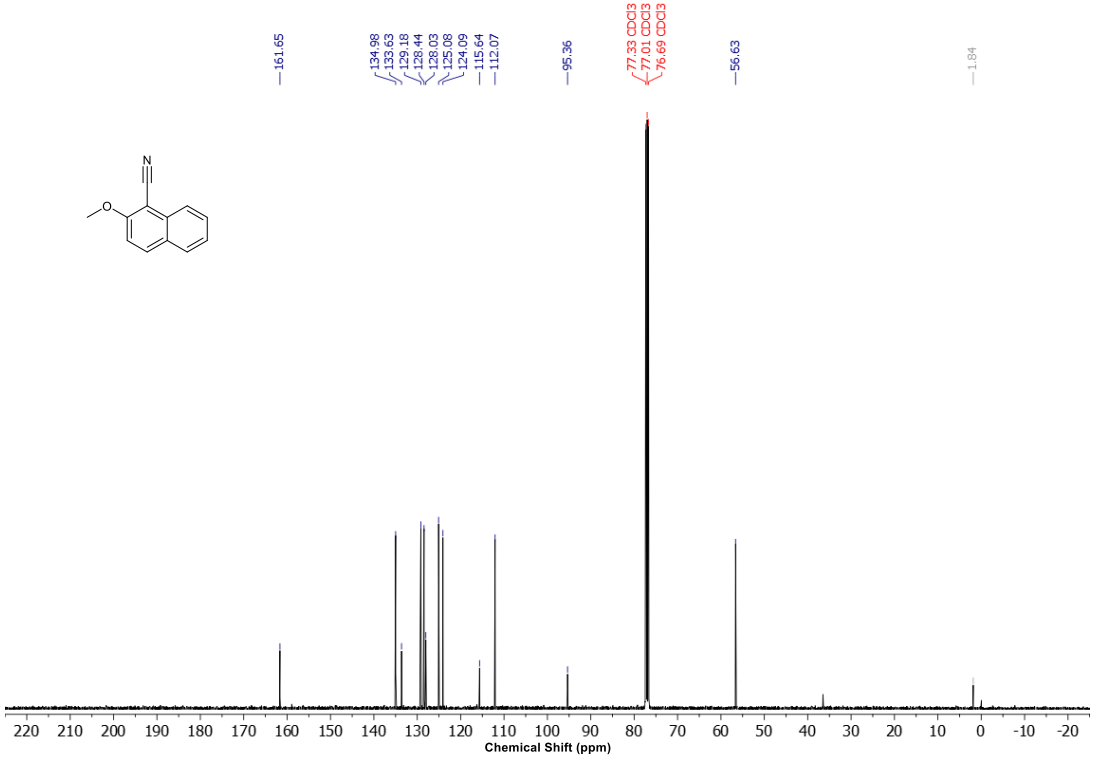

^{1}H-NMR (400 MHz, $CDCl_3$) of product isolated from synthesis of **197**

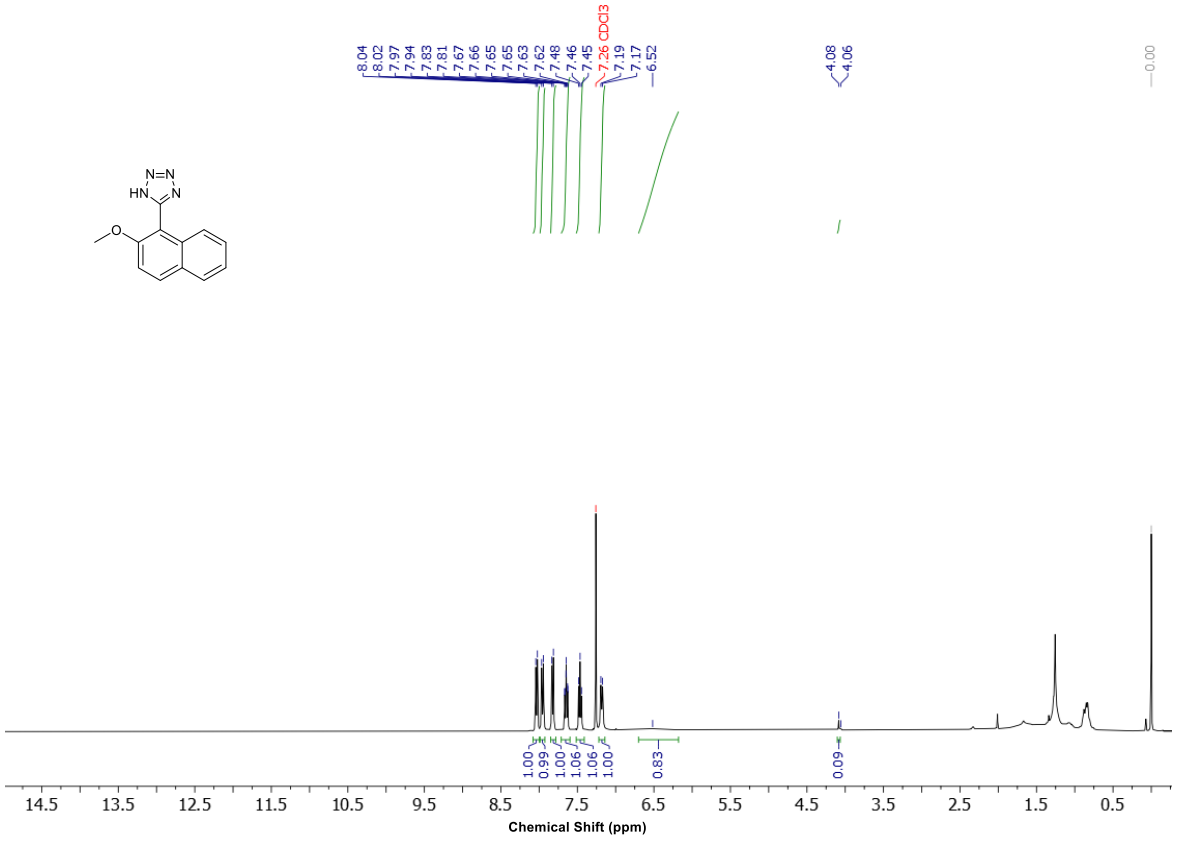

^{13}C-NMR (101 MHz, $CDCl_3$) of product isolated from synthesis of **197**

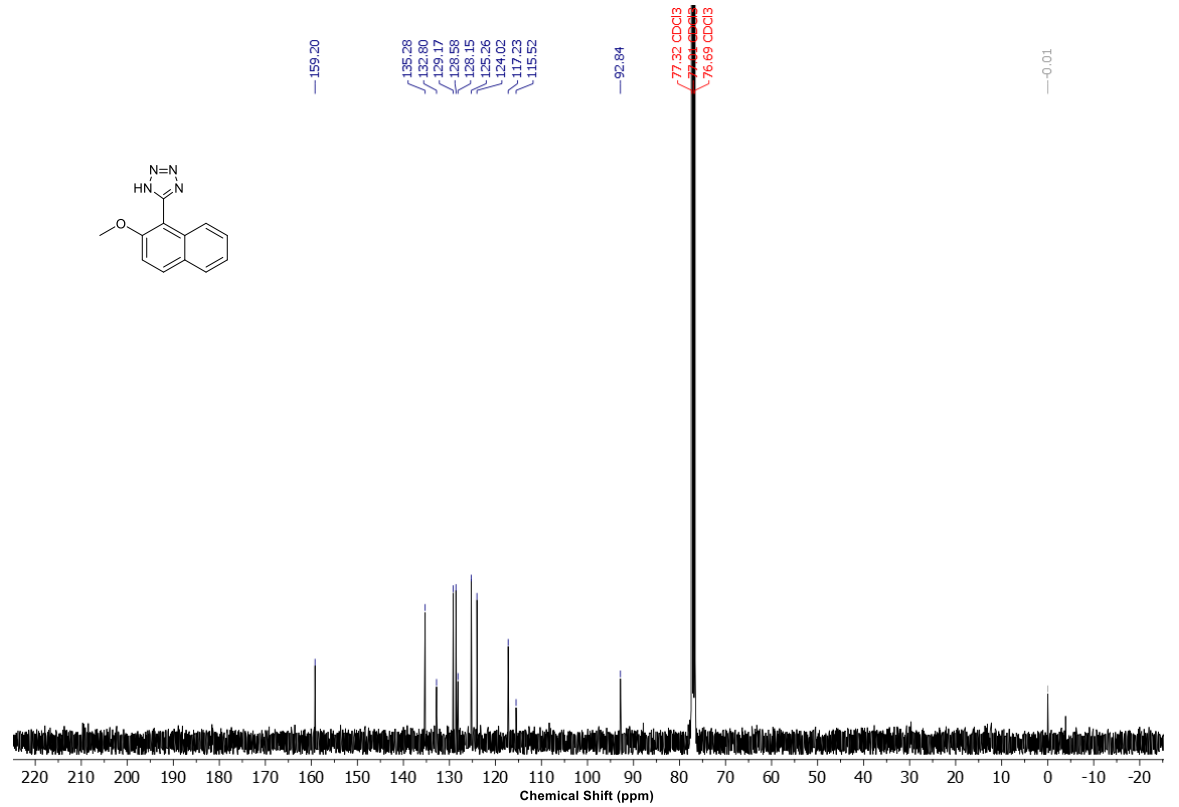

^{1}H-NMR (400 MHz, $CDCl_3$) of **211**

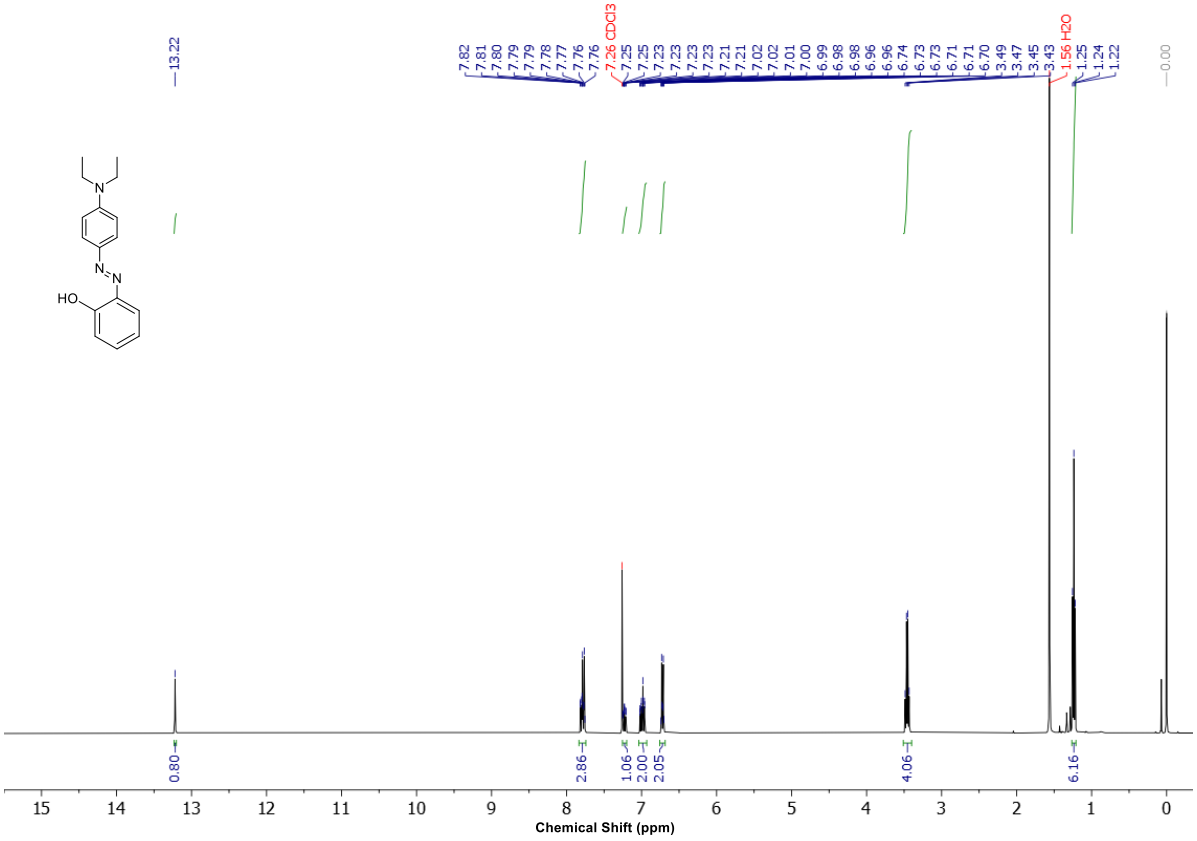

^{13}C-NMR (101 MHz, $CDCl_3$) of **211**

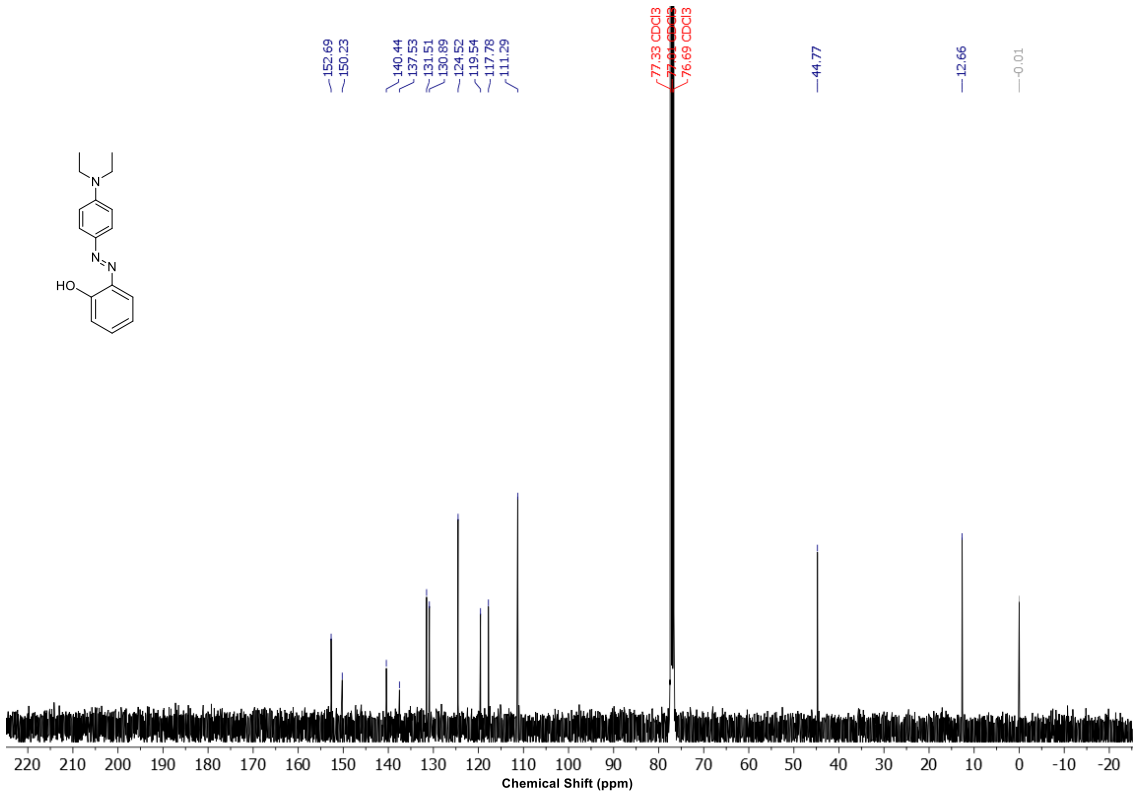

^{1}H-NMR (400 MHz, $CDCl_3$) of **224**

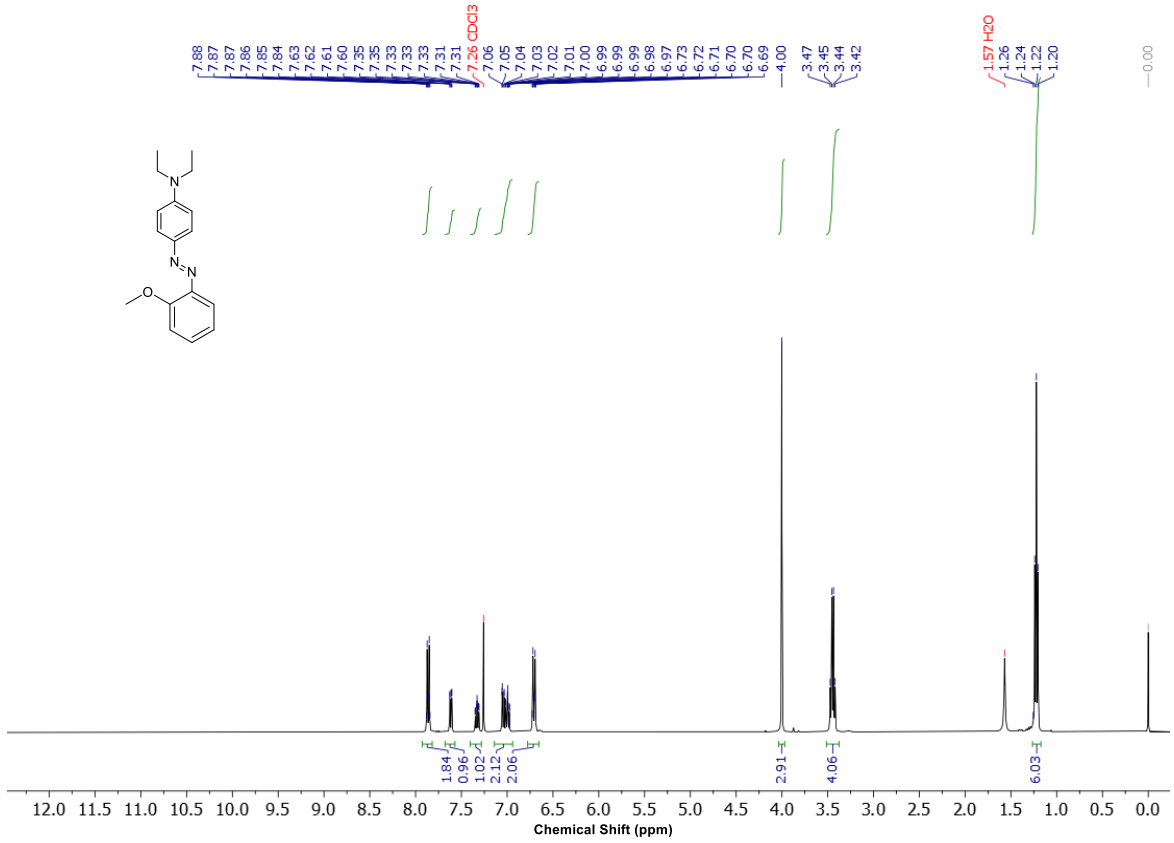

^{13}C-NMR (101 MHz, $CDCl_3$) of **224**